APPLICATION OF JOINT TIME-FREQUENCY METHODS AND ARTIFICIAL NEURAL NETWORKS FOR MONITORING CO-FIRING BURNERS

PALANIAPPAN VALLIAPPAN

A submission presented in partial fulfilment of the
requirements of the University of South Wales / Prifysgol De Cymru
for the degree of Doctor of Philosophy

This research programme was carried out in collaboration with

Institute Energitky

with partial funding from

Research Fund for Coal and Steel

University of South Wales
Faculty of Computing, Engineering and Science

2 Nov 2016

University of South Wales
Prifysgol De Cymru

Graduate Research Office
Swyddfa Ymchwil Graddedigion

R11

Certificate of Research

This is to certify that, except where specific reference is made, the work described in this thesis is the result of the candidate's research. Neither this thesis, nor any part of it, has been presented, or is currently submitted, in candidature for any degree at any other University.

Signed V. Palaniappan .....
Candidate

Date 12 MAY 2016 .....

Signed S. J. Wilcox .....
Director of Studies

Date 12/5/2016 .....

ABSTRACT

Conventional coal-fired burners are designed to operate within specific limits that, in part, result from the need to efficiently burn the fuel, ensure stable combustion and result in the lowest emissions. However, recent requirements to reduce CO_2 emissions from coal-fired boiler plant as part of the drive to reduce the carbon footprint of energy suppliers has focussed on the co-firing of biomass, primarily wood, either by delivering the pulverised biomass with the coal or through separate burners. Typically this approach has taken place at substitution levels of around 10 % or less by mass and at these levels the operation of the burner and boiler are not adversely affected. However, as the proportion of biomass is increased in a boiler designed for coal, the fuel characteristics of the blend moves further away from the burner design parameters. This can lead to combustion instabilities and in extreme cases extinction of the flame. In order to co-fire higher concentrations of biomass a system or technique is required that can detect the onset of these instabilities and warn before the combustion conditions become dangerous.

This research presents an investigation of a system that monitored the combustion flame using photodiodes with responses in the Ultra Violet (UV), Infrared (IR) and Visible (VIS) bands. The collected data was then processed using the Wigner-Ville Distribution (WVD) joint time-frequency method and subsequently classified using a Self-organising Map (SOM). It was found that it was possible to relate the classification of the sensor data to operational parameters such as the burner airflow rate, CO and NO_x emissions. Then using a simple rule based approach the developed system was successfully tested at pilot scale ($500\,kW_{th}$) where the ability of the system to optimise the combustion for a variety of unseen coal/biomass blends was demonstrated.

With wide range of operating conditions and the inherent complex nature of coal combustion, a set of stable conditions were recorded to be processed and train the developed system. Such a trained system was subsequently used for monitoring and was able to classify the conditions accurately. The system was also able to relate the sensor data to varying combustion conditions and hence suggest changes to bring the combustion back to a desired state. This system is capable of making such predictions correctly even with some variation in fuel properties and has been demonstrated to do so in both pilot and full scale power plants.

ACKNOWLEDGEMENTS

I would like to express my gratitude to Prof. Steve Wilcox, my director of studies for his guidance, support and encouragement through out my studies and the endless hours he spent reviewing my work and reports. I would also like to thank Dr. Alex Chong, Dr. CK Tan and Dr. Shee Meng Thai for their support during my research and writing up.

I would also like to acknowledge the funding from the European Union through the Research Fund for Coal and Steel (RFCS) which supported this research. Thanks to Dr. Krzysztof Jagiełło and his team at Institute Energitky - Institute of Power Engineering for their cooperation and expertise during the experiments at their pilot scale plant and later on at Dolna Odra power station in support of this research. Thanks to a number of colleagues and friends for their companionship and support during the project, namely Dr. Dirk Aljets, Francisco Sierra, Joao Ramos, Paul King, Alexander Matthews, Abel Ezimokhai, Mohammed Bisaye and Hedwalina Silva. Finally, thanks to my mother, father and siblings for their encouragement and support that enabled me to complete this research.

Contents

DECLARATION i

ABSTRACT ii

ACKNOWLEDGEMENTS iii

TABLE OF CONTENTS iv

LIST OF FIGURES viii

LIST OF TABLES xviii

GLOSSARY xx

SUBSCRIPT xxii

1 INTRODUCTION 1
- 1.1 Co-Firing Higher Proportions of Biomass . . . 1
  - 1.1.1 Flame Monitoring . . . 3
- 1.2 Aim and Objectives . . . 4
  - 1.2.1 Objectives . . . 4
- 1.3 Thesis Structure . . . 5

2 LITERATURE REVIEW 7
- 2.1 Energy Needs . . . 7
- 2.2 Importance of Coal . . . 8
- 2.3 Coal Power Plants . . . 8
- 2.4 Carbon Footprint . . . 9
  - 2.4.1 Industrial Needs . . . 9
  - 2.4.2 Coal's Footprint . . . 10
  - 2.4.3 Policy Enabling / Moving Towards Carbon Footprint Reduction . . . 10
- 2.5 Combustion Efficiency Improvements . . . 11
  - 2.5.1 NO_x Effects . . . 12
- 2.6 Biomass . . . 12
  - 2.6.1 Biomass for Energy . . . 13
  - 2.6.2 Biomass Combustion . . . 14
  - 2.6.3 Co-Firing Biomass . . . 15
- 2.7 Monitoring . . . 17
  - 2.7.1 Coal Flame Monitoring . . . 18

2.7.2 Camera & Image Processing . . . 19
2.7.3 Flame Flicker Monitoring . . . 20
2.7.4 Emission Spectroscopy . . . 21
2.7.5 Implications for Current Work . . . 22
2.8 Signal Processing . . . 22
2.8.1 Joint Time Frequency Domain . . . 23
2.8.2 Wigner-Ville Distribution . . . 25
2.9 Detection Algorithms . . . 26
2.9.1 Artificial Neural Network . . . 26
2.9.2 Application of Supervised ANN . . . 28
2.9.3 Deep Learning . . . 29
2.9.4 Fuzzy Logic . . . 29
2.9.5 Support Vector Machines . . . 30
2.9.6 Self-organising Map . . . 30
2.10 Summary . . . 31

3 EXPERIMENTAL APPARATUS & PROCEDURES 34
3.1 Pilot Scale – Experimental Apparatus . . . 34
3.1.1 Fuel Feed and Pre-Combustion Setup . . . 36
3.1.2 Burner and Combustion Chamber . . . 38
3.1.3 Existing Burner Control System . . . 41
3.2 Full Scale – Experimental Apparatus . . . 43
3.2.1 Fuel Feed and Pre-Combustion Setup . . . 43
3.2.2 Burner and Combustion Chamber . . . 45
3.2.3 Existing Burner Control System . . . 46
3.3 Fuel Characterisation . . . 48
3.3.1 Pilot Scale . . . 49
3.3.2 Full Scale . . . 50
3.4 Sensor Specification and Setup . . . 50
3.4.1 Instrumentation . . . 51
3.4.2 Sampling . . . 51
3.4.3 Pilot Scale . . . 51
3.4.4 Full Scale . . . 52
3.5 Experiments . . . 56
3.5.1 Pilot Scale . . . 56
3.5.2 Full Scale . . . 58
3.6 Summary . . . 59

4 EXPERIMENTS AND RESULTS 60
4.1 Time Domain . . . 60
4.2 Frequency Domain . . . 62
4.3 Joint Time Frequency Analysis . . . 65
4.3.1 Wavelets . . . 65
4.3.2 Wigner-Ville Distribution . . . 67
4.4 Summary . . . 70

5 MONITORING AND CONTROL SYSTEM DEVELOPMENT 71
5.1 Simple Set Point Based System 71
5.2 Artificial Neural Network 72
5.2.1 RMS Based ANN Modelling 73
5.2.2 PSD Based ANN Modelling 88
5.2.3 Wavelet Coefficients Based ANN Modelling 90
5.2.4 Review of Back Propagation ANN Based Results 92
5.2.5 Further Evaluation of ANN Based Prediction 95
5.2.6 Evaluation of Other Methods for Flame Stability Detection 106
5.3 Self-organising Map 106
5.3.1 WVD Preliminary Analysis 107
5.3.2 WVD Result Analysis for Experiments with Varying Secondary Air 107
5.3.3 SOM Based Control System Using WVD 116
5.3.4 SOM for NO_x Classification 121
5.3.5 SOM for CO Classification 124
5.4 Control System – Training and Application of SOM Model 130
5.5 Summary 133

6 MONITORING AND CONTROL SYSTEM - TESTING AND RESULTS 134
6.1 Pilot Scale Testing 134
6.1.1 Experiments 134
6.1.2 Results & Discussion 136
6.2 Full Scale Testing 149
6.2.1 Experiments 149
6.2.2 Results & Discussion - Single Burner 150
6.2.3 Results & Discussion - Multi-Burner Balancing 155
6.3 Summary 156

7 CONCLUSIONS AND FURTHER WORK 157
7.1 Conclusions 157
7.2 Recommendations for Further Work 159

Bibliography 160

Appendices 175

A DEVELOPED CODE 176
A.1 Supervised ANN 176
A.2 Supervised ANN with PCA 179
A.3 Developed Algorithm 182

B SIGNAL PROCESSING RESULTS 190
B.1 RMS results 190
B.2 FFT results 195
B.3 PSD results 224
B.4 Wavelet results 229

B.5 WVD results 234

C WVD Results **247**

C.1 Results for experiments with varying secondary airflow 247

C.1.1 UV Sensor 247

C.1.2 VIS Sensor 251

List of Figures

1.1 Common obstacles faced with cofiring [9, 23] 2

2.1 A sample signal with two distinct frequencies over time 24
2.2 FFT of sample signal 24
2.3 JTF of sample signal 24
2.4 SOM - 5x5 grid of neurons 31
2.5 SOM - showing an activated / winning neuron 31

3.1 Overall schematic of pilot scale CTF 35
3.2 CTF with sensor location highlighted with regards to the combustion chamber layout 36
3.3 Fuel feed system showing hopper, feed mechanism and carrier air piping 37
3.4 CTF image showing the connections to the burner 38
3.5 Side view of burner cross section with the sighting tube for the sensors 39
3.6 Production drawing of CTF front plate for the burner end 40
3.7 Picture of CTF front plate for the burner end 41
3.8 Location of the flue gas sampling probes and thermocouples on the CTF 42
3.9 Gas analyser(s) used during experiments 43
3.10 Overall layout of boiler eight at Dolna Odra power station 44
3.11 Temperature profile on the investigated level (lowest row of burners) on the basis of CFD simulation of the boiler from Dolna Odra power plant 45
3.12 Gas sampling probe mounted to the observation port on the left and a close up view of the gas sampling probe on the right 47
3.13 Gas analyser setup with laptop for recording the data 48
3.14 Schematic of the instrumenation - showing a sensor, amplifier and filter 52
3.15 Picture showing the instrumentation box connected to a trifurcated fibre optic cable and lens assembly 53
3.16 Production drawing of sighting tube to mount lens assembly and purge / cooling air 53
3.17 Picture of the sighting tube to mount the lens assembly and purge / cooling air 54
3.18 Probe mount attached to the observation port next to the burner 55

4.1 RMS of UV, VIS & IR photodiode signals Vs averaged O_2 for Tests 1 to 9 - 100 % Coal - 50° Swirl 61
4.2 FFT of UV photodiode signal for Tests 1 to 9 - 100 % Coal - 50° Swirl 63
4.3 PSD of UV, VIS & IR photodiode signals Vs averaged O_2 for Tests 1 to 9 - 100 % Coal - 50° Swirl 64
4.4 Wavelet packet decomposition tree to level 3 66
4.5 RMS of largest wavelet coefficient of UV, VIS & IR photodiode signals Vs averaged O_2 for Tests 1 to 9 - 100 % Coal - 50° Swirl . 66
4.6 WVD (averaged) of UV photodiode signal for Tests 1 to 9 - 100 % Coal - 50° Swirl 68
4.7 WVD (averaged) of VIS photodiode signal for Tests 1 to 9 - 100 % Coal - 50° Swirl 69
4.8 WVD (averaged) of IR photodiode signal for Tests 1 to 9 - 100 % Coal - 50° Swirl 69

5.1 ANN sampling for training and testing 73
5.2 ANN prediction of NO_x - Training & Testing - trained with RMS - 10 hidden neurons 74
5.3 ANN prediction of NO_x - Validation - trained with RMS - 10 hidden neurons 75
5.4 ANN prediction of NO_x - Training & Testing - trained with RMS - 12 hidden neurons 76
5.5 ANN prediction of NO_x - Validation - trained with RMS - 12 hidden neurons 76
5.6 ANN prediction of NO_x - Training & Testing - trained with RMS - 15 hidden neurons 77
5.7 ANN prediction of NO_x - Validation - trained with RMS - 15 hidden neurons 78
5.8 ANN prediction of NO_x - Training & Testing - trained with RMS - 20 hidden neurons 78
5.9 ANN prediction of NO_x - Validation - trained with RMS - 20 hidden neurons 79
5.10 ANN prediction of NO_x - Training & Testing - trained with RMS - 25 hidden neurons 80
5.11 ANN prediction of NO_x - Validation - trained with RMS - 25 hidden neurons 80
5.12 ANN prediction of O_2 - Training & Testing - trained with RMS - 10 hidden neurons 81
5.13 ANN prediction of O_2 - Validation - trained with RMS - 10 hidden neurons 82
5.14 ANN prediction of O_2 - Training & Testing - trained with RMS - 12 hidden neurons 83
5.15 ANN prediction of O_2 - Validation - trained with RMS - 12 hidden neurons 83
5.16 ANN prediction of O_2 - Training & Testing - trained with RMS - 15 hidden neurons 84

5.17 ANN prediction of O_2 - Validation - trained with RMS - 15 hidden neurons . . . 85
5.18 ANN prediction of O_2 - Training & Testing - trained with RMS - 20 hidden neurons . . . 85
5.19 ANN prediction of O_2 - Validation - trained with RMS - 20 hidden neurons . . . 86
5.20 ANN prediction of O_2 - Training & Testing - trained with RMS - 25 hidden neurons . . . 87
5.21 ANN prediction of O_2 - Validation - trained with RMS - 25 hidden neurons . . . 87
5.22 ANN prediction of NO_x - Validation - trained with PSD - 15 hidden neurons . . . 89
5.23 ANN prediction of O_2 - Validation - trained with PSD - 10 hidden neurons . . . 90
5.24 ANN prediction of NO_x - Validation - trained with wavelet coefficients - 25 hidden neurons . . . 91
5.25 ANN prediction of O_2 - Validation - trained with PSD - 15 hidden neurons . . . 92
5.26 ANN prediction of NO_x - Validation - trained with RMS, PSD and RMS of the best wavelet coefficients - 20 hidden neurons . . . 94
5.27 ANN prediction of O_2 - Validation - trained with RMS, PSD and RMS of the best wavelet coefficients - 25 hidden neurons . . . 95
5.28 ANN prediction of NO_x - Validation - trained with RMS, PSD and RMS of the best wavelet coefficients - 12 hidden neurons . . . 96
5.29 ANN prediction of O_2 - Validation - trained with RMS, PSD and RMS of the best wavelet coefficients - 10 hidden neurons . . . 97
5.30 ANN prediction of NO_x - Validation - trained with RMS, PSD and RMS of the best wavelet coefficients with PCA - 10 hidden neurons . . . 99
5.31 ANN prediction of O_2 - Validation - trained with RMS, PSD and RMS of the best wavelet coefficients with PCA - 25 hidden neurons 100
5.32 ANN prediction of NO_x - Validation - trained with RMS, PSD and RMS of the best wavelet coefficients with PCA - 10 hidden neurons . . . 101
5.33 ANN prediction of O_2 - Validation - trained with RMS, PSD and RMS of the best wavelet coefficients with PCA - 12 hidden neurons 102
5.34 ANN prediction of total airflow - Validation - trained with RMS, PSD and RMS of the best wavelet coefficients with PCA - 12 hidden neurons . . . 104
5.35 ANN prediction of total airflow - Validation - trained with RMS, PSD and RMS of the best wavelet coefficients with PCA - 25 hidden neurons . . . 105
5.36 Test 98 – "normal conditions", secondary air flow: 160 Nm^3/h . . 108
5.37 Test 98 – "decreased excess air", secondary air flow: 50 Nm^3/h . . 108
5.38 Test 98 – "increased excess air", secondary air flow: 280 Nm^3/h . 108
5.39 WVD of the IR sensor signal for the test (Test 97a) with decreasing secondary air with 100 % coal . . . 110

5.40 NO_x / CO Emissions and Total Airflow recorded for the test (Test 97a) with decreasing secondary air with 100 % coal 110
5.41 WVD of the IR sensor signal for the test (Test 98a) with decreasing secondary air with 90 % coal & 10 % biomass 111
5.42 NO_x / CO Emissions and Total Airflow recorded for the test (Test 98a) with decreasing secondary air with 90 % coal & 10 % biomass 111
5.43 WVD of the IR sensor signal for the test (Test 99a) with decreasing secondary air with 80 % coal & 20 % biomass 112
5.44 NO_x / CO Emissions and Total Airflow recorded for the test (Test 99a) with decreasing secondary air with 80 % coal & 20 % biomass 112
5.45 WVD of the IR sensor signal for the test (Test 97b) with increasing secondary air with 100 % coal 113
5.46 NO_x / CO Emissions and Total Airflow recorded for the test (Test 97b) with increasing secondary air with 100 % coal 113
5.47 WVD of the IR sensor signal for the test (Test 98b) with increasing secondary air with 90 % coal & 10 % biomass 114
5.48 NO_x / CO Emissions and Total Airflow recorded for the test (Test 98b) with increasing secondary air with 90 % coal & 10 % biomass 114
5.49 WVD of the IR sensor signal for the test (Test 99b) with increasing secondary air with 80 % coal & 20 % biomass 115
5.50 NO_x / CO Emissions and Total Airflow recorded for the test (Test 99b) with increasing secondary air with 80 % coal & 20 % biomass 115
5.51 Total airflow vs instability prediction - 100 % Coal - decreasing secondary air from stable condition 117
5.52 Total airflow vs instability prediction - 100 % Coal - increasing secondary air from stable condition 117
5.53 Total airflow vs instability prediction - 90 % Coal & 10 % Biomass - decreasing secondary air from stable condition 118
5.54 Total airflow vs instability prediction - 90 % Coal & 10 % Biomass - increasing secondary air from stable condition 119
5.55 Total airflow vs instability prediction - 80 % Coal & 20 % Biomass - decreasing secondary air from stable condition 120
5.56 Total airflow vs instability prediction - 80 % Coal & 20 % Biomass - increasing secondary air from stable condition 121
5.57 NO_x measured vs prediction - 100 % Coal - decreasing secondary air from stable condition 122
5.58 NO_x measured vs prediction - 100 % Coal - increasing secondary air from stable condition 122
5.59 NO_x measured vs prediction - 90 % Coal & 10 % Biomass - decreasing secondary air from stable condition 123
5.60 NO_x measured vs prediction - 90 % Coal & 10 % Biomass - increasing secondary air from stable condition 123
5.61 NO_x measured vs prediction - 80 % Coal & 20 % Biomass - decreasing secondary air from stable condition 125

5.62 NO_x measured vs prediction - 80 % Coal & 20 % Biomass - increasing secondary air from stable condition 125
5.63 CO measured vs prediction - 100 % Coal - decreasing secondary air from stable condition 126
5.64 CO measured vs prediction - 100 % Coal - increasing secondary air from stable condition 126
5.65 CO measured vs prediction - 90 % Coal & 10 % Biomass - decreasing secondary air from stable condition 128
5.66 CO measured vs prediction - 90 % Coal & 10 % Biomass - increasing secondary air from stable condition 128
5.67 CO measured vs prediction - 80 % Coal & 20 % Biomass - decreasing secondary air from stable condition 129
5.68 CO measured vs prediction - 80 % Coal & 20 % Biomass - increasing secondary air from stable condition 129
5.69 Algorithm for training the SOM model 131
5.70 Algorithm for application of the SOM model 132

6.1 Schematic of the Monitoring, Control and Optimisation (MCO) system 136
6.2 Comparison of Actual Vs Predicted NO_x in relation to Total airflow for 90 % Janina Coal + 10 % Biomass (Test P1 of Table 6.1) 137
6.3 Comparison of Actual Vs Predicted CO in relation to Total airflow for 90 % Janina Coal + 10 % Biomass (Test P1 of Table 6.1) . . . 138
6.4 Comparison of Actual Vs Predicted NO_x in relation to Total airflow for 90 % Janina Coal + 10 % Biomass (Test P2 of Table 6.1) 139
6.5 Comparison of Actual Vs Predicted NO_x in relation to Total airflow for 90 % Janina Coal + 10 % Biomass (Test P2 of Table 6.1) 140
6.6 Comparison of Actual Vs Predicted NO_x in relation to Total airflow for 100 % Russian Coal (Test P3 of Table 6.1) 141
6.7 Comparison of Actual Vs Predicted NO_x in relation to Total airflow for 100 % Russian Coal (Test P3 of Table 6.1) 142
6.8 Comparison of Actual Vs Predicted NO_x in relation to Total airflow for 100 % Russian Coal (Test P4 of Table 6.1) 143
6.9 Comparison of Actual Vs Predicted NO_x in relation to Total airflow for 100 % Russian Coal (Test P4 of Table 6.1) 144
6.10 Comparison of Actual Vs Predicted NO_x in relation to Total airflow for 100 % Russian Coal (Test P5 of Table 6.1) 145
6.11 Comparison of Actual Vs Predicted NO_x in relation to Total airflow for 100 % Russian Coal (Test P5 of Table 6.1) 146
6.12 Comparison of Actual Vs Predicted NO_x in relation to Total airflow for 100 % Russian Coal (Test P6 of Table 6.1) 147
6.13 Comparison of Actual Vs Predicted NO_x in relation to Total airflow for 100 % Russian Coal (Test P6 of Table 6.1) 148
6.14 Comparison of Actual Vs Predicted NO_x in relation to Total airflow for 100 % Coal F at thermal load of 15 000 kg/h (to the lowest level of burners)(Test F1 of Table 6.2) 151

6.15 Comparison of Actual Vs Predicted CO in relation to Total airflow for 100 % Coal F at thermal load of 15 000 kg/h (to the lowest level of burners)(Test F1 of Table 6.2) 152
6.16 Comparison of Actual Vs Predicted NO_x in relation to Total airflow for 100 % Coal E at thermal load of 20 000 kg/h (to the lowest level of burners)(Test F2 of Table 6.2) 153
6.17 Comparison of Actual Vs Predicted NO_x in relation to Total airflow for 90 % Coal H + 10 % Biomass at thermal load of 15 000 kg/h (to the lowest level of burners)(Test F3 of Table 6.2) 154
6.18 Comparison of predicted NO_x in burners 1 and 2 in relation to Total airflow for 100 % Coal at thermal load of 20 000 kg/h (to the lowest level of burners)(Test F2 of Table 6.2) 155

A.1 MCO system front panel in LabVIEW 182
A.2 MCO system DAQ initialisation 182
A.3 MCO system DAQ recording for 30 s 183
A.4 Calculating the WVD for three sensor data and calling the SOM matlab function to do the prediction 183

B.1 RMS of UV, VIS & IR photodiode signals Vs averaged O_2 for Tests 10 to 18 - 90 % Coal & 10 % Straw - 50° Swirl 190
B.2 RMS of UV, VIS & IR photodiode signals Vs averaged O_2 for Tests 82 to 90 - 80 % Coal & 20 % Straw - 50° Swirl 191
B.3 RMS of UV, VIS & IR photodiode signals Vs averaged O_2 for Tests 55 to 63 - 70 % Coal & 30 % Straw - 60° Swirl 191
B.4 RMS of UV, VIS & IR photodiode signals Vs averaged O_2 for Tests 37 to 45 - 100 % Coal - 60° Swirl 192
B.5 RMS of UV, VIS & IR photodiode signals Vs averaged O_2 for Tests 46 to 54 - 90 % Coal & 10 % Straw - 60° Swirl 192
B.6 RMS of UV, VIS & IR photodiode signals Vs averaged O_2 for Tests 64 to 72 - 80 % Coal & 20 % Straw - 60° Swirl 193
B.7 RMS of UV, VIS & IR photodiode signals Vs averaged O_2 for Tests 28 to 36 - 100 % Coal - 40° Swirl 193
B.8 RMS of UV, VIS & IR photodiode signals Vs averaged O_2 for Tests 19 to 27 - 90 % Coal & 10 % Straw - 40° Swirl 194
B.9 RMS of UV, VIS & IR photodiode signals Vs averaged O_2 for Tests 73 to 81 - 80 % Coal & 20 % Straw - 40° Swirl 194
B.10 FFT of VIS photodiode signal for Tests 1 to 9 - 100 % Coal - 50° Swirl 195
B.11 FFT of IR photodiode signal for Tests 1 to 9 - 100 % Coal - 50° Swirl 196
B.12 FFT of UV photodiode signal for Tests 10 to 18 - 90 % Coal & 10 % Straw - 50° Swirl 197
B.13 FFT of VIS photodiode signal for Tests 10 to 18 - 90 % Coal & 10 % Straw - 50° Swirl 198
B.14 FFT of IR photodiode signal for Tests 10 to 18 - 90 % Coal & 10 % Straw - 50° Swirl 199
B.15 FFT of UV photodiode signal for Tests 82 to 90 - 80 % Coal & 20 % Straw - 50° Swirl 200

B.16 FFT of VIS photodiode signal for Tests 82 to 90 - 80 % Coal & 20 % Straw - 50° Swirl 201
B.17 FFT of IR photodiode signal for Tests 82 to 90 - 80 % Coal & 20 % Straw - 50° Swirl 202
B.18 FFT of UV photodiode signal for Tests 55 to 63 - 70 % Coal & 30 % Straw - 60° Swirl 203
B.19 FFT of VIS photodiode signal for Tests 55 to 63 - 70 % Coal & 30 % Straw - 60° Swirl 204
B.20 FFT of IR photodiode signal for Tests 55 to 63 - 70 % Coal & 30 % Straw - 60° Swirl 205
B.21 FFT of UV photodiode signal for Tests 37 to 45 - 100 % Coal - 60° Swirl 206
B.22 FFT of VIS photodiode signal for Tests 37 to 45 - 100 % Coal - 60° Swirl 207
B.23 FFT of IR photodiode signal for Tests 37 to 45 - 100 % Coal - 60° Swirl 208
B.24 FFT of UV photodiode signal for Tests 46 to 54 - 90 % Coal & 10 % Straw - 60° Swirl 209
B.25 FFT of VIS photodiode signal for Tests 46 to 54 - 90 % Coal & 10 % Straw - 60° Swirl 210
B.26 FFT of IR photodiode signal for Tests 46 to 54 - 90 % Coal & 10 % Straw - 60° Swirl 211
B.27 FFT of UV photodiode signal for Tests 64 to 72 - 80 % Coal & 20 % Straw - 60° Swirl 212
B.28 FFT of VIS photodiode signal for Tests 64 to 72 - 80 % Coal & 20 % Straw - 60° Swirl 213
B.29 FFT of IR photodiode signal for Tests 64 to 72 - 80 % Coal & 20 % Straw - 60° Swirl 214
B.30 FFT of UV photodiode signal for Tests 28 to 36 - 100 % Coal - 40° Swirl 215
B.31 FFT of VIS photodiode signal for Tests 28 to 36 - 100 % Coal - 40° Swirl 216
B.32 FFT of IR photodiode signal for Tests 28 to 36 - 100 % Coal - 40° Swirl 217
B.33 FFT of UV photodiode signal for Tests 19 to 27 - 90 % Coal & 10 % Straw - 40° Swirl 218
B.34 FFT of VIS photodiode signal for Tests 19 to 27 - 90 % Coal & 10 % Straw - 40° Swirl 219
B.35 FFT of IR photodiode signal for Tests 19 to 27 - 90 % Coal & 10 % Straw - 40° Swirl 220
B.36 FFT of UV photodiode signal for Tests 73 to 81 - 80 % Coal & 20 % Straw - 40° Swirl 221
B.37 FFT of VIS photodiode signal for Tests 73 to 81 - 80 % Coal & 20 % Straw - 40° Swirl 222
B.38 FFT of IR photodiode signal for Tests 73 to 81 - 80 % Coal & 20 % Straw - 40° Swirl 223
B.39 PSD of UV, VIS & IR photodiode signals Vs averaged O_2 for Tests 10 to 18 - 90 % Coal & 10 % Straw - 50° Swirl 224

B.40 PSD of UV, VIS & IR photodiode signals Vs averaged O_2 for Tests 82 to 90 - 80 % Coal & 20 % Straw - 50° Swirl 225
B.41 PSD of UV, VIS & IR photodiode signals Vs averaged O_2 for Tests 55 to 63 - 70 % Coal & 30 % Straw - 60° Swirl 225
B.42 PSD of UV, VIS & IR photodiode signals Vs averaged O_2 for Tests 37 to 45 - 100 % Coal - 60° Swirl 226
B.43 PSD of UV, VIS & IR photodiode signals Vs averaged O_2 for Tests 46 to 54 - 90 % Coal & 10 % Straw - 60° Swirl 226
B.44 PSD of UV, VIS & IR photodiode signals Vs averaged O_2 for Tests 64 to 72 - 80 % Coal & 20 % Straw - 60° Swirl 227
B.45 PSD of UV, VIS & IR photodiode signals Vs averaged O_2 for Tests 28 to 36 - 100 % Coal - 40° Swirl 227
B.46 PSD of UV, VIS & IR photodiode signals Vs averaged O_2 for Tests 19 to 27 - 90 % Coal & 10 % Straw - 40° Swirl 228
B.47 PSD of UV, VIS & IR photodiode signals Vs averaged O_2 for Tests 73 to 81 - 80 % Coal & 20 % Straw - 40° Swirl 228
B.48 RMS of largest wavelet coefficient of UV, VIS & IR photodiode signals Vs averaged O_2 for Tests 10 to 18 - 90 % Coal & 10 % Straw - 50° Swirl 229
B.49 RMS of largest wavelet coefficient of UV, VIS & IR photodiode signals Vs averaged O_2 for Tests 82 to 90 - 80 % Coal & 20 % Straw - 50° Swirl 230
B.50 RMS of largest wavelet coefficient of UV, VIS & IR photodiode signals Vs averaged O_2 for Tests 55 to 63 - 70 % Coal & 30 % Straw - 60° Swirl 230
B.51 RMS of largest wavelet coefficient of UV, VIS & IR photodiode signals Vs averaged O_2 for Tests 37 to 45 - 100 % Coal - 60° Swirl 231
B.52 RMS of largest wavelet coefficient of UV, VIS & IR photodiode signals Vs averaged O_2 for Tests 46 to 54 - 90 % Coal & 10 % Straw - 60° Swirl 231
B.53 RMS of largest wavelet coefficient of UV, VIS & IR photodiode signals Vs averaged O_2 for Tests 64 to 72 - 80 % Coal & 20 % Straw - 60° Swirl 232
B.54 RMS of largest wavelet coefficient of UV, VIS & IR photodiode signals Vs averaged O_2 for Tests 28 to 36 - 100 % Coal - 40° Swirl 232
B.55 RMS of largest wavelet coefficient of UV, VIS & IR photodiode signals Vs averaged O_2 for Tests 19 to 27 - 90 % Coal & 10 % Straw - 40° Swirl 233
B.56 RMS of largest wavelet coefficient of UV, VIS & IR photodiode signals Vs averaged O_2 for Tests 73 to 81 - 80 % Coal & 20 % Straw - 40° Swirl 233
B.57 WVD (averaged) of UV photodiode signal for Tests 10 to 18 - 90 % Coal & 10 % Biomass - 50° Swirl 234
B.58 WVD (averaged) of VIS photodiode signal for Tests 10 to 18 - 90 % Coal & 10 % Biomass - 50° Swirl 235
B.59 WVD (averaged) of IR photodiode signal for Tests 10 to 18 - 90 % Coal & 10 % Biomass - 50° Swirl 235

B.60 WVD (averaged) of UV photodiode signal for Tests 82 to 90 - 80 % Coal & 20 % Biomass - 50° Swirl 236
B.61 WVD (averaged) of VIS photodiode signal for Tests 82 to 90 - 80 % Coal & 20 % Biomass - 50° Swirl 236
B.62 WVD (averaged) of IR photodiode signal for Tests 82 to 90 - 80 % Coal & 20 % Biomass - 50° Swirl 237
B.63 WVD (averaged) of UV photodiode signal for Tests 37 to 45 - 100 % Coal - 60° Swirl 237
B.64 WVD (averaged) of VIS photodiode signal for Tests 37 to 45 - 100 % Coal - 60° Swirl 238
B.65 WVD (averaged) of IR photodiode signal for Tests 37 to 45 - 100 % Coal - 60° Swirl 238
B.66 WVD (averaged) of UV photodiode signal for Tests 46 to 54 - 90 % Coal & 10 % Biomass - 60° Swirl 239
B.67 WVD (averaged) of VIS photodiode signal for Tests 46 to 54 - 90 % Coal & 10 % Biomass - 60° Swirl 239
B.68 WVD (averaged) of IR photodiode signal for Tests 46 to 54 - 90 % Coal & 10 % Biomass - 60° Swirl 240
B.69 WVD (averaged) of UV photodiode signal for Tests 64 to 72 - 80 % Coal & 20 % Biomass - 60° Swirl 240
B.70 WVD (averaged) of VIS photodiode signal for Tests 64 to 72 - 80 % Coal & 20 % Biomass - 60° Swirl 241
B.71 WVD (averaged) of IR photodiode signal for Tests 64 to 72 - 80 % Coal & 20 % Biomass - 60° Swirl 241
B.72 WVD (averaged) of UV photodiode signal for Tests 28 to 36 - 100 % Coal - 40° Swirl 242
B.73 WVD (averaged) of VIS photodiode signal for Tests 28 to 36 - 100 % Coal - 40° Swirl 242
B.74 WVD (averaged) of IR photodiode signal for Tests 28 to 36 - 100 % Coal - 40° Swirl 243
B.75 WVD (averaged) of UV photodiode signal for Tests 19 to 27 - 90 % Coal & 10 % Biomass - 40° Swirl 244
B.76 WVD (averaged) of VIS photodiode signal for Tests 19 to 27 - 90 % Coal & 10 % Biomass - 40° Swirl 244
B.77 WVD (averaged) of IR photodiode signal for Tests 19 to 27 - 90 % Coal & 10 % Biomass - 40° Swirl 245
B.78 WVD (averaged) of UV photodiode signal for Tests 73 to 81 - 80 % Coal & 20 % Biomass - 40° Swirl 245
B.79 WVD (averaged) of VIS photodiode signal for Tests 73 to 81 - 80 % Coal & 20 % Biomass - 40° Swirl 246
B.80 WVD (averaged) of IR photodiode signal for Tests 73 to 81 - 80 % Coal & 20 % Biomass - 40° Swirl 246

C.1 WVD of the UV sensor signal for the test (Test 97a) with decreasing secondary air with 100% coal 247
C.2 WVD of the UV sensor signal for the test (Test 97b) with increasing secondary air with 100% coal 248

C.3 WVD of the UV sensor signal for the test (Test 98a) with decreasing secondary air with 100% coal 248
C.4 WVD of the UV sensor signal for the test (Test 98b) with increasing secondary air with 100% coal 249
C.5 WVD of the UV sensor signal for the test (Test 99a) with decreasing secondary air with 100% coal 249
C.6 WVD of the UV sensor signal for the test (Test 99b) with increasing secondary air with 100% coal 250
C.7 WVD of the VIS sensor signal for the test (Test 97a) with decreasing secondary air with 100% coal 251
C.8 WVD of the VIS sensor signal for the test (Test 97b) with increasing secondary air with 100% coal 251
C.9 WVD of the VIS sensor signal for the test (Test 98a) with decreasing secondary air with 100% coal 252
C.10 WVD of the VIS sensor signal for the test (Test 98b) with increasing secondary air with 100% coal 252
C.11 WVD of the VIS sensor signal for the test (Test 99a) with decreasing secondary air with 100% coal 253
C.12 WVD of the VIS sensor signal for the test (Test 99b) with increasing secondary air with 100% coal 253

List of Tables

3.1 Gas analysers used and the gases measured at the CTF 42
3.2 Gas analysers used and the gases measured at full scale 48
3.3 Composition of the fuel used during pilot scale testing at the CTF 49
3.4 Particle size distribution of the fuel used during pilot scale testing at the CTF 49
3.5 Composition of the fuel used during full scale testing at the Dolna Odra power station 50
3.6 Sensor specification 51
3.7 Summary of test conditions at the CTF 56
3.8 Summary of test conditions at the CTF, while varying the primary to secondary air ratio 57
3.9 Summary of test conditions at the CTF while varying the secondary air from normal level 58
3.10 Summary of test conditions at the full scale power plant 58

5.1 Case studies initially selected to evaluate the various input features to be applied to an ANN 72
5.2 Comparison of performance of NO_x prediction results for ANN trained with RMS 75
5.3 Comparison of performance of O_2 prediction results for ANN trained with RMS 82
5.4 Comparison of performance of NO_x prediction results for ANN trained with PSD 88
5.5 Comparison of performance of O_2 prediction results for ANN trained with PSD 89
5.6 Comparison of performance of NO_x prediction results for ANN trained with Wavelet coefficients 90
5.7 Comparison of performance of O_2 prediction results for ANN trained with Wavelet coefficients 91
5.8 Additional case studies to evaluate varying the input features to be applied to train an ANN 93
5.9 Comparison of performance of NO_x prediction results for ANN trained with RMS, PSD & Wavelet coefficients 93
5.10 Comparison of performance of O_2 prediction results for ANN trained with RMS, PSD & Wavelet coefficients 94
5.11 Additional case study to evaluate larger number of input tests to train the ANN 95

5.12 Comparison of performance of NO_x prediction results for ANN trained with RMS, PSD & Wavelet coefficients 96
5.13 Comparison of performance of O_2 prediction results for ANN trained with RMS, PSD & Wavelet coefficients 97
5.14 Additional case studies to evaluate application of PCA 98
5.15 Comparison of performance of NO_x prediction results for ANN trained with RMS, PSD & Wavelet coefficients together with PCA 98
5.16 Comparison of performance of O_2 prediction results for ANN trained with RMS, PSD & Wavelet coefficients together with PCA 99
5.17 Comparison of performance of NO_x prediction results for ANN trained with RMS, PSD & Wavelet coefficients together with PCA 100
5.18 Comparison of performance of O_2 prediction results for ANN trained with RMS, PSD & Wavelet coefficients together with PCA 102
5.19 Additional case studies to evaluate total airflow predictions 103
5.20 Comparison of performance of total airflow prediction results for ANN trained with RMS, PSD & Wavelet coefficients 103
5.21 Comparison of performance of total airflow prediction results for ANN trained with RMS, PSD & Wavelet coefficients 105
5.22 Simple rule based algorithm for control of airflow (AF = Air Flow) 130

6.1 MCO system testing at pilot scale CTF 135
6.2 MCO system testing at full scale at Dolna Odra, Poland 150

GLOSSARY

ANN	Artificial Neural Network
ANS	Artificial Neural Systems
$\approx$	approximate
BR	Bayesian Regularisation
CAAA	Clean Air Act Amendments
CCA	Climate Change Act
CCD	charge coupled device
CCL	Climate Change Levy
CFD	Computational Fluid Dynamics
CH^*	CH radical
CH_4	Methane
CN^*	CN radical
CO	Carbon monoxide
CO_2	Carbon dioxide
CTF	Combustion Test Facility
DAQ	Data Acquisition
DECC	Department of Energy and Climate Change
$^\circ$	degree
$^\circ$C	degree Celsius
DEM	Deutsche Mark
DTI	Department of Trade and Industry
EC	European Commission
EPA	Environmental Protection Act - 1990
ETS	Emission Trading Scheme
EU	European Union
FFT	Fast Fourier Transform
gCO_2eq/kWh	grams of CO_2 equivalent per kilo Watt hour of energy produced
GW	Giga Watt
Hz	Hertz
HMIP	Her Majesty's Inspectorate of Pollution
IEA	International Energy Agency
IEn	Institute Energitky - Institute of Power Engineering
IR	Infrared
JTF	Joint Time Frequency
kg/h	kilogram per hour
kW	kilo Watt
LCP	Large Combustion Plant

m^3/h	cubic meter per hour
MCO	Monitoring, Control and Optimisation
MIT	Massachusetts Institute of Technology
MJ/kg	Mega Joule per kilogram
MLP	Multilayer perceptron
MPPE	mean percentage prediction error
MW	Mega Watt
NI	National Instruments Incorporated
nm	nano meter
Nm^3/h	Normalised cubic meter per hour - flow measurements
NO	Nitrogen oxide
NO_2	Nitrogen dioxide
NO_x	Nitrogen oxides (NO, NO_2)
O_2	Oxygen
OFA	Over Fire Air
OH^*	OH radical
PC	Pulverised Coal
PCA	Principal Component Analysis
PDP	Parallel Distributed Processing
%	percentage
POST	Parliamentary Office of Science and Technology
ppm	parts per million
PSD	Power Spectral Density
RFCS	Research Fund for Coal and Steel
RMS	Root Mean Square
SO_x	Sulphur oxides
SO_2	Sulphur dioxide
SOM	Self-organising Map
UBC	un-burnt carbon
µm	micro meter
UN	United Nations
US EPA	US Environmental Protection Agency
UV	Ultra Violet
VIS	Visible
WVD	Wigner-Ville Distribution

SUBSCRIPT

$_e$	electrical
$_{th}$	thermal

Chapter 1

INTRODUCTION

This chapter introduces the problem addressed by this work, defines the objectives of the research undertaken and provides an outline of the overall layout of the thesis.

1.1 Co-Firing Higher Proportions of Biomass

Coal is the world's most abundant and widely distributed fossil fuel, and its combustion generates a significant proportion of the global electricity production [1]. Coal has been burnt in utility boilers for many years for the production of electricity for either industrial or domestic use. Steady improvements have been made in overall thermal efficiency, primarily through the development and use of new high temperature materials [2, 3]. With worldwide demand for electricity generally increasing, and in particular the rapid rise in demand in developing countries such as India and China, there has been a rapid worldwide expansion of coal fired utility boilers [2, 4, 5]. For example, India's energy consumption has doubled since 2000 with coal accounting for over 70 % of electricity generation there [6] and China has been the largest contributor to the growth for global energy usage for the past 20 years [7].

Coal burners and boilers have been used for electricity production for many years and with increasing demand, a large number of new plants are being built [8]. Burning coal produces CO_2, NO_x and other emissions which contribute to the global emission of greenhouse gases and hence to global warming [2, 9–11]. This has led to countries making commitments to decrease net emissions by switching to renewable sources of energy and new cleaner technologies [12]. Such agreements have been made between many countries under the auspices of the United Nations (UN) in Kyoto [13] to limit emissions in a sustainable way and the latest in Paris [14] to be ratified by member countries to limit global warming to 2 °C.

Pulverised Coal (PC) boilers are the most widely used type of utility boiler due to their higher efficiency and account for most of the coal based generation of electricity around the world [15, 16]. The carbon footprint of industrial processes coupled with increasing energy demand has led many countries to look at low carbon sources of energy, especially with the newer regulations and international agreements. Biomass, defined as the biodegradable fraction of products, waste and residues of biological origin, is considered a low carbon or carbon neutral

source of fuel [17, 18]. Biomass combustion accounts for 95 % of all usage, of which more than 50 % is used for domestic space heating and cooking [16]. Combustion of biomass in larger scale plants, such as in district heating systems or for the production of steam and/or electricity, has better emission control [16].

Combustion of biomass has many advantages, such as emission reduction in PC boilers, socio-economic benefits such as being a source of energy, employment and income, but requires investment in terms of combustion facilities [19, 20]. Biomass can be converted to energy using a variety of methods, though direct combustion accounts for the majority of biomass usage. Of the various ways to combust biomass, co-firing is being pursued aggressively as a short term approach to increase biomass usage. This is due to needing lower investment, ease of implementation and reducing the net CO_2 emissions [18, 21, 22].

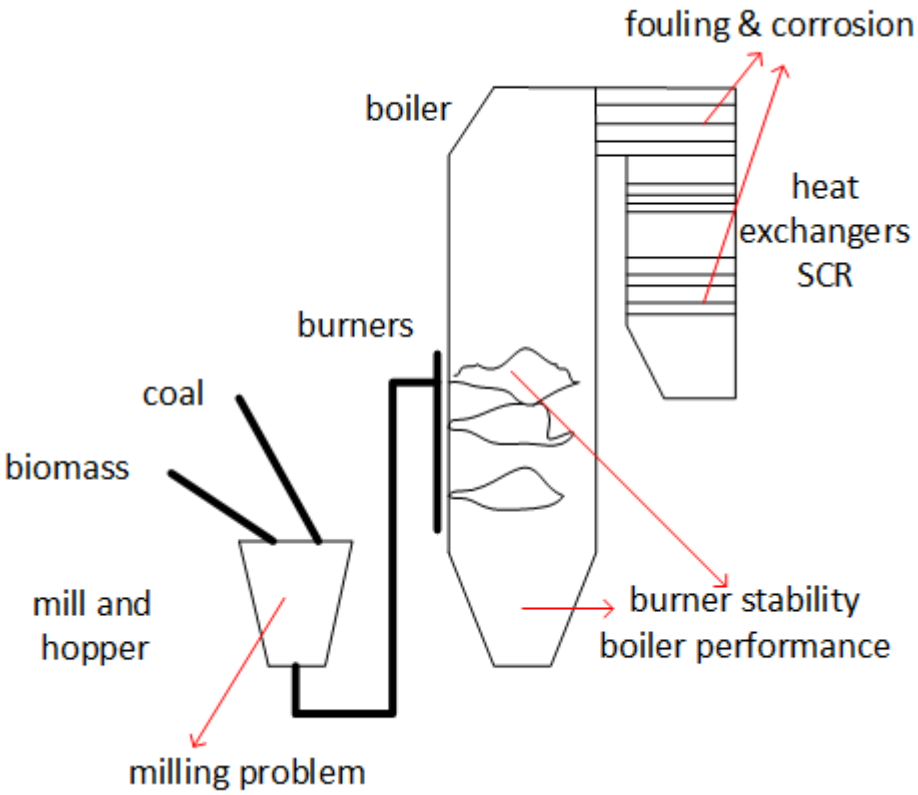

Figure 1.1: Common obstacles faced with cofiring [9, 23]

Co-firing biomass together with coal in pulverised coal burners has some obstacles in terms of available technology and gaps in know-how as reviewed by Sami *et al.* [9]. Summarily these are (as shown in Figure 1.1) the issue of fouling and corrosion at high temperature, the prepared biomass particle size and its use with existing feed mechanisms, and the pulveriser performance as the lower calorific value of biomass requires higher fuel flow rates to maintain thermal output levels [9, 23, 24].

Typically biomass substitution has remained at 10 % or less by mass for pulverised coal burners primarily due to the limitations of particle size and pulveriser performance [9]. The push to meet CO_2 targets has led DRAX in the UK which had set itself a target of producing at least 10 % of energy from co-firing, to have

already converted three of their boilers to 100 % biomass combustion [25, 26]. The International Energy Agency (IEA) Clean Coal Centre's publication highlights only two facilities in the UK that have co-fired higher than 10 % biomass, Drax and Fiddler's Ferry Plant [27]. The introduction of a higher percentage of biomass can lead to unstable flame conditions as the coal biomass blend has a lower heating value than coal alone, requiring a higher volume of fuel to be burnt compared to the original design for coal only and hence pushing the operating boundary for the same thermal output. This increased fuel flow rate has a tendency to move the flame further from the burner quarl which affects flame stability and also can lead to higher NO_x emissions [9].

1.1.1 Flame Monitoring

Monitoring is needed for the detection of changes in processes or systems, to avoid faults or to rectify them [28, 29]. Early detection of fault conditions are usually made by processing of measurable signals/parameters of the process being monitored [28]. When no or little information is known about a process, experimentally trained classification methods are useful for fault detection [28, 29].

The monitoring regime of most large scale boilers combusting fossil fuels is inadequate [30, 31]. Most burners have had installed safety devices that detect the presence of a flame since the 1950s [32], but these are only useful as a safety device to cut off further fuel being supplied to the burner. Measurement of O_2 and other emissions in the stack have been used as an indirect method to control the combustion process [33], but this is not very efficient as local burner conditions tend to differ from overall measurements at the stack. Also burning a higher volume of fuel due to the lower calorific value of biomass tends to challenge the stability of the burner designed for coal combustion and hence a method or system to detect such changes in real time is required. There are advantages to monitoring individual flames as this could be used for better control [33] and could maximise the combustion efficiency of individual burners. Such monitoring was shown to have interesting advantages such as the detection of near burner slagging that can adversely affect the flame [34].

Flame diagnostics is widely believed to be of importance for better combustion and in maintaining stability [35, 36]. Most detection techniques are dependent on the chemiluminescence of the flame, that arises from excited species or radicals which emit distinct wavelengths during their excited state [37, 38]. Basic flame detectors typically employed in utility boilers are passive, non-intrusive safety devices, which operate in the Infrared (IR) region detecting the presence of the flame [39, 40]. The flame is generally detected through a natural flicker which is not affected by background blackbody radiation unlike methods dependent on signal intensity alone [41].

Traditionally signal processing methods like Root Mean Square (RMS), Fast Fourier Transform (FFT) and Power Spectral Density (PSD) have been employed to quantify signals. More advanced Joint Time Frequency (JTF) signal processing methods like wavelet and Wigner-Ville Distribution (WVD) have been utilised to process the sensor data. Artificial Neural Network (ANN) have been applied to complex problems where conventional computing is unable to per-

form adequately and have been used to monitor co-firing and other combustion processes [42–44].

Combustion of coal and coal biomass blends is a complex process and despite the considerable research to develop comprehensive models of the process, gaps still remain in our understanding [45, 46]. It is not possible therefore to use a model based approach to develop control algorithms for the boiler. An alternative approach is to focus on controlling individual burners. In order to safely co-fire higher proportions of biomass a system capable of avoiding unstable operation whilst at the same time maintaining combustion efficiency and lowering the emission of pollutants is required. With the increasingly stringent requirements for emission control and carbon cost reduction, such a system would aid the uptake of co-firing in utility boilers. In fact, this research work was undertaken as part of an European Union (EU) funded Research Fund for Coal and Steel (RFCS) project, under contract RFCR-CT-2008-00009 which aimed to increase the biomass percentage being co-fired and investigate the associated problems, one of which was development of a control system capable of detecting these unfavourable flame conditions [47].

1.2 Aim and Objectives

The overall aim of the work presented here was the development and investigation of the performance of a complete flame monitoring and control system that runs in real-time to be able to detect abnormal combustion while co-firing biomass in facilities built for coal combustion and make suggestions as to how to effect change.

1.2.1 Objectives

To achieve the above mentioned aim, several objectives were defined. These were:

1. Development of a novel three sensor optical monitoring instrumentation system.

2. Application of a combination of advanced signal processing techniques in a novel way to co-firing flames.

3. Investigation into the performance of the developed system at pilot and full scale plants.

The rationale for these were to see if data can be extracted from the broadband sensors would be able to adequately detect changes seen in the flame with variations to the input to the burner, through a systematic set of experiments to be conducted at pilot scale. If relationships could be established through identification of a suitable signal processing method to input changes, then this could be used to develop a rule based control and monitoring system that could be initially tested off-line with the data acquired from the systematic set of experiments. If that was successful then the performance of such a system to suggest

changes to the burner operator to correct the operation to previously identified ideal conditions at both pilot and full scale plants would be carried out to understand the viability of such a system to operate in real-time.

1.3 Thesis Structure

This thesis is organised into seven chapters that provide the reader with the background to the methodology, experiments undertaken and results obtained that together describe the outcome of this research.

Chapter 2 provides a brief introduction to coal, its application and importance in power production and energy security. Subsequently, problems with emissions from coal combustion and the adverse environmental effects to the efforts in stemming this issue are discussed, concentrating especially on the attractive option to co-firing biomass in coal burners with little cost and infrastructural change. A critical review of combustion monitoring and related techniques employed are discussed with the need for the current research to fill gaps in the pathway to co-fire a higher percentage of biomass being identified. The signal processing methods and an introduction to ANN are presented with references to the numerous applications of such networks to fault detection and monitoring.

Chapter 3 describes the research methodology, the experimental apparatus at both the pilot and full scale plants, the selection of appropriate sensors, data acquisition techniques and related signal conditioning applied are discussed. This chapter also tabulates all the experiments carried out towards the realisation of the objectives of this research, at both the facilities together with the available gas analysers to measure emissions from the combustion to be utilised for the monitoring system development.

Chapter 4 presents the results from the systematic experiments carried out at the pilot scale plant. The sensor data are discussed with the burner operation parameters to illustrate the methodology used in the selection of the signal processing. This discussion highlights the complex nature of the signal variations with changes to burner conditions and the need for a method to classify the data and so identify the complex relationships present in the input data that are not readily visible with simple signal processing methods.

Chapter 5 discusses the development of the monitoring system capable of identifying changes to the burner operating conditions. The various features extracted from the three sensors and their application in various detection methods before arriving at the final system with a Self-organising Map (SOM) is illustrated. The architecture of the ANN and the appropriate signal processing methods and features used in the detection algorithm are explained. This also shows the training and application of the SOM model for this Monitoring, Control and Optimisation (MCO) system.

Chapter 6 discusses the results of the series of experiments carried out to test the developed algorithm at the Combustion Test Facility (CTF). The limitations and solution to large changes to the fuel properties are discussed. This is followed by a discussion of the results obtained from the application of this novel system during real-time experiments carried out at the full scale Dolna Odra power plant.

Chapter 7 draws the conclusions from this research project and the results obtained with respect to the developed intelligent MCO system to detect changes in flame conditions whilst co-firing coal and biomass. Further work that could be of relevance to this research and other recommendations are presented in the last section of this chapter.

Chapter 2

LITERATURE REVIEW

This chapter discusses the most relevant literature regarding coal flame monitoring together with the reasons for monitoring and a number of related topics including coal usage, combustion efficiency, biomass, signal processing algorithms, Artificial Neural Networks (ANN) and special instrumentation.

2.1 Energy Needs

Energy usage, especially electricity generation is linked to the prosperity of developed countries according to the International Energy Agency (IEA) [48]. Energy usage has also been linked to poverty reduction, as a by-product of economic growth, in developing and especially Asian countries [48]. A number of publications from the IEA have also highlighted the need for a balanced mix through a range of cleaner fossil fuels, nuclear and renewable energy, together with improved energy efficiency, to provide stability in the energy markets. This should then maintain and promote prosperity / growth in developed and developing countries [48, 49]. This need for development in the Asian economies is fuelling more urbanisation and infrastructure development, which in turn drives demand for electricity, steel and cement which are all very reliant on coal for their production [48].

Energy demand is increasing, especially the usage of coal, due to the volatile cost of oil and gas compared to the relatively stable price of coal. In addition, coal has widespread availability and multiple sources of supply [48, 50–52]. Energy demand globally is projected to increase by 55.1 % over the period to 2030, compared to 2005 levels according to the World Energy Outlook [53]. Fossil fuels fulfil 80 % of the energy need according to 'The Future of Coal' reported by the Massachusetts Institute of Technology (MIT) in 2007, of which 25 % comes from coal [52]. This can be expected to be maintained unless the usage of fossil fuels is reduced to mitigate the impact on climate [48, 53]

Clean coal technologies aim to improve the energy efficiency of coal power plants (in 2006 mean of 35 % efficiency) to more than 50 % by 2050, which would also reduce CO_2 emissions significantly [54]. The largest user of coal for electricity - China, could save about 20 % of the coal used by improving the efficiency of its plants to that of Japan for example [54].

2.2 Importance of Coal

Coal is the result of the complex transformation of vegetation through decay and geological pressure and heating [55]. Coal is a natural solid fuel which consists primarily of pure carbon, hydrocarbons, mineral compounds and water [45]. Chomiak's textbook section on the combustion of coal provides a wealth of details, including a basic description of the fractional analysis of coal. This proximate analysis and classification of coal based on the organic rock nature and petrographic based on the occurrence of the principal mineral types in coal [45]. Primary energy is, to a large extent, derived from the combustion of fossil fuels, one of which is coal [52, 56, 57]. Coal is the second most important source of energy in the US, after oil, which is largely used for transportation [8, 57], and accounts for 50 % of the electricity produced in the USA [3, 52]. The USA is the largest user of coal for energy production with China being the overall largest coal user across all industries [58]. Nine countries account for 90 % of the reserves of coal in the world [8] of which USA, China and India have the largest [52].

Global energy demand has been increasing due to economic growth, especially from developing countries like Brazil, China & India, and has a direct link to population growth [59, 60]. Oil, one of the primary sources of energy at 33.6 %, is the largest contributor but this is due to use of oil predominantly in transportation. Coal at 39 % has the biggest stake in electricity production in the world [58, 61]. The importance of coal as a primary source of fuel, especially for electricity production, is due to coal being cheaper than other fossil fuels, having the largest proven reserves of any fossil fuel, thus providing energy security [3, 5, 8, 52, 58, 62]. In addition, the rapid development seen in Asian economies is driving a rapid investment in new infrastructure, thus driving growth in the consumption of steel and cement [48]. Coal is fundamental to steel and cement production, which in turn is needed for these new infrastructure developments [48, 50, 52].

In the European context, if current levels of growth in energy needs are to be met by 2050 an additional 300 GW of capacity needs to be added to the grid by then [60]. This additional need for capacity would be 500 GW if the growth in electricity demand rises as expected [60]. If one also factors in the need to replace the ageing fleet, a number of fuel options would have to be considered and coal due to its availability and relatively steady price would be expected to play a considerable part [60].

In spite of the stable price and availability advantage, coal impacts on the environment while being extracted and also when burnt for energy, especially through polluting the air [45, 52]. According to the UK Parliamentary Office of Science and Technology (POST), coal is a major source of emissions, especially from energy intensive industries [63] and is also responsible for 41 % of all CO_2 emissions from energy production [52].

2.3 Coal Power Plants

Coal burners and boilers have been used for many years to produce electricity. With the increasing worldwide demand for electricity, a large number of new

plants have been or are in the process of being built [8], particularly in China [52]. At the current pace of economic development, the need for electricity is so high in China that its annual capacity is increasing at roughly the size of the power grid of the UK [2, 52]. This in turn leads to increasing emissions of CO_2, NO_x and SO_2, the main causes of acid rain and global warming. Combustion efficiency depends in part, on the burner and there have been improvements in utility boiler thermal efficiency, though these have mainly been through the development and use of high temperature materials in their construction that allow the boiler to operate under supercritical conditions [2, 3].

According to Overend *et al.* [16] the major types of industrial and power generation boilers in use are pile burners, grate boilers, suspension fired boilers, fluidized beds and circulating fluidized beds. Of these, Pulverised Coal (PC) boilers, also known as suspension fired boilers, so called due to the fuel or pulverised coal being suspended in air as it's burnt in the boiler, have a higher efficiency than other boiler types [15]. PC boilers are widely used and account for 92 % of coal based generation in the USA [15, 16, 45, 57, 61].

The main design goals of burners and boilers are power efficiency, durability and reliability [56]. Many complex chemical and physical transformations happen during the combustion of coal [45]. This makes modelling difficult due to the complex interactions that occur. De-volatilization of the volatile matter in coal during combustion, gas temperature, oxygen concentration and quality & quantity of char varies based on the type of coal [45].

2.4 Carbon Footprint

According to the POST 'carbon footprint' refers to the overall CO_2 and other greenhouse gas emission emanating from the whole lifecycle of a process or product [64]. This is usually calculated to evaluate the impact on the environment over the entire lifetime, 'cradle-to-grave', of the said process or product [64].

2.4.1 Industrial Needs

As highlighted in sections 2.2 and 2.3, coal is used as an energy source in both energy production and industrial processes. Many industrial processes require combustion as one of the core process needs and hence, its efficiency has a huge impact on economics and the possible environmental impact of the process [45, 51, 65]. Coal is the second largest CO_2 emission source after oil, as oil is used for transportation [8], even though coal has the highest emissions of CO_2 per kW of energy generated [64]. So, environmental factors and large emissions from the combustion of fossil fuels highlight the need for low carbon or carbon neutral technologies in an effort to reduce the carbon footprint from industrial processes and power generation [8, 45, 51, 64, 66].

A number of measures, especially related to low carbon technologies, are being pursued by many countries. One such measure is to reduce the emissions of man-made greenhouse gas from large industrial and power plants in the European Union (EU). The EU Emission Trading Scheme (ETS) which places emission reduction targets on member countries to achieve through renewable energy usage and efficiency improvement as part of the response to climate change [67, 68]. The

target announced in October 2014 for EU member countries is a 40 % reduction of greenhouse gas emission levels by 2030 (compared to 1990) [26]. Usually these low carbon technologies utilise renewables or nuclear, but these are not completely carbon emission free as they have indirect emissions emanating from preparation, transportation and production and not directly during power production like fossil fuels [64].

2.4.2 Coal's Footprint

Coal combustion has the highest carbon foot print of any fossil fuel (or otherwise) with conventional power plants especially producing emissions in the region of 1000 gCO_2eq/kWh [58, 64].

A number of countries, especially in the EU, are attempting to reduce their carbon foot prints, which would also enable them to reduce their dependence on imported fossil fuels and also increase the amount of energy generated from renewable sources. One of the sources of renewable energy is biomass and an approach is to substitute coal with biomass in the coal burner, quite often with very minimal changes to plant operation and cost compared to building new biomass boilers. Biomass combustion has near zero net emission of CO_2, so the substitution of coal with biomass in the large number of coal power plants throughout the world (installed capacity of 800 GW_e) would effectively lead to a significant reduction of CO_2 [69–71]. This would also help the target set by the European Parliament for the percentage of energy to be produced from renewable sources in the near future, thereby giving incentives to further the use of biomass in coal power plants [72]. The results used in this report are in fact part of a project that had funding from the EC (SMARTBURN) for such research.

2.4.3 Policy Enabling / Moving Towards Carbon Footprint Reduction

The United Nations' Framework Convention on Climate Change agreed (Kyoto Protocol 1997) to reduce the emission of greenhouse gases among all the signatories of the protocol [13, 73]. This came into force from 2005, which required the signatory countries to comply through promotion of energy efficiency, usage of renewable sources of energy and other measures like taxation and duty on activities that generate greenhouse gases to progressively reduce emissions [13]. The main mechanisms adopted for the Kyoto protocol were emissions trading, sustainable sources of energy development and taking into account emission reduction measures funded in another country towards the funder's emission total [73].

One of the first regulations on emissions in the UK was by Her Majesty's Inspectorate of Pollution (HMIP) in Scotland on large combustion plants under the Environmental Protection Act - 1990 (EPA) [31].

In the UK context, the Energy White Paper 2003 "Our energy future – creating a low carbon economy" calls for carbon reduction as the UK government's policy towards 2050 [74]. This is in addition to the UK's very aspirational target of a 20 % reduction of the six main greenhouse gases, as agreed under the Kyoto Protocol. Other energy strategies point towards the use of other sources

of energy especially renewables. The Renewables Obligation placed on electricity suppliers aims towards the usage of biomass and biomass co-firing [74]. The Department of Trade and Industry (DTI), has highlighted the need for carbon abatement and their current strategy is to switch to lower carbon alternatives of which biomass is an important element with possible emission reductions of 5 to 10 % just from co-firing [75].

The Climate Change Act (CCA) signed into UK law in 2008 sets a target of 34 % and 80 % reduction of major greenhouse gases by 2020 and 2050 respectively, compared to 1990 levels [63]. The Climate Change Levy (CCL) in the UK tries to also improve efficiency in industry through taxation of electricity from coal for example, while electricity from renewable sources are exempt from this levy [63].

The EU wide ETS agreed between member states came into effect in 2005 [67, 68]. ETS is a cap and trade type system where the total permitted emissions are set and the allowable limits allocated to different organisations and industries. These organisations can trade these permits with others who have low emissions in a way fixing the price according to demand and promoting measures in all those industries to reduce the amount of greenhouse gas emissions [68]. ETS covers a range of industries and processes covering 45 % of all emissions throughout Europe [67].

Similar to ETS, a number of other countries including some states in the USA, Canada, Japan, Australia, Switzerland, New Zealand, Mexico, South Korea and Taiwan have either proposed or implemented systems for carbon trading [68]. Further, the EU and some of these countries are in discussion to have an integrated system so as to avoid some of the so called 'carbon leakage', where companies and industries move to other countries with little or no carbon pricing without much effort in terms of emissions reduction [63, 68].

The EU Renewable Energy Directive (2009) calls for member countries to implement and achieve mandatory targets for energy derived from renewables; 20 % for overall energy consumption and 10 % for transport by 2020 [17, 76]. In addition, with such directives the demand for electricity might also rise (double by 2050) as heating and road transport might increasingly use electricity to achieve targets for the reduction of greenhouse gas emissions [76].

2.5 Combustion Efficiency Improvements

Most of the improvements seen until now in boiler efficiency have been from the use of high temperature materials [2]. So there have been numerous projects investigating methods to reduce pollutant emissions through intelligent monitoring, control and optimisation of burner and boiler systems to improve combustion efficiency [37, 77]. There is also a global trend to increase the sustainable production of energy which brings with it the additional advantage of decreasing CO_2 emissions as well as reduced usage of coal. One short term approach that is being aggressively investigated and implemented is to supplement a proportion of the calorific content of the coal with biomass [21, 70, 71]. This has the advantage of using the same equipment with minimal changes reducing cost of adoption. Other advantages are a reduction in the carbon foot print, as biomass is a car-

bon neutral fuel, reduction in NO_x and SO_2, reduction in fuel costs and other benefits, dependent upon the source of biomass, such as reduction / avoidance of CH_4 emissions from straw / crops after harvesting, which might otherwise end up in landfill sites [9, 46, 70, 71].

2.5.1 NO_x Effects

NO_x is one of the emission products from the combustion of fossil fuels, which is held chiefly responsible for smog problems affecting especially urban areas [78–80]. NO_x is also considered as a precursor to acid rain and contributes to acidification of aquatic systems and reduction in visibility [79]. NO_x also affects human health, with the nervous system being affected by NO and irritation of the lung and other complications with NO_2 [45].

The options for NO_x (and also SO_x) reduction are combustion control, post combustion techniques or a mixture of both [79]. NO_x reduction through combustion control reduces the NO_x at source, as in, at the start of the combustion process. There are three mechanisms of NO_x formation, namely fuel NO_x which accounts for about 75 % from the oxidation of nitrogen in the fuel, thermal NO_x which accounts for about 25 % due to the reaction of nitrogen with oxygen in the combustion air and very minimal amounts of prompt NO_x from the complex interaction of nitrogen with hydrocarbons in the flame front [45, 78, 79, 81].

In order to reduce NO_x, combustion modifications included in low NO_x burners aim to delay the mixing of the fuel and air, and hence reducing the temperature and turbulence at the start of the flame to reduce NO_x formation [79, 81, 82]. Even though these modifications reduce thermal NO_x formation to a large extent, they don't completely eliminate it. At the same time, even small fluctuations in the flow to the burner could affect fuel mixing and increase NO_x which necessitates better control techniques to identify such changes. Modelling of NO_x emission is difficult, as NO_x formation is highly non-linear with regards to boiler operational parameters [83]. In addition to that, low NO_x burners can also impact the fly ash quality due to un-burnt carbon (UBC) which has an economic value by being sold to the cement industry and also high UBC can affect particulate control systems and their effectiveness [79]. The EU directive for Large Combustion Plant (LCP) implemented by member states and US Clean Air Act Amendments (CAAA) employed by the US Environmental Protection Agency (US EPA) regulate(s) NO_x (and other) emissions from a large number of sources of combustion which help mitigate or reduce NO_x emissions, which to a large extent applies to coal power plants [80, 84, 85].

2.6 Biomass

According to EU Directive 2009/28/EC, biomass is defined as *"biodegradable fraction of products, waste and residues from biological origin from agriculture ..., forestry and related industries ..., as well as the biodegradable fraction of industrial and municipal waste"* [17].

Biomass is derived from photosynthesis where plants convert carbon dioxide in the air using energy from the sun to chemical energy [16]. Biomass encompasses a variety of plant or organic matter and elemental analysis has shown

about 50 % is carbon, especially in wood and grasses [16]. The major source of energy derived from biomass currently comes from the residues of timber and food crops, as they are being processed to other products and these residues usually equal the amount of grain or timber produced, e.g. 1 tonne of grain would give 1 tonne of biomass residue from the plant [16].

In the US, small diameter trees and debris in forests add to fire hazard and are regularly removed and are already utilised for fuel, like in other parts of the world [16]. So biomass is converted to energy, for example, to supply heat or run combined heat and power plants to change to electricity or other forms of fuel [16, 70]. Biomass use has socio-economic benefits such as being a source of energy, employment and income; and is also an impetus in some countries and regions for increased power production in addition to other benefits like emission reduction [19, 20].

2.6.1 Biomass for Energy

EU directive 2001/77/EC urges member countries to utilise more renewable sources of energy for electricity production to achieve sustainable development, for environmental protection, for local employment and also to contribute to the security of energy supply from different fuels sourced, if possible, locally [86]. In addition to this, the EU has set targets for member states, for example to achieve at least 12 % of all energy usage from renewables from just 6 % in 1997 or electricity from renewables of 22.1 % by 2010 [86, 87]. This target has been further increased to 27 % contribution from renewables by 2030 [26]. The EU green paper on energy security suggests the significance of biomass for the energy security of the EU [19, 87]. Four countries, namely Portugal, Finland, Austria and Sweden, account for significant use of renewable sources of energy (including biomass and hydro) exceeding the 12 % target and a number of other countries in the EU are either harmonising their laws to the EU directive or increasing their share of renewables for energy, one of which is biomass [87].

According to Connor [88], UK government intentions towards renewables were observed through, 'Energy Paper 55 – Renewable energy in the UK: the way forward', published by the Department of Energy and Climate Change (DECC) in 1988 through to 'The renewables obligation statutory consultation' from the DTI in 2000, which promote the usage of / set targets for renewables in UK [88]. One of the main targets of the UK government publications, was the reduction of emissions including greenhouse gases to meet both national and international commitments in addition to providing sustainable energy supply and local employment [88].

According to Upreti *et al.* [89], UK governments' long term grants for use of renewables by electricity suppliers under the Renewables Obligations, is one of the ways the government is promoting the use of renewables and this also fulfils the UK government obligations towards various national and international commitments [89, 90]. In 2010, biomass electricity capacity stood at 2.5GW, which is the largest electricity contribution from any renewable source of energy [91]. Cornelissen *et al.* have highlighted the potential of biomass for energy production to meet all needs globally and also sustainably by 2050, and also to avoid fossil fuels and hence reduce greenhouse gas emissions from the energy

supply networks throughout the world [92].

Biomass is used for energy in a number of ways as follows [15, 16, 18, 91, 93, 94]:

1. direct combustion to produce heat which can be used for heating, and other processes like producing electricity;

2. thermal gasification to produce gaseous fuel, which can also be converted to liquid form for usage elsewhere as either gaseous or liquid fuels; and

3. other advanced conversion methods like anaerobic digestion.

Combustion of biomass accounts for 95 % of all biomass usage in the world [16]. More than 50 % is accounted for by household use of biomass for cooking and space heating, which is usually of poor combustion efficiency. Slightly better efficiency is seen with wood log combustion for space heating around forested areas in the northern hemisphere and Latin America; and much improved efficiency with reduced emissions from district heating systems burning biomass especially in Europe [16]. Some of the large scale district heating systems also produce steam for industries and electricity for the grid with better emission control [16].

Biomass can be a sustainable fuel with lean carbon and lower levels of pollutants like SO_2, compared to fossil fuels [95]. For example, Tilbury power station would reduce SO_x, NO_x and particulate emissions considerably by burning biomass for just the few years before it reaches its end of life [91]. Biomass can also contribute to the economy and provide business opportunities to the local area if sourced locally and also avoid release of CO_2, and the 21 times more potent methane (for the greenhouse effect), to the atmosphere, if left unused for energy or other applications [91, 95]. Dalkia biomass plant in county Durham uses waste wood that would have ended up at landfill and at the same time produces electricity and heat and contributes socially through local jobs [91].

2.6.2 Biomass Combustion

Combustion is the major way biomass is used throughout the world, so this section details some of its advantages and challenges [16]. Biomass is a high volatile fuel, which can produce large amounts of gas during rapid combustion unlike other solid fuels, so this has to be taken into consideration for combustors [16]. As mentioned in section 2.6, biomass is directly burned in households either for cooking or space heating without much effort in fuel preparation. Larger scale systems for district heating achieve better efficiency according to Overend *et al.* [16, 18] due to the larger scale and hence also lower emissions.

Industrial applications employ co-generation or combined heat and power systems to generate heat and also produce electricity or use the heat to process or dry other ingredients. For example, pulp or cane sugar manufacturing processes burn the residue as a fuel and also use it to fulfil other process needs [16]. Biomass is also used for power generation, usually requiring some transportation and fuel processing, but with much lower or a neutral carbon footprint compared to other fossil fuels and better efficiency than other methods of biomass combustion [15, 16, 18, 93].

As mentioned in section 2.3, according to Overend *et al.* and Kayhanian *et al.* PC boilers are the most widely used boilers for power generation [15, 16]. In this context, biomass can be combusted in a few ways as follows:

1. In separate biomass boilers – this usually entails substantial capital outlay for building and also, location of the boilers would impact the carbon footprint if the transportation of biomass becomes necessary when the source is not local [18]. The advantages of direct burning are the availability of technology and ready turnkey suppliers but the disadvantages are the thermal efficiency penalty for burning high moisture fuels (biomass); fouling due to alkali compounds in the biomass; and, low efficiencies for steam power plants due to the lower calorific value of biomass compared to fossil fuels [15, 93].

2. Biomass burners with separate transportation mechanisms in existing PC boilers - retrofitting of biomass burners in existing PC boilers to burn 100 % biomass separately needs planning and space to install the burners and the additional biomass transport mechanisms to carry the biomass to the burner. This suffers from most of the disadvantages of direct burning except the low efficiency, as coal provides higher heat release; but then has additional costs involved with the initial retrofit [93].

3. Co-firing - where a portion of coal is substituted with pulverised biomass in the same transportation mechanisms to the PC boiler. The option to use biomass in existing burners for co-firing with coal eliminates the need for separate transport mechanisms and space consideration with respect to the existing PC boiler. This also doesn't suffer from the low thermal efficiency of 100 % biomass burners due to coals' higher heat release. Coal usually contains a very high carbon content and takes a long time to burn, unless pulverised [16], so adding pulverised biomass (which usually has much lower carbon content than most fossil fuels) should be cheaper and easier to achieve, without drastic changes to the operational conditions of the PC boiler except for small reductions in the thermal capacity due to the portion of fuel being substituted with biomass which has a lower heating value [18, 66].

2.6.3 Co-Firing Biomass

As highlighted in the DECC UK Renewable Energy Roadmap [91], co-firing is the second largest contributor to electricity generation at 21 % after generation from waste for renewable energy sources. Biomass through co-firing on average contributes 3 % of the energy produced from major UK power plants [96]. A number of power plants in the EU have started combusting biomass, including Drax in the UK [26]. In addition to that, ETS and the current carbon pricing is likely to push co-firing competitiveness with many power plants adopting this to reduce their cost on carbon pricing [18].

Co-firing is an alternative, where a portion of coal is replaced with biomass for combustion in PC boilers as opposed to only biomass in PC boilers which either were designed for coal or additional separate biomass burners in PC boilers with

separate fuel transport mechanisms, which entail cost and space considerations in proximity to the boiler [15, 18, 93]. Some of the advantages of co-firing are as follows [15, 16, 18, 21, 26, 46, 57, 66, 71, 93, 97–101]:

1. A reduction of biomass wastes ending up in landfill (and the associated costs) from industries such as lumber mills and paper companies
2. Sulphur emission reduction, which is relatively cheaper than other options
3. Fuel flexibility
4. CO_2 reduction
5. Reduced ash-fouling issues (compared to biomass only burners or plants)
6. Maybe fulfilling emission targets depending on the location, as some countries give additional allowances for usage of renewable sources of energy in PC boilers
7. NO_x abatement
8. Lower investment costs (77 - 153 € per kW compared to 409 - 767 € per kW for new decentralised biomass only plants[1])
9. Rapid adaptation of PC boilers at modest cost implication (compared to biomass only burners or plants)
10. Better combustion control with some coal types

One of the principal disadvantages of co-firing is the reduction in the capacity of the boilers due to the lower energy density of biomass compared to coal and the higher moisture content [15, 16].

As discussed in sections 2.4.2 and 2.5.1, one approach to the reduction of emissions is to co-fire biomass with coal in PC boilers without major alterations [18, 20–22, 24, 69, 77, 93]. Also with regulations like the industrial emissions directives [103], there is continued pressure on many coal fired boilers to reduce emissions further and co-firing is a short term approach to fulfil this need. Co-firing biomass with coal in PC boilers has some obstacles in terms of the available technology and gaps in knowledge according to Sami *et al.* [9] including: fouling and corrosion in the boiler; grinding of biomass; delivery of the biomass to the combustion zone and maintaining thermal output.

Until now biomass substitution has remained at around 10 % by mass or less, as at these levels the burner characteristics are not adversely affected, primarily to reduce the effect of these issues. In addition, the introduction of a higher percentage of biomass has been observed to result in unstable flame conditions as the blend has different combustion characteristics (compared to the original design specifications for coal only combustors). This primarily results from the increased fuel flow rate needed to maintain thermal performance which tends to move the flame front further from the burner quarl which as well as affecting flame stability can also lead to higher NO_x emissions [9, 21].

[1] Conversion of Deutsche Mark (DEM) 1.955 83 to € 1 [102]

One option to solve this issue of flame stability might be modelling of the combustion process. Modelling of burner systems in large utility boilers is a resource intensive process, and as such it's not feasible at this point in time to do so in real time for prediction of flame conditions. However, modelling of burner systems and burner instabilities is an active area of research in the Computational Fluid Dynamics (CFD) community, especially biomass combustion kinetics as these are essential for modelling co-firing in industrial boilers [100]. In addition to this, the interaction of two different sizes of particles from the coal and biomass adds to the mix of inherent complexity of the combustion process and particle flow parameters of large power station boilers. So to avert this possibility of burner instability and in extreme cases flame extinction, a very important consideration in view of the safety implications with increased usage of biomass, a monitoring system capable of detecting these changes in real time is needed.

DECC's 'UK Renewable Energy Roadmap' highlights the need for cost effective (fuel) monitoring and sampling systems to meet environmental legislation requirements by renewable energy plants [91]. In fact, the research presented here was funded by the EU, under the Research Fund for Coal and Steel (RFCS) contract RFCR-CT-2008-00009 which aimed to increase the biomass percentage being co-fired and investigate the associated problems, one of which was development of a control system capable of detecting these unfavourable flame conditions [47].

2.7 Monitoring

Monitoring or supervision is needed for detecting changes in processes or systems, which helps to resolve those changes to avoid faults in the system / process(es) being monitored [28, 29]. The need for improved reliability and safety and economic reasons, necessitates increasingly advanced monitoring and fault diagnosis for various industrial processes [28, 104]. The main reason for such early detection and fault identification is to provide sufficient time for corrective actions or stoppage for fault rectification before it's compounded to a larger issue [28, 32], and this also enhances the economic advantage [29, 32]. Such early detection can be achieved by quantifying measurable parameters and applying with known relationships between the different measured values to generate mathematical models to represent the process [28]. When no or little information is known about a process, experimentally trained classification methods are useful for fault detection [28, 29].

There are two types of combustion based on the mixing of fuel and air, basically premixed and non-premixed. Non-premixed flames can be subdivided into two, based on the flow of the air / oxidiser, laminar or turbulent. Out of the two, turbulent non-premixed flames play a hugely important part in lots of industrial processes due to the safety factor of prevention of the mixing of the fuel and oxidiser before combustion, but has a complex combustion chemistry and is more difficult to control compared to the other combustion types mentioned earlier [65]. Visual confirmation of flame performance is difficult for even experienced operators due to the very turbulent nature of non-premixed coal flames found in PC burners [65].

So monitoring of boilers is important to achieve efficient and safe combustion [32, 104]. This is usually of two types, direct and indirect measurements. According to Rodríguez *et al.* [30] these measurements can be classed as post combustion, conventional intrusive probes, wall or contour sensors and pre-combustion measurements. Again wall or contour sensors can be further divided into two: passive measurement like cameras and infrared sensors, and active measurements like acoustic emission systems with a transmitter and receiver [30]. As also highlighted by Rodríguez *et al.*, the monitoring regime of most large scale boilers combusting fossil fuels is inadequate [30, 31], but even then most burners have safety devices monitoring the presence of a flame from the 1950s [32]. Beèr *et al.* have also highlighted that indirect measurement of O_2 and / or CO_2 of a large conventional boiler has many limitations and is not very efficient for control [33].

Monitoring the flame is an indirect approach to burner control, as the primary parameters are the airflow and coal feed to the burner. According to Beèr *et al.* [33], monitoring the flame front can provide flame quality information which could be used for better control of the flame condition. However, in a power station boiler the burners are arranged in a bank of maybe four or five burners with only information relating to the bank generally being available to the control system. For pollutant emissions there is generally only one measurement site which is located in the exhaust stack. There are therefore advantages to taking an indirect approach as the combustion efficiency and pollutant emissions can be estimated for each flame and through individual burner control it should be possible to minimise emissions and maximise the efficiency for each flame. In fact this very dependence allows interesting features such as near burner slagging to be detected [34].

2.7.1 Coal Flame Monitoring

As the flame is the 'heart' of the combustion system, estimating the characteristics of the flame using flame diagnostics is widely believed to be of importance for the quality of the combustion or stability of the combustion system [35, 36, 81, 105] and also the possibility of responding quickly to unforeseen events [106]. Local burner conditions differ from overall measurements at the stack and lead to possible stoichiometric errors in the control of burners and hence there is a need for individual burner control and monitoring compared to global control [30, 31, 33, 81]. This compounds the identification of inefficient combustion in multi-burner / boiler setups with a common flue, also highlighting the need for individual burner control [31]. Rodri´guez *et al.* claim existing plants also have limitations in terms of monitoring options as most were built when emissions or efficiency wasn't high up on the factors for design other than operational and economic parameters [30]. In addition to that, coal flame detection is difficult when compared to oil / gas fired boilers, due to particles of pulverised coal travelling further into the furnace before ignition and the variation of intensity within a flame and between burners [32, 107].

Generally, basic flame detectors are employed by most utility boilers in almost all their burners as a safety device to detect if a flame is present, so as to stop further fuel from being introduced to the boiler in case of flame blowout which can be very dangerous [32, 107–109]. These detectors are simple devices that

operate either in the Ultra Violet (UV), Visible (VIS) and/or Infrared (IR) region monitoring flame flicker to monitor the presence of a flame, quite often together with other parameters [39–41, 108]. Most diagnostic techniques depend on the analysis of the light emitted by flames, particularly chemiluminescence, when chemical reactions during combustion produce electronically excited species or radicals which emit at distinct wavelengths before returning to their ground states [32, 37, 38, 45, 104, 107, 108, 110–112].

Usually such flame monitoring (more a flame safety device), a type of passive wall or contour type measurement, is carried out by monitoring the spectral characteristics of the flame [39, 41, 108], together with measurements of temperature, fuel flow and air flow rates and flue gas emissions through other sensors or flow meters to regulate the combustion in burners. This is then related to flame stability and the efficiency of the burner [32, 106, 113]. Improvement of flame stability and combustion control with the application of sensors and signal processing has been discussed in previous works [30, 35, 37, 108, 114–116]. Continuous monitoring has also been attributed to be an advantage with regards to energy saving and pollutant reduction [117].

Optical methods such as laser induced fluorescence though commonly used in laboratories for flame temperature measurement is unsuitable for industrial applications for online continuous monitoring (for accurate NO_x predictions) due to their cost and complexity of usage [117].

Some features looked at for quantifying a flame, like flame flicker, fluctuation of the measured amplitude and fluctuation symmetry have been studied before by others [118] and a lot of these flame visualisation based measurements are based on optical sensors in a non-intrusive manner thereby not disturbing the actual evolution of the flame under study [21, 41, 104, 118, 119]. These flame features extracted from digital signal processing can then be interpreted as identifying some 'unique' features of that particular flame together with the rest of the measured physical parameters of the flame [118]. An additional advantage of using such burner monitoring techniques is the ability to troubleshoot problems with individual burners in multi burner boilers as has been highlighted by Kay [31].

Other authors have also looked at modelling entire boilers to aid operation of PC boilers, but these usually use black box modelling as not all the reactions and variables are well known or understood in solid fossil fuel combustion [30, 45]. NO_x production is highly non-linear with regards to burner operational parameters as highlighted in section 2.5.1, hence black box modelling approach is often used [83]. So most of these modelling or measurement methods utilise global or stack values to evaluate the combustion efficiency or pollutant production instead of local or direct flame measurements [30].

2.7.2 Camera & Image Processing

A number of researchers have undertaken flame condition monitoring using cameras and image processing to characterise flame properties like flicker, geometry and temperature [39, 117, 120, 121]. Though the cost of cameras, especially solid state ones like CCD has reduced [117], the rest of the optical chain still entails some cost and maintenance effort to keep it dust free. Image processing

inevitably involves a lot of processing and usually requires the application of high speed cameras. This increases the cost of employing such systems as the maintenance cost and the number of such cameras and the processing power required to support the multi-burner setups usually found in utility boilers would be cost prohibitive.

Colour flame images have been utilised, together with neural networks for the prediction of NO_x emission for a coal boiler [121]. An analogue camera with a video card was used by Yu *et al.* for predicting the efficiency of a boiler and also NO_x and SO_2 emissions [65], where luminous and colour features were extracted and analysed from a 2 dimensional image of a 3 dimensional flame. Yu *et al.* discussed a link between flame measurement values (obtained through image processing) from the cameras to that of existing process condition monitoring data from the boiler control system [65]. Yu *et al.* and Chen *et al.* also demonstrated the features with the greatest relevance from the data (extracted from the processed camera images) could be obtained by applying Principal Component Analysis (PCA) for monitoring the flame [65, 122]. PCA is a variable reduction procedure, where by highly correlated variables are eliminated to just use the variables that produce the most variance in the signal [123, 124].

The application of image processing (or other signal processing) generally involves following three stages to identify flame features: Data acquisition, image processing (and / or other signal processing) and the development of relationship to other physical parameters being measured [118]. The relationship development is a complex search as many of these features may not directly correlate to any physical parameters and hence exhaustive experiments and a large signal processing effort is required to relate these values to the combustion under observation [118]. For example flame stability has been linked to geometrical and luminous parameters being extracted from flame imaging [39, 125, 126]. This discussion will now move to other monitoring methods and their characteristics compared to camera based monitoring which have a less stringent need for processing and a greater ease of use.

2.7.3 Flame Flicker Monitoring

The combustion process is dominated by the mixing of fuel and air through the burner quarl and hence consists of many eddies of different amplitudes in and around the combustion zone. These contribute to flame flicker as different sized eddies produce different frequency components [116]. So flame sensors reflect the turbulence of the flame region being monitored, usually the root of the flame [127].

Most detection techniques are dependent on the chemiluminescence of the flame, that arises from excited species or radicals which emit distinct wavelengths during their excited state [37, 38]. Basic flame detectors typically employed in utility boilers are passive, non-intrusive safety devices, which operate in the IR region detecting the presence of the flame [39, 40]. The flame is generally detected through a natural flicker which is not affected by background blackbody radiation unlike methods dependent on signal intensity alone [41]. All flames are known to pulsate and some fuels tend to have specific flicker frequency that is not affected by burner dimensions or fuel flow [128].

The usage of flicker characteristics of IR monitors in flame detection depend upon the discrimination of the flicker observed between a flame on or off condition, especially in multiburner cases [128]. The two common problems encountered with such flame presence detectors, especially for coal combustion are the fail-safe operation of such detectors and the need for gain control, as coal flames tend to vary hugely in brightness with varying firing rates [128].

Flame flicker has been employed in flame monitoring to increase the detecting reliability of flame sensing as this method is not affected by the blackbody background radiation and hence avoids the unreliability of visible and infrared spectra sensing based on intensity alone [41]. Though the flicker frequency varies with changes in load, fuel, other flow conditions to the burner and to the design and layout of burners, the typical dominant fundamental frequency is in the range of 1 to 40 Hz [41, 107]. Flame flicker has also been related to combustion stability and emissions [129]. Also flame flicker characteristics have been associated with combustion efficiency among others [127], which has been applied to control and monitoring of coal flames. The main advantage of the detection of flame flicker frequency is that the intensity level (direct current (DC) signal) of the flame signals can be ignored, which usually varies when sensor(s) or the lens becomes obstructed through dust or slagging [41].

As noted from literature above, the monitoring of flame flicker has many advantages for the current research. Chiefly, the general type of flame monitors being used for safety in most modern boilers employ such flame flicker methods but only for checking presence of a flame, which could be extended in the future if features from the processing of such raw signals can yield features that could be related to various flame conditions and / or emissions. Secondly, flame flicker is not affected by signal intensity levels there by avoiding issues with viewing ports / lenses becoming obstructed through dust or slagging. The possibility of reuse or extension of existing flame monitors to give flame quality information has cost benefit as reduces cost of replacement for the boiler operator.

2.7.4 Emission Spectroscopy

Emission spectroscopy techniques have been used widely for the detection of combustion radicals, especially in the UV region of 300 nm to 450 nm for the emission radials OH^* and CH^* [104, 130]. This technique of flame monitoring of combustion in power stations is simple and cost effective compared to laser absorption techniques, as it just needs a lens assembly and the spectrometer according to Leipertz *et al.* [38, 106].

As highlighted in section 2.7.1, emissions from electronically excited species in the flame have been used for flame monitoring, using two types of sensors depending on the wavelength ranges: narrowband and broadband sensors, as discussed below. Chemiluminescence has been applied for the monitoring and control of flames, especially premixed gas flames for OH^* and CH^* in the 300 nm to 320 nm and 420 nm to 440 nm [40, 47, 130–132] using narrowband sensors, as most hydrocarbon flames tend to emit these luminescent species [110, 133] in the UV and visible spectral range [106, 130, 134]. This type of monitoring has been carried out using sensors which are usually more expensive as the sensitivity needed to amplify very small amplitude signals resulting from the very selective

bandwidth ranges 10 or 20 nm need good optics and cooled sensors that are highly amplified and with minimal noise.

Most burners have a flame detector as a safety device, usually using either UV or VIS and / or IR based sensing element(s). Such commercially available detectors have shown promising results with regard to control of burner performance when applied with advanced data analysis techniques [109, 135]. So sensors with relatively broad coverage of these frequency ranges, especially UV, VIS and near IR have been utilised before [36, 47, 106, 109, 136]. So the thought process for using such broadband sensors, which are similar to commercially available sensors for this research is the possibility of piggybacking onto existing sensors which are already installed in power stations for flame presence monitoring. This could also be used for detecting changes in flames with appropriate signal processing and other detection algorithms provided the raw signals could be extracted. This research makes use of broadband sensors in the UV, VIS and IR spectral region with an appropriate lens assembly to record the spectral emissions from coal and biomass blended flames.

2.7.5 Implications for Current Work

As discussed in section 2.7.4, the broadband sensors were chosen for monitoring of the flame spectral emissions from individual flames as they closely resemble commercially available flame detectors in terms of the wavelengths covered. If the entire range can be covered from UV to near IR, a number of different flame types can also be monitored using the same instrumentation adding to its general applicability. Such optical, non-intrusive methods using various sensors are known to be used for flame diagnostics as discussed by Thai *et al.* [36, 42, 137].

The general issue with sensors and electronics is that dust and temperature affect their performance greatly, especially when placed next to high temperature coal flames. Another issue is accessibility and space for placement of sensors, so fibre optic cables have been employed before to avoid these issues by Tan *et al.* [56, 109, 138, 139]. Advantages of fibre optic cable usage include portability and smaller dimension, which eases usage of sensors in areas with limited accessibility and space constraints [139]. Romero *et al.* applied bifurcated fibre-optic cables with a spectrometer for monitoring gas burners used in glass melting as this allowed usage in the high temperature environment [108]. Yamaguchi *et al.* also utilised fibre optic cables with photodiodes to maintain combustion conditions in a premix gas boiler, thus shielding the photodiode sensors from heat produced during combustion [140].

2.8 Signal Processing

A signal can be represented or transformed in many different ways to aid understanding [141]. Quite often signals are non-stationary and tend to be represented in the time domain to capture or understand the changes in amplitude of the signal over time. This simple representation only shows changes with time but the other important nature of such signals is the variation interval, which is usually represented in the frequency domain. Traditionally the Fast Fourier Transform

(FFT) is used to convert between the time and frequency domains, where the signal is decomposed as the sum of weighted sinusoidal frequencies [141, 142].

The data recorded during experiments for this research was initially analysed with widely used signal processing methods such as Root Mean Square (RMS) and Power Spectral Density (PSD) in the time domain and frequency domain respectively. This analysis indicated that it was unlikely that a single feature could be identified to predict the changes in flame conditions with respect to changes in air and fuel flow rates, air / fuel ratio and emissions like NO_x. This led to an investigation of advanced signal processing methods like the Wigner-Ville Distribution (WVD) and Gabor function to analyse the data to extract features which correlate to changes in flame spectral characteristics with time.

According to Qian *et al.*, a lot of real signals, like human speech, could be better understood with joint time frequency analysis, as not only the frequency components and change in amplitude of the whole signal is seen, but also the moments at which each frequency component within the signal changes [141, 142]. Using the classical FFT for signals that change over short periods is also unsuitable as it assumes a stationary signal, basically losing time information when processed [142].

Coal combustion is a complex process and with flame flicker the spectral emissions are of non-periodic in nature with complex variations. So these are similar to human speech and the application of Joint Time Frequency (JTF) methods is an appropriate area of application as discussed by Qian *et al.* [142].

2.8.1 Joint Time Frequency Domain

JTF domain analysis characterises the frequency information over the entire time period, whereby it combines both the time and frequency domain analyses to reveal a better understanding of the signal changes over time. This localises the frequency information or spectral components as it changes with time. So this has many advantages over either time or frequency domain analysis alone [141–144]. Figure 2.1 shows a very simple sample signal, which consists of two distinct frequencies over time. The higher frequency is present in the first half of the signal and the lower frequency during the second half with no over lap. Simple time domain analysis using FFT in figure 2.2 shows the two frequencies accurately but completely loses the time domain data of when the frequencies were present. This could be avoided to some extent by windowing and using smaller periods but still wouldn't be as good as some of the JTF methods. Figure 2.3 shows the two frequencies present as well as when the transition happened.

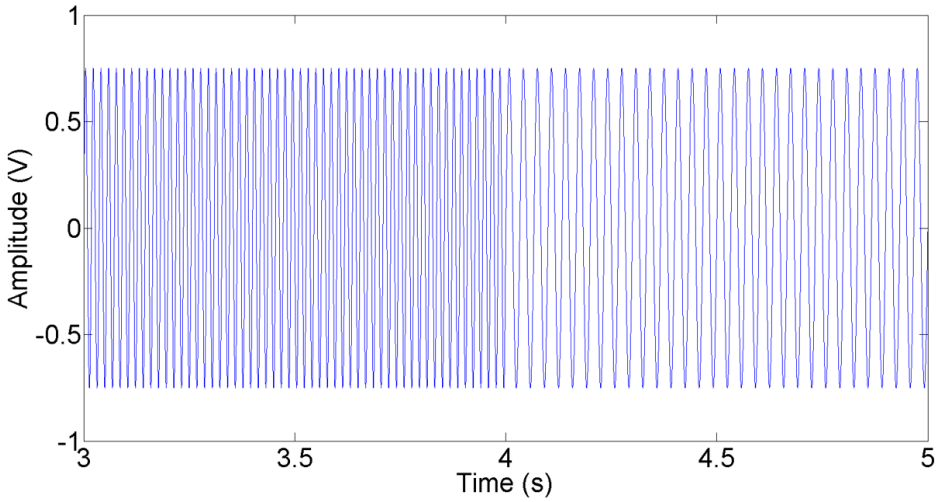

Figure 2.1: A sample signal with two distinct frequencies over time

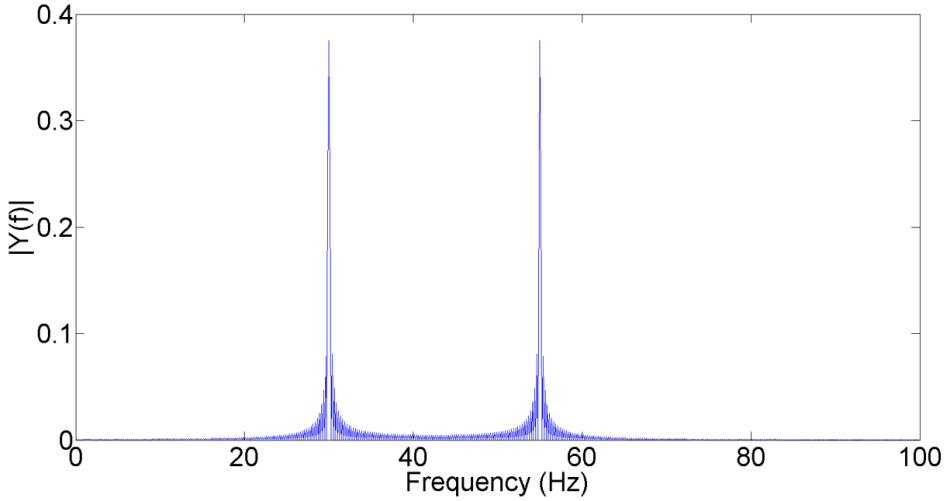

Figure 2.2: FFT of sample signal

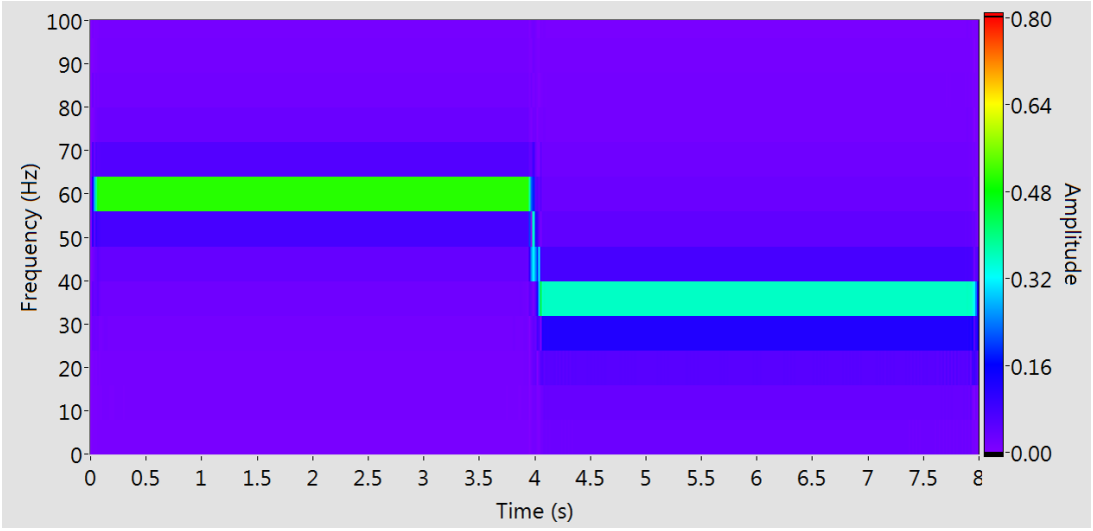

Figure 2.3: JTF of sample signal

The advantage and usage of JTF started with analysis undertaken for acous-

tics and speech processing research, according to Thayaparan *et al.* [143], who also quoted a number of fields in which JTF has been utilised such as radar signal analysis, where they discuss in depth the various JTF methods available and their effectiveness in various signal analysis [143].

As discussed in section 2.8, the frequency spectrum is estimated using a spectral energy density function such as the FFT which show the various frequencies present but don't identify at what instance in time those frequencies were present or if that changed. So JTF would be of great advantage to realise any changes in frequency with time. This is particularly relevant to the research presented here as there are signal fluctuations in a flame front that would be very important to understand and have large implications for flame monitoring. This has also been emphasised by Thayaparan *et al.* while dealing with non-stationary signals as encountered in radar signal processing [143].

The WVD is one of the JTF methods as listed by Cohen [145] and Thayaparan *et al.* [143] that has very good resolution in both the time and frequency domains [144, 146–148]. This would be beneficial when applied to the flame monitoring signal as the changes in the flame fluctuations could be utilised without loss of resolution in either the time or frequency domains. As identified by Thayaparan *et al.* [143], the technique does lead to the occurrence of interference cross terms [141, 146, 147], but these wouldn't be much of an issue in this research as the output from the transform was not utilised to quantify the signal / frequency present but to feed into pattern classification (section 2.9.6).

2.8.2 Wigner-Ville Distribution

Time-frequency analysis focuses on a distribution of the total energy of the signal at a particular time and frequency. WVD was one of the first JTF techniques to be introduced and has been extensively studied since. It was developed in quantum mechanics by Wigner [149] and implemented as a signal processing paradigm by Ville [150]. Many further developments have been made since, as reviewed by Cohen [145].

The distribution was 'rediscovered' at the beginning of the 1980s in a series of papers by Claasen and Mecklenbrauker [151–153] who also introduced the first discrete approach to the WVD. These developments have resulted in the application of the WVD to areas as varied as acoustics, speech processing, image processing, detection and estimation problems, seismology, and engineering [144, 147, 148, 154].

WVD is a representation of the energy distribution of a signal in the time and frequency domains and has better resolution in both domains compared to other JTF analysis [142, 144, 146, 155]. Though the WVD is afflicted by cross term interference, it possesses many characteristics desirable for analysis [141, 142, 146–148]. Qian *et al.* [142] highlight this issue as one of the reasons for the WVD being not used for real applications, which is not strictly true as Thayaparan *et al.* [143] have shown examples of it being used elsewhere and National Instruments Incorporated (NI) LabVIEW (authors of [142] work for NI) also implements the WVD.

The Gabor spectrogram is similar to the WVD in many aspects but reduces the cross term issues to some extent at lower resolution. However when the order

of Gabor spectrogram is increased to increase the resolution, it tends towards the WVD output with the addition of cross terms [142]. Shie *et al.* also mention the WVD has better performance in terms of JTF domain analysis [142, 156] and WVD decomposition is optimally concentrated in the joint time-frequency domain and also results in improved computational speed [142].

WVD is not known to be applied in the monitoring of coal biomass blends before, so this research would be one of the first to explore such usage. So the choice of WVD would give the best possible resolution in both time and frequency domains and performance, and the cross terms might not be a huge issue as the signals are not being quantified as such to absolute values or flame conditions but more as an output which is used in pattern classification as discussed in Section 2.9.6.

2.9 Detection Algorithms

Detection algorithms are capable of identifying changes from a given input. In this case the change in the flame conditions from the optimal condition which needs to be detected to be rectified. As discussed in section 2.6.3, the modelling of co-firing is of interest to the CFD community but hasn't been implemented in a way that could be readily used online and in real time, but is of great aid while designing or retrofitting boilers.

There are many soft computing techniques used to learn from data, usually grouped under machine learning, where machines or computers modify or adapt their actions based on prior data hence the term learning [157]. The way the data is used to learn and how the learnt data is used for future generalisation based on the quantised error gives many techniques as outlined in Marsland's book [157]. A wide number of techniques are available, and a few like ANN, deep learning, fuzzy logic and Support Vector Machines (SVM) are discussed briefly here.

Despite the wide ranging applications of the WVD, it appears that no effective and well established method exists for an automatic fault detection procedure based on the WVD alone. However, the contour plot of the WVD can be regarded as a two-dimensional image. Thus, the problem of automatic fault detection can be dealt with using pattern classification procedures. There exist many different pattern recognition methods, some of which have been outlined in Schalkoff's book [158]. Classical pattern recognition techniques have been applied to the problem of fault detection for some time. Only relatively recently have neural networks attracted attention as a possible technique for fault detection [154].

2.9.1 Artificial Neural Network

Conventional computing has been used in multiple fields, especially to solve equations and compute data and arrive at results from a set of inputs, but when these inputs deviate or are of a complex nature, then the capability of the computer or algorithm extends only to those it's been defined or made for especially. So this need to have computers perform complex pattern recognition problems, based on physiology of the brain, leads to Artificial Neural Systems (ANS), generally

referred to as neural networks, to solve problems that conventional computing is unable to perform [159].

ANNs are algorithms inspired by biological neural systems, and are capable of handling complex information of unknown and non-linear functional relationships among the different inputs and outputs [160–163]. Since Warren McCulloch and Walter Pitts introduced the first models on artificial neurons in 1943, there has been steady improvements and proposals for various types of ANNs and architectures [162, 164]. ANN development was motivated by the differences in the way the human brain and digital computers compute, especially the parallel nature of the brain's computing and the capability to solve complex and non-linear problems [160]. This capability in biological brains is thought to be achieved through cells called neurons which connect to each other that increase their bonds based on learning, strengthening when needed to activate a particular action. Similarly such structures used in simple digital computer based models store weights and align based on the inputs to the ANN neurons [160]. ANN are also referred to as Parallel Distributed Processing (PDP) and usually consist of simple processing units, called neurons, which are connected to each other sharing information over weighted connections [164]. These neurons simply receive input from their neighbours or input sources and compute an output that is shared through the weighted connections with neighbouring neurons [164].

ANNs are generally classed into two types based on the way the network realises its learning process, namely supervised and unsupervised. Supervised learning is where the weights of the synapses are modified based on the output derived after the network processes an input and comparing this with the desired output. Such networks are further classed based on their architecture as feed-forward or recurrent networks according to Haykin *et al.* [160, 162]. Of this, the simplest and most used network topology, feed-forward where the input only moves in one direction, from the input to the output, through any hidden layers if present is classed into two types, single layer feed-forward network or multilayer feed-forward network [160].

The simplest single layer feed-forward network has an input layer which is connected to the output layer of neurons, thereby only having one layer of computation neurons which are directly connected to the input [160]. On the other hand, multilayer feed-forward networks have one or more hidden layers between the input and output layers and are able to extract higher order statistics and contribute to the capability of the ANNs' computational power, though with increased complexity [160, 162]. The other type of supervised network is the recurrent neural network, the major difference compared to feed-forward networks is that these networks have feedback loop(s) where the output of a neuron would be fed back to the input of other neurons [160].

In the classification of ANNs based on the learning process, the other type is unsupervised learning, where the neurons learn competitively. These were first introduced by Von der Malsburg in 1973 as the Self-organising Map (SOM) [160]. This is further discussed in section 2.9.6.

Empirical modelling for diagnostics and operation control is advantageous as it's easier to interpret and apply to systems, and one of the very popular methods is the ANN [165]. ANNs have been applied extensively for boiler operation and control of emissions of pollutants; and also for power plant condenser performance

[165]. Rusinowski *et al.* have noted the usage of ANN over other methods, especially when other methods have failed or are computationally very intensive [165]. Computational control needs mathematical modelling and takes longer to compute compared to an ANN [165].

A US government project with commercial partners tested the effectiveness of intelligent systems based on ANN for NO_x reduction [79]. This was tested on a large scale in open loop mode as an advisory system to reduce NO_x, and at the same time reduce UBC and maximise efficiency, but also was capable of being operated in closed loop if the plant required it, trying to achieve economic and operational constraints [79]. In this research, the pulverised coal combustion process in itself is a complex process but the addition of biomass with different particle size and calorific value for example, adds to the complexity. Hence, the application of an ANN might be very appropriate to analyse data from this combustion process, as the relationships between inputs and outputs are not very well known and are very difficult to predict in such conditions involving biomass burning [42–44, 83, 165–167].

2.9.2 Application of Supervised ANN

Multilayer feed-forward networks are also referred to as Multilayer perceptron (MLP) where the input signal propagates through the network from input to output. These networks have an input and output layer and at least one hidden layer, so its multilayer network as the name suggests. MLPs have been utilised to solve many problems in various fields in supervised training, often utilising a popular algorithm known as error-back propagation. In this, the training of the system happens over two passes through the network: forward and backward passes. The synaptic weights of the network are fixed during a forward pass with an input (training) data set applied to the ANN and an output is produced. This output is compared to the desired output and the error or correction is passed back through the network in the backward pass where the synaptic weights in the network are modified using an error correction rule to reduce the difference between the desired and actual output obtained. This back propagation is a recursive gradient descent algorithm which reduces the mean squared error for each training pass, called the epoch. Hence the network gets its name of back propagation algorithm [160]. The synaptic weights are modified over many iterations / epochs until the error is reduced to a satisfactory value.

Examples of a number of combustion related applications of ANN are given in papers by Tan *et al.* [34, 44] and energy related examples by Kalogirou [168]. According to Basheer and Rohwer *et al.*, MLP with back propagation is the most used network [162, 169], therefore this was chosen to be investigated in this research. This ANN was chosen to be used for this research as this type of supervised network is known to be able to extract higher order statistics [160, 162]; such networks have been previously used for combustion related applications [44]; capability to model wide range of complex relationships [160] and the availability of off-the-shelf software for the implementation of such networks.

As highlighted earlier, combustion of coal (biomass blend) is a complex process and not very well understood for effective real time modelling. A number of signal processing methods have been utilised and haven't been found suffi-

ciently capable of identifying features present in the flame that could be related to changes in the flame. Hence a detection algorithm is needed that is capable of identifying the complex relationships present in the signals obtained from the chosen sensors. ANNs are known to be able to pick these complex relationships present in the input data, flame monitoring sensor signals in this case, which are not easily achieved using conventional methods. One such method is the back propagation based MLP which has been applied by others to combustion monitoring and also one of the most used methods for such complex processing, hence easy availability of ready to use software to implement such networks.

Due to these advantages and the complex nature of coal combustion, this seems a very appropriate method to be utilised for this research. Training data is important for such networks as the generalisation capability of the such networks depend on the capability of such networks to learn. Usually a number of parameters such as learning rate, momentum factor, number of hidden layers and number of hidden neurons affect the learning capability of a multilayer feed-forward network with back propagation. Usage of too many hidden neurons or too much training might lead to over fitting, which would lead the network to produce too much error for an unseen data set. Hence the choice of hidden neurons should be in such a way the network is able to learn sufficiently to generalise and not too much it takes longer to process or over learn / fit the data. High number of training epochs can also lead to over fitting and has to be arrived at experimentally for the generalisation capability of the network to be maintained with the least complexity and processing.

2.9.3 Deep Learning

In section 2.9.2, MLP was discussed where by a network with a hidden layer is used to learn. If more learning is needed for a function even more nodes are needed and hence more learning time [157]. As the features to learn and nodes grow, such a back propagation MLPs search space the algorithm searches for a minimum increases and would make the estimates noisier [157]. Deep learning networks use combinations of derived inputs and many neurons over multiple hidden layers to achieve the learning, which makes the training phase difficult. These in addition to requirement to be able to retrain relatively easily and running in real time makes this method not very suitable for this application.

2.9.4 Fuzzy Logic

Fuzzy logic in contrast to boolean logic, allows values between 0 and 1. Lofti Zadeh proposed this as a measure of vagueness, where partial truth can be established [170]. He proposed this as an alternative to boolean logic, which allows a higher level abstraction and dealing with imprecise input data [171]. This is useful to establish when the certain values could be partially true and belong to two different sets based on partial or vague input reasoning [170, 172]. Fuzzy based control employ mapping input and output values from real world to fuzzy rules [172]. According to Russell *et al.* successful applications of fuzzy logic have had small rule bases, no chaining of inferences and tunable parameters [172]. The application in the case of the flame monitoring sensor data might be quite

difficult with the number of conditions and variations encountered, where by the rule base might be quite considerable.

2.9.5 Support Vector Machines

SVM is a type of supervised competitive learning network with algorithms that could be used for classification and regression [170, 172]. A SVM tries to find a hyperplane that could separate the data into the two classes using training data called support vectors by transforming the input data to a higher dimension non linear mapping [171, 172]. SVM have the advantage of being extremely accurate due to using higher order complex non linear modelling and are much less prone to over fitting [171]. SVM is designed for binary classification and the training of even the fastest SVM could be extremely slow [171]. SVM separation line or hyper plane depends on all the data used for training but some data might be more important than others needs attention to what data are used for training [172]. So application of SVM for the flame monitoring sensor data might not be ideal as coal flame tends be dynamic and also the slow learning phase and attention needed to select training data might make the model more specific to each burner or rig instead of being generic.

2.9.6 Self-organising Map

SOM is a type of unsupervised network, which is similar to the optical processing neurobiological structure, where the inputs are clustered without any prior knowledge of the system or process being modelled [173, 174]. SOM has been used to recognise patterns in the data and then organise itself so that it can remember them for future reference [34].

Haykin described self-organised learning as updating the synaptic weights associated to neurons repetitively according to a set of predefined rules until a value is reached below the set error allowance [160]. SOM is based on competitive learning [160, 162], where the neurons in the output layer compete among themselves to be activated. As only one neuron is activated at any one time, the neuron is called *'winner-takes-all'*. The two types of SOMs are: Willshaw-von der Malsburg model and Kohonen model [160, 173]. Willshaw-von der Malsburg model was prosed to map retina to visual cortex as seen in higher vertebrates and specifically needs to have the same number of dimensions in both the input and output layers [160].

Kohonen's SOM model was developed to visualise high-dimensional data to a two dimensional grid of nodes [175–177]. Figure 2.4 shows an example of a SOM consisting of 25 neurons on a 5 by 5 grid. This aids in two ways, one by visualising high dimensional data sets as a single or two dimensional grid and two by, abstraction of the data to grids without knowing pre-set conditions of the relationship of the input data [175, 177]. This is illustrated in figure 2.5, where an activated neuron, or in other words the 'winner-takes-all' neuron, is highlighted after an input is processed. The input data is computed in a non-parametric, recursive regression process where similar models are kept closer to each other and dissimilar ones further apart, hence clustering the high dimensional input data [160, 175]. Due to these characteristics, SOMs have been applied in many

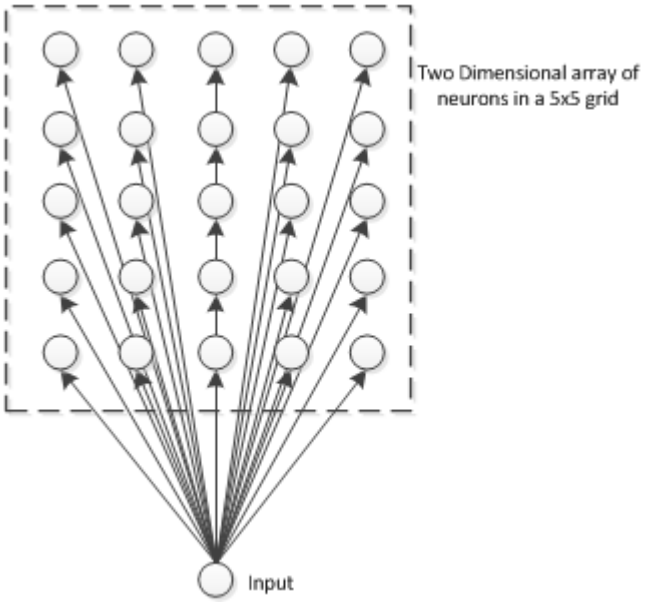

Figure 2.4: SOM - 5x5 grid of neurons

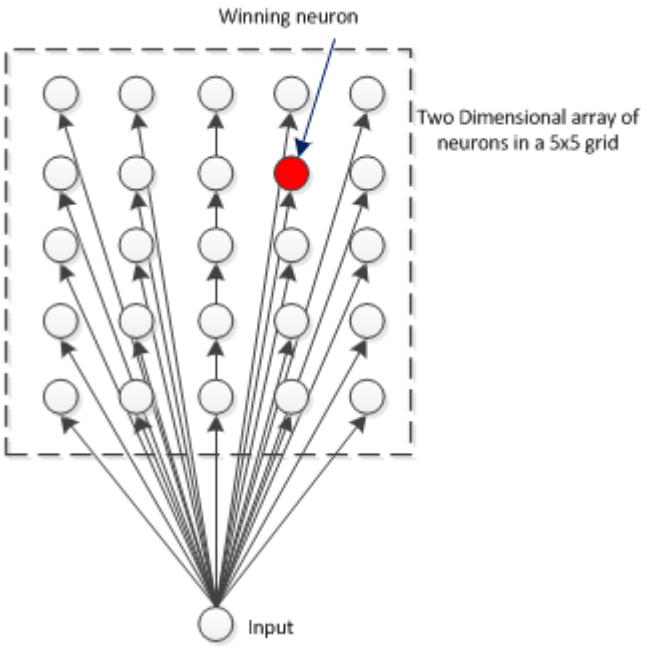

Figure 2.5: SOM - showing an activated / winning neuron

fields, such as medicine, biology, chemistry, image analysis, speech processing, engineering and numerous others as highlighted by Wehrens *et al.* [178], and bibliography of a few thousand papers on SOM are available at Helsinki University of Technologies website [179] where Kohonen initiated SOM research.

2.10 Summary

Due to climate change implications from greenhouse gases and health problems, smog, NO_x and other emissions from fossil fuel combusting plants, there are concerted efforts from utilities and governments throughout the world for energy

efficiency and emission reduction. One of the ways this is being pushed is through legislation for green energy, in other words renewable sources of energy. A range of legislation limiting pollution emission and promoting energy efficiency have been highlighted earlier.

One short term approach to achieve this is the partial utilisation of biomass in pulverised coal power plants with little modification to the existing plant at a low cost compared to new 100 % biomass plants. This has the advantage of utilisation of carbon neutral biomass, some of which is otherwise not utilised leading to greenhouse gas emission reduction and it is also much easier to implement in existing plants with minimal modifications to the pulverised coal plant.

Co-firing of biomass has many advantages as highlighted earlier but there are a few technical issues associated with this that need some research, like fouling and corrosion in the boiler and maintaining thermal output. Biomass has a lower calorific value than coal and also lower density, thus requiring large quantities to be mixed with coal to achieve similar overall thermal output from the boiler. This requires a large amount of biomass to be transported to the burners, and hence requires a lot more primary carrier air which in turn affects the flame, as opposed to a coal only flame in burner designed for coal. Combustion chemistry of coal is very complex and the addition of biomass exacerbates this with differences in biomass particle size and volatility compared to coal. It would be very difficult & costly to develop real time models of the process to aid monitoring and control. So this research tries to identify features from measurement of the flame to identify abnormal conditions as the flame deviates for a given input, as real time models would be extremely difficult due to above mentioned reasons.

PC plants are usually controlled indirectly from measurements of the emissions and O_2 from the emission stack. The individual burners themselves usually have flame safety devices that only indicate the presence or absence of flames and not flame condition. Generally, power station boilers tend to have multiple burners in a single boiler but are controlled from values in the emission stack while individual burners themselves may not be combusting efficiently. So there is a need for a system capable of identifying these changes in individual flames, especially when biomass is co-fired and which is able to rectify that in real time, instead of only being fine-tuned while commissioning or servicing boilers as is currently done. One of the objectives of this research is to develop such a system, that runs in real time and aids the plant operator to change input to the burner to bring it back to ideal condition for co-firing.

Current flame safety and other devices in flame detection make use of UV, VIS and IR based sensors with many different wavelengths and algorithms for detection. In existing burners such flame safety devices are already utilised for individual burners, so an algorithm capable of identifying changes from such sensors would be beneficial. This would avoid the need to have multiple devices mounted near burners for flame safety and monitoring flame conditions. The idea of being able to piggy back on to such sensors if the raw data could be extracted from such sensors for further processing, makes creating a software sensor attractive. So off-the-shelf broadband sensors in these three wavelengths were selected for this research, whereby if a system using such sensors is capable of monitoring successfully, such a system could be extended to existing instrumentation in use.

Combustion chemistry is complex for co-firing coal and biomass flames, and

the changes in flame are not consistent with varying thermal load and biomass percentage while co-firing. A systematic set of experiments while varying one parameter are to be carried out in this research to find if any features that are directly proportional and useful could be extracted from the sensors used. If such features are found than a simple rule based algorithm could be utilised for control. If not, an intelligent system capable of learning such changes, that is able to identify such flame conditions that affect efficiency, is needed. So this research utilised ANNs, which are of nonlinear nature and can learn complex relationships in the data to identify flame conditions and be able to suggest changes to have near ideal flame conditions in the burner.

The following chapters will detail the methodology utilised for this research (Chapter 3), the experiments carried out (Chapter 4), the development of the monitoring and controls system in pilot scale (Chapter 5), validation of the control system at pilot and full scale (Chapter 6) and finally discussion and conclusion (Chapter 7).

Chapter 3

EXPERIMENTAL APPARATUS & PROCEDURES

This chapter describes the test facilities used, plant instrumentation and their placement, photodiode sensor placement and the experimental methodology for all the data presented in later chapters. The pilot scale experiments were carried out at the 500 kW_{th} Combustion Test Facility (CTF) located at the Institute Energitky - Institute of Power Engineering (IEn), Warsaw, Poland and the full scale experiments were carried out at the 220 MW_e boiler 8 of the Dolna Odra Power station, Poland.

3.1 Pilot Scale – Experimental Apparatus

The 500 kW_{th} CTF for the investigation of the combustion of pulverised fuels was located at the IEn, Warsaw. The overall schematic of the CTF is presented in figure 3.1.

The CTF was equipped with a horizontal, cylindrical combustion chamber that had a 500 kW_{th} burner on a back plate with the necessary ports for observing the flame. The left side of figure 3.1 illustrates the primary and secondary air intake fans with the electrical pre-heaters on either duct, leading to the burner and combustion chamber. The electrical pre-heaters allowed the simulation of combustion air temperatures similar to those of large power plants. The primary air also carries the fuel from a hopper fuel feed mechanism, which is described in detail in section 3.1.1. The cooling air ducts surrounding the combustion chamber in figure 3.1 could be used for cooling the chamber wall (these are the blue coloured fixtures surrounding the combustion chamber in figure 3.2), but these weren't in use during the experiments for this research.

With reference to figure 3.1, the right hand side of the combustion chamber shows the exit from the burner with the cyclone and suction fan, which was utilised to maintain the pressure in the combustion chamber. Further to this, the emissions were released through the stack. The flue gas at the exit of the combustion chamber was monitored using gas analysers at two points, as explained in section 3.1.2. The control unit shown in the schematic in figure 3.1 is the plant control system utilised to control as well as record the various sensors. The data acquisition system highlights the portable computer, sensor electronics and the analogue to digital converter used for logging the sensor data during the

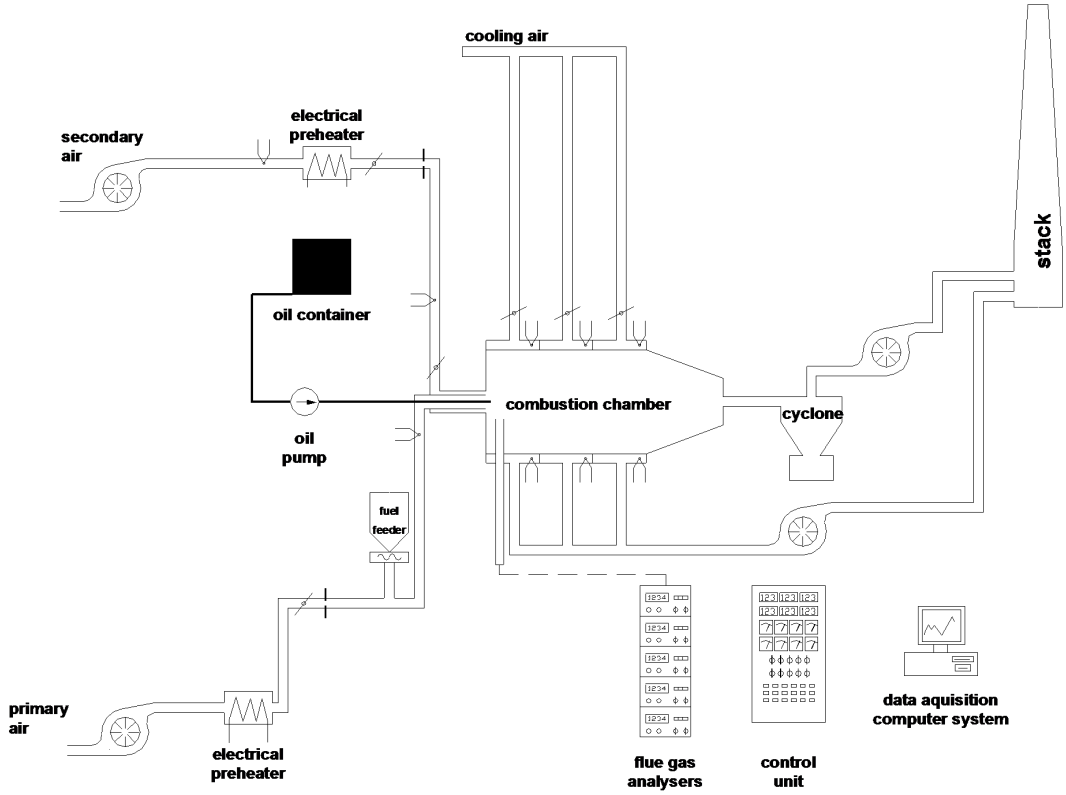

Figure 3.1: Overall schematic of pilot scale CTF

experiments at the CTF.

During start, up the combustion chamber was preheated by an auxiliary oil burner located in the centre of the coal burner, as shown on the left side of the schematic in figure 3.1. Pulverised coal / coal and biomass for combustion was prepared in advance and placed in a coal feed hopper and delivered to the burner via a two-worm dust conveyor that fed the coal / coal and biomass particles into the primary air duct.

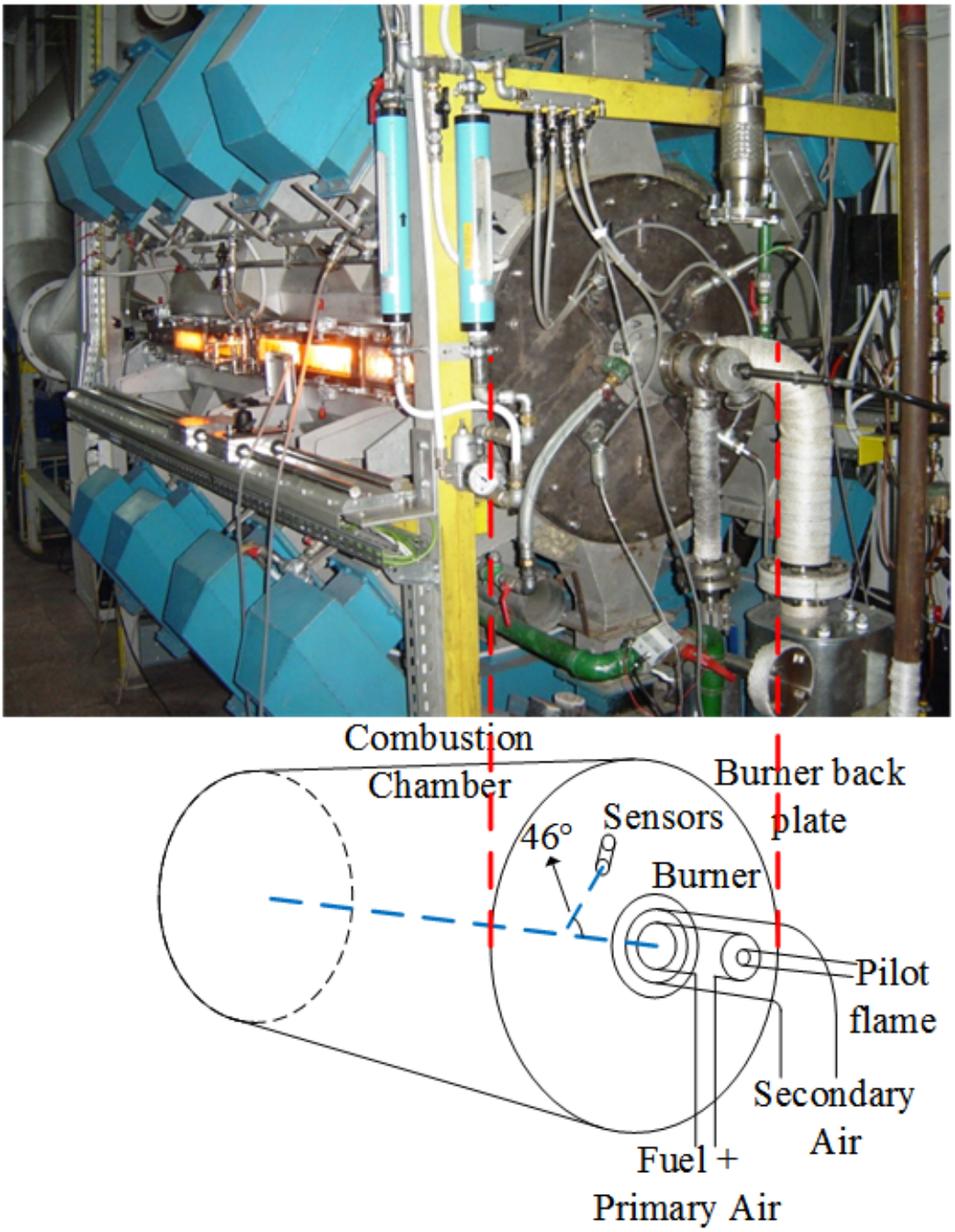

Figure 3.2: CTF with sensor location highlighted with regards to the combustion chamber layout

3.1.1 Fuel Feed and Pre-Combustion Setup

The various coals and biomass were milled separately and stored in large bags at the facility by IEn personnel. Fuel characterisation analysis for all fuels used at pilot scale are presented in section 3.3.1. Fuel was premixed for all co-firing experiments carried out where different proportions of biomass (straw) were mixed to coal at 10, 20 and 30 % on a mass basis before the experiments. This was accomplished manually by using a cement mixer to mix and bag them for usage in the future.

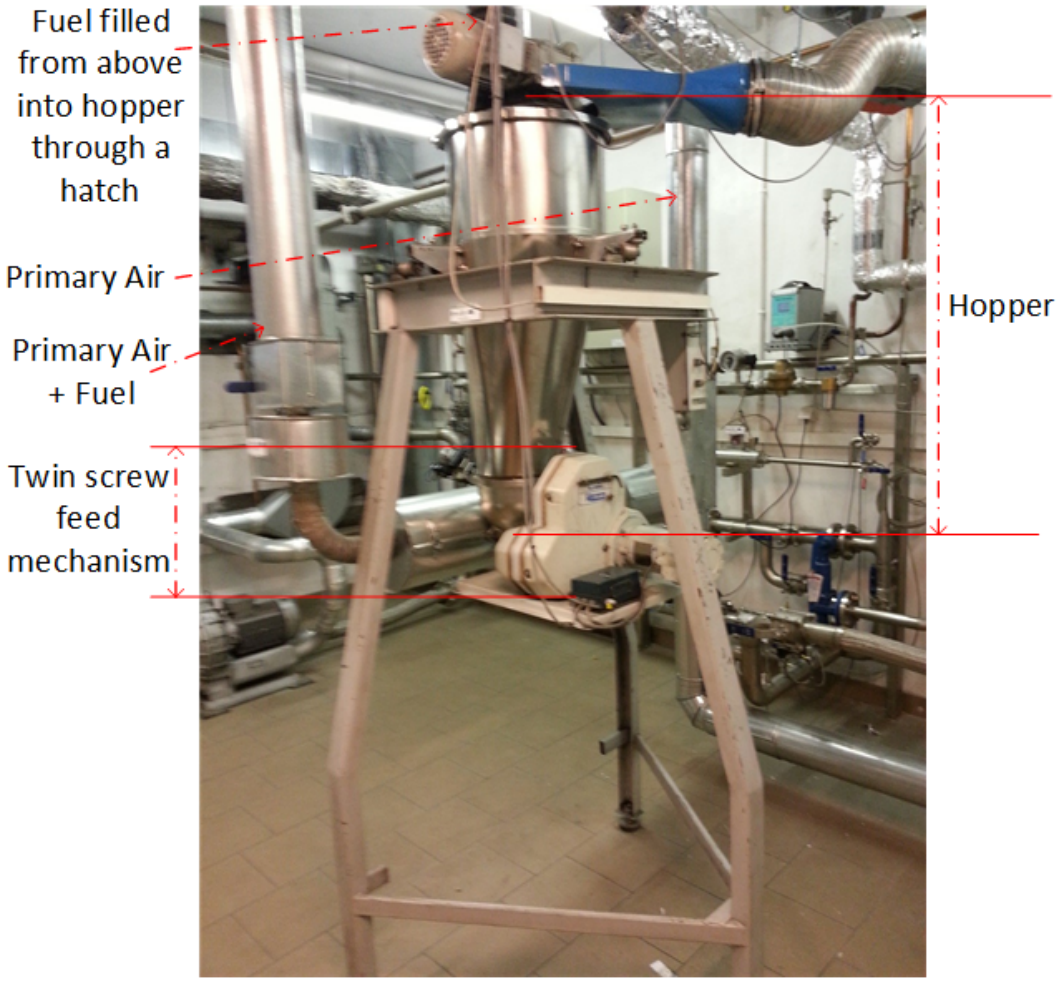

Figure 3.3: Fuel feed system showing hopper, feed mechanism and carrier air piping

These premixed bags were emptied into the fuel hopper as needed so as to ensure the hopper never completely emptied. In order to minimise in-experiment variations this was not done while experimental data was being recorded.

The pulverised fuel was fed from the hopper by T35 K-Tron volumetric twin screw feed mechanism, which varied the rotation speed of the screws to keep the fuel flow constant as the weight in the hopper changed, into the preheated primary airflow which carried it to the burner. Due to confidentiality reasons the calibration data is not available for the twin screw feed mechanism, similar to a number of other calibration documents such as that of the gas analysers for example, even though these were calibrated everyday.

Figure 3.3 shows the fuel feed system, where the hopper and the fuel feed mechanism were supported by a stand and the piping for the primary air met at the bottom of the hopper mechanism. The piping immediately to the left of the bottom of the hopper that bend upwards is the primary air to the burner, as the fuel feed mechanism was situated one level below the combustion chamber.

As shown in figure 3.1, both the primary and secondary air supply to the burner was preheated using electrical heaters. These were individually metered and controlled to ensure the correct stoichiometric ratios for the various experi-

ments described in section 3.5.1.

3.1.2 Burner and Combustion Chamber

The CTF had a horizontal, cylindrical combustion chamber 0.7 m in diameter and 2.5 m long, one end of which was fitted with a 500 kW_{th} swirl burner that had a throat diameter of 0.1 m and was mounted on the front wall as shown in figures 3.2 and 3.4. The sighting panel along the side of the combustion chamber (figure 3.2, flame is visible along the sighting panel) aided observation of the flame and burner stability while conducting the experiments and avoided conditions where flame blowout was a danger.

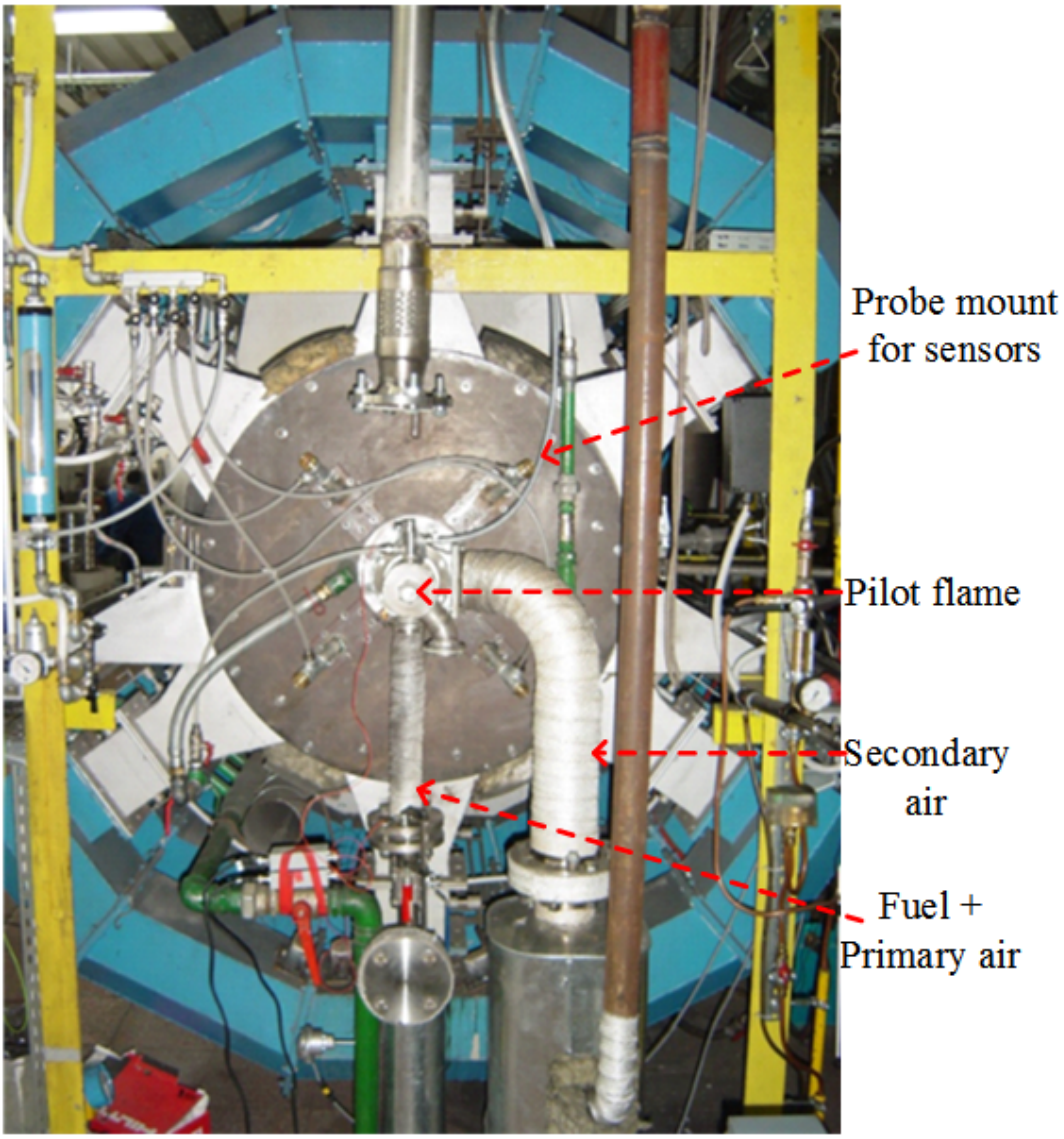

Figure 3.4: CTF image showing the connections to the burner

The combustion chamber of the CTF wasn't equipped with a flame detector and only had the sighting panel along the side for the burner operator to control. This sighting panel was made of multiple transparent windows that needed cooling and purging to keep it clear and cool. As these experiments were carried out

as part of a larger European Union (EU) research project, other measurements were carried out through the side sighting panel of the combustion chamber that also allowed additional air ingress that couldn't be metered.

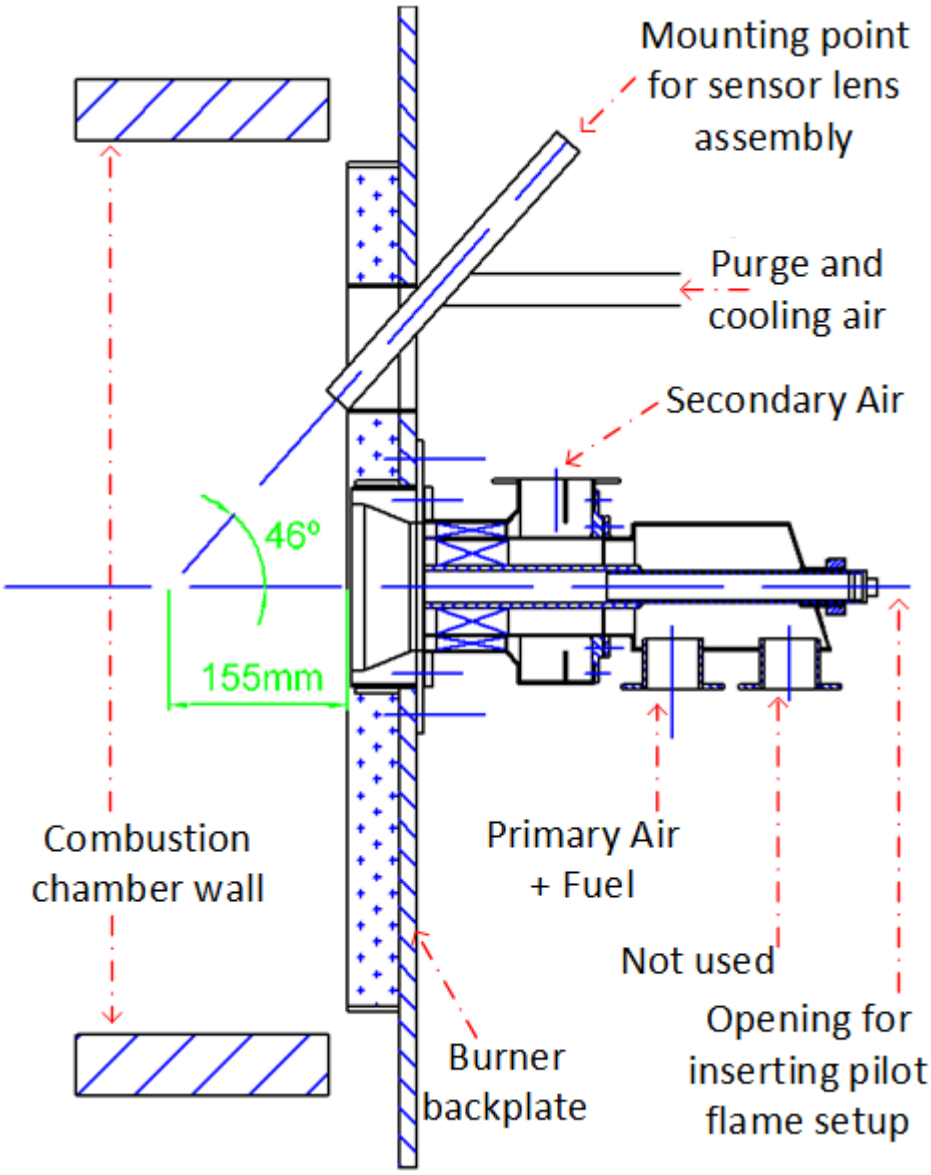

(Image courtesy of IEn, Poland)

Figure 3.5: Side view of burner cross section with the sighting tube for the sensors

Figure 3.5 shows the burner cross section when attached to the end plate of the combustion chamber. The innermost horizontal dashed blue line shows the axis of the burner, the tube immediately around it is the pilot oil burner assembly. The next concentric tube / assembly with two inlets from the bottom was for the primary air and fuel; only one of the two was used during these experiments. The secondary air came from the right as shown in figure 3.4, which is the third inlet from the right as highlighted in figure 3.5. Figure 3.5 also shows the distance (155 mm) at which the sensors were able to monitor the flame through the sighting tube from the burner quarl at an angle of 46° from

the axis of the burner.

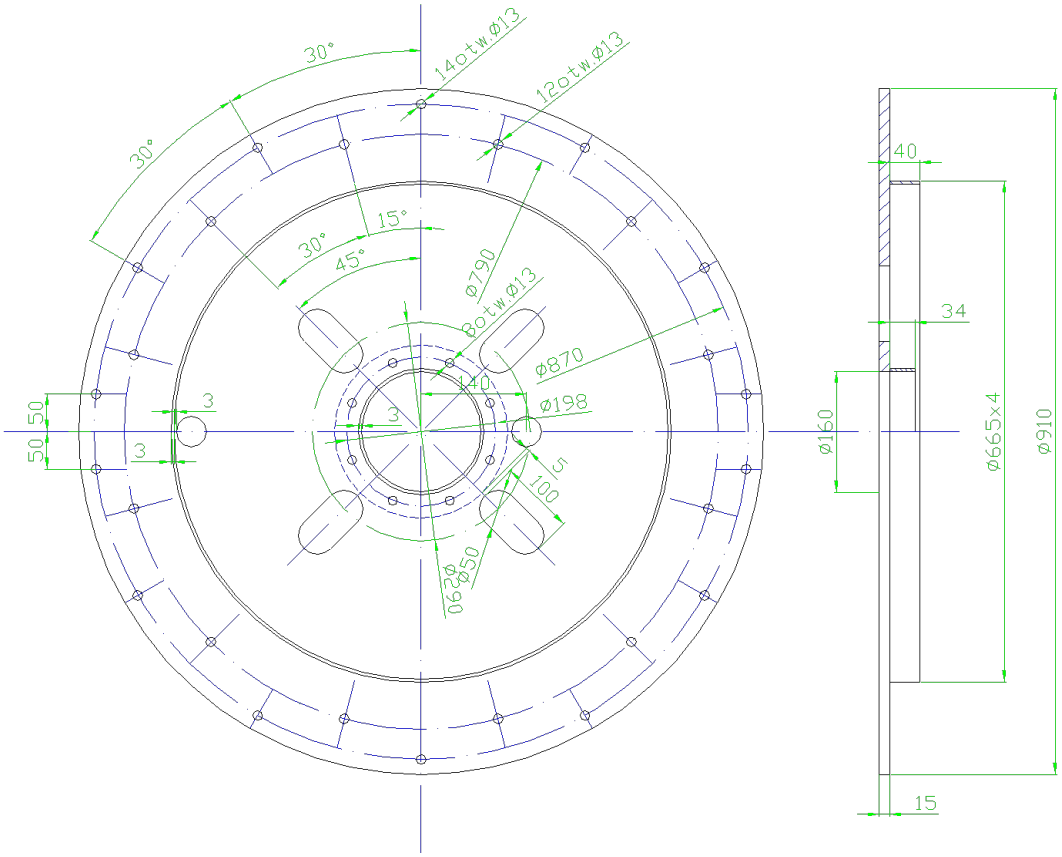

(Image courtesy of IEn, Poland)

Figure 3.6: Production drawing of CTF front plate for the burner end (Large middle opening for the burner and smaller oval openings for the sensor mounts)

Figures 3.6 and 3.7 show the production drawing and image of the end plate to which the burner assembly and the sensor mounts were attached. The large circular opening in the middle was for the burner assembly and the oval openings were for the sighting tubes for sensor mounts.

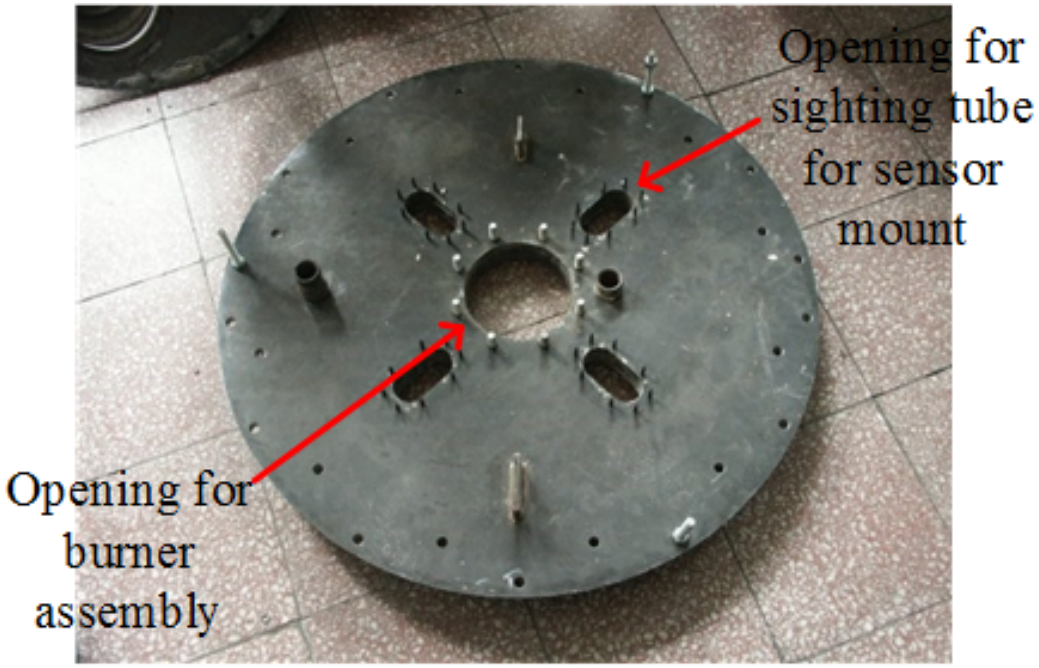

(Image courtesy of IEn, Poland)

Figure 3.7: Picture of CTF front plate for the burner end
(Large middle opening for the burner and smaller oval openings for the sensor mounts)

3.1.3 Existing Burner Control System

The pilot scale CTF was controlled using National Instruments Incorporated (NI) CompactRIO controllers with a number of daughter cards for both analogue and digital inputs and outputs. The data gathering and acquisition system was based on NI PXI series, again with several cards for thermocouples, analogue and digital inputs.

There was no flame detector attached to the burner during these experiments, only visual confirmation of the presence of the flame was made when starting up the burner with an oil flame. Once the CTF had warmed up, the coal (or coal blends with biomass) flame was transitioned from the oil flame gradually which was aided by the sighting panel running through the entirety of one side of the combustion chamber, as can been seen in figure 3.2.

Figure 3.8 shows the location of the points of measurement relevant to this set of experiments, namely the two points at which the gas sampling was done with reference to the burner and thermocouples on the CTF.

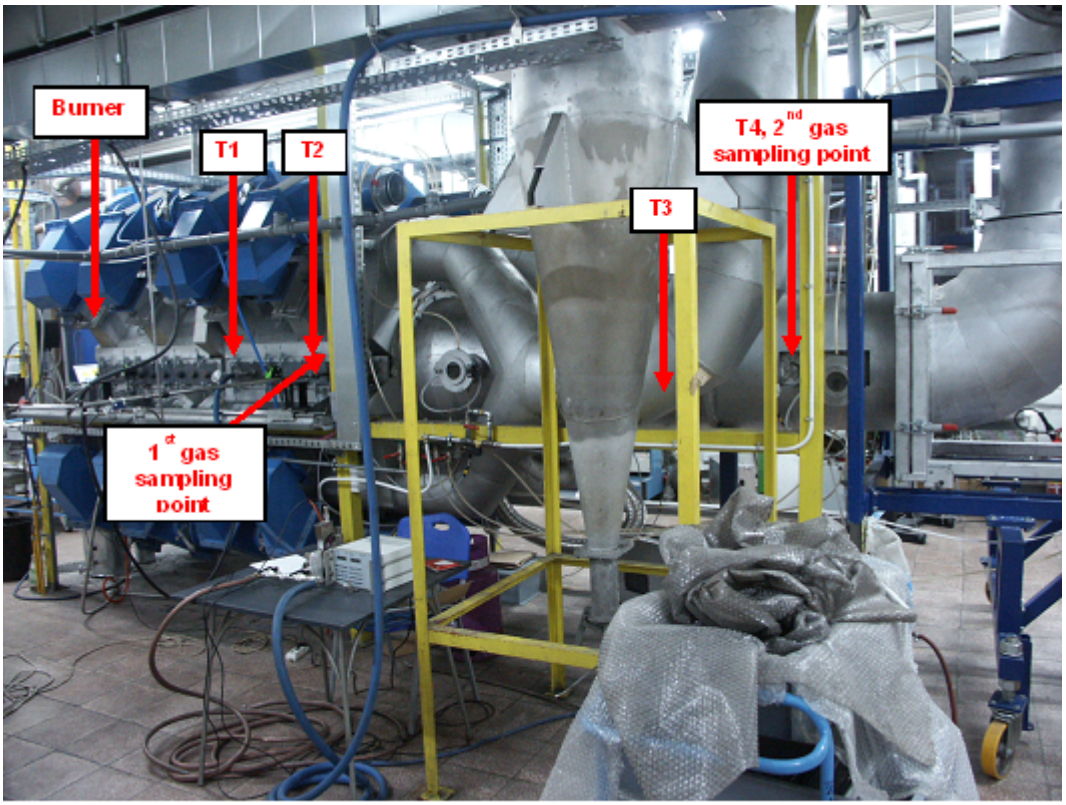

Figure 3.8: Location of the flue gas sampling probes and thermocouples on the CTF

Table 3.1: Gas analysers used and the gases measured at the CTF

Gas analyser	**Gases measured**	**Measurement unit(s)**	**Resolution**	**Range**	
				Low	**High**
Ultramat 23	O_2	%	0.01	0	100
	CO	ppm	0.5	0	2500
	NO_x	ppm	1	0	2500
	SO_2	ppm	1	0	2500
Ultramat 22	CO	ppm	1	0	1000
	CO	%	0.01	0	10
Maihak S710	CO_2	%	0.1	0	25
Servomex 1400	O_2	%	0.01	0	25

Gas sampling was carried out using four gas analysers (Table 3.1), namely Ultramat 23, Ultramat 22, Maihak and Servomex to measure O_2, CO, CO_2, NO_x and SO_2 which recorded the sample analysis once every second using the CTF NI PXI system as discussed above. Figure 3.9 shows the gas analysers used during the experiments. The gas sample from the sampling points were conveyed wet to the analysers through a pump and filter. The analysers were calibrated at least

once a day at the start of the experiments but often additional calibration was done when there was other downtimes during the experiments throughout the day. Unfortunately due to confidentiality and operational reasons, the detailed calibration data were not made available.

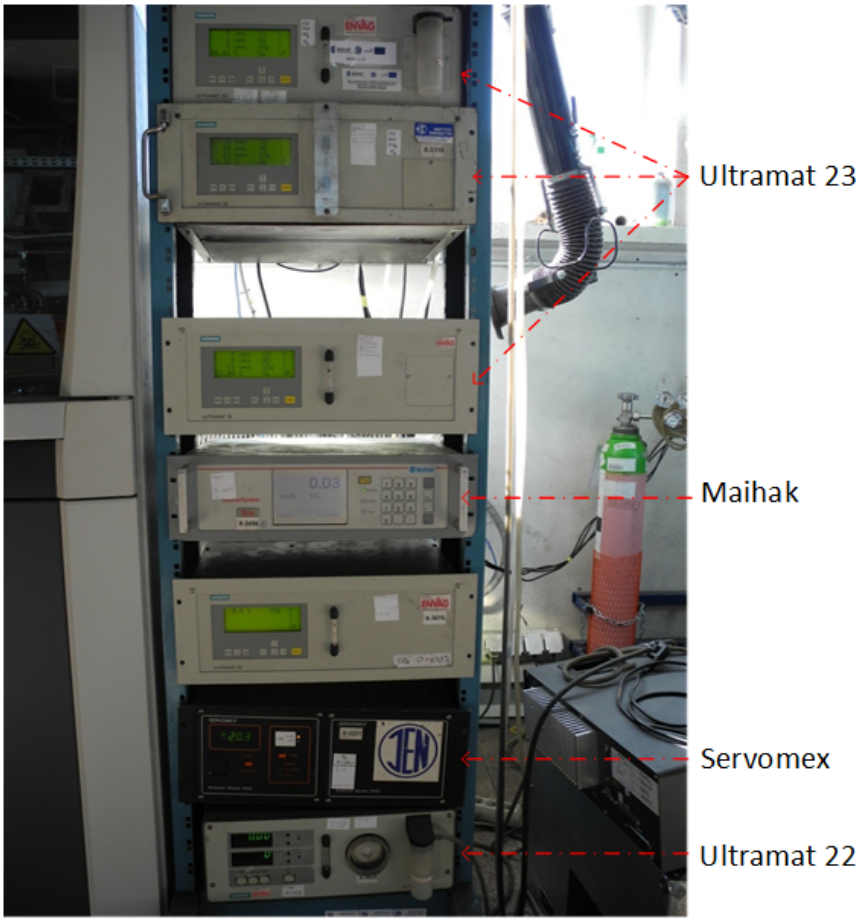

Figure 3.9: Gas analyser(s) used during experiments

3.2 Full Scale – Experimental Apparatus

Full scale tests were carried out at the Dolna Odra power station in Poland. The facility consists of eight units each capable of producing 200 to 230 MW_e. The experiments were carried out on the boiler of the eighth unit, which was a tangentially fired unit that had 20 burners distributed over 5 levels. The overall boiler layout is shown in figure 3.10. Much of the specifications of the boiler and layout are confidential and weren't made available by the boiler operator.

3.2.1 Fuel Feed and Pre-Combustion Setup

The boiler was designed to fire bituminous coal, but because of the need to reduce carbon emissions, often blends of biomass and coal were burned, usually with approximately 10 % of biomass on a mass basis. Biomass used for co-firing was mainly agricultural biomass (briquetted straw). Fuel characterisation analysis for all fuels used at full scale are presented in section 3.3.2.

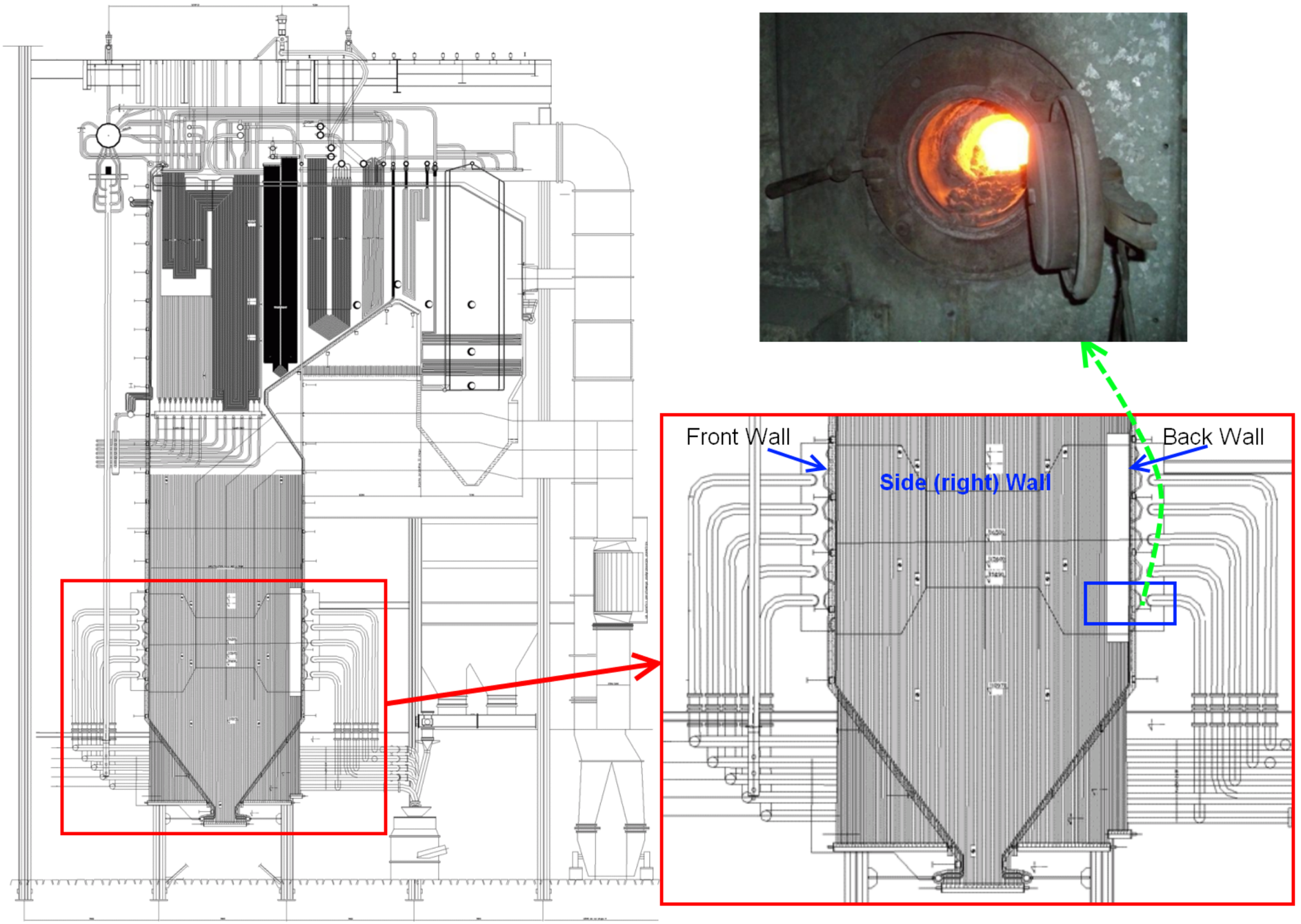

Figure 3.10: Overall layout of boiler eight at Dolna Odra power station

(On the left, the diagram shows the five levels of burners in the boiler; on the right, the location of the lower level monitored burners is shown, with a photograph of the observation port used for the three low cost sensors as well as the gas sampling probe.)

Each level had four burners which were supplied with pulverised fuel from a dedicated mill which supplied the blended coal and biomass fuel. This pulverised fuel was stored in hoppers and fed to the primary airflow through volumetric screw feed mechanisms. The primary air fuel mixture was between 95 to 105 °C before entering the burner quarl. Much of the specifications are confidential and weren't made available by the boiler operator.

3.2.2 Burner and Combustion Chamber

The boiler was a tangentially fired Pulverised Coal (PC) boiler equipped with 20 low NO_x swirl burners, arranged over 5 levels with over fire air. The dimension of the boiler was 10.81 x 12.05 x 23 m. The burners were located in the four corners of the combustion chamber. Each level, or bank, of burners was fed with pulverised fuel from separate mills.

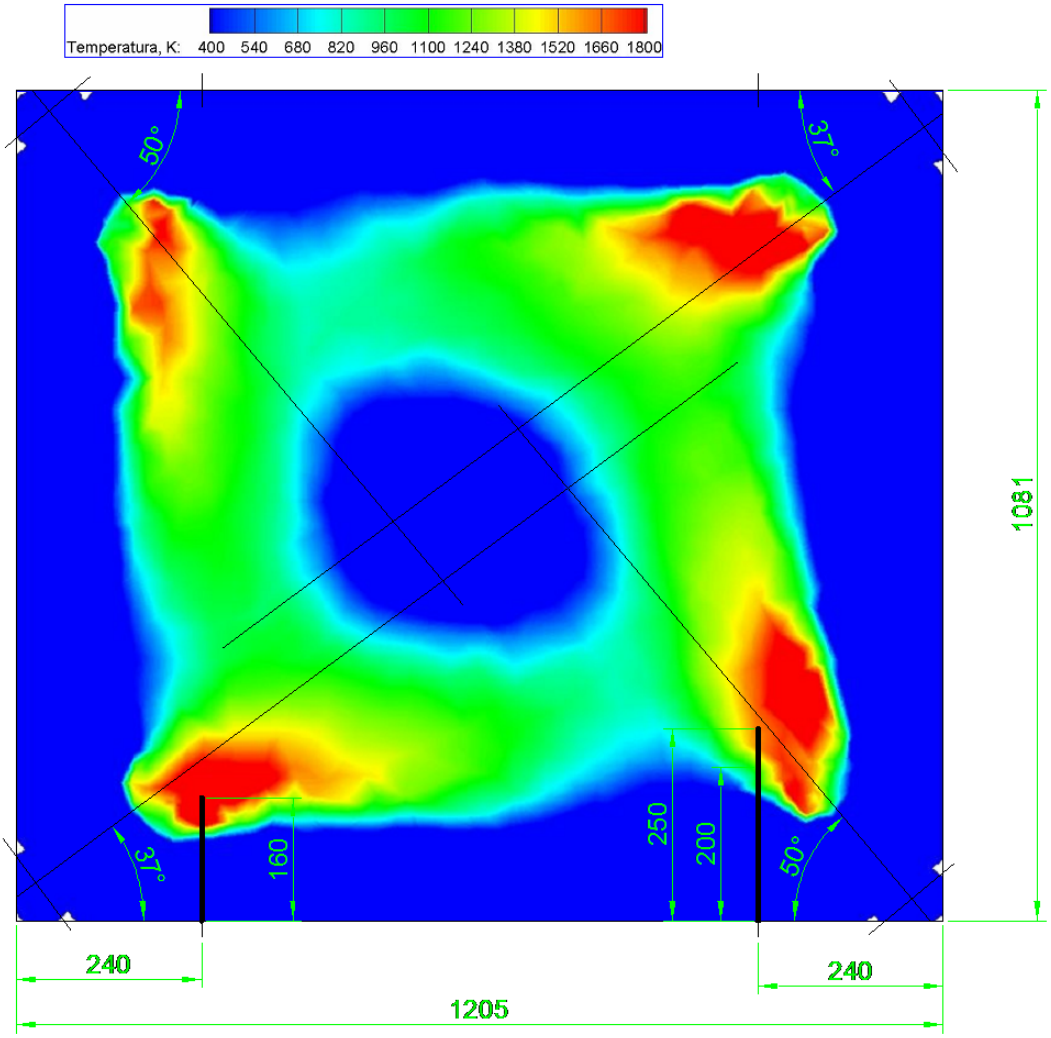

(Courtesy of IEn, Poland)

Figure 3.11: Temperature profile on the investigated level (lowest row of burners) on the basis of CFD simulation of the boiler from Dolna Odra power plant

Note: The black lines towards the bottom indicate the location of the viewing ports and position of gas sampling probes.

Due to accessibility and availability of the required monitoring ports for the optical probes and gas sampling lance, the lowest level of burners were used. Figure 3.10 shows the general layout of boiler eight at Dolna Odra. On the left schematic, the red region highlights the area of interest, the boiler and its five levels of burners. On the right bottom figure the boiler area is enlarged with one of the lowest burners being highlighted by a blue rectangle. The green arrow highlights the observation port located on the back wall, not visible in this layout. A picture of the observation port is located at the top right of the figure.

Figure 3.11, shows a Computational Fluid Dynamics (CFD) simulation of the temperature profile of the lowest level of burners, courtesy of IEn. This CFD temperature profile figure is utilised solely to illustrative the placement of the sensors and the point at which the gas was sampled in the boiler and is not part of the research presented in this work. It also highlights the ports available for monitoring the burners and the dimensions of the boiler and distance of the ports from the burner. The ports were approximately 240 cm from the edge of the boiler where the burner quarl is located. There was only one port available for each of the burners. Again due to confidentiality reasons, the finer details about the layout were unavailable.

3.2.3 Existing Burner Control System

The boiler utilised a custom made control system for control and data gathering which was recorded continuously for archival and analysis. A large number of boiler operational parameters such as fuel flow rate, primary and secondary air-flows, mill configurations, flue gas emissions in the exhaust chute, were acquired using the existing power plant supervisory and data acquisition unit. Again due to confidentiality, no details could be obtained about the instrumentation, except for the data from select sensors which were used for the process monitoring for further evaluation. Each of the burners was monitored using the InSight 95IRS2 flame scanners, located along the axis of the burner and monitoring the root of the flame. These were Infrared (IR) based sensors which detected the presence or absence of a flame.

The plant control systems monitored the emissions only at the stack level. As mentioned in section 3.2.2, only one port was available for each of the burners. This necessitated the gas sampling probes to be swapped with the optical sensors whenever samples were taken. Gas sampling was performed courtesy of IEn and its personnel throughout the experimental campaigns.

The gas probes were constructed from three concentric tubes with the inner most tube being used to transport the gas sample for analysis. The other two tubes were connected to the water mains to cool the probe when in use due to the high temperatures experienced inside the boiler. Figure 3.12 illustrates the gas sampling probe in use and figure 3.11 shows two black lines on the lower half of the image indicating the distance to which the gas sampling probes were inserted into the boiler to make the measurements.

In a similar manner to the pilot scale testing at IEn; CO, NO, NO_2 and O_2 were measured using the gas analysers. Figure 3.13 shows the analysers in operation. The big grey boxes in the figure house the pump, filters and dryer to extract the gas sample for processing by the gas analysers with the values being

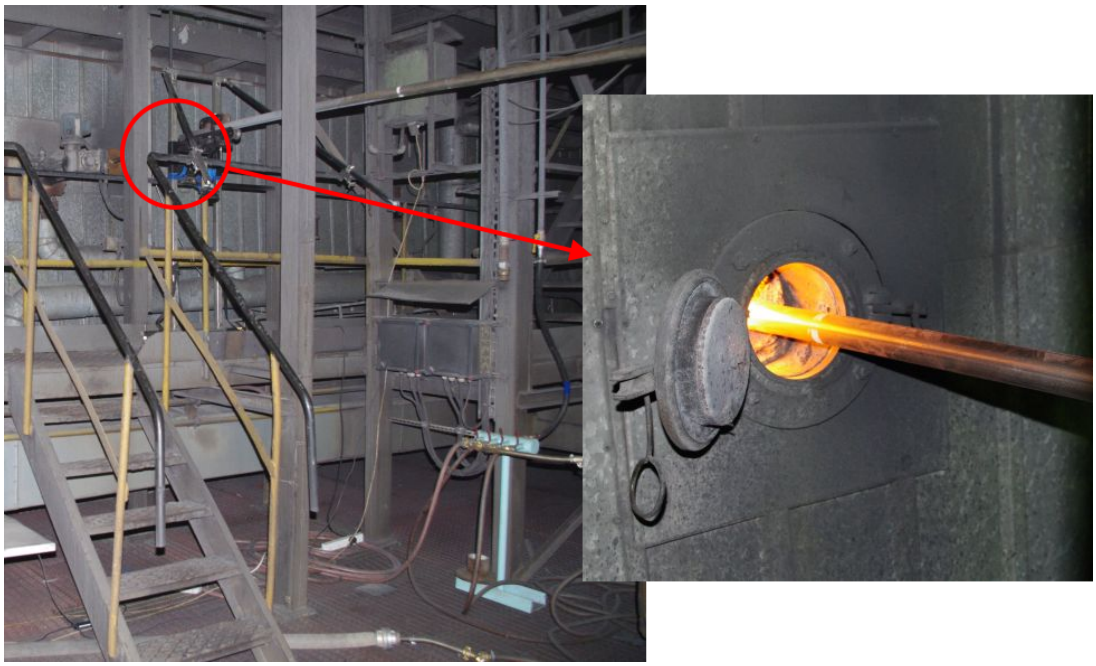

Figure 3.12: Gas sampling probe mounted to the observation port on the left and a close up view of the gas sampling probe on the right

recorded every second in an identical manner to the pilot scale tests. Table 3.2 lists all the gas analysers utilised for full scale experiments, which are essentially the same as the ones used in pilot scale experiments (Table 3.1) except for the addition of Eco Physics CLD gas analyser. Similar to the pilot scale experiments, the gas sample from the sampling points were conveyed wet to the analysers through a pump and filter. The analysers were calibrated at least once a day at the start of the experiments but often additional calibration was done when there was other downtimes during the experiments throughout the day. Unfortunately due to confidentiality and operational reasons, the detailed calibration data were not made available.

Figure 3.13: Gas analyser setup with laptop for recording the data

Table 3.2: Gas analysers used and the gases measured at full scale

Gas analyser	**Gases measured**	**Measurement unit(s)**	**Resolution**	**Range**	
				Low	**High**
Ultramat 23	O_2	%	0.01	0	100
	CO	ppm	0.5	0	2500
	NO_x	ppm	1	0	2500
	SO_2	ppm	1	0	2500
Ultramat 22	CO	ppm	1	0	1000
	CO	%	0.01	0	10
Maihak S710	CO_2	%	0.1	0	25
Servomex 1400	O_2	%	0.01	0	25
Eco Physics	NO	ppm	0.01	0	500
CLD	NO_2	ppm	0.01	0	500

3.3 Fuel Characterisation

A number of bituminous coals and biomass in the form of straw were used during the set of tests carried out at the CTF. The analysis carried out and the fuel characteristics are presented in section 3.3.1. Similar to the pilot scale experiments, samples were taken at least once a day at the full scale experiments at Dolna Odra and the analysis of the coal/biomass blends are presented in section 3.3.2.

3.3.1 Pilot Scale

The fuels used at the CTF and their characterisation (courtesy of IEn) are presented in this section. The coal selected was representative of that used in the Dolna Odra power plant hosting full-scale tests together with straw as an agricultural residue biomass as this biomass is used for co-firing in Dolna Odra. The main properties of the fuels used are shown in Table 3.3.

Table 3.3: Composition of the fuel used during pilot scale testing at the CTF

Fuel Type †	**Moisture** (%)	**Ash Content** (%)	**Lower Heating Value** (MJ/kg)
100 % R	3.10	14.90	26.054
90 % R + 10 % B	3.78	13.99	24.989
80 % R + 20 % B*	4.46	13.08	23.924
70 % R + 30 % B*	5.14	12.17	22.859
100 % J	7.05	13.10	23.412
90 % J + 10 % B	7.34	12.37	22.611
80 % J + 20 % B*	7.63	11.64	22.810
100 % E	1.00	19.60	25.456
90 % E + 10 % B	1.89	18.22	24.451
80 % E + 20 % B*	2.78	16.84	23.446

† R - Russian coal J - Janina (Polish) coal
E - Ekogroszek (Polish) coal
B - Biomass in the form of agricultural straw
* Calculated values

Table 3.4: Particle size distribution of the fuel used during pilot scale testing at the CTF

Particle size	**Fuel type** (%)			
distribution (µm)	**Russian coal**	**Janina (Polish) coal**	**Ekogroszek (Polish) Coal**	**Agricultural straw (Polish)**
355				16.980
200	5.500	0.715	8.810	35.280
125	11.600	5.087	22.481	23.720
90	12.090	8.210	14.303	11.070
63	7.720	11.342	10.137	6.650
32	27.480	31.511	25.962	3.670
<32	35.610	41.291	17.659	0.370

Table 3.4 shows the particle size distribution of the various fuels used during the pilot scale tests at the CTF. A pre-treatment of the fuel was needed in order to obtain a narrow band of particle sizes to work with, since the use of a broad

band of sizes and the effect of size on combustion rates would severely mask the actual fuel kinetics. In the case of the coals, the band chosen was 53-63 µm, and 300-400 µm for the biomass. The Polish coals were received as lumps of different sizes, which were first dried in open air, and then milled and thoroughly (and repetitively) sieved to select range. The bituminous Russian coal was received as a dry powder, and so it was directly sieved. The Polish straw was received as dry briquettes and they were cut down to ≈10 mm and then milled and sieved to the 300-400 µm range.

3.3.2 Full Scale

The fuels used at the full scale trials and their characterisation (courtesy of IEn) are presented in this section. The tests were carried out over two test campaigns, that occurred with a couple of months separation, lasting eight days each. The amount of coal utilised was quite large, it being a power station and there was considerable variation within each campaign, changes even on a day to day basis, as shown in Table 3.5.

Table 3.5: Composition of the fuel used during full scale testing at the Dolna Odra power station

ID Tag	**Fuel Type**†	**Moisture** (%)	**Ash Content** (%)	**Lower Heating Value** (MJ/kg)
A	100 % Coal	10.00	22.14	21.231
B	100 % Coal	10.00	22.14	21.231
C	90 % Coal + 10 % Biomass	10.67	18.81	20.961
D	90 % Coal + 10 % Biomass	10.67	18.81	20.961
E	100 % Coal	8.18	16.20	26.636
F	100 % Coal	6.27	13.70	27.908
G	90 % Coal + 10 % Biomass	12.98	17.10	26.078
H	90 % Coal + 10 % Biomass	9.93	16.90	25.868

† C - Coal B - Biomass in the form of agricultural straw

It wasn't possible to obtain samples after milling the coal or coal & biomass blends before it entered the burner. Hence the particle size distribution couldn't be measured for these experiments.

3.4 Sensor Specification and Setup

The combustion chamber was installed with a number of sensors; Ultra Violet (UV) - EPD-440-0/1.4 [180], Visible (VIS) - S1226-18BK [181] and Infrared (IR) - G8376-05 [182] photodiode sensors. The sensor specifications are shown in Table 3.6. As discussed in section 2.7.4, existing usage of such spectral wavelengths in commercial sensors used for flame safety detectors and applicability of such sensors for similar usage by other researchers guided the selection of these sensors [36, 47, 106, 109, 136]. These sensors were selected as they respond to three

broad spectral bands with wavelengths that include the emissions of the OH^*, CN^* and CH^* radicals that arise within the flame itself [38, 106, 113], detect the visible emissions of the flame and provide information that is related to the flame and furnace temperature [21, 39].

Table 3.6: Sensor specification

Sensor Detail	**Responsive Wavelength** (nm)	**Peak Sensitivity** (nm)	**Light Transmission Mode**
UV - EPD-440-0/1.4	190 - 570	440	Trifurcated
VIS - S1226-18BK	320 - 1000	720	fibre optic
IR - G8376-05	900 - 1700	1550	cable

3.4.1 Instrumentation

The instrumentation comprised of the sensors connected to a current to voltage converter / amplifier, which was then amplified by an inverting voltage amplifier. This was filtered in the hardware using a 1 kHz low pass 5^{th} order Bessel filter to avoid anti-aliasing while converting from analogue to digital in the DAQ unit, where data was recorded at 8192 samples/second. The schematic of the electronic circuit used for the three sensors is shown in figure 3.14. Figure 3.15 shows an image of the instrumentation box which contains the circuitry for all three sensors which is connected to the trifurcated fibre optic cable which on the other end is attached to the lens assembly which focuses the electromagnetic emissions from the combustion chamber on to the fibre optic cable.

3.4.2 Sampling

The data from the CTF like air flow rates, load and monitoring of emissions such as CO and NO_x were recorded at a rate of 1 sample / second. The sensor signals were recorded at 8192 samples / second, so when these were compared with various CTF data, the sampling rate was matched usually by up sampling the plant data or by down sampling the sensor signals from their original rate for ease of plotting or analysis.

3.4.3 Pilot Scale

The set up used three photodiodes measuring the Ultra Violet (UV), Visible (VIS) and IR at an angle of 46° between the centre line of the burner and the viewing port positioned on the back of the furnace, monitoring the flame at a distance of approximately 155 mm from the burner quarl as shown in figures 3.5, 3.6 and 3.7. The sensors in the sighting tube are air purged to avoid overheating as well as dust accumulation, which would adversely affect the signal if left unchecked.

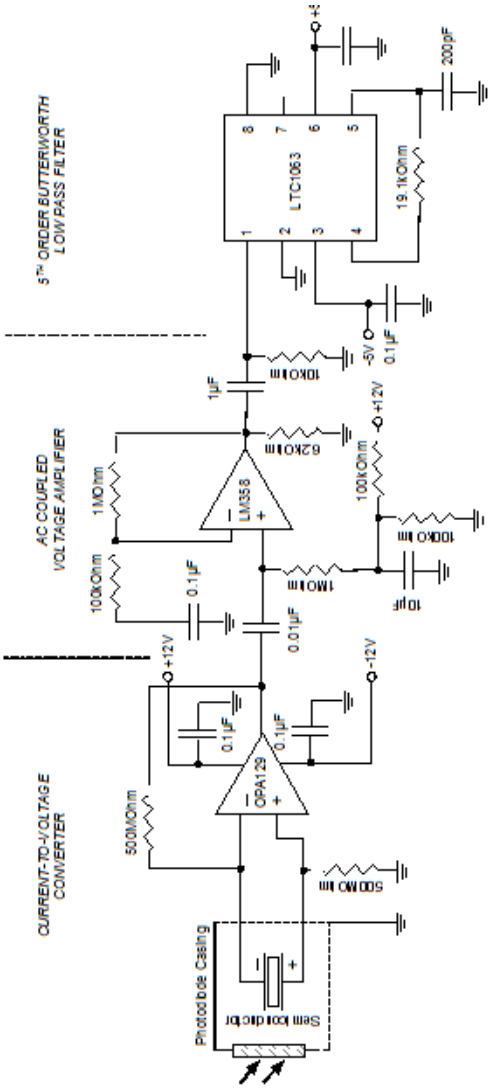

Figure 3.14: Schematic of the instrumenation - showing a sensor, amplifier and filter

Figures 3.16 and 3.17 show the layout of the sighting tube to mount the optical probes to the CTF front plate (figures 3.6 and 3.7). In figure 3.17, the brass connector pointing to the left bottom of the figure was used to mount the lens assembly and the silver coloured connected at 90° allowed for the purge air connection.

3.4.4 Full Scale

The three optical sensors used previously in the pilot scale testing at IEn were used again with the same hardware. However, due to the intensity of the flame in the power station, it was necessary to introduce neutral density filters that reduced the light transmitted to 10 % and 20 % (the limited availability of ports meant the flames were monitored at different distances from the side wall) of the actual intensity impinging on the lens. This avoided saturation of the signal in the electronic amplifiers, as the flames were much brighter than experienced at the pilot scale CTF. In the pilot scale tests, the sensors focussed on the root of

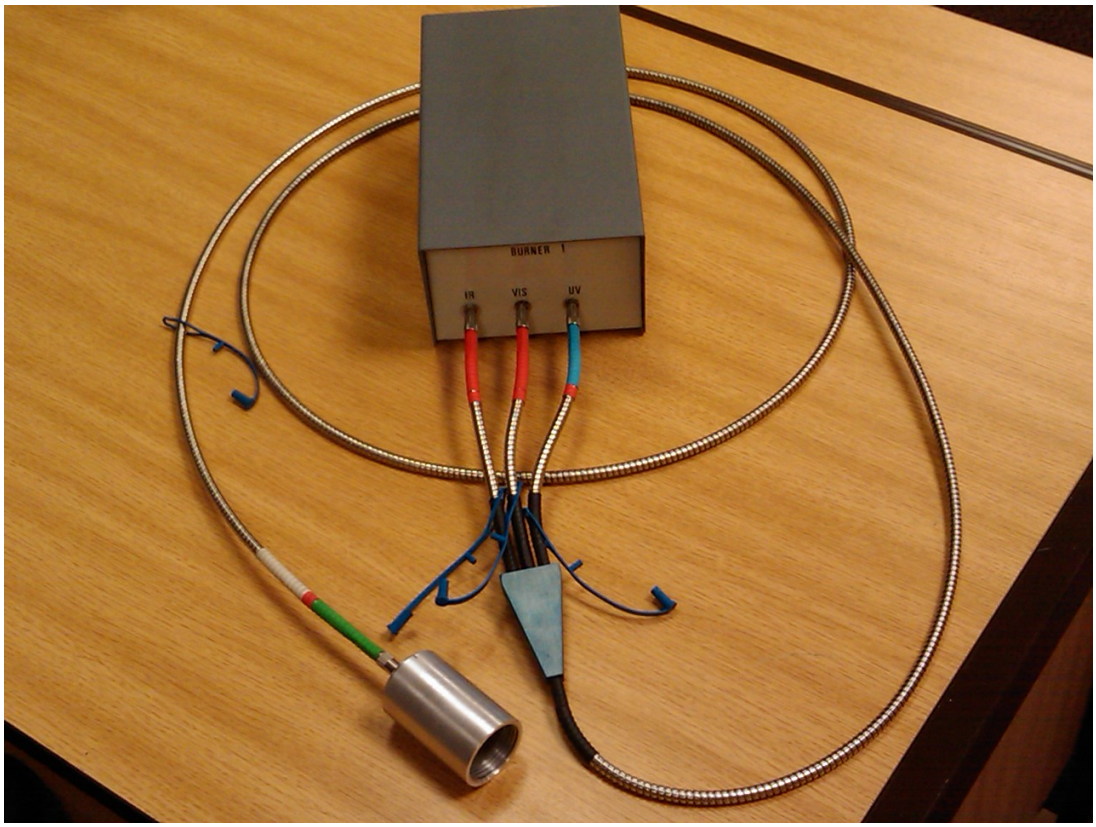

Figure 3.15: Picture showing the instrumentation box connected to a trifurcated fibre optic cable and lens assembly

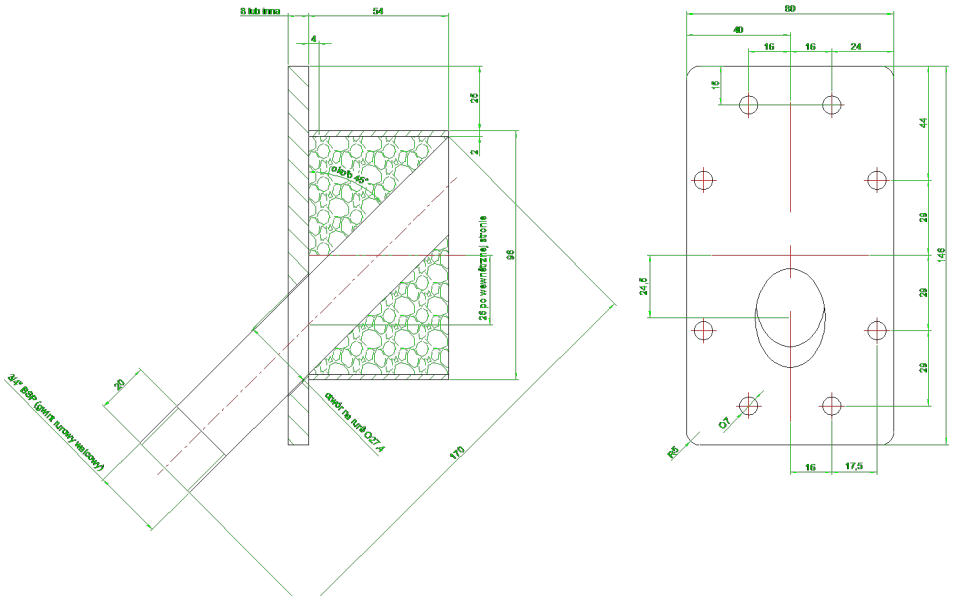

(Image courtesy of IEn, Poland)

Figure 3.16: Production drawing of sighting tube to mount lens assembly and purge / cooling air

the flame and were relatively close to the burner quarl. In the case of the full scale experiments, as there was only one port available on the side of the boiler, as shown in figure 3.10 (top right image) and figure 3.11, it was not possible to

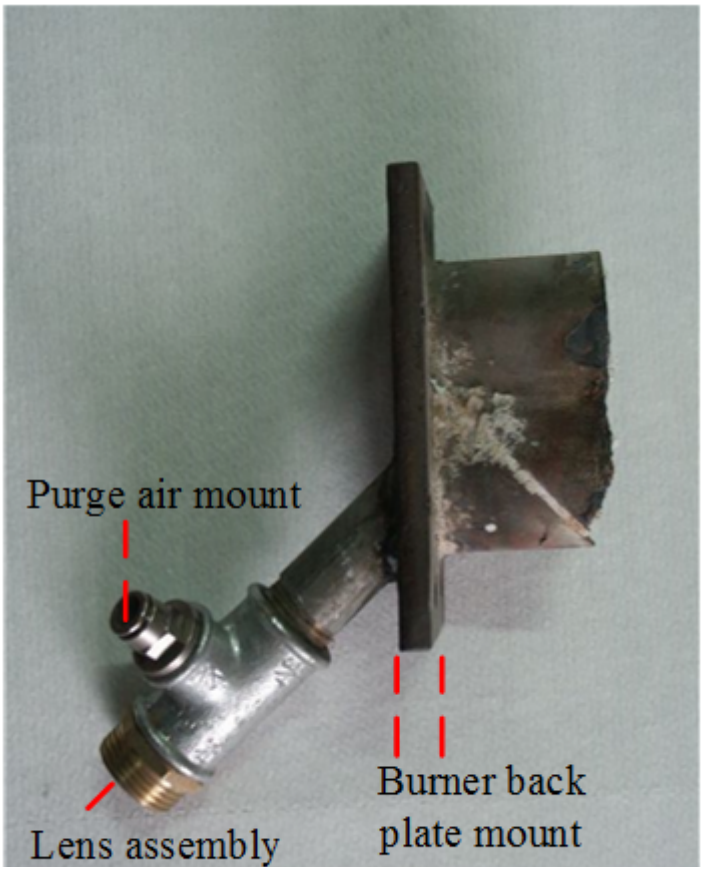

(Image courtesy of IEn, Poland)

Figure 3.17: Picture of the sighting tube to mount the lens assembly and purge / cooling air

select which part of the flame the sensors were focussed on.

The probe mount design and picture are shown in figure 3.18. This shows how the lens assembly for the sensors were mounted on the burner wall with the probe mount. This mount was especially made by IEn to hold the sensors and direct the necessary cooling air. Cooling air was required for the optical sensing system due to the high temperatures experienced by the lens assembly when placed near the wall of the boiler, and was directed through the T-junction employed which kept the optical assembly from overheating during the experiments.

Due to the lack of additional ports, the optical sensors were mounted on the same ports. This necessitated the swapping of the gas sampling probes with the optical sensors whenever gas samples were taken.

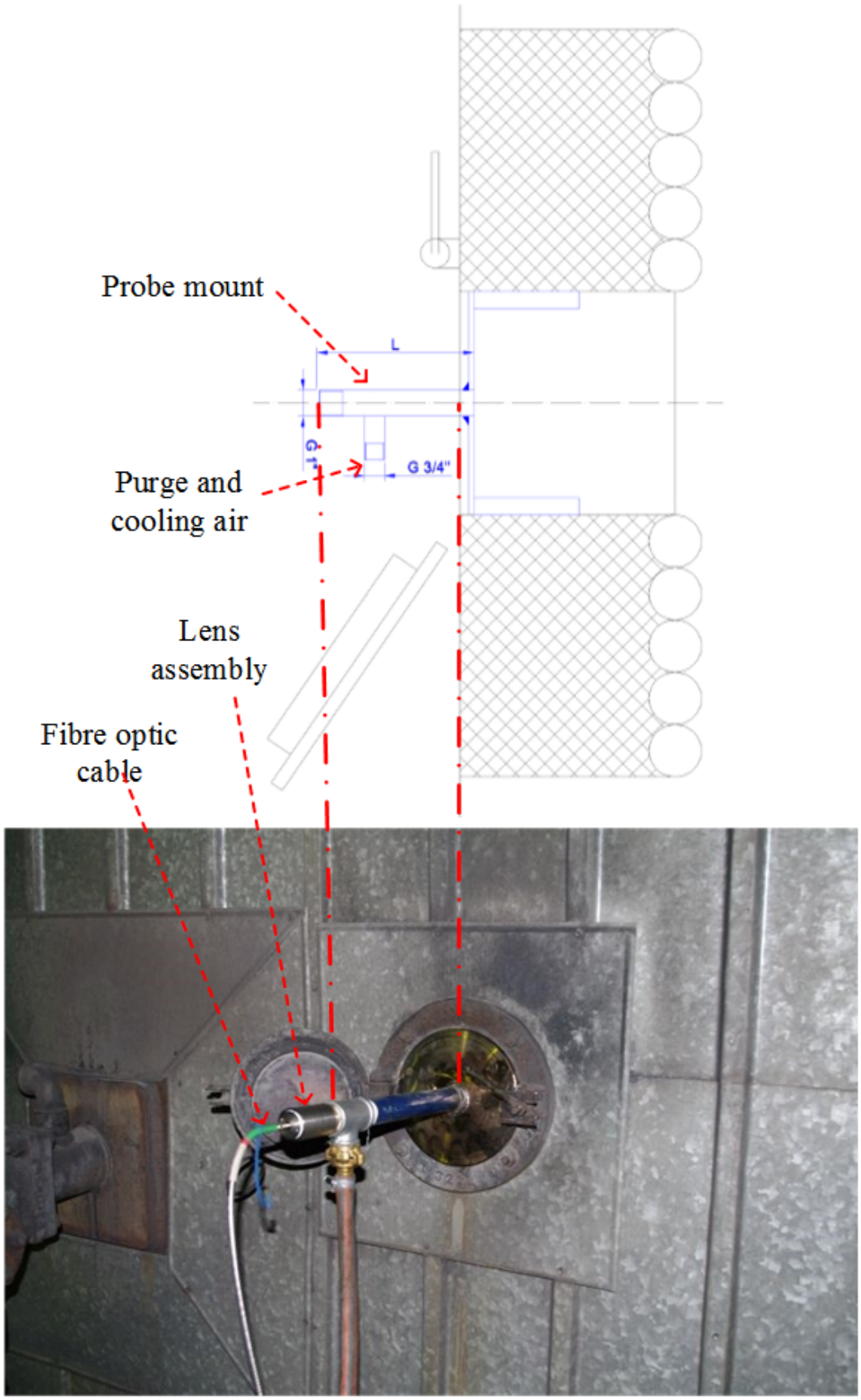

Figure 3.18: Probe mount attached to the observation port next to the burner
The design drawing (Image courtesy of IEn, Poland) on the top shows the probe in blue and the picture below shows the lens assembly and fibre optic cable in addition to the probe mount.

3.5 Experiments

Experiments at steady state were initially conducted at pilot scale and used to select appropriate signal processing. Further to this, the control system was demonstrated at pilot scale and then this developed system was demonstrated at the full scale plant in Dolna Odra.

3.5.1 Pilot Scale

As mentioned in the objectives of this research (section 1.2.1), there is a growing need for reduction of emissions, of which one short term approach has been to co-fire biomass. So higher proportions of biomass have to be substituted for coal to achieve bigger reductions, which lead to burner instability issues. Therefore, recognisable parameter(s) have to be identified with respect to these changes so that an algorithm can be developed.

Table 3.7: Summary of test conditions at the CTF

<table>
<tr><th>Test Number</th><th>Fuel†</th><th>Swirl Setting (°)</th><th>Thermal Load (kW)</th><th>Excess air</th></tr>
<tr><td>1 – 9</td><td>100 % C</td><td rowspan="2">50</td><td rowspan="5">≈320, 250 & 200</td><td rowspan="9">Low, Normal & High</td></tr>
<tr><td>10 – 18</td><td>90 % C & 10 % S</td></tr>
<tr><td>19 – 27</td><td>90 % C & 10 % S</td><td rowspan="2">40</td></tr>
<tr><td>28 – 36</td><td>100 % C</td></tr>
<tr><td>37 – 45</td><td>100 % C</td><td rowspan="2">60</td></tr>
<tr><td>46 – 54</td><td>90 % C & 10 % S</td></tr>
<tr><td>55 - 63</td><td>70 % C & 30 % S</td><td rowspan="2">60</td><td rowspan="3">≈400, 300 & 200,</td></tr>
<tr><td>64 – 72</td><td>80 % C & 20 % S</td></tr>
<tr><td>73 – 81</td><td>80 % C & 20 % S</td><td>40</td></tr>
<tr><td>82 – 90</td><td>80 % C & 20 % S</td><td>50</td><td>≈320, 250 & 200</td><td></td></tr>
</table>

† C - Coal S - Straw

A series of steady state tests were conducted at the CTF, which included firing pulverised (Russian) coal and different proportions of biomass, namely 10, 20 and 30 % on a mass basis whilst varying thermal loads, excess air levels and

secondary air swirl settings to identify such systematic changes as these are varied. As this research was carried out as part of an EU funded project, one of the additional things looked into was the effect of swirl in the 40° to 60° with respect to co-firing. Tests at 30 % biomass by weight had to be abandoned on safety grounds as the flame was unstable and couldn't be sustained for even short periods without flameout. These experiments and their steady state settings are presented in Table 3.7. During each set of nine experiments where a fuel blend and swirl setting was chosen, three thermal loads and for each thermal load three different excess air settings were performed for the steady state experiments. Only exception being the 30 % biomass blend, for which only nine experiments were carried out with many interruptions and finally abandoned on safety grounds.

Table 3.8: Summary of test conditions at the CTF, while varying the primary to secondary air ratio

Test Number	**Fuel**†	**Excess air**	**Primary to secondary air ratio condition during experiment**	
			Start	**End**
91	80 % C &	normal	normal	high
92	20 % S			low
93	100 % C			high
94				low
95	90 % C &			high
96	10 % S			low

† C - Coal S - Straw
All experiments carried out with swirl of 50° and thermal load of ≈320 kW

In addition to the systematic steady state experiments where one parameter was varied to identify the effect on the monitoring sensors, tests that varied primary to secondary air ratios were also performed to stimulate burner instability whilst burning different levels of biomass fuel. A summary of two sets of these test conditions are in Tables 3.8 and 3.9. During transition from one test condition to another, the burner was allowed to stabilise before data acquisition began to avoid spurious changes being taken into account during analysis.

Tests while varying the primary to secondary air ratio (Tests 91 – 96) were conducted by increasing or decreasing the primary air by 10 Nm^3/h from the original setting of 40 Nm^3/h. These tests are presented in Table 3.8, where the primary air was varied while excess air was kept constant. Additional tests to simulate burner instability (Tests 97 – 99) were also conducted where excess air was originally set to a normal condition and gradually decreased or increased to a level where blow-off was about to occur. These tests are presented in Table 3.9, where the secondary air was varied while primary air was kept constant. A number of these tests were carried out to observe the continuous changes in the sensor signals as opposed to the steady state experiments.

Table 3.9: Summary of test conditions at the CTF while varying the secondary air from normal level

Test Number	**Fuel†**	**Excess air**		**Secondary air during experiment**	
		Start	**End**	**Start**	**End**
97a	100 % C	normal	low	normal	decreased
97b			high		increased
98a	90 % C &		low		decreased
98b	10 % S		high		increased
99a	80 % C &		low		decreased
99b	20 % S		high		increased

† C - Coal S - Straw
All experiments carried out with swirl of 50° and thermal load of ≈320 kW

3.5.2 Full Scale

Table 3.10: Summary of test conditions at the full scale power plant

Test	**Thermal Load***	**Secondary Airflow*†** (kg/h)		
number	(kg/h)	**low**	**medium**	**high**
101 - 103	15 000	8000	11 000	14 000
104 - 106	20 000	7800 - 8400	12 200	16 000
107 - 109	25 000	9600 - 12 000	14 000	18 000

***** of the lowest level/bank of (four) burners in the boiler
† Secondary airflow corresponding to Excess air of low, medium and high

In a similar manner to the experiments at the CTF, it was decided to use three different thermal loads and three different excess air settings for each thermal load during the full scale experiments at the Dolna Odra power plant. In the case of this boiler, this resulted in fuel flow rates of 15 000, 20 000 and 25 000 kg/h to the monitored burners on the lowest level. This fuel flow was the total fuel supplied to the four burners on this level with the corresponding airflows being; low, medium (optimal) and high. The three excess air conditions, namely low, medium and high correspond to the secondary air flows shown as low, medium and high in table 3.10. Overall combustion was staged during normal operation of the boiler, and this lowest level of burners were operated sub-stoichiometrically to maintain NO_x below Polish and EU regulatory limits. The implication of this was that the burners did not have a condition where the CO levels were ever low. The full scale plant was producing electricity as these experiments were carried out. Varying numbers of burners were active during the tests due to varying electricity production demands.

3.6 Summary

This chapter has outlined the pilot scale CTF and the full scale plant experimental apparatus and layout. The existing and additional plant instrumentation and their positioning with respect to the burner were highlighted. Coal characterisation and the experimental conditions were listed, which will be referred to when discussing results in the next chapter.

The specifications of the relatively cheap broadband sensors used in this research project are provided, that cover a broad range of spectral emissions from flames, in addition to those generally covered by the standard flame detectors employed on burners. This would enable the acquisition of data from the flame, with the additional option of deriving features which could be utilised from existing flame detectors in the future. The data acquired from these sensors (with additional signal processing) together with the gas analyser data were utilised in the detection algorithms to monitor the flames and detect changes.

Chapter 4

EXPERIMENTS AND RESULTS

This chapter presents the results obtained from the initial experiments conducted on the pilot scale 500 kW_{th} Combustion Test Facility (CTF) at Institute Energitky - Institute of Power Engineering (IEn) to get baseline data to evaluate and obtain various features to develop the control system to be discussed in the next chapter. The idea behind these experiments was to vary one parameter at a time to evaluate if features could be extracted from the flame monitoring signals obtained, for these systematic set of experiments. These results are analysed using a range of signal processing methods in an attempt to better understand the relationships between the sensor signals and the test facility operating parameters.

As previously discussed a signal can be represented in many different ways, at its most fundamental processing in the time domain by using for example the Root Mean Square (RMS) or in the frequency domain using for example the Fast Fourier Transform (FFT) or Power Spectral Density (PSD), are techniques that have been demonstrated to enhance / make more visible the information contained in the raw signal. These techniques do have limitations so other methods that use a Joint Time Frequency (JTF) approach, such as wavelets and the Wigner-Ville Distribution (WVD) were utilised to analyse the data and are also presented in this chapter.

4.1 Time Domain

The data recorded from the three photodiodes, namely the Ultra Violet (UV), Visible (VIS) and Infrared (IR) were analysed in the time domain to see if the energy of the signal over time could be related to changes in the input to the flame, such as thermal load and excess air (O_2) while combusting the various fuel blends (Table 3.7). In the time domain, the RMS averaging method was applied to the sensor data from the experiments highlighted in Table 3.7 to quantify the energy of the flame radiation signal as both the intensity and turbulent fluctuations of the flame greatly influence the characteristics of the signals acquired by the sensors.

The results presented in this section consists of a set of nine experiments based on a particular fuel blend and swirl setting (with reference to Table 3.7), where

the thermal load and excess air were varied. The results consist of three plots for each of the UV, VIS and IR sensors signals after processing. Each plotted point is the mean of the RMS calculated every second over 300 s duration of an experiment and the minimum and maximum values of the RMS being plotted as the error bar.

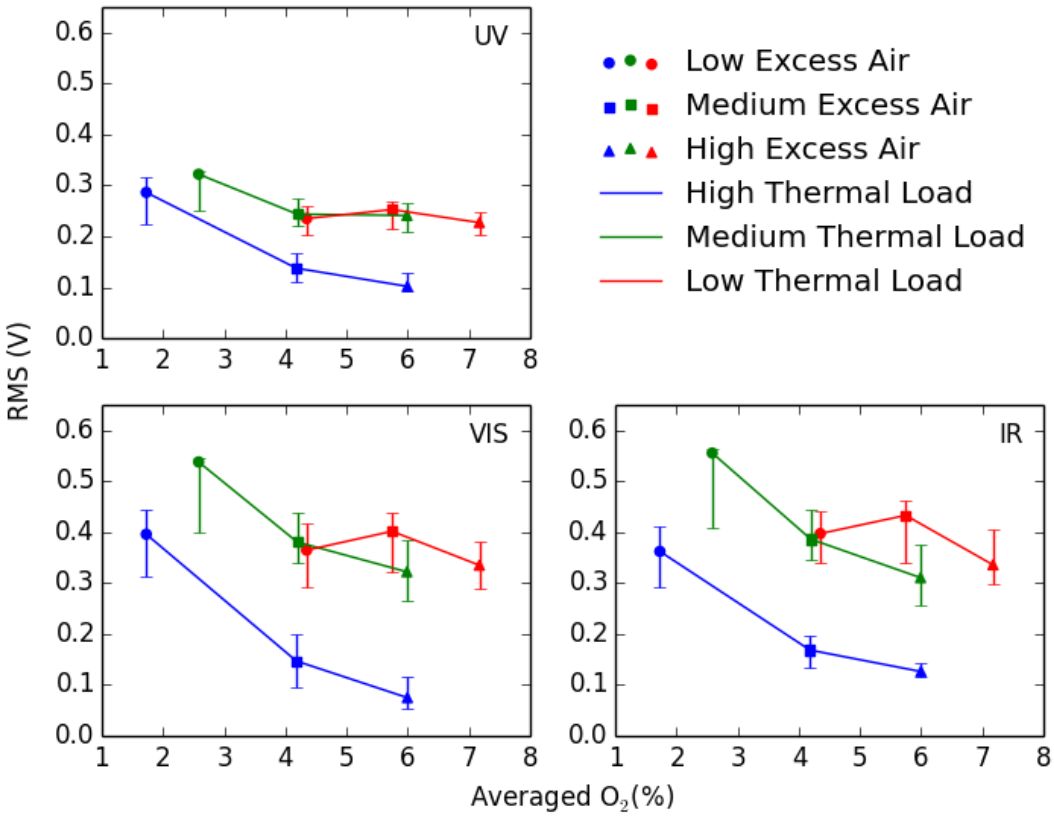

Figure 4.1: RMS of UV, VIS & IR photodiode signals Vs averaged O_2 for Tests 1 to 9 - 100 % Coal - 50° Swirl

Figure 4.1 shows the RMS of the UV, VIS and IR sensors plotted against the mean of the two oxygen concentrations (figure 3.8) when firing 100 % pulverised coal and 50° swirl. Tests 1 to 3 at the high thermal load (320 kW), shown in Table 3.7, while varying excess air from low to high respectively. Similarly, Tests 4 to 6 and Tests 7 to 9 show the variation of the sensor signals as the excess air is varied from low to high, for medium (250 kW) and low (200 kW) thermal loads respectively.

A general trend in the sensor signals to decrease with increasing excess air (total airflow to the burner) for Tests 1 to 3 for the high thermal load (320 kW) could be observed. The same inverse relation between the sensor signals and the excess O_2 can be noticed for the other thermal loads, though it's less pronounced in the low thermal load (and is different for Test 7). The changes in thermal load in turn changes the total airflow to the burner and this affects experiments with a low thermal load especially. This could be due to the flame getting leaner and hence emitting less as the excess air is increased. Another factor was that fairly similar amounts of excess purge air (to cool the lens assembly for the sensors and the transparent side sighting panel running one side of the combustion chamber)

was supplied to the combustion chamber and the fraction of this air was high at low thermal load.

The results from other experiments (as listed in Table 3.7) are presented in Appendix B.1. A general trend could be noticed in the sensor signals to decrease with increasing excess air for all thermal loads.

Figure B.9 shows the RMS of the UV, VIS and IR sensors plotted against the mean of the two oxygen concentrations (figure 3.8) when firing 80 % pulverised coal with 20 % biomass and 40° swirl. Again, a general trend could be noticed in the sensor signals to decrease with increasing excess air for all thermal loads, except for low thermal load experiments (Tests 79 to 81) and Test 76. This change in trend for the low thermal load experiments is thought be due to the percentage of purge air being a larger percentage of the leakage into the combustion chamber, hence affecting the set up of experiments as the O_2 readings at the exit were used by the boiler operator to control airflow to the combustion chamber. Test 76 seems to have very high variation as shown by the error bar, this experiment is an outlier as the steady state couldn't be maintained during the experiment with variation in the total airflow to the burner.

A general trend can be noticed in all experiments where by the sensor RMS signal amplitude decreases with increases in excess air for these sets of experiments for all thermal loads, but is less pronounced at lower thermal loads. This is thought to be due to the higher percentage of purge air to the total airflow to the burner. The responses of the UV, VIS and IR photodiodes exhibit fairly similar trends with respect to these operating conditions and this might be explained by the fact the there is some overlapping over the wavelength response of these sensors. Later chapters will investigate using these general trends to control the burner (Chapter 5).

4.2 Frequency Domain

In the frequency domain, the FFT was applied to the sensor data on the experiments highlighted in Table 3.7 initially to find the range of the frequency components present in signals acquired by the sensors. Also based on the literature (Section 2.7.3), the majority of the signal power was expected to be in the flame flicker range. The following figures show a range of 0 Hz to 500 Hz to demonstrate the range of frequencies of significance. The PSD was also calculated for the sensor data as another feature to be analysed to relate to changes in burner conditions and subsequently for use with the Artificial Neural Network (ANN).

The results presented for the FFT each consist of a set of nine plots of experiments based on a particular fuel blend and swirl setting (with reference to Table 3.7), where the thermal load and excess air were varied for each of the UV, VIS and IR sensors. Each plotted FFT is the mean of the FFTs calculated every second over each 300 s duration experiment.

Figure 4.2 shows the FFT output of the UV sensor data for Tests 1 to 9 when firing 100 % pulverised coal and 50° swirl. The test numbers are with reference to Table 3.7. The graphs from left to right show the variation of excess air from low, medium (normal) and high respectively for the three thermal loads. Similarly,

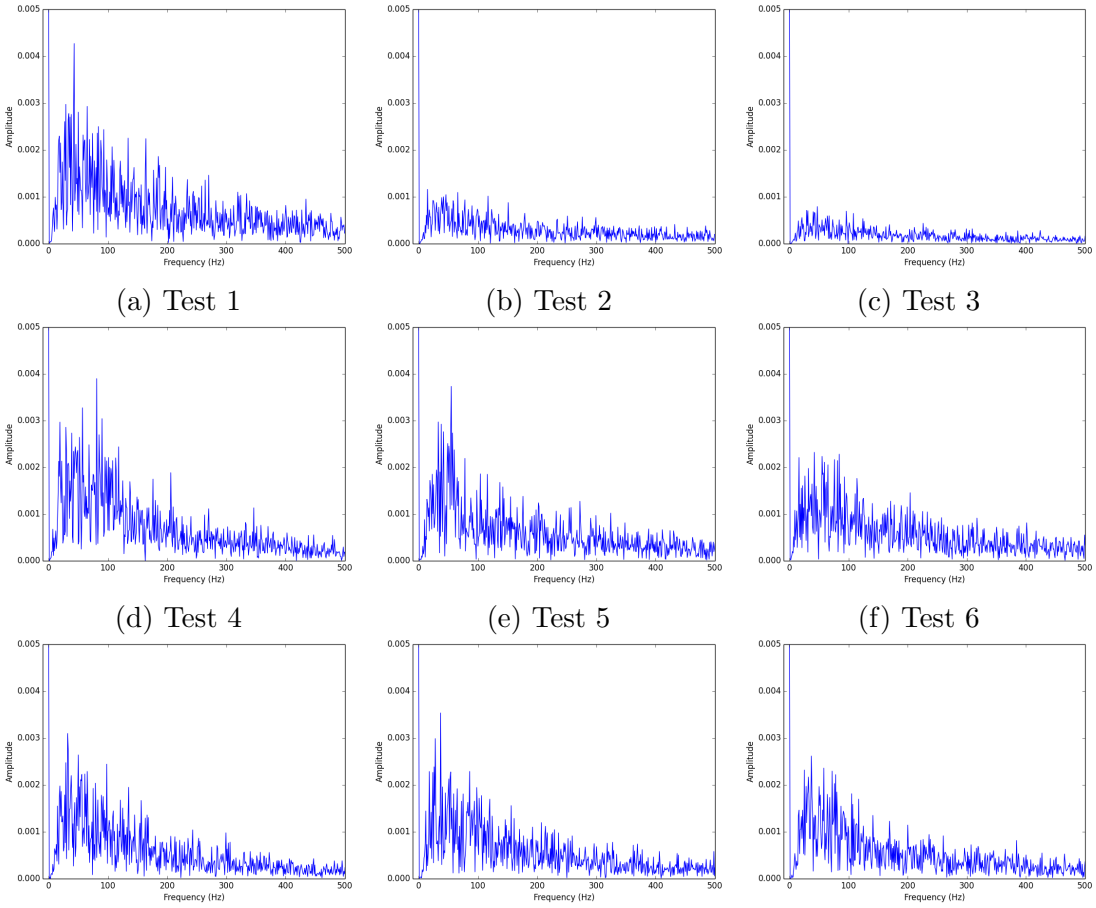

(a) Test 1 (b) Test 2 (c) Test 3

(d) Test 4 (e) Test 5 (f) Test 6

(g) Test 7 (h) Test 8 (i) Test 9

Figure 4.2: FFT of UV photodiode signal for Tests 1 to 9 - 100 % Coal - 50° Swirl
(Test numbers with reference to Table 3.7)

the graphs top to bottom vary from high to low thermal load, for the three excess air settings.

As previously observed with the RMS results, the FFT results for UV sensor show a decreasing trend with increasing excess air to the burner for all thermal loads. It could also be observed that with the high thermal load, the increase in the excess air shows a distinct change in amplitude for the dominant flame flicker frequency (between 0 to 40 Hz) for Tests 1 to 3 in figures 4.2(a) to 4.2(c). The general trend of decreasing signal intensity with increasing excess air is also noted with the VIS and IR sensors and other experiments as shown in Appendix B.2.

The FFT results of the three photodiode sensors analysed to relate changes to flame conditions, clearly shows a decrease in signal strength with increase in airflow rates to the burner. In addition, a slight frequency shift can also be observed with increasing airflow rates. Similar to the RMS variations these are neither proportional nor linearly change with changes to load or excess air.

The PSD was estimated using the Welch's averaged modified periodogram method and was applied to the sensor data on the experiments highlighted in Table 3.7. The results presented in this section each consist of a set of nine experiments based on a particular fuel blend and swirl setting (with reference

to Table 3.7), where the thermal load and excess air were varied. Also each result, consists of three plots for each of the UV, VIS and IR sensors signals after processing. Each plotted point is the mean area under the curve of the PSD calculated every second over 300 s duration of an experiment and the minimum and maximum values of the PSD being plotted as the error bar for each plotted point.

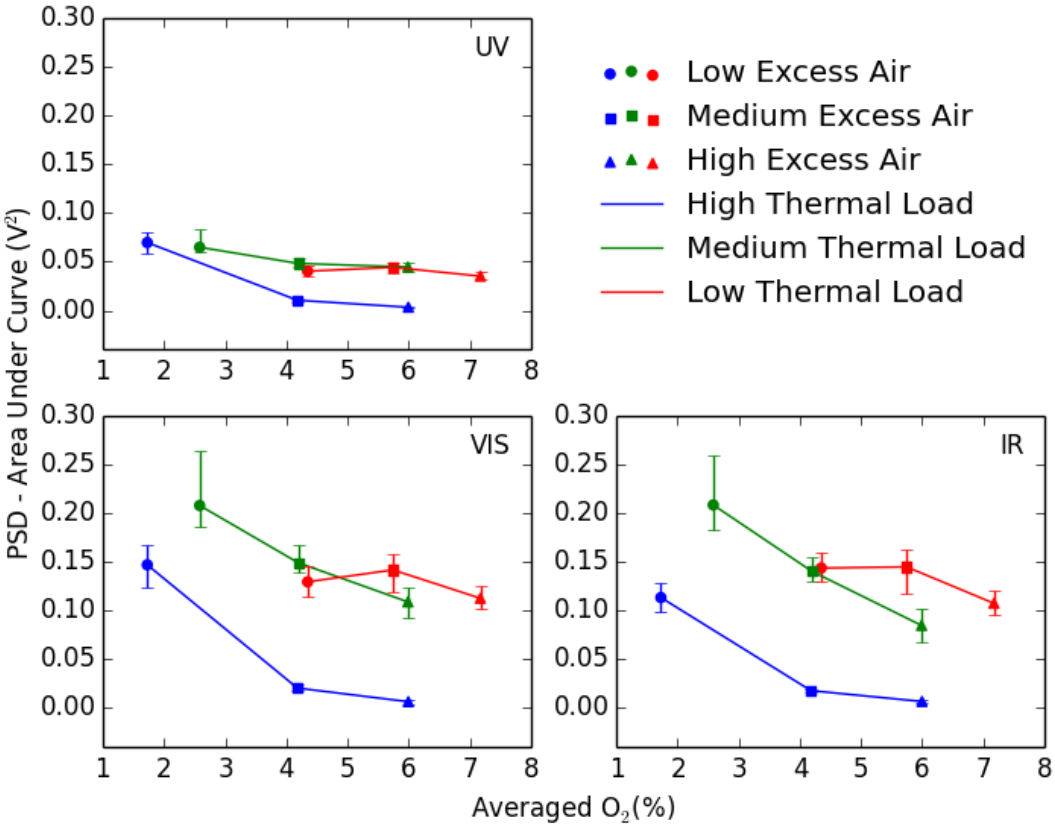

Figure 4.3: PSD of UV, VIS & IR photodiode signals Vs averaged O_2 for Tests 1 to 9 - 100 % Coal - 50° Swirl

Figure 4.3 shows the relationship between the energy of the PSD of the UV, VIS and IR photodiode signals with respect to the averaged oxygen concentration (figure 3.8) when firing 100 % pulverised coal and 50° swirl for Tests 1 to 9; Tests 1 to 3 at the high thermal load (320 kW), shown in Table 3.7, while varying excess air from low to high respectively. Similarly, Tests 4 to 6 and Tests 7 to 9 show the variation of the sensor signals as the excess air is varied from low to high, for medium (250 kW) and low (200 kW) thermal loads respectively. The energy is the area under curve within the 0 - 1000 Hz band when the PSD is plotted in linear scale. Each data point is the average of 60 five-second samples and the standard deviation of each data point is plotted as an error bar. As observed with other signal processing methods before, a general trend observed was the decreasing variance of power of the sensor signals with increasing excess air.

As previously observed with Tests 1 to 9, the variance of power of the three sensors were observed to decrease with increases in excess air for all thermal loads for other experiments presented in Appendix B.3. The general trend would help in a simple algorithm to detect changes within a thermal load for most of these

experiments but one that is able to distinguish between thermal loads would be difficult as the changes in the signal strength are neither linear nor directly proportional to the change in excess air and thermal loads.

Fairly consistent trends can be observed when the burner was subject to different operating conditions whilst firing pulverised coal and different proportions of coal/biomass blends and mostly exhibit downward trend with the increase in oxygen concentration. In general the area under the PSD curve (a measure of signal energy) reduces with increases in O_2 for the IR sensor for all load conditions, a result that was replicated for each of the optical photodiode sensors. However, the consistency of the results, as measured by the error bars in each graph, can be quite variable. This trend is similar for the other signal processing methods previously discussed as well, therefore requiring a different signal processing algorithm capable of distinctly identifying these changes.

4.3 Joint Time Frequency Analysis

Even though a general trend could be observed for the experiments with variation in excess air and thermal load for the various blends of coal and biomass these trends depend on many of the combustion parameters with no easy to define algorithm that could relate the features to control parameters or identify abnormal combustion conditions. The final signal processing approach of JTF methods allows the observer to see changes in the frequency domain over time. Two such methods, namely wavelet decomposition and WVD were utilised to analyse the three photodiode sensors data from the experiments in the following sections.

4.3.1 Wavelets

A one-dimensional wavelet packet decomposition function, which belongs to one of the wavelet packet analysis in MATLAB® Wavelet Toolbox™ was used to decompose the sensor signals. The signals were decomposed to level-3 using a Daubechies 4 or db4 wavelet and the RMS of each packet coefficient at level-3 was computed. This resulted in 8 wavelet coefficients per sensor and the wavelet coefficient which best correlated to the operating parameter was chosen. Figure 4.4 below shows the wavelet decomposition tree to level-3 which resulted in 8 wavelet coefficients as represented by the packets of (3, 0), (3, 1), etc. As noted in figure 4.4, lower frequencies are represented in (1, 0) while higher details are correlated in (1, 1) at level-1, so at each level the lower frequencies are represented in the first bin. At level-3 the approximation of the lowest frequency signals would be in (3, 0) where most of the flame flicker frequency should be present while (3, 7) represents the higher frequency components.

The results presented in this section each consist of a set of nine experiments based on a particular fuel blend and swirl setting (with reference to Table 3.7), where the thermal load and excess air were varied. Also each result, consists of three plots for each of the UV, VIS and IR sensors signals after processing. Each plotted point is the mean of the RMS of the best correlating wavelet coefficient - (3, 0), calculated every second over 300 s duration of an experiment and the

minimum and maximum values being plotted as the error bar for each plotted point.

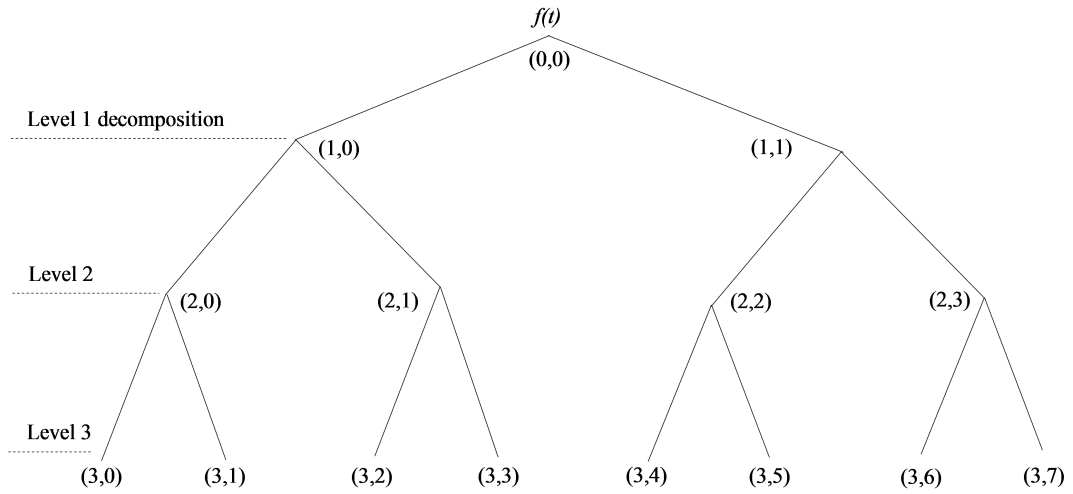

1,0 – Approximation (low frequency signal) 1,1 – Detail (high frequency signal)

Figure 4.4: Wavelet packet decomposition tree to level 3

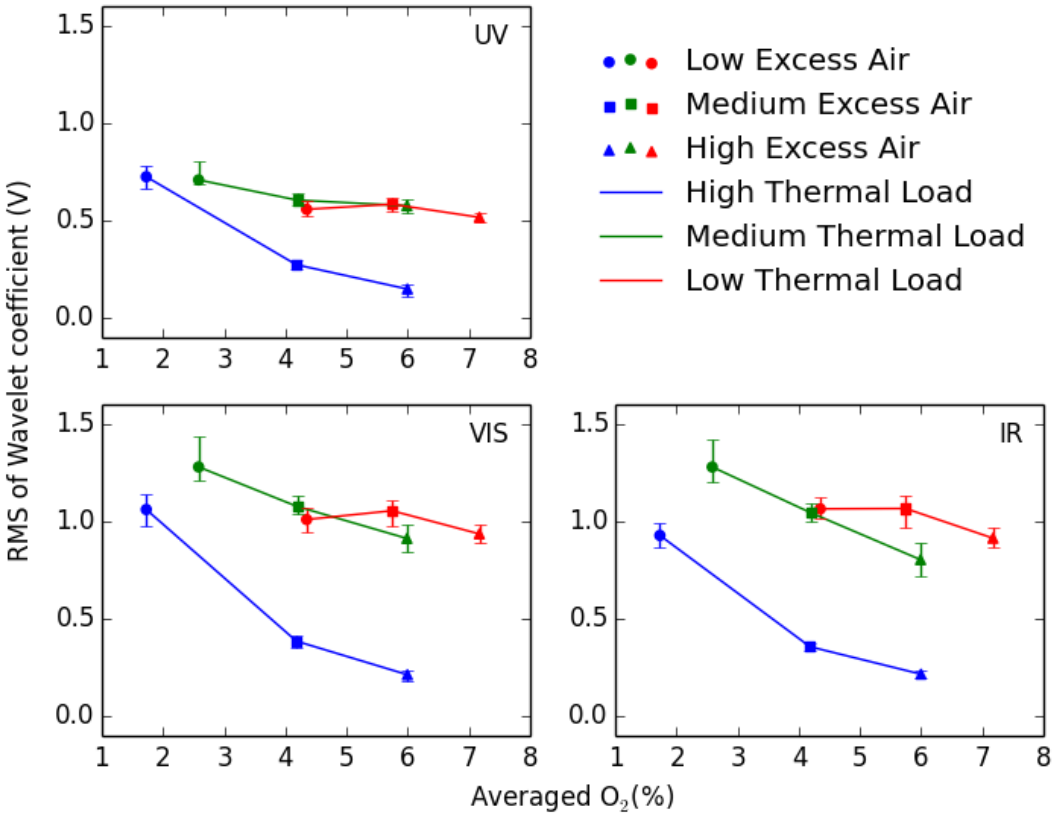

Figure 4.5: RMS of largest wavelet coefficient of UV, VIS & IR photodiode signals Vs averaged O_2 for Tests 1 to 9 - 100 % Coal - 50° Swirl

Figure 4.5 shows the best correlation - (3, 0) from the wavelet packet decomposition observed of the UV, VIS and IR photodiode sensor signals with respect

to the oxygen levels for Tests 1 to 9 for 100 % pulverised coal and 50° swirl. A degree of correlation is evident with a general reduction in the amplitude of the features with increasing O_2, although the precise nature of the underlying correlation in the data is unclear.

The best wavelet coefficient (3, 0) had a general trend of decreasing amplitude with increasing excess air for the various fuel blends for the different thermal loads. There were some anomalies, especially with lower thermal load due to the purge air being a higher percentage compared to the other thermal loads but the underlying trend was still present even though this was neither proportional nor linear with changes to excess air and thermal load. Hence this technique would be difficult to apply directly to detect changes to burner conditions for use with the monitoring and control system as the multivariate analysis of this signal together with others from the CTF would be complex, and especially so with coal combustion being a complex process thus making application of ANN an attractive option due to the complex not very well understood combustion process and in the presence of incomplete information. Other results (packets (3, 1), etc.) did not yield any consistent results and have therefore not been presented.

4.3.2 Wigner-Ville Distribution

The WVD maps a time variant signal to the two dimensions of time and frequency, with the same resolution in both domains. In this case, the WVD was obtained using National Instruments Incorporated (NI) Advanced Signal Processing Toolbox™ in the LabVIEW™ software. As the sampling rate for all optical sensors were set at 8192 Hz, using the Nyquist-Shannon sampling theorem, the highest frequency that could be measured was 4096 Hz. The frequency or time resolution are normally of the order of N = 512 and in the current application this was limited due to the available memory resources on the computer. The raw signals fed to the WVD function were normalised using the largest standard deviation among the whole set of experiments.

The WVD spectrum output contains spurious negative energies, but by using the absolute values, only the magnitude of the output was taken into consideration for further processing. In this case, the output consists of the absolute energies of the sensor signal for each frequency bin (4096 Hz / 512 frequency bins) of 8 Hz during each time interval, which is based on the total duration of each test. Since the WVD has equal resolution, for a typical experiment duration of 5 min (300 s), the time resolution is approximately 0.6 s. The time resolution could be improved by performing multiple WVDs for the same test duration, but in the case of a power station boiler such sudden dynamic changes are not common as changes in thermal load or combustion parameters are usually undertaken gradually.

The results presented in this section each consist of a set of nine experiments based on a particular fuel blend and swirl setting (with reference to Table 3.7), where the thermal load and excess air were varied for each of the three photodiode sensors. Also for comparison of the various experiments, each result consists of the averaging of the 512 bins of ≈0.6 s of the WVD calculated over the entire 300 s duration of an experiment for each of the frequency bins of about 8 Hz. As

observed before with the frequency domain results (section 4.2) and from the literature (section 2.7.3), the flame flicker frequency is in the 0 Hz to 40 Hz range and to avoid any loss of any other overlooked features a range of 0 Hz to 400 Hz was chosen for the analysis. The range of the colour bars have been maintained (for each sensor) through out all the results for each of the three sensors at a set value to make comparison easier, so some experiments might seem to have no signal information present but there are changes that are not very visible with the overall range that has been adopted to visualise and compare all the experiments. The range of colours represent the voltage of the signals acquired but since the original voltage measurements weren't calibrated with a source, the units in the figures have been avoided as this can't be established appropriately without the need for measuring absolute values. Hence for this research outputs means, the values are used only for comparison and could be used to compare different signals within the set but cannot be related to real values, even though these are voltage measurements. The x axis represents the set of nine experiments and the y axis, the frequency.

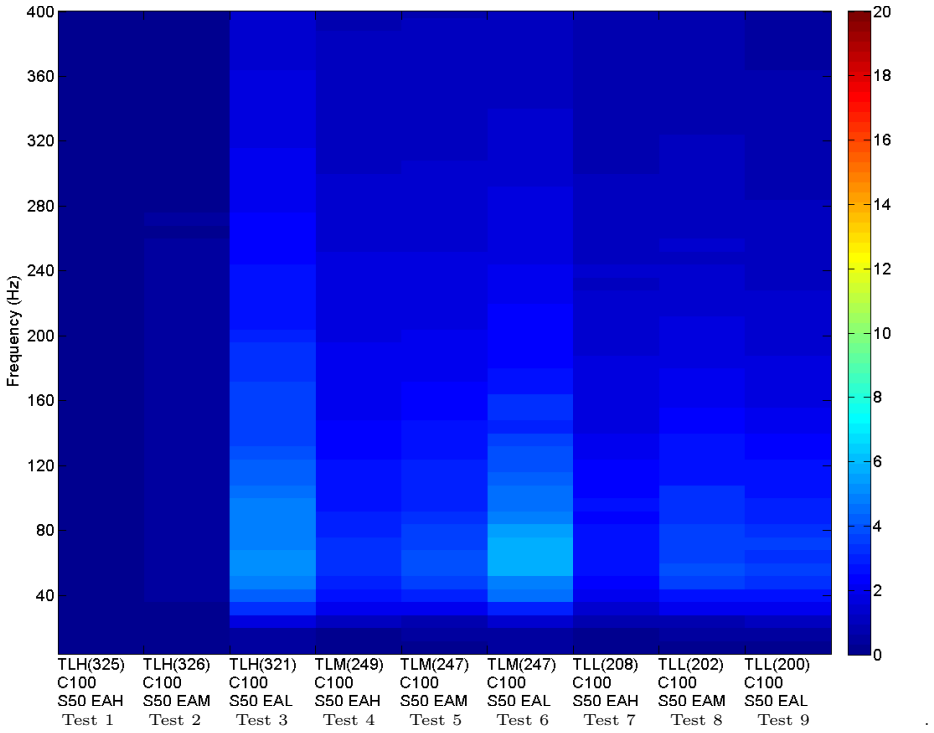

Figure 4.6: WVD (averaged) of UV photodiode signal for Tests 1 to 9 - 100 % Coal - 50° Swirl

Figures 4.6, 4.7 and 4.8 show the WVD of the UV, VIS and IR sensor respectively for Tests 1 to 9 for 100 % coal and 50° swirl. The first three tests starting from the left of these figures (Tests 1 to 3) clearly show that with decrease in excess air the signal intensity increases for high thermal load (320 kW). This same trend can be noticed in Tests 4 to 6 and Tests 7 to 9 for medium (250 kW) and low (200 kW) thermal loads while excess air was being decreased. Another interesting aspect of this representation of the signal is that it shows the increased frequency spread as the excess air decreases for the various thermal loads.

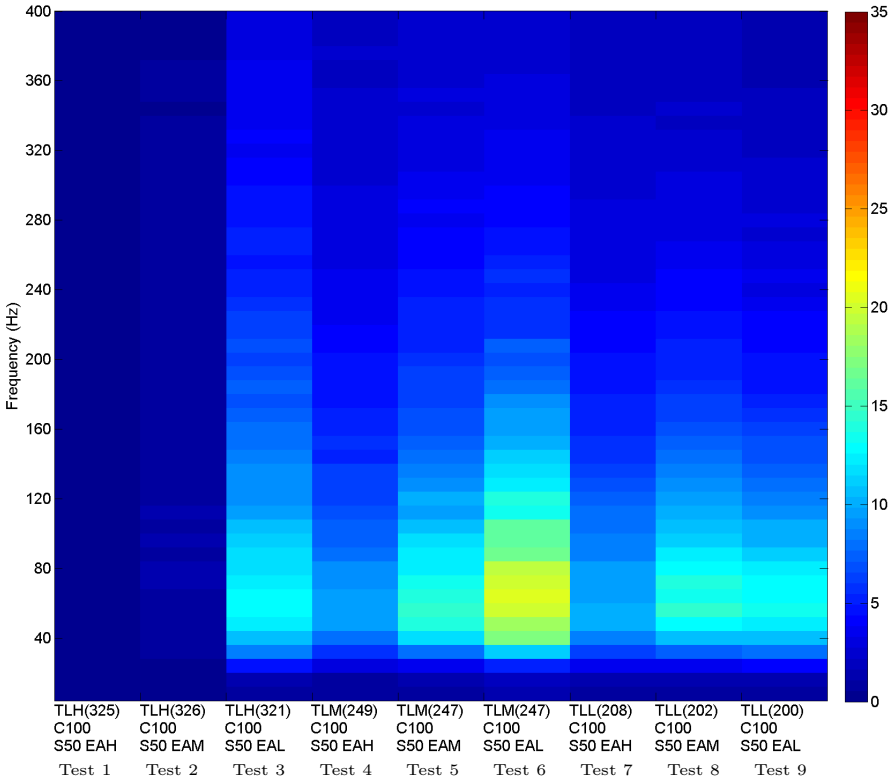

Figure 4.7: WVD (averaged) of VIS photodiode signal for Tests 1 to 9 - 100 % Coal - 50° Swirl

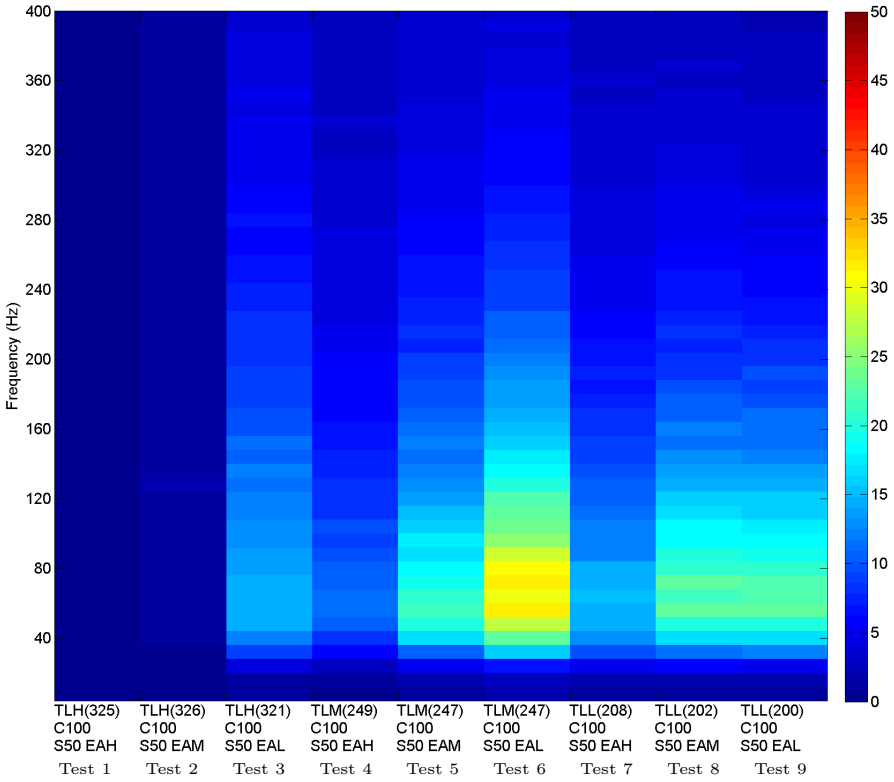

Figure 4.8: WVD (averaged) of IR photodiode signal for Tests 1 to 9 - 100 % Coal - 50° Swirl

The results for the three sensors from the rest of the experiments listed in Table 3.7 is presented in Appendix B.5. The magnitude of the frequencies present in the WVD output had a general trend of decreasing amplitude with increasing excess air for the various fuel blends for the different thermal loads. Again this cannot be directly applied to detect changes to burner conditions for use with the monitoring and control system as its not consistent or change proportionally with changes to the burner conditions. The multivariate analysis of this signal together with others from the CTF would be complex, and especially so with coal combustion being a complex process.

4.4 Summary

This chapter outlined the various signal processing algorithms applied to the sensor data obtained from the three sensors used to monitor the flames during the systematic variations of the operating conditions carried at the CTF. Initially starting with simpler methods in the time and frequency domains before moving on to more complex JTF methods. The reason behind carrying out such analysis was to choose an appropriate signal processing method that could identify changes in the sensor signal as each parameter was varied. Though trends in the sensor signals could be observed with changes to the operating condition, they weren't systematic with the changes made to the operating conditions. The trends were however much clearer with JTF methods for the same experiments compared to the other signal processing methods used in this research.

A general trend was observed with all the signal processing algorithms, the signal amplitude decreased with increases in excess air. Some anomalies were observed, especially with lower thermal load with the time and frequency domain results which is thought to be due to the purge air being a higher percentage compared to the other thermal loads but the underlying trend was still present even though this was neither proportional nor linear with changes to excess air and thermal load. Hence, a simple system just utilising the signal processing data of the sensors wouldn't be appropriate to detect changes based on fixed cut-off / band of values and coal combustion (in this case coal biomass blends) being a complex process with many unknowns would be an ideal candidate for the application of an ANN, as these have been applied to predict / estimate values based on large number of inputs without prior knowledge of the process or system. The following chapter (Chapter 5) describes the development of such a system for the monitoring and control of co-firing flames to detect abnormal combustion.

Chapter 5

MONITORING AND CONTROL SYSTEM DEVELOPMENT

This chapter describes the monitoring and control system development and its testing at the pilot scale 500 kW_{th} Combustion Test Facility (CTF) located at the Institute Energitky - Institute of Power Engineering (IEn), Poland. This involves a discussion of the signal processing methods applied in the development of the monitoring and control system and a performance evaluation of the system on the CTF.

The control system was not intended as a replacement for existing plant automated control, but to produce a simple rule-based system able to advise on the manual adjustments to the burner, required to provide near optimal burner settings by adjusting the airflow to the burner for stable combustion and appropriate NO_x and CO emissions. It is intended for monitoring individual flames within multi-burner applications commonly found on power station boiler plant.

5.1 Simple Set Point Based System

A simple set point based control system would be beneficial in terms of time taken for development and testing, due to the simplicity of such a system. As it has been observed in Section 4.1 there are trends in terms of the variation of Root Mean Square (RMS) of the sensor signals with changes to O_2, but these changes are not systematic enough to be used with certain set points to detect if a condition is present as there are many varying factors. It also has to be noted that, similar levels of RMS values can be seen for two completely different conditions (e.g. different thermal loads - as detailed for figure B.8) which can result in false identification of a condition and hence corrective actions not relevant for such a condition being suggested.

Similarly a simple rule based system based on the Fast Fourier Transform (FFT), Power Spectral Density (PSD) or wavelet coefficients of the sensor signals would not be feasible for the same reasons. Similar to the RMS, this wouldn't be of much use as the change to O_2 does not produce proportional or linear changes to the sensor signals, which could be utilized to identify an undesirable condition.

5.2 Artificial Neural Network

The combustion process is complex and its control is a challenging multi-variable problem that is tackled in the presence of incomplete information. Such a process with multiple variables and outcomes based on small changes would be an appropriate candidate for use of Artificial Neural Networks (ANN) [42–44, 83, 161, 165–167] (Section 2.9).

In order to test the appropriateness of a range of techniques a subset of the experiments presented and discussed in Chapters 3 and 4 were selected. These were Tests 1 to 9 (Table 3.7) at 50° swirl and 100 % Russian coal.

Initially three case studies were investigated and different input features generated from the CTF tests were considered. The three case studies used the features generated from the CTF where the input variables to the ANNs were the sets of the RMS, PSD and wavelet features of the three photodiode signals (i.e. Ultra Violet (UV), Visible (VIS) and Infrared (IR)) as shown in Table 5.1.

Table 5.1: Case studies initially selected to evaluate the various input features to be applied to an ANN

Case Study	Number of features	Input features
1	3	RMS of UV, VIS and IR sensors
2	3	PSD of UV, VIS and IR sensors
3	3	RMS of the best wavelet coefficient of UV, VIS and IR sensors

The main advantages of using neural networks in the current work are the ability to learn the complex relationships that exist in the real system, rather than describing it analytically or physically. For complex systems, once trained, the network has a relatively low computational cost when compared to simulation models based on physics. ANN modelling has been applied in this project for this very reason. Examples of combustion related applications of ANN are given in [34, 44].

The ANN with the least resource intensive signal processing method needs to be tested, as a developed system needs to be applied in an online, real-time basis to make predictions of the O_2 concentration, NO_x and CO emissions. NO_x and CO emissions have been used for combustion control for Pulverised Coal (PC) flames by others such as Lu *et al.* [117] in their work where NO_x or CO has been related to combustion quality and hence used for control, as discussed in section 2.7.1. Similar to comparisons of the three photodiode signals with reference to O_2 in chapter 4 and Appendix B, similar comparisons were carried out for NO_x but have not been presented for brevity. With reference to [34, 44], an ANN was used due to its massively parallel approach which is able to learn complex patterns between input and output data. This was due to observed trends in the sensor signals with changes to O_2 as seen in the results from the systematic set of steady state experiments varying one parameter in Chapter 4. Initially the three case studies in Table 5.1 were studied with the selected experiments to see the viability of such an approach with varying numbers of hidden neurons. The aim

of neural network modelling was to establish a methodology for relating measurements from the flame monitoring system to burner operating parameters. A standard feed-forward neural network with Bayesian Regularisation (BR) was explored with the aim of improving the capture of any non-linearity that might exist in the underlying correlation function and which weren't observed from the various signal processing methods employed in Chapter 4.

5.2.1 RMS Based ANN Modelling

According to Basheer and Rohwer *et al.*, Multilayer perceptron (MLP) with back propagation is the most used network [162, 169], therefore this was chosen to be investigated in this research (Section 2.9.2). Multilayer feed-forward networks have one or more hidden layers between the input and output layers and are able to extract higher order statistics and contribute to the capability of the ANNs' computational power [160, 162] (Section 2.9.1). The data modelling was carried out using MATLAB^{TM} software, where a standard feed-forward neural network with error back-propagation was used to train and predict the O_2 and NO_x. The network constituted an input layer, one hidden layer with a hyperbolic tangent sigmoid transfer function and an output layer with a linear activation function. The RMS features generated from the CTF at IEn (Tests 1 to 9) whilst combusting 100 % coal (Table 3.7) were used to train the ANN. These input variables were divided so that 75 % of the data was used for training with the remaining 25 % being used to test the neural network model to unseen conditions. Two separate networks were trained to estimate the excess air level and NO_x emissions and the performance of the ANN was evaluated by the mean percentage prediction error (MPPE) on the "unseen" test data set (25 % not used for training). Different numbers of hidden neurons were considered with the optimum number being decided on the lowest MPPE obtained from the testing data. The code used to carry out this is presented in Appendix A.1.

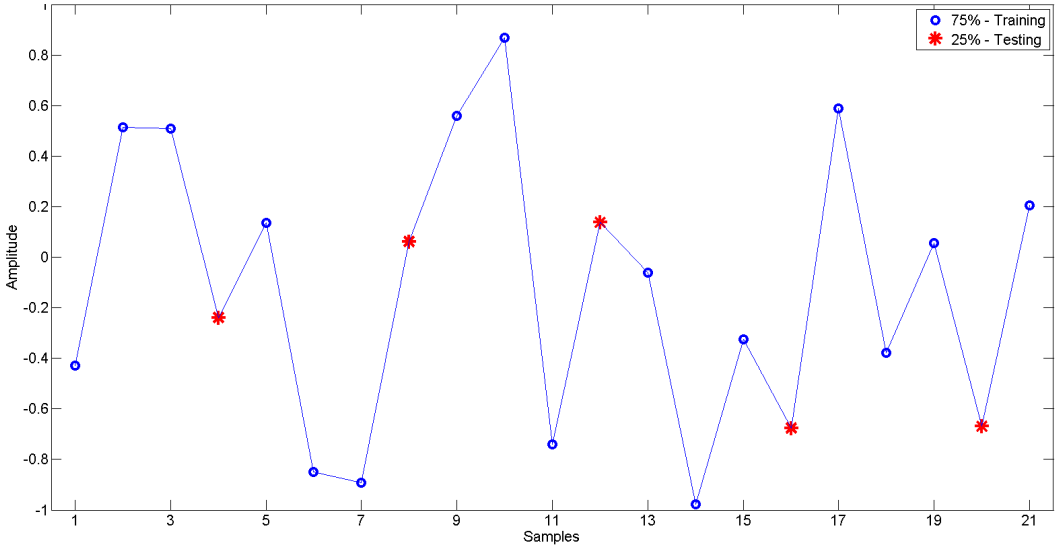

Figure 5.1: ANN sampling for training and testing

Figure 5.1 shows a sample of how the data was divided for training and testing ANNs. 75 % was used for training and the remainder used only while evaluating

the model. Hence the training data wasn't continuous, but 3 out of every 4 points used for training, highlighted as blue circles in figure 5.1.

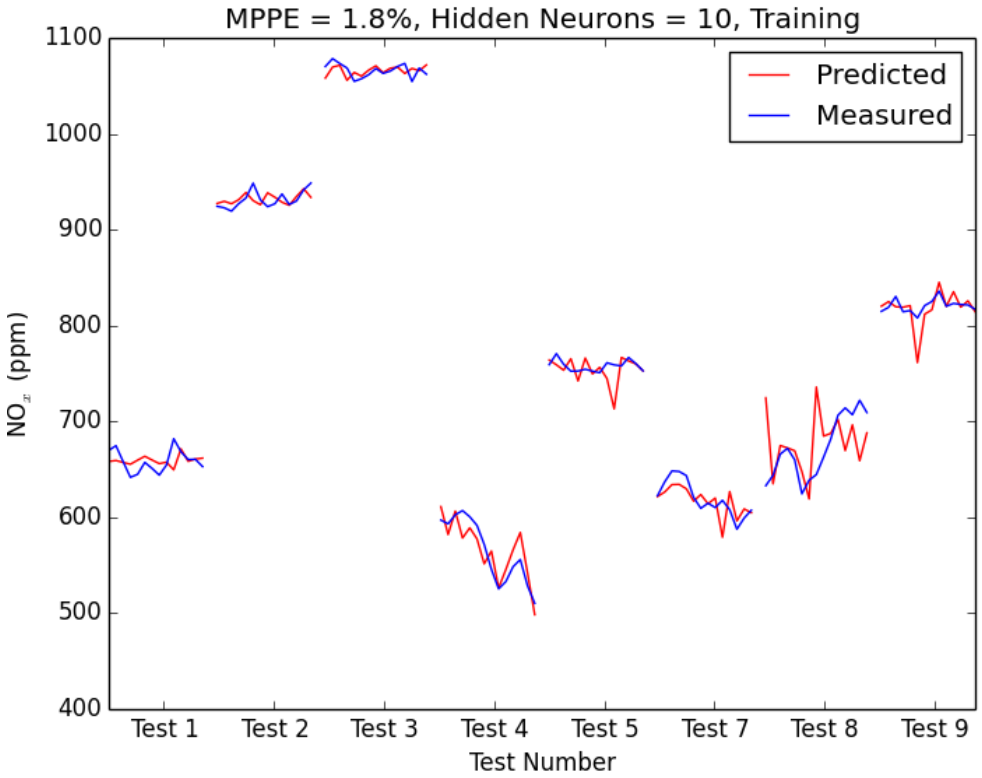

Figure 5.2: ANN prediction of NO_x - Training & Testing - trained with RMS - 10 hidden neurons

Figure 5.2 shows the predicted NO_x results of the tests used to the train the ANN with 10 hidden neurons. The input features used to train the ANN with 10 hidden neurons were the RMS values of the three - UV, VIS and IR photodiode signals and the NO_x emissions recorded during the tests. After the ANN was trained with 75 % of the data (3 out of every 4 points) from Tests 1 to 5 and 7 to 9, the remainder (25 %) was applied to the trained ANN to get a prediction. This training and testing was carried out at least 5 times and the best performing network, based on the lowest MPPE was chosen. The best performing ANN trained with 10 hidden neurons was acceptable with a MPPE of 1.8 %. As noted in Section 4.1, the low thermal load experiments (Tests 7 to 9) exhibit higher variation, this is thought to be from the higher proportion of purge air with respect to total airflow to the combustion chamber compared to the rest of the experiments. The results from this case study, while predicting NO_x with varying numbers of hidden neurons used for the ANN are presented in Table 5.2.

Figure 5.3 shows the results of validation - Test 6, which wasn't presented to the ANN during its training phase. This shows the performance of the ANN trained with unseen data, essentially the capability of the trained ANN model to learn from the previously presented data to predict. The ANN seems to be under predicting the NO_x emissions, with a MPPE of 17.1 %.

Figures 5.4 and 5.5 show the NO_x prediction with an ANN with 12 hidden neurons. MPPEs of 1.7 % and 5.17 % were observed.

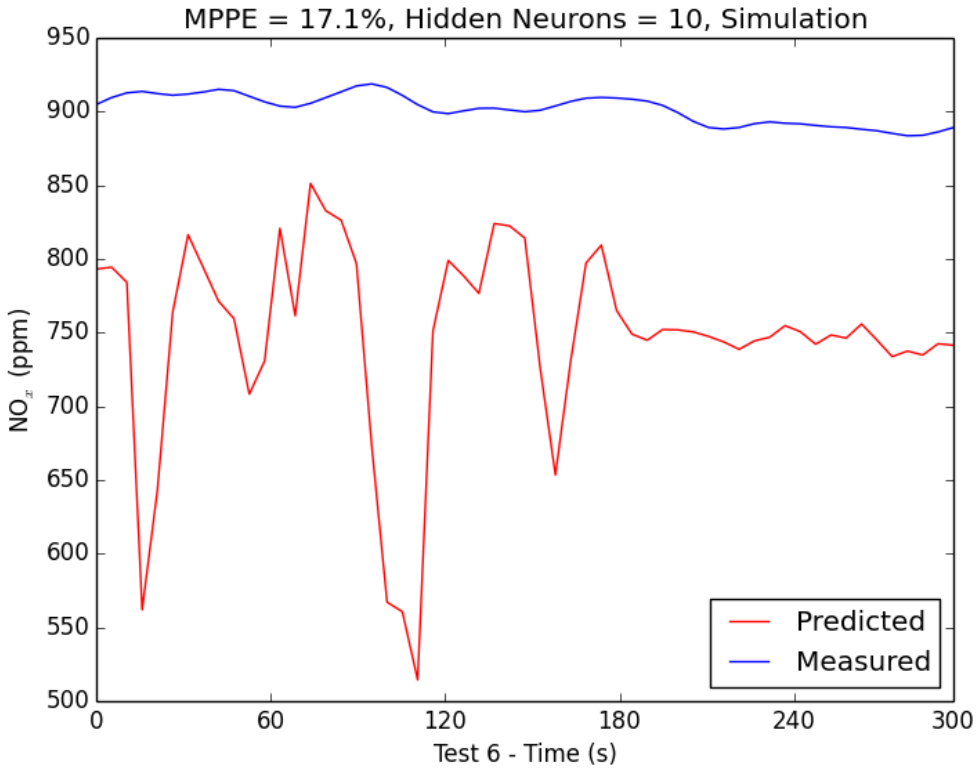

Figure 5.3: ANN prediction of NO_x - Validation - trained with RMS - 10 hidden neurons

Table 5.2: Comparison of performance of NO_x prediction results for ANN trained with RMS

Hidden Neurons	MPPE (%)	
	Training	Validation
10	1.8	17.1
12	1.7	5.17
15	1.7	4.9
20	1.8	13.8
25	1.7	5.74

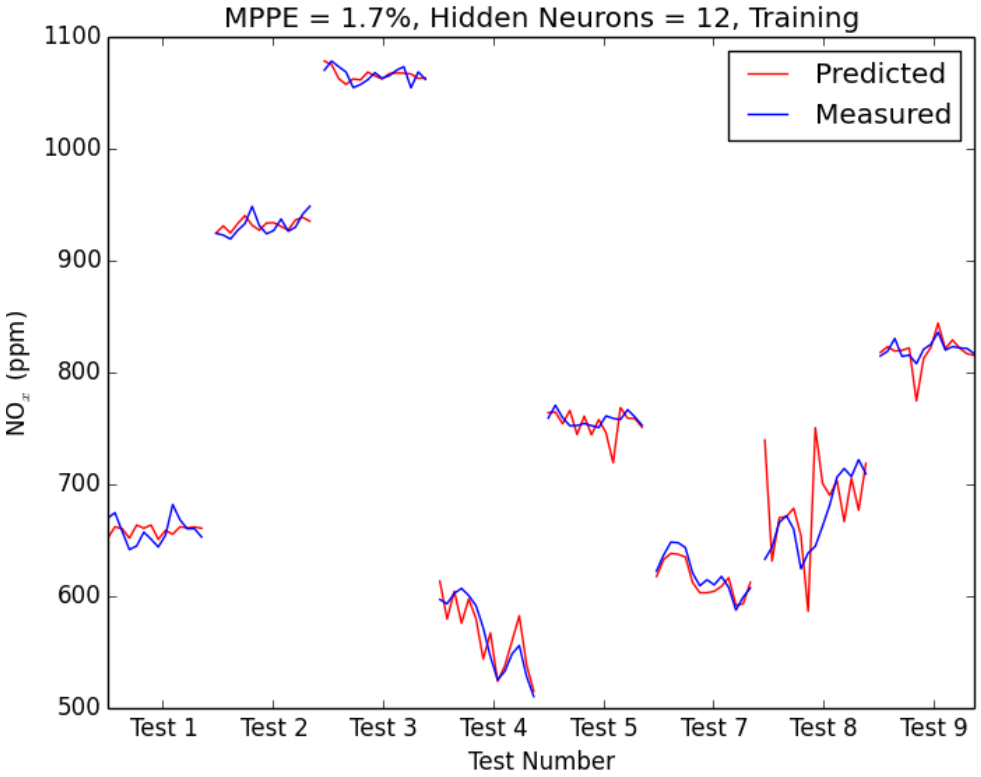

Figure 5.4: ANN prediction of NO_x - Training & Testing - trained with RMS - 12 hidden neurons

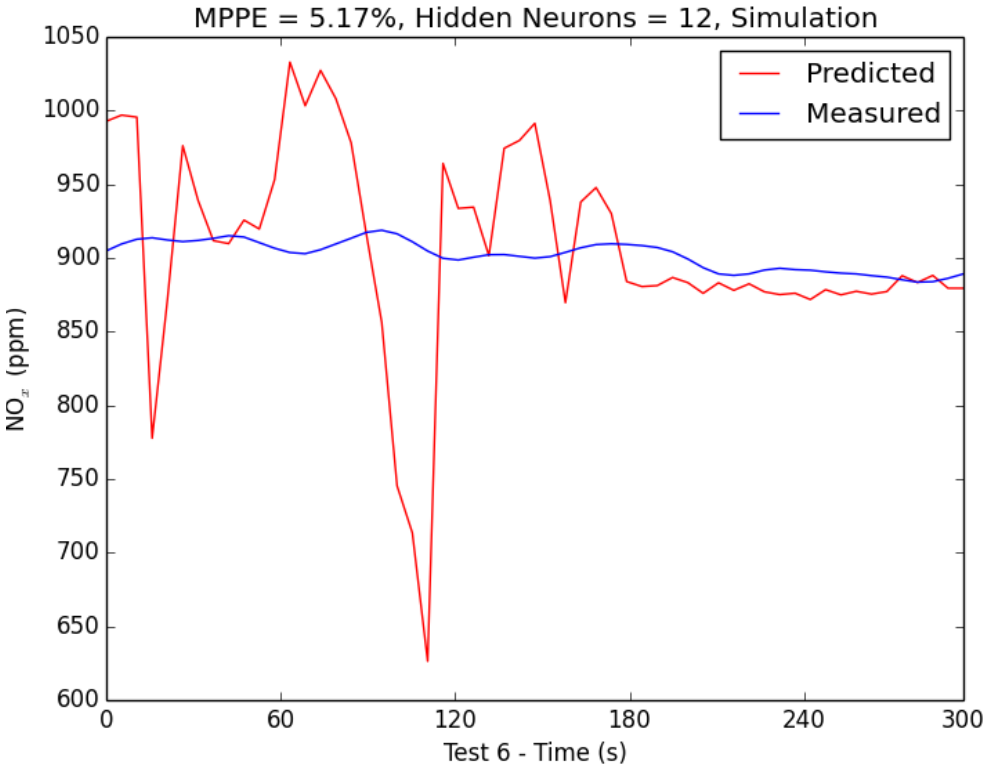

Figure 5.5: ANN prediction of NO_x - Validation - trained with RMS - 12 hidden neurons

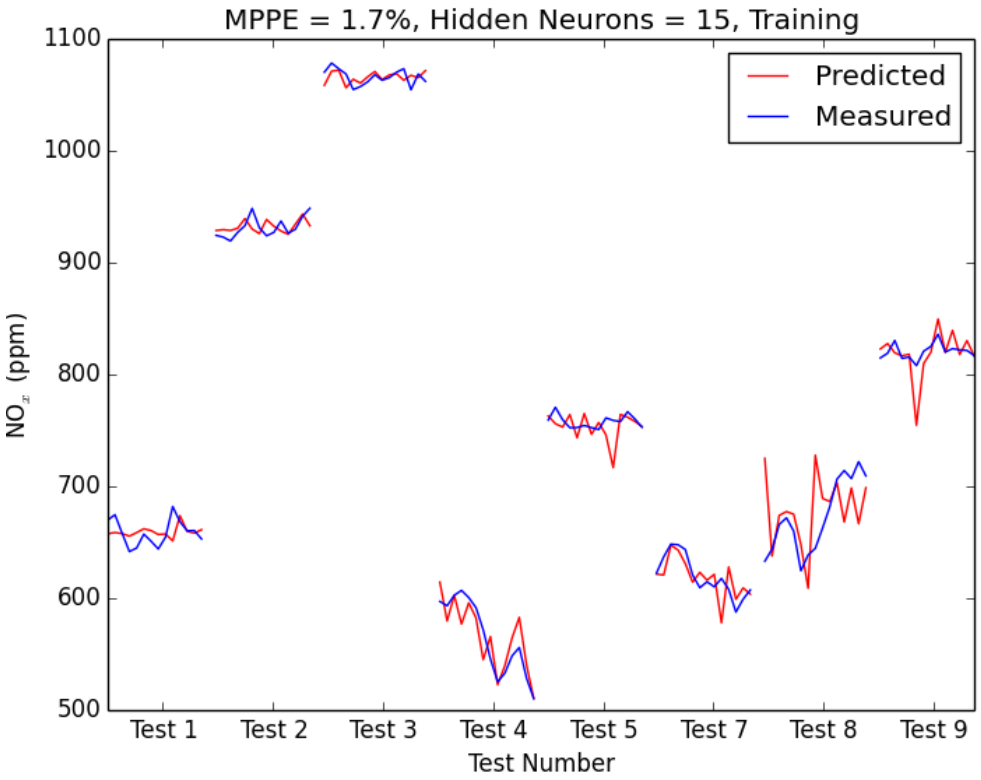

Figure 5.6: ANN prediction of NO_x - Training & Testing - trained with RMS - 15 hidden neurons

Figures 5.6 and 5.7 show the NO_x prediction with an ANN with 15 hidden neurons. MPPEs of 1.7 % and 4.9 % were observed.

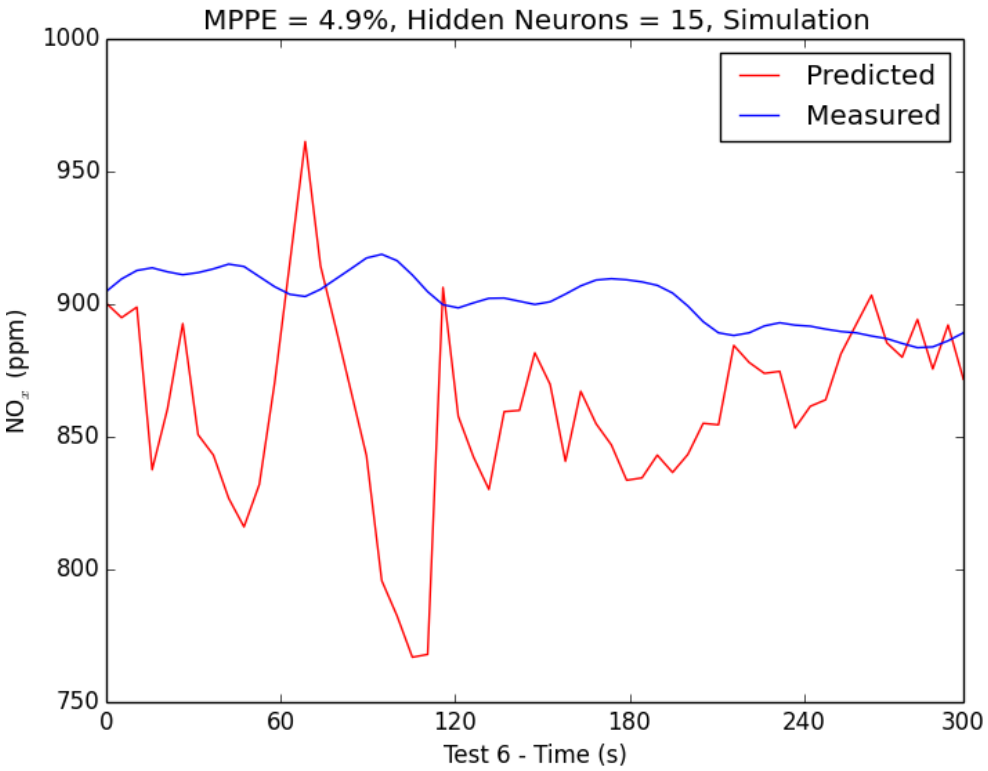

Figure 5.7: ANN prediction of NO_x - Validation - trained with RMS - 15 hidden neurons

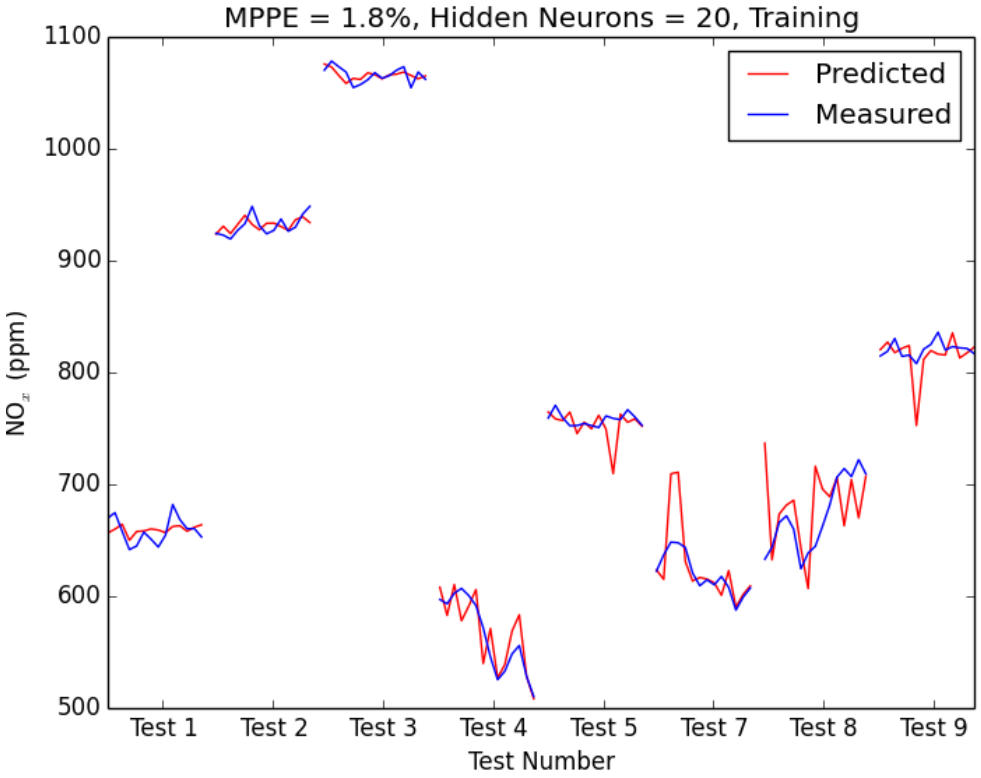

Figure 5.8: ANN prediction of NO_x - Training & Testing - trained with RMS - 20 hidden neurons

Figures 5.8 and 5.9 show the NO_x prediction with an ANN with 20 hidden neurons. MPPEs of 1.8 % and 13.8 % were observed.

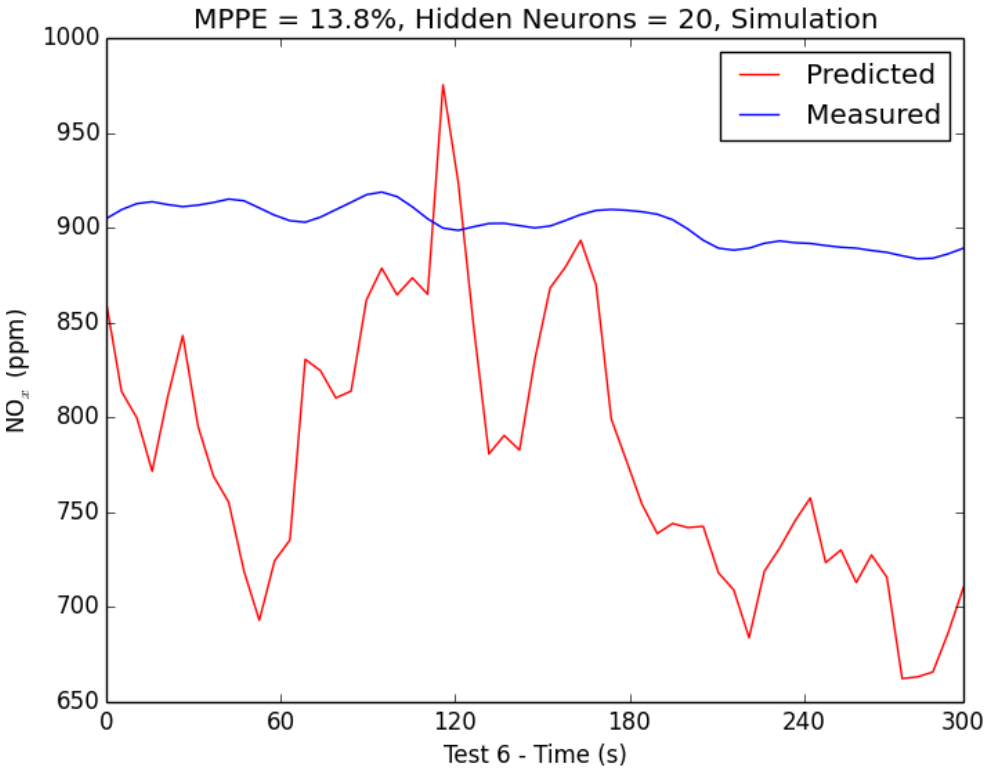

Figure 5.9: ANN prediction of NO_x - Validation - trained with RMS - 20 hidden neurons

Figures 5.10 and 5.11 show the NO_x prediction with an ANN with 25 hidden neurons. MPPEs of 1.7 % and 5.74 % were observed.

ANN with 15 hidden neurons showed the best performance in the prediction of NO_x for this set of tests, though even for this best case some of the predictions are some way from the measured values. NO_x prediction alone wouldn't be sufficient as, quite often boiler operators using low-NO_x burners and tend to operate some burners at low airflow (sub-stoichiometric) conditions to reduce thermal NO_x but have over fire air to enable complete combustion. Hence another parameter like O_2 would be beneficial to regulate burners as just regulating to achieve lower NO_x could still lead to poor combustion conditions.

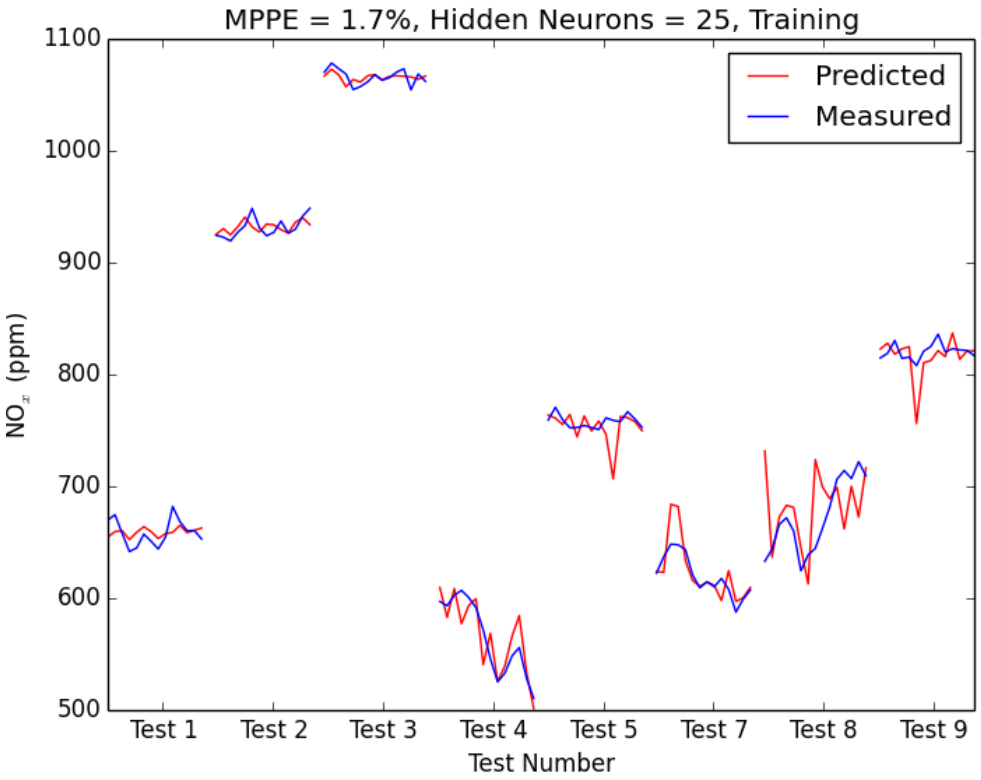

Figure 5.10: ANN prediction of NO_x - Training & Testing - trained with RMS - 25 hidden neurons

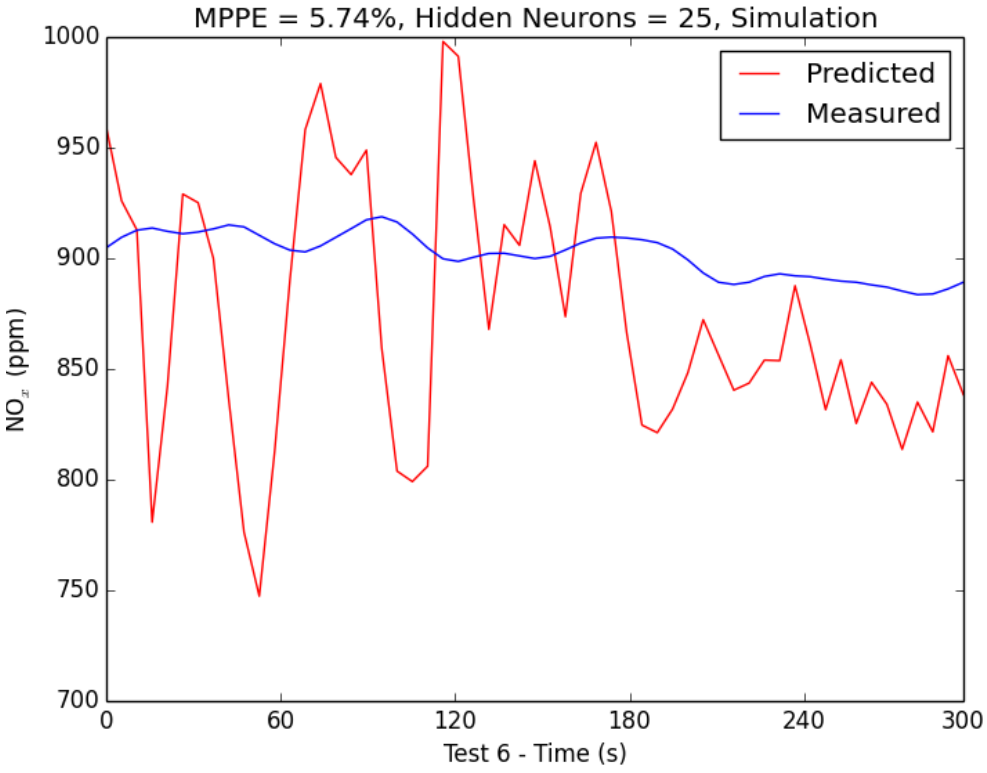

Figure 5.11: ANN prediction of NO_x - Validation - trained with RMS - 25 hidden neurons

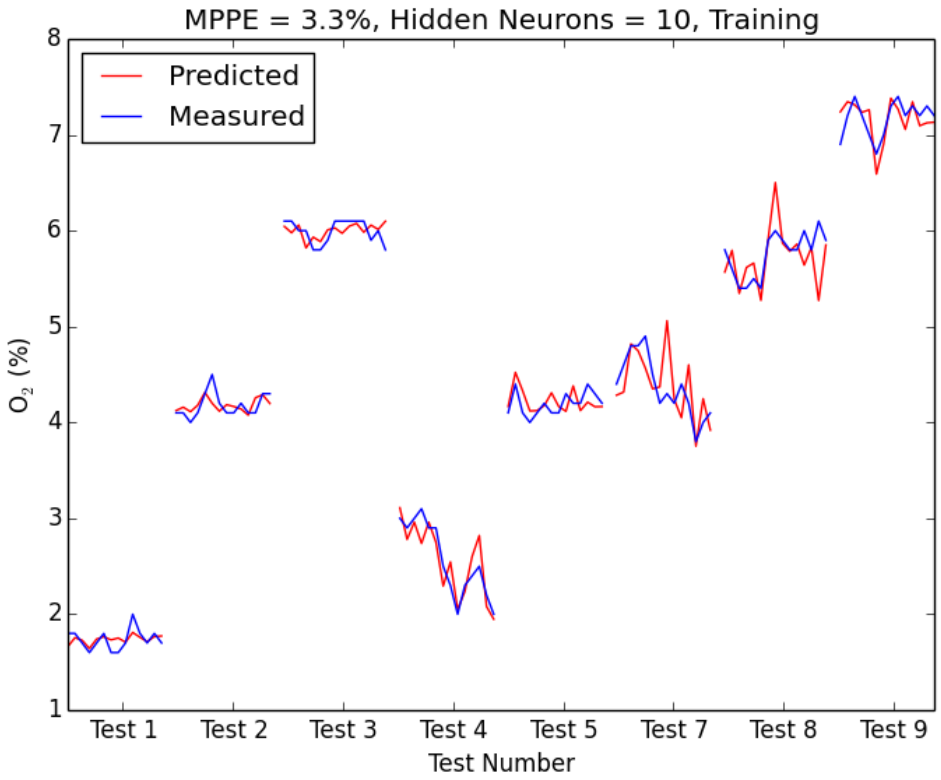

Figure 5.12: ANN prediction of O_2 - Training & Testing - trained with RMS - 10 hidden neurons

Figure 5.12 shows the predicted O_2 results of the tests used to the train the ANN with 10 hidden neurons. The input features used to train the ANN with 10 hidden neurons were the RMS values of the three - UV, VIS and IR photodiode signals and the O_2 emissions recorded during the tests. After the ANN was trained with 75 % of the data (3 out of every 4 points) from Tests 1 to 5 and 7 to 9, the remainder (25 %) was applied to the trained ANN to get a prediction. Again this training and testing was carried out at least 5 times and the best performing network, based on the least MPPE was chosen, similar to NO_x predictions. The best performing ANN trained with 10 hidden neurons was acceptable with a MPPE of 3.3 %. The MPPE result of 3.3 % is good (MPPE values for all the graphs are presented just above the plot), as can be seen with the predicted O_2 values (y axis) in red shadowing the measured values in blue for the various tests as indicated on the x axis, for the remaining 25 % of the data used to validate the trained ANN model. As noted in Section 4.1, the low thermal load experiments (Tests 7 to 9) exhibit higher variation, this is thought to be from the higher proportion of purge air with respect to total airflow to the combustion chamber compared to the rest of the experiments. The results from this case study, while predicting O_2 with varying numbers of hidden neurons used for the ANN are presented in Table 5.3.

Figure 5.13 shows the results of validation - Test 6, which wasn't presented to the ANN during its training phase. The ANN predicted the O_2 emissions, with a MPPE of 20.1 %.

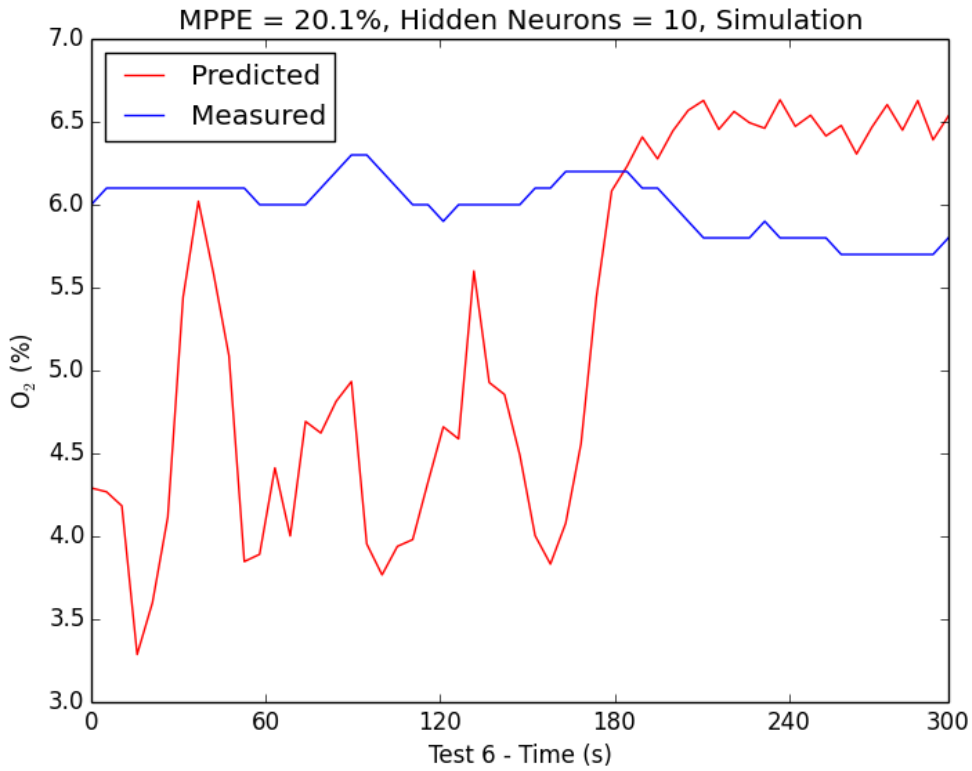

Figure 5.13: ANN prediction of O_2 - Validation - trained with RMS - 10 hidden neurons

Table 5.3: Comparison of performance of O_2 prediction results for ANN trained with RMS

Hidden Neurons	MPPE (%)	
	Training	Validation
10	3.3	20.1
12	3.3	56.7
15	3.3	71.2
20	3.4	72.2
25	3.9	82.1

Figures 5.14 and 5.15 show the O_2 prediction with an ANN with 12 hidden neurons. MPPEs of 3.3 % and 56.7 % were observed.

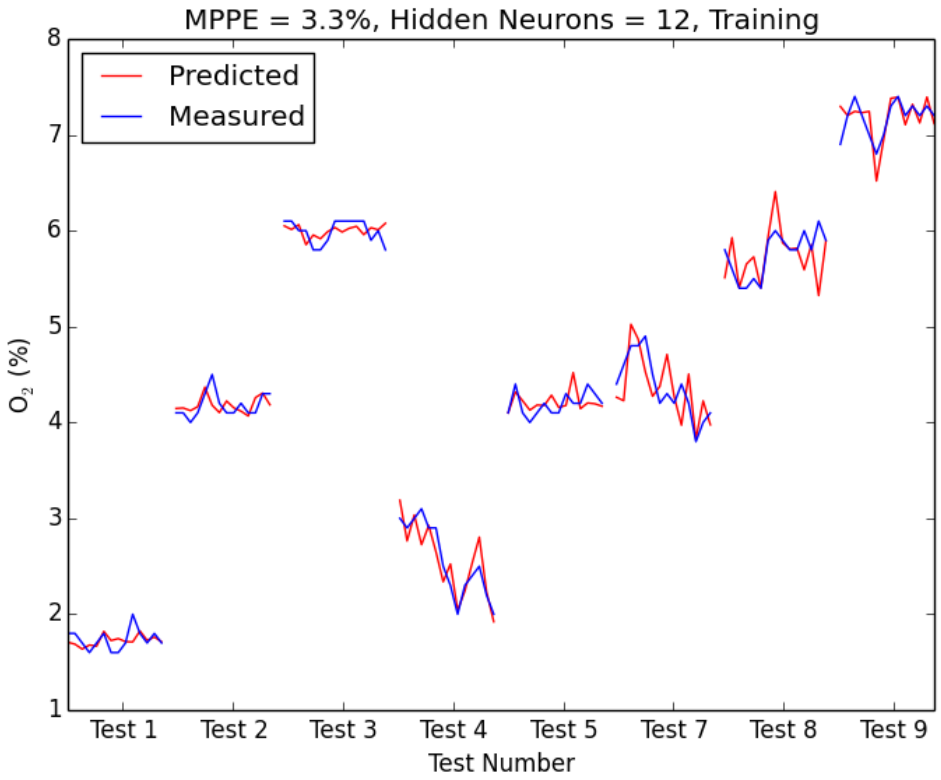

Figure 5.14: ANN prediction of O_2 - Training & Testing - trained with RMS - 12 hidden neurons

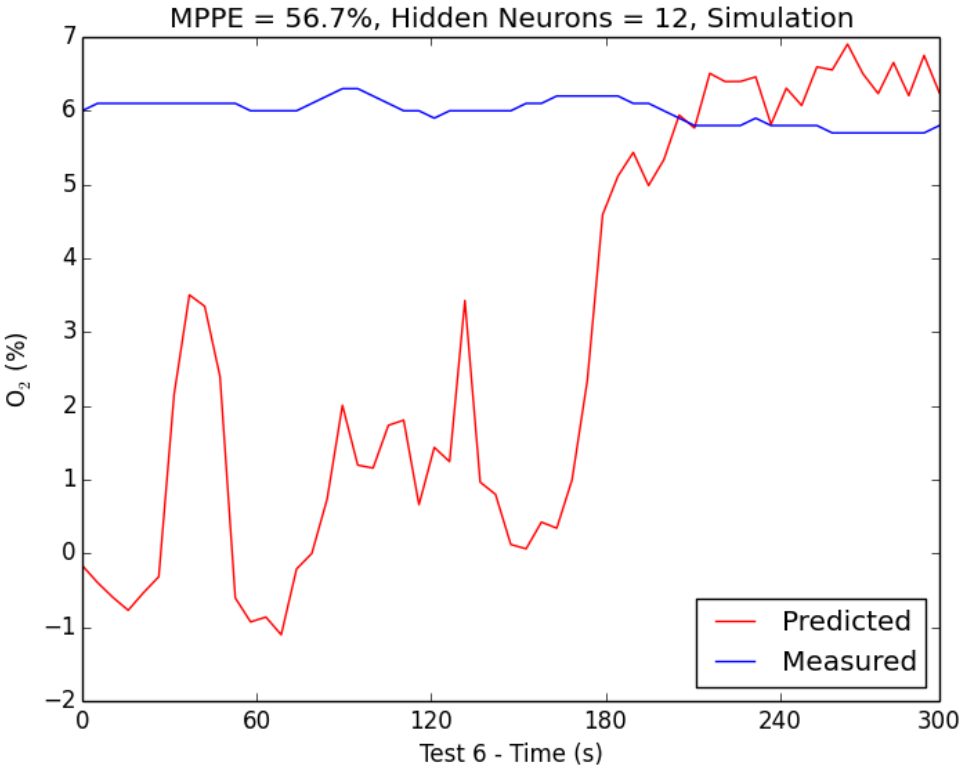

Figure 5.15: ANN prediction of O_2 - Validation - trained with RMS - 12 hidden neurons

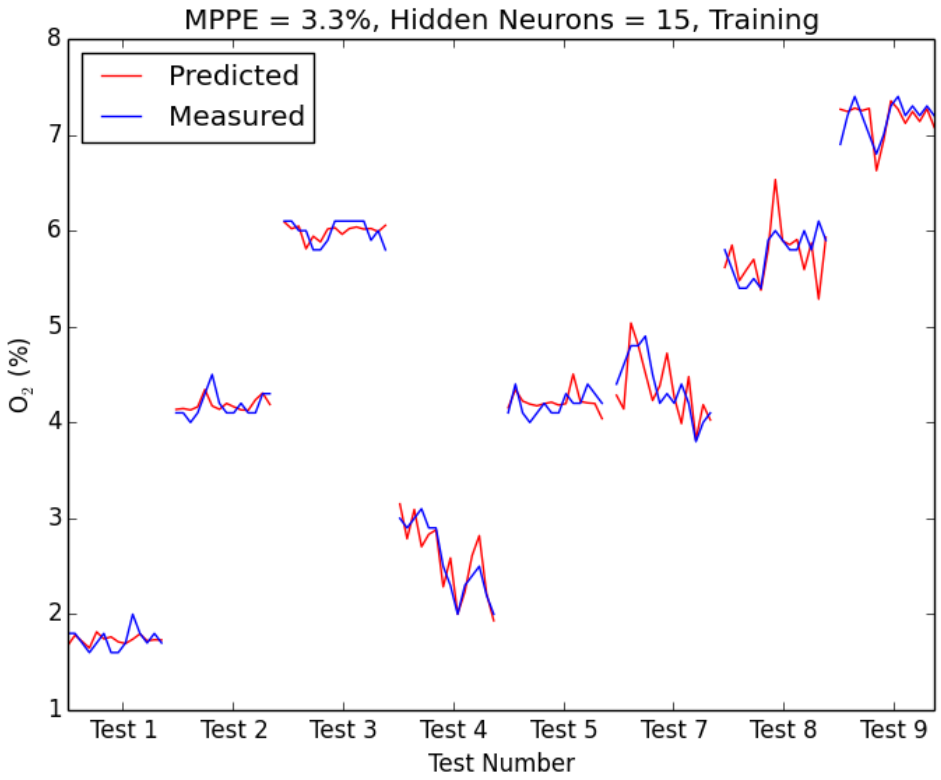

Figure 5.16: ANN prediction of O_2 - Training & Testing - trained with RMS - 15 hidden neurons

Figures 5.16 and 5.17 show the O_2 prediction with an ANN with 15 hidden neurons. MPPEs of 3.3 % and 71.2 % were observed.

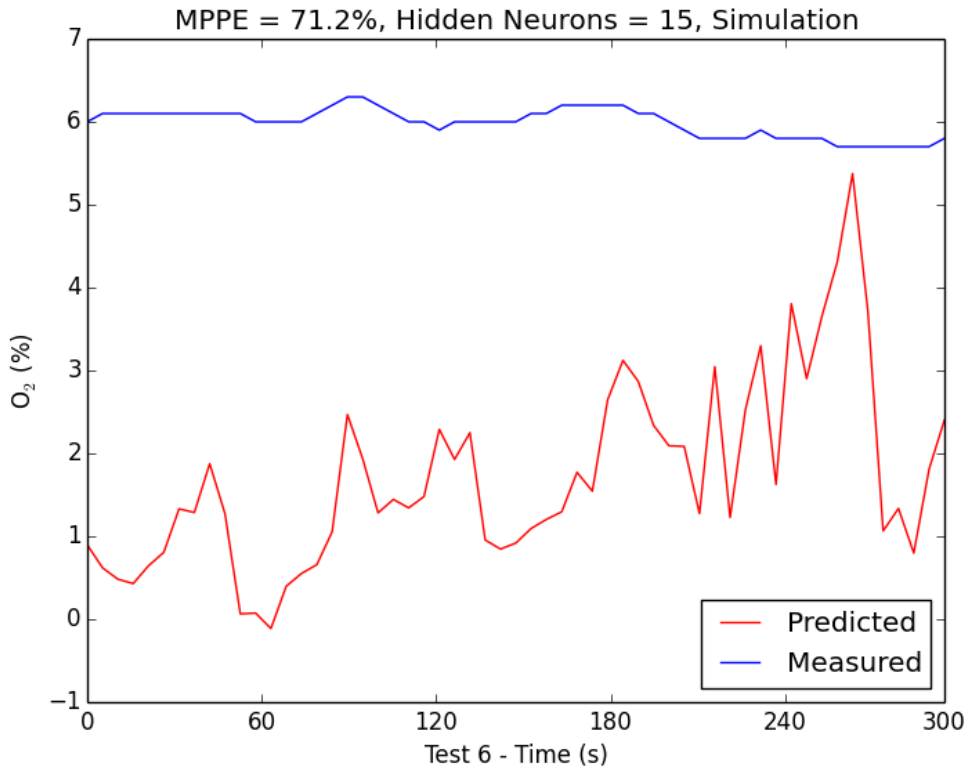

Figure 5.17: ANN prediction of O_2 - Validation - trained with RMS - 15 hidden neurons

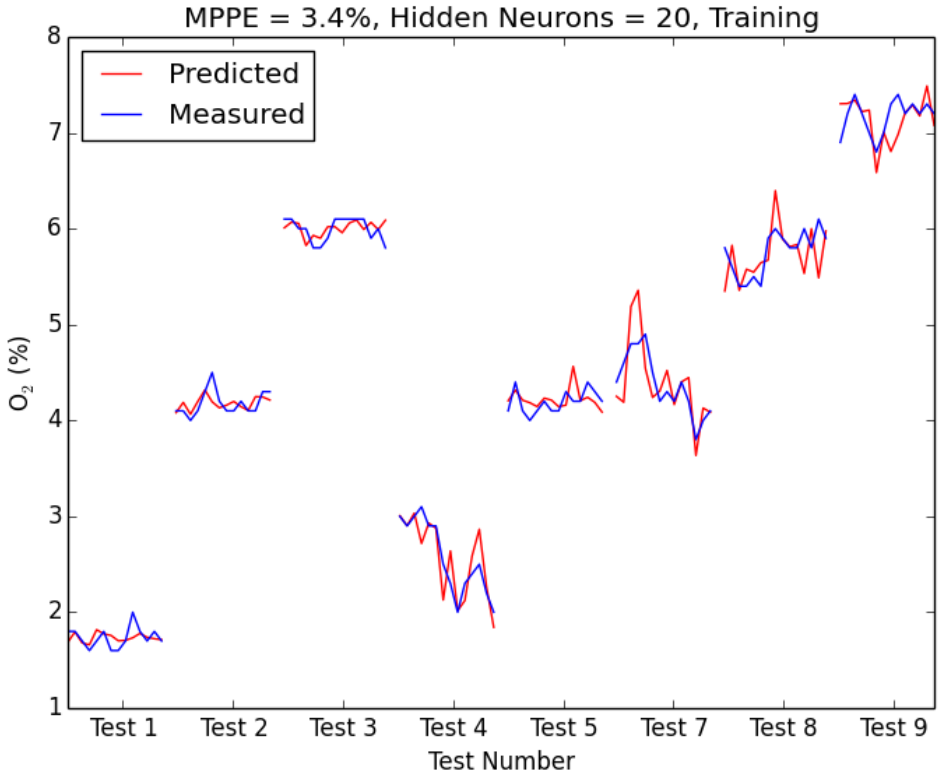

Figure 5.18: ANN prediction of O_2 - Training & Testing - trained with RMS - 20 hidden neurons

Figures 5.18 and 5.19 show the O_2 prediction with an ANN with 20 hidden neurons. MPPEs of 3.4 % and 72.2 % were observed.

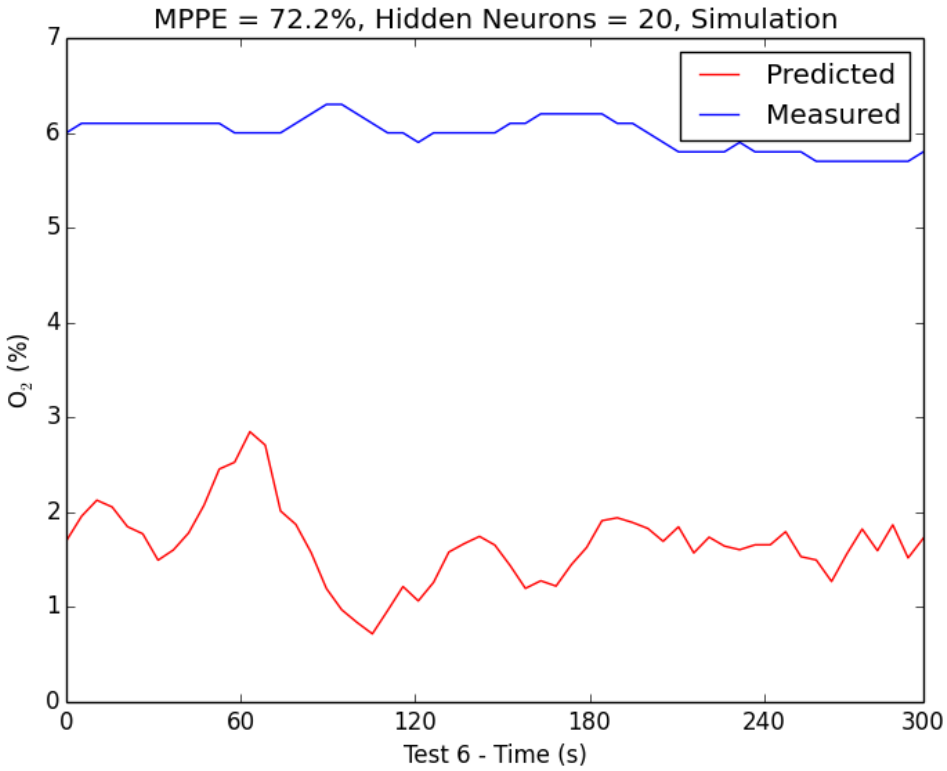

Figure 5.19: ANN prediction of O_2 - Validation - trained with RMS - 20 hidden neurons

Figures 5.20 and 5.21 show the O_2 prediction with an ANN with 25 hidden neurons. MPPEs of 3.9 % and 82.1 % were observed.

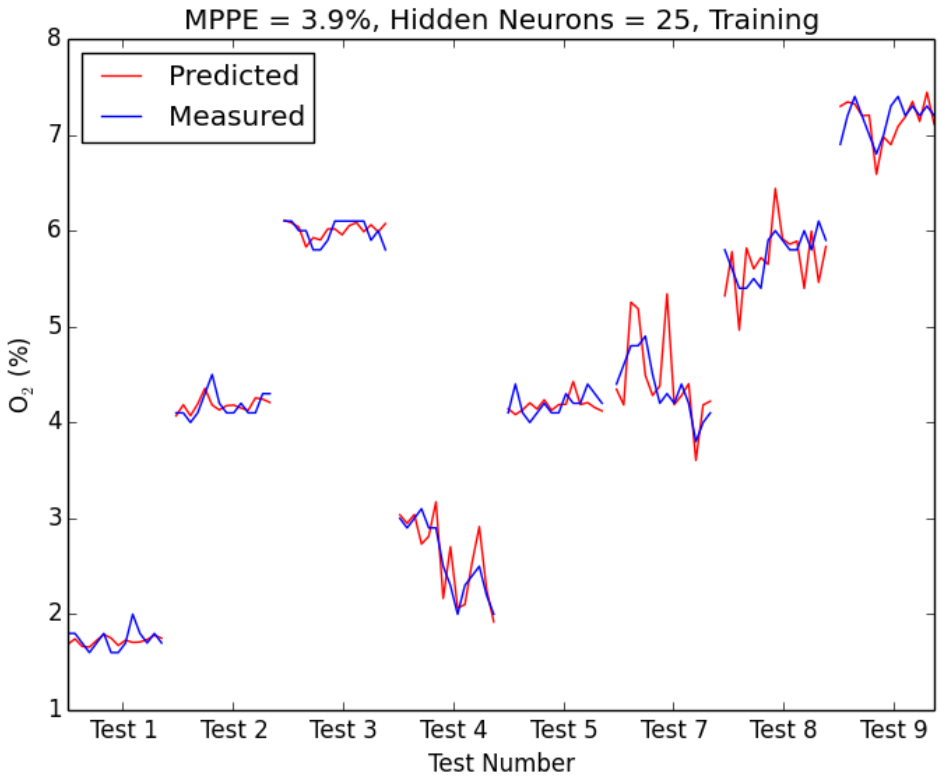

Figure 5.20: ANN prediction of O_2 - Training & Testing - trained with RMS - 25 hidden neurons

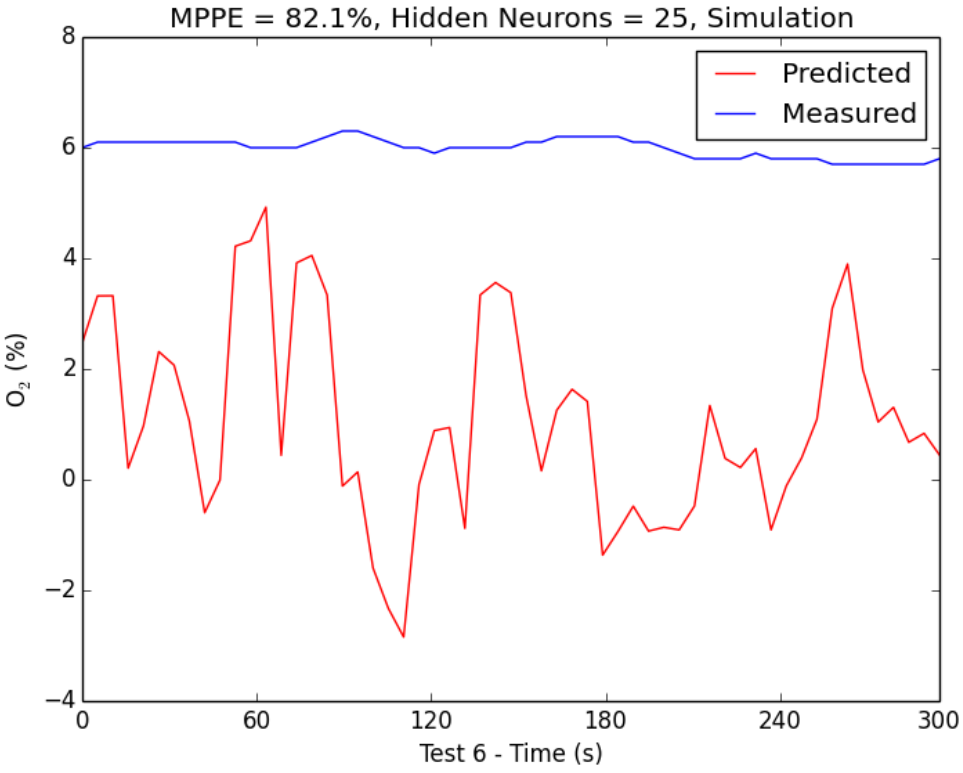

Figure 5.21: ANN prediction of O_2 - Validation - trained with RMS - 25 hidden neurons

ANN with 10 hidden neurons showed the best performance in the prediction of O_2 for this set of tests. What is clear from these results is that there is not enough information being presented to the neural network to be able to capture the completeness of the data and hence the coming sections will investigate the use of more complex signal processing.

5.2.2 PSD Based ANN Modelling

The PSD features generated from the CTF at IEn (Tests 1 to 9) while combusting 100 % coal (Table 3.7) were used for training ANNs in the second case study, similar to the ANN based on RMS (Section 5.2.1). Again the input variables were divided so that 75 % of the data was used for training with the remaining (25 %) being used to test the model, similar to previous Section 5.2.1, on ANN with RMS. Two separate networks were trained to estimate the excess O_2 level and NO_x emissions and the performance of the ANN was evaluated by MPPE on the "unseen" test - Test 6 not used for training.

Table 5.4: Comparison of performance of NO_x prediction results for ANN trained with PSD

Hidden Neurons	MPPE (%)	
	Training	Validation
10	1.9	33.9
12	2	37.4
15	1.7	24.4
20	1.8	37.3
25	2.2	70.7

Table 5.4 shows the NO_x prediction results for the various ANNs trained with different number of hidden neurons ranging between 10 to 25. The training and testing phase of the ANNs were carried out at least 5 times for each of the different number of hidden neurons being evaluated and the best performing network, based on the least MPPE was chosen. The input features used to train the ANNs were the PSD values of the three - UV, VIS and IR photodiode signals and the NO_x emissions recorded during the tests.

Figure 5.22 shows the NO_x prediction results of the best performing ANN with 15 hidden neurons, with a MPPE of 24.4 % for "unseen" data - Test 6.

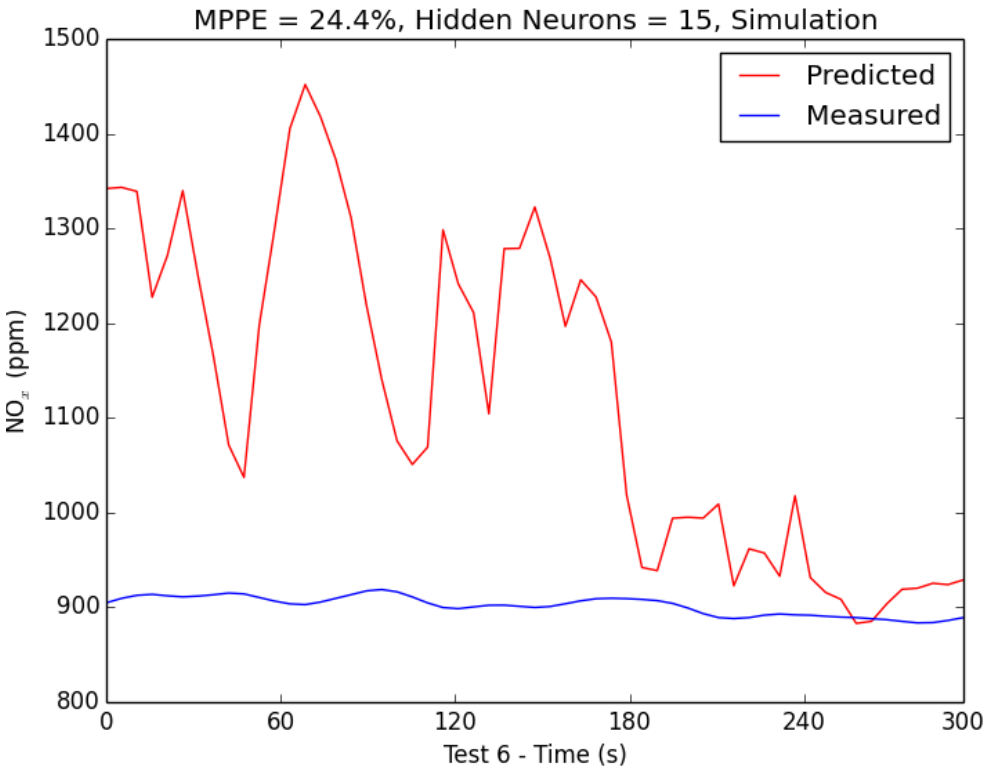

Figure 5.22: ANN prediction of NO_x - Validation - trained with PSD - 15 hidden neurons

Table 5.5: Comparison of performance of O_2 prediction results for ANN trained with PSD

Hidden Neurons	MPPE (%)	
	Training	Validation
10	3.6	24.5
12	3.5	57.2
15	3.3	81.4
20	3.8	86.9
25	3.7	44.2

Table 5.5 shows the O_2 prediction results for the various ANNs trained with different number of hidden neurons ranging between 10 to 25. The input features used to train the ANNs were the PSD values of the three - UV, VIS and IR photodiode signals and the O_2 recorded in the stack during the tests. Figure 5.23 shows the O_2 prediction results of the best performing ANN with 10 hidden neurons, with a MPPE of 24.5 % for "unseen" data - Test 6.

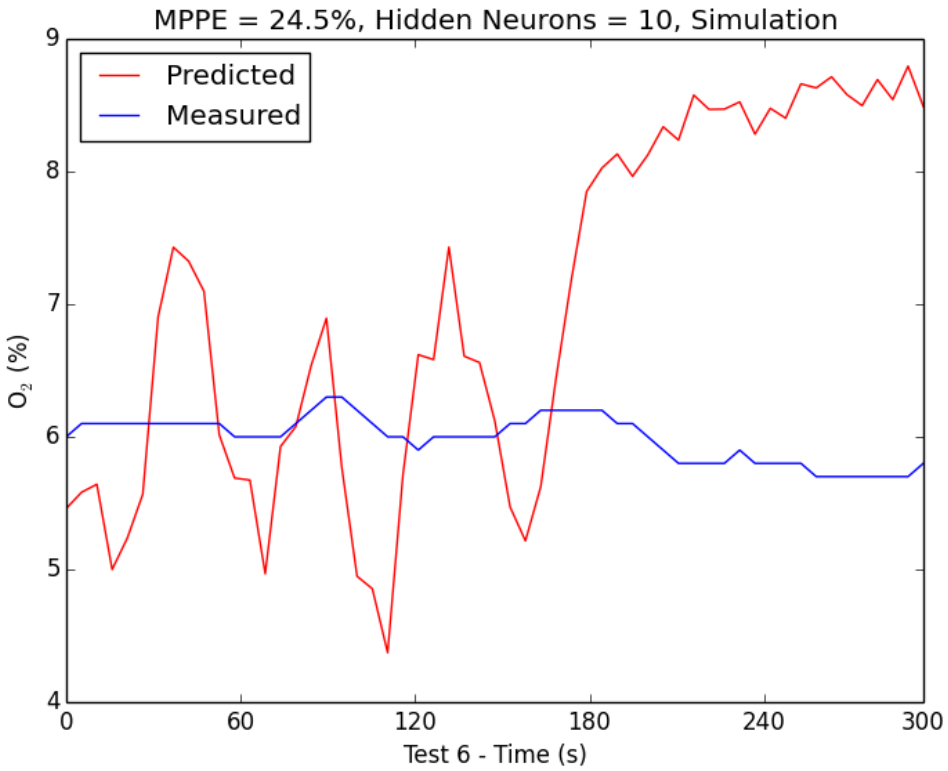

Figure 5.23: ANN prediction of O_2 - Validation - trained with PSD - 10 hidden neurons

5.2.3 Wavelet Coefficients Based ANN Modelling

The wavelet coefficients generated from the CTF at IEn (Tests 1 to 9) while combusting 100 % coal (Table 3.7) were used for training ANNs in the third case study, similar to the ANN based on RMS (Section 5.2.1). Again the input variables were divided so that 75 % of the data was used for training with the remaining (25 %) being used to test the model, similar to previous Section 5.2.1, on ANN with RMS. Two separate networks were trained to estimate the excess O_2 levels and NO_x emissions and the performance of the ANN was evaluated by MPPE on the "unseen" test - Test 6 not used for training.

Table 5.6: Comparison of performance of NO_x prediction results for ANN trained with Wavelet coefficients

Hidden Neurons	MPPE (%)	
	Training	Validation
10	1.9	32.3
12	1.7	21.4
15	1.7	31.7
20	1.7	32.8
25	1.7	18.1

Table 5.6 shows the NO_x prediction results for the various ANNs trained with different number of hidden neurons ranging between 10 to 25. The training

and testing phase of the ANNs were carried out at least 5 times for each of the different number of hidden neurons being evaluated and the best performing network, based on the least MPPE was chosen. The input features used to train the ANNs were the RMS of the best wavelet coefficients of the three - UV, VIS and IR photodiode signals and the NO_x emissions recorded during the tests.

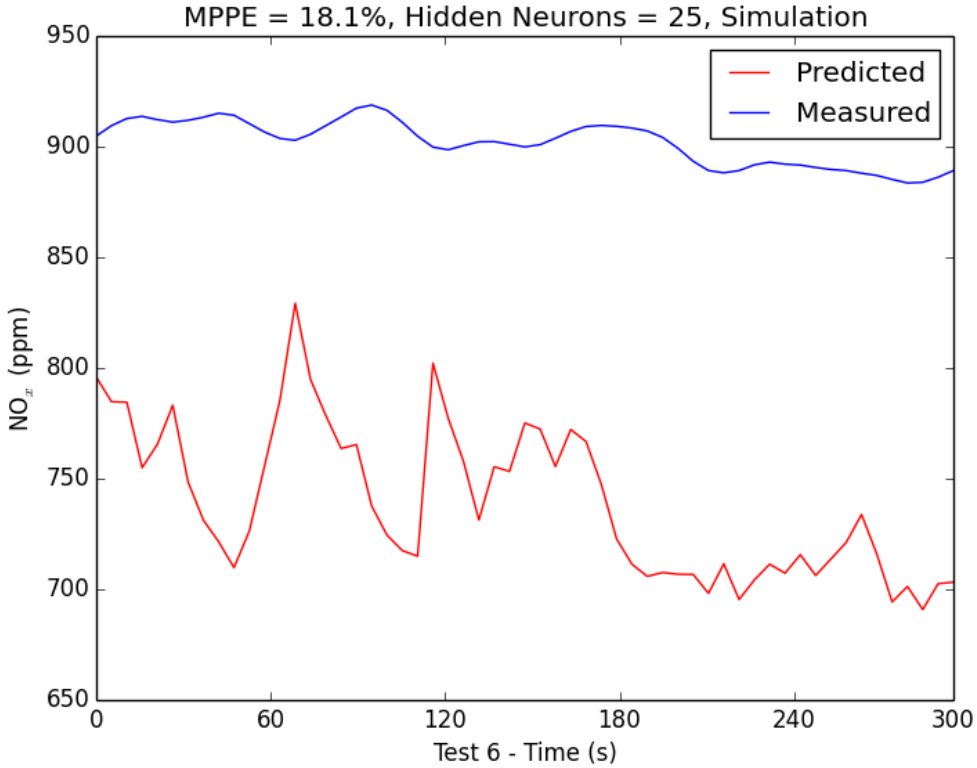

Figure 5.24: ANN prediction of NO_x - Validation - trained with wavelet coefficients - 25 hidden neurons

Figure 5.24 shows the NO_x prediction results of the best performing ANN with 25 hidden neurons, with a MPPE of 18.1 % for "unseen" data - Test 6.

Table 5.7: Comparison of performance of O_2 prediction results for ANN trained with Wavelet coefficients

Hidden Neurons	MPPE (%)	
	Training	Validation
10	3.4	43.1
12	3.4	46.2
15	3.5	24.3
20	3.5	63
25	3.5	37.8

Table 5.7 shows the O_2 prediction results for the various ANNs trained with different number of hidden neurons ranging between 10 to 25. The input features used to train the ANNs were the RMS of the best wavelet coefficients of the three - UV, VIS and IR photodiode signals and the O_2 recorded in the stack during the

tests. Figure 5.25 shows the O_2 prediction results of the best performing ANN with 15 hidden neurons, with a MPPE of 24.3 % for "unseen" data - Test 6.

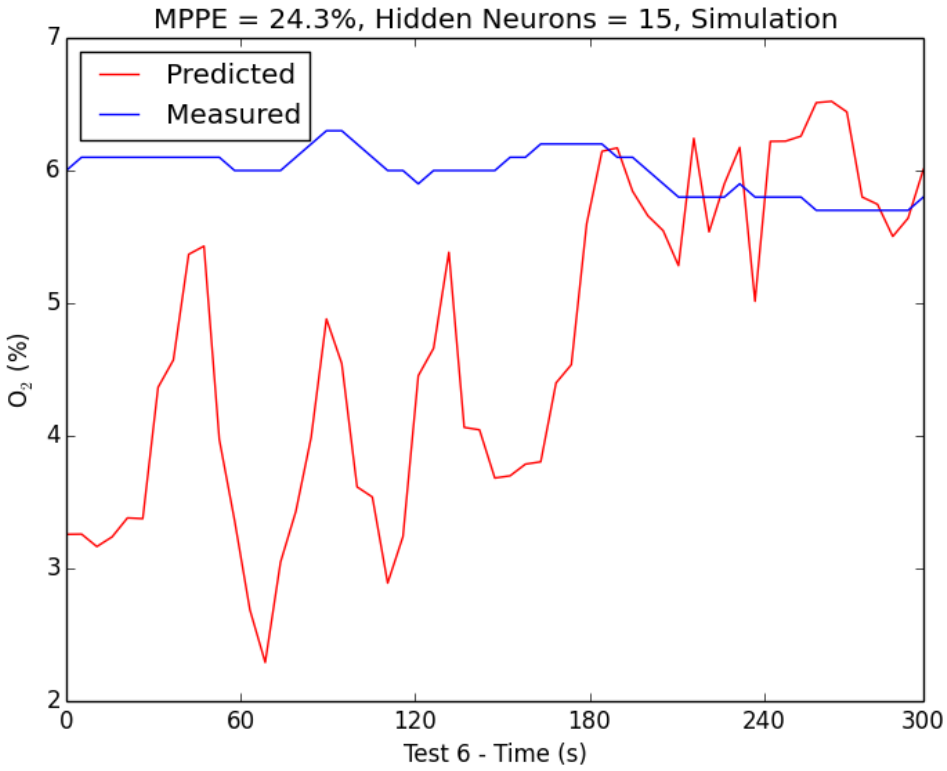

Figure 5.25: ANN prediction of O_2 - Validation - trained with PSD - 15 hidden neurons

5.2.4 Review of Back Propagation ANN Based Results

The neural network training results of the three case studies Sections 5.2.1 to 5.2.3 using three different signal processing algorithms for predicting the excess O_2 levels and NO_x emissions are presented in Tables 5.2 to 5.7. It could be observed that the NO_x predictions were the least inaccurate, especially case study 1 where only RMS of the three photodiode signals were used. The excess O_2 predictions were not very consistent and had huge MPPEs variations between the various ANN models with varying hidden neurons and input features. Hence a fourth case study was planned to consider the implications of using more input features to the ANN models, to check if the model could better generalise with additional information with the disadvantage of increasing the calculation times, especially for training the networks.

The input features used previously (Sections 5.2.1 to 5.2.3), namely the RMS, PSD and RMS of the best wavelet coefficients generated from the CTF at IEn (Tests 1 to 9) while combusting 100 % coal (Table 3.7) were used for training ANNs in the fourth case study. Again the input variables were divided so that 75 % of the data was used for training with the remaining (25 %) being used to test the model, similar to previous case studies. Two separate networks were trained to estimate the excess O_2 levels and NO_x emissions and the performance

Table 5.8: Additional case studies to evaluate varying the input features to be applied to train an ANN

Case Study	Number of features	Input features
4	9	RMS, PSD and RMS of the best wavelet coefficient of UV, VIS and IR sensors

of the ANN was evaluated by MPPE on the "unseen" test - Test 6 not used for training.

Table 5.9: Comparison of performance of NO_x prediction results for ANN trained with RMS, PSD & Wavelet coefficients

Hidden Neurons	MPPE (%)	
	Training	Validation
10	1.2	21.5
12	1.1	33
15	1.3	27.5
20	1.2	19.7
25	1.5	55.6

Table 5.9 shows the NO_x prediction results for the various ANNs trained with different number of hidden neurons ranging between 10 to 25. The training and testing phase of the ANNs were carried out at least 5 times for each of the different number of hidden neurons being evaluated and the best performing network, based on the least MPPE was chosen. The input features used to train the ANNs were the RMS, PSD and RMS of the best wavelet coefficients of the three - UV, VIS and IR photodiode signals and the NO_x emissions recorded during the tests.

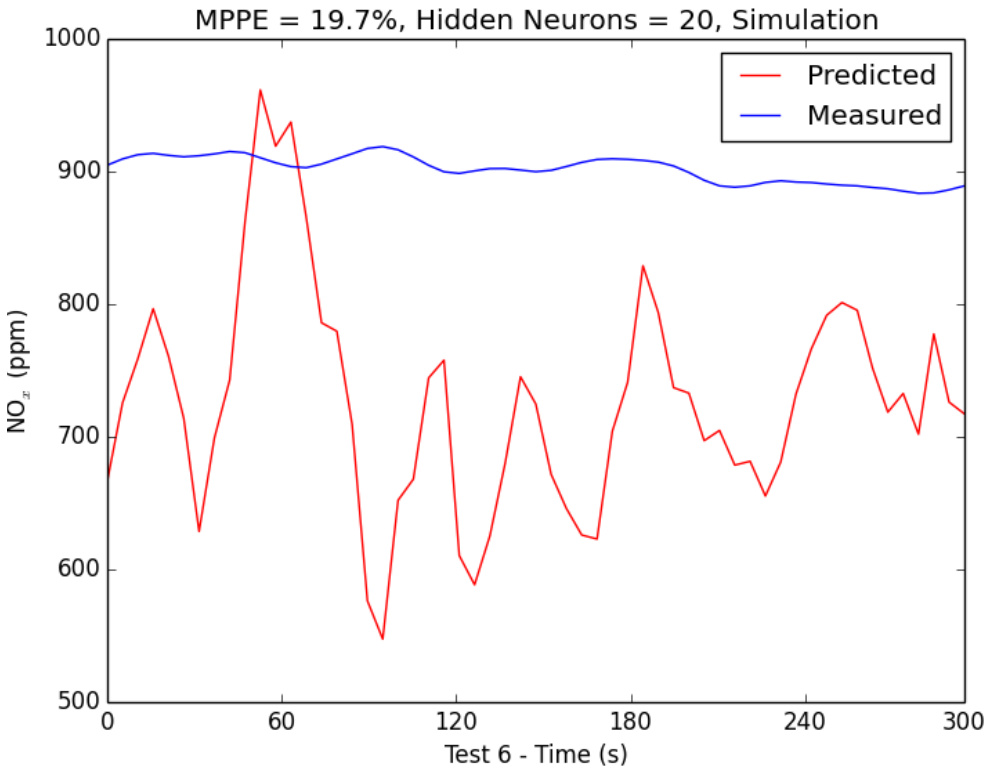

Figure 5.26: ANN prediction of NO_x - Validation - trained with RMS, PSD and RMS of the best wavelet coefficients - 20 hidden neurons

Figure 5.26 shows the NO_x prediction results of the best performing ANN with 20 hidden neurons, with a MPPE of 19.7 % for "unseen" data - Test 6.

Table 5.10: Comparison of performance of O_2 prediction results for ANN trained with RMS, PSD & Wavelet coefficients

Hidden Neurons	MPPE (%)	
	Training	Validation
10	3.5	28.3
12	2.8	36
15	2.7	57.7
20	3	27.2
25	3	24.6

Table 5.10 shows the O_2 prediction results for the various ANNs trained with different number of hidden neurons ranging between 10 to 25. The input features used to train the ANNs were the RMS, PSD and RMS of the best wavelet coefficients of the three - UV, VIS and IR photodiode signals and the O_2 recorded in the stack during the tests. Figure 5.27 shows the O_2 prediction results of the best performing ANN with 25 hidden neurons, with a MPPE of 24.6 % for "unseen" data - Test 6.

The results from case study four showed that the application of RMS, PSD and RMS of the best wavelet coefficient of the UV, VIS and IR sensors as input features to the ANN models being trained generally improved prediction

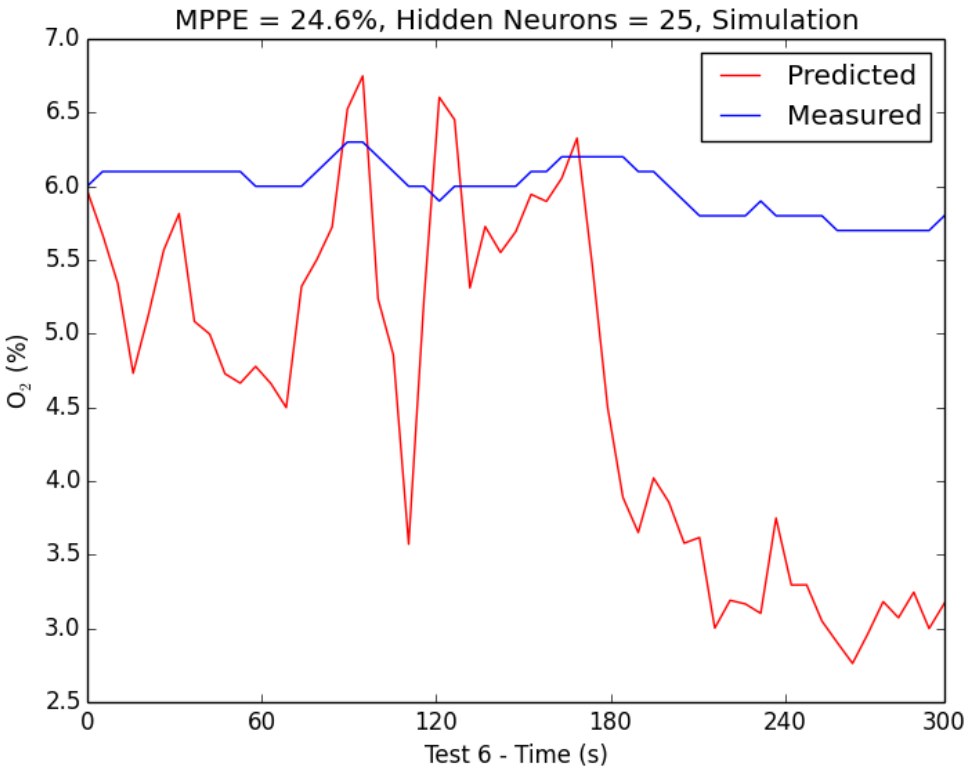

Figure 5.27: ANN prediction of O_2 - Validation - trained with RMS, PSD and RMS of the best wavelet coefficients - 25 hidden neurons

compared to individually using those signal processing features. The exception being some of the RMS results, especially for NO_x (with 3 input features) being better than the case study four results. Since only a small subset of experiments were tried so far, additional case studies were planned to evaluate the other experiments as described in Section 5.

5.2.5 Further Evaluation of ANN Based Prediction

In case studies 1 to 4 the performance of a back propagation ANN with a varying number of input features from various signal processing methods were applied to a smaller subset of experiments. Since the performance of the ANN with 9 input features (with the three signal processing methods from the three sensor data) was acceptable, the case studies were extended to include all the experiments except for the ones with 30 % biomass. The additional case studies carried out are shown in Table 5.11.

Table 5.11: Additional case study to evaluate larger number of input tests to train the ANN

Case study	Number of features	Input features	Training tests	Validation tests
5	9	RMS, PSD and RMS of the best wavelet coefficient of UV, VIS and IR sensors	1 to 9, 19 to 54 & 64 to 90	10 to 18

Table 5.12: Comparison of performance of NO_x prediction results for ANN trained with RMS, PSD & Wavelet coefficients

Hidden Neurons	MPPE (%)	
	Training	Validation
10	4.6	10.6
12	4.3	9.19
15	3.9	10.3
20	3.3	9.36
25	3.1	10

Table 5.12 shows the NO_x prediction results for case study 5 (Table 5.11) for the various ANNs trained with different number of hidden neurons ranging between 10 to 25. The training and testing phase of the ANNs were carried out at least 5 times for each of the different number of hidden neurons being evaluated and the best performing network, based on the least MPPE was chosen. As before in case study 4, the input features were the same - RMS, PSD and RMS of the best wavelet coefficients of the three photodiodes.

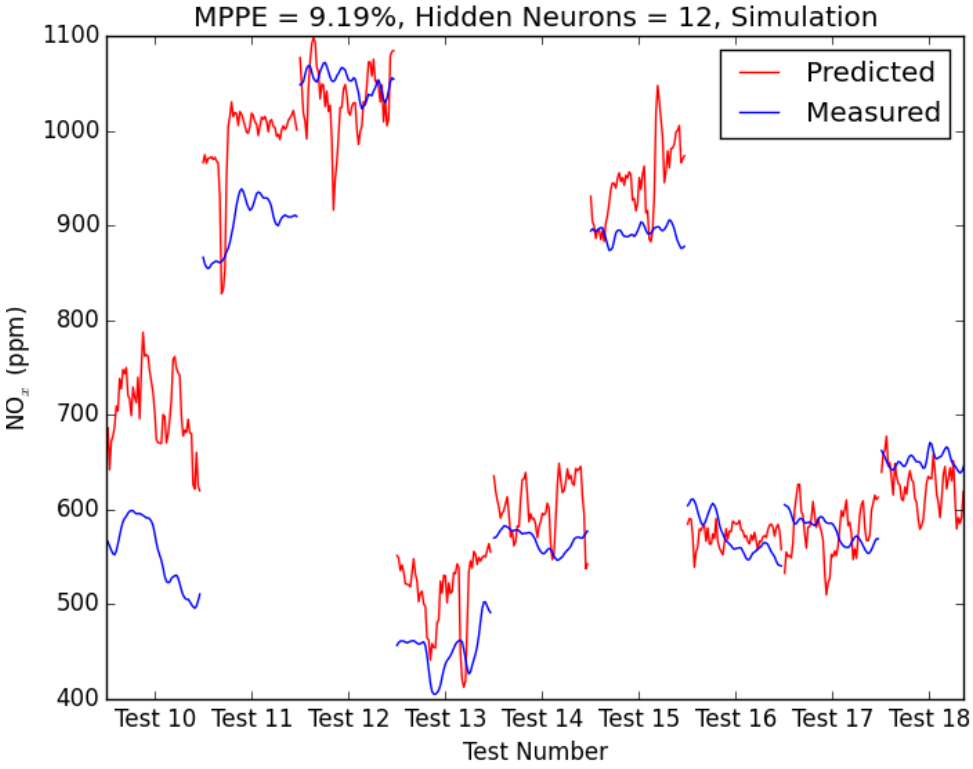

Figure 5.28: ANN prediction of NO_x - Validation - trained with RMS, PSD and RMS of the best wavelet coefficients - 12 hidden neurons

Figure 5.28 shows the NO_x prediction results of the best performing ANN with 12 hidden neurons, with a MPPE of 9.19 % for "unseen" data - Tests 10 to 18. The experiments used to train this network were Tests 1 to 9, 19 to 54 and 64 to 90. The prediction MPPE has improved compared to 19.7 % seen for case

study 4 (figure 5.26), but the prediction for low excess air conditions, especially Test 10 is over predicted by a margin of more than 10 %.

Table 5.13: Comparison of performance of O_2 prediction results for ANN trained with RMS, PSD & Wavelet coefficients

Hidden Neurons	MPPE (%)	
	Training	Validation
10	12	26.1
12	10	33.8
15	9.8	27.6
20	8	26.8
25	8.3	34.3

Table 5.13 shows the O_2 prediction results for the various ANNs trained with different numbers of hidden neurons ranging between 10 to 25. The input features are similar to the NO_x networks shown in Table 5.12, except for measured O_2 being used instead of NO_x.

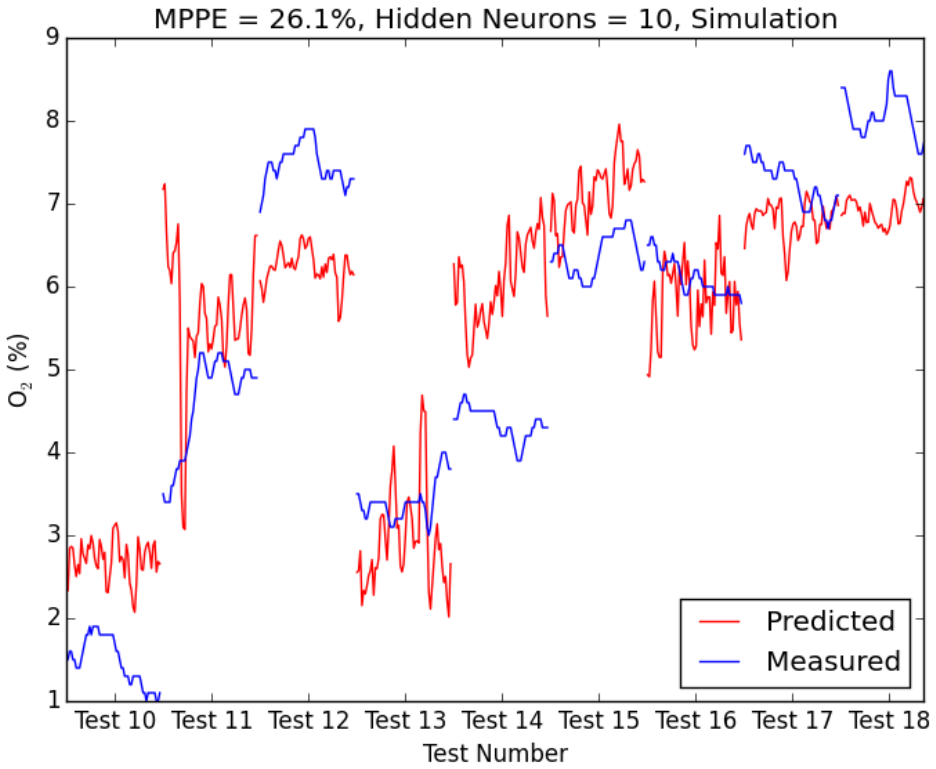

Figure 5.29: ANN prediction of O_2 - Validation - trained with RMS, PSD and RMS of the best wavelet coefficients - 10 hidden neurons

Figure 5.29 shows the O_2 prediction result of the best performing ANN with 10 hidden neurons, with a MPPE of 26.1 % for "unseen" data - Tests 10 to 18. The experiments used to train this network were Tests 1 to 9, 19 to 54 and 64 to 90. The O_2 prediction MPPE hasn't improved, unlike NO_x predictions seen for case study 4 and especially some Tests 10, 12 and 14 are over predicted by a margin of more than 10 %.

Some improvements, especially in NO_x prediction can be seen in case study 5 compared to case study 4, by increasing the number of tests being used to train the system but with the draw back of increased training and testing time. Yu *et al.* have demonstrated the features with the greatest relevance from the data could be obtained by applying Principal Component Analysis (PCA) for monitoring the flame [65, 122] (Section 2.7.2). PCA is an orthogonal transform of the input data data, which reduces the dimension of the input vector. So case study 6 and 7 were carried out to see if the application of PCA would eliminate some redundant / highly correlated inputs and hence reduce the training and testing time with the increased number of input tests. PCA was applied in these case studies to eliminate those principal components that contribute to less than 2 % to the total variation in the input dataset.

Table 5.14: Additional case studies to evaluate application of PCA

Case study	Number of features	Input features	Training tests	Validation tests
6	2(PCA)	RMS, PSD and RMS of the best wavelet coefficient of UV, VIS and IR sensors	1 to 5 & 7 to 9	6
7			1 to 9, 19 to 54 & 64 to 90	10 to 18

Table 5.15: Comparison of performance of NO_x prediction results for ANN trained with RMS, PSD & Wavelet coefficients together with PCA

Hidden Neurons	MPPE (%)	
	Training	Validation
10	2.3	6.46
12	2.1	15.7
15	2	18.2
20	2	27.4
25	2	36.3

Table 5.15 shows the NO_x prediction results for case study 6 (Table 5.14) for the various ANNs trained with different number of hidden neurons ranging between 10 to 25, with the application of PCA to reduce the dimensionality of the input to train the ANN. The training and testing phase of the ANNs were carried out at least 5 times for each of the different number of hidden neurons being evaluated and the best performing network, based on the least MPPE was chosen. As before in case study 4, the input features were the same - RMS, PSD and RMS of the best wavelet coefficients of the three photodiodes, except for the application of PCA. The input to the ANNs for training were Test 1 to 5 and 7 to 9 and Test 6 was utilised to test the performance of the trained model (test not present for training the network).

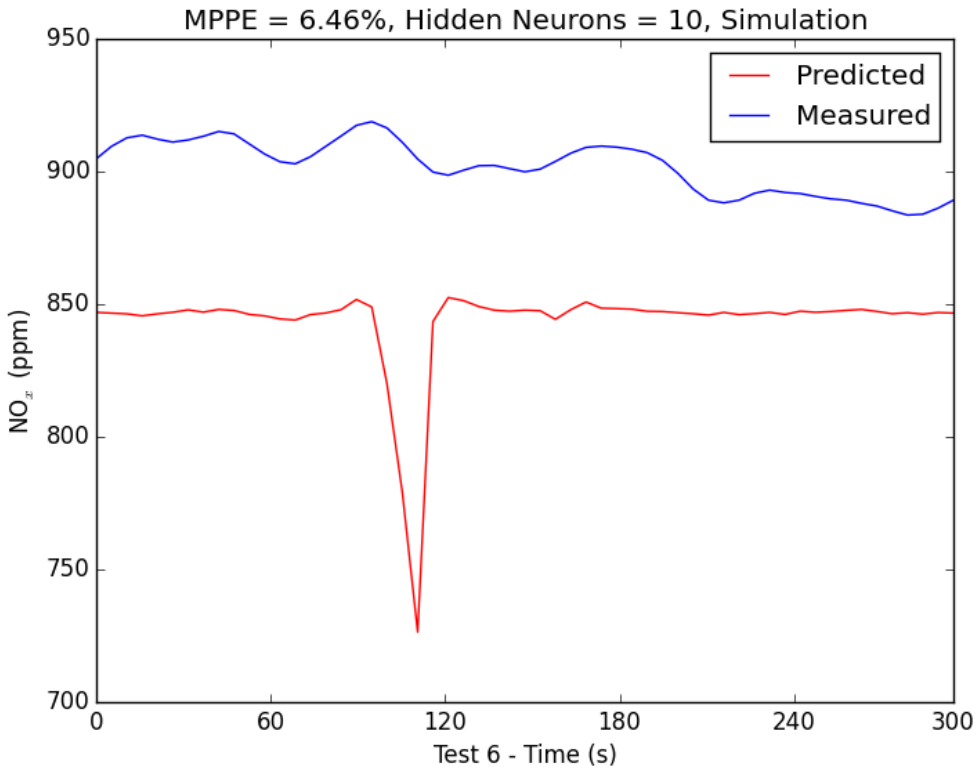

Figure 5.30: ANN prediction of NO_x - Validation - trained with RMS, PSD and RMS of the best wavelet coefficients with PCA - 10 hidden neurons

Figure 5.30 shows the NO_x prediction results of the best performing ANN with 10 hidden neurons, with a MPPE of 6.46 % for "unseen" data - Test 6. The experiments used to train this network were Tests 1 to 5 and 7 to 9. The prediction MPPE has improved compared to 19.7 % seen for case study 4 (figure 5.26) for the same number of input tests.

Table 5.16: Comparison of performance of O_2 prediction results for ANN trained with RMS, PSD & Wavelet coefficients together with PCA

Hidden Neurons	MPPE (%)	
	Training	Validation
10	4.3	33.4
12	4.5	23.4
15	4.1	41.5
20	4.4	48
25	4.2	21.1

Table 5.16 shows the O_2 prediction results for case study 6 (Table 5.14) for the various ANNs trained with different number of hidden neurons ranging between 10 to 25, with the application of PCA to reduce the dimensionality of the input to train the ANN. The training and testing phase of the ANNs were carried out at least 5 times for each of the different number of hidden neurons being evaluated and the best performing network, based on the least MPPE was chosen. As before in case study 4, the input features were the same - RMS, PSD

and RMS of the best wavelet coefficients of the three photodiodes, except for the application of PCA. The input to the ANNs for training were Test 1 to 5 and 7 to 9 and Test 6 was utilised to test the performance of the trained model (test not present for training the network).

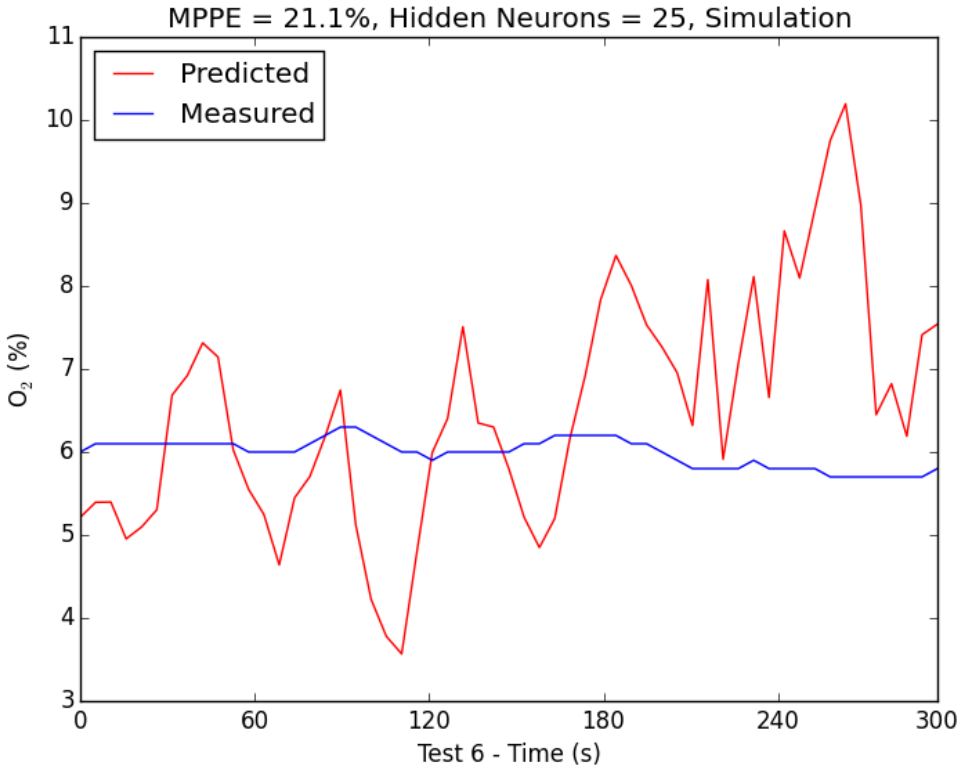

Figure 5.31: ANN prediction of O_2 - Validation - trained with RMS, PSD and RMS of the best wavelet coefficients with PCA - 25 hidden neurons

Figure 5.31 shows the O_2 prediction results of the best performing ANN with 25 hidden neurons, with a MPPE of 21.1 % for "unseen" data - Test 6. The experiments used to train this network were Tests 1 to 5 and 7 to 9. The prediction MPPE has improved compared to 24.6 % seen for case study 4 (figure 5.27) for the same number of input tests.

Table 5.17: Comparison of performance of NO_x prediction results for ANN trained with RMS, PSD & Wavelet coefficients together with PCA

Hidden Neurons	MPPE (%)	
	Training	Validation
10	8.3	20.4
12	8.1	21
15	8.2	21.4
20	7.7	21.3
25	6.9	20.9

Table 5.17 shows the NO_x prediction results for case study 7 (Table 5.14) for the various ANNs trained with different number of hidden neurons ranging

between 10 to 25, with the application of PCA to reduce the dimensionality of the input to train the ANN. The training and testing phase of the ANNs were carried out at least 5 times for each of the different number of hidden neurons being evaluated and the best performing network, based on the least MPPE was chosen. As before in case study 5, the input features were the same - RMS, PSD and RMS of the best wavelet coefficients of the three photodiodes, except for the application of PCA. The input to the ANNs for training were Test 1 to 9, 19 to 54 and 64 to 90 and Tests 10 to 18 were utilised to test the performance of the trained model (these tests not presented for training the network).

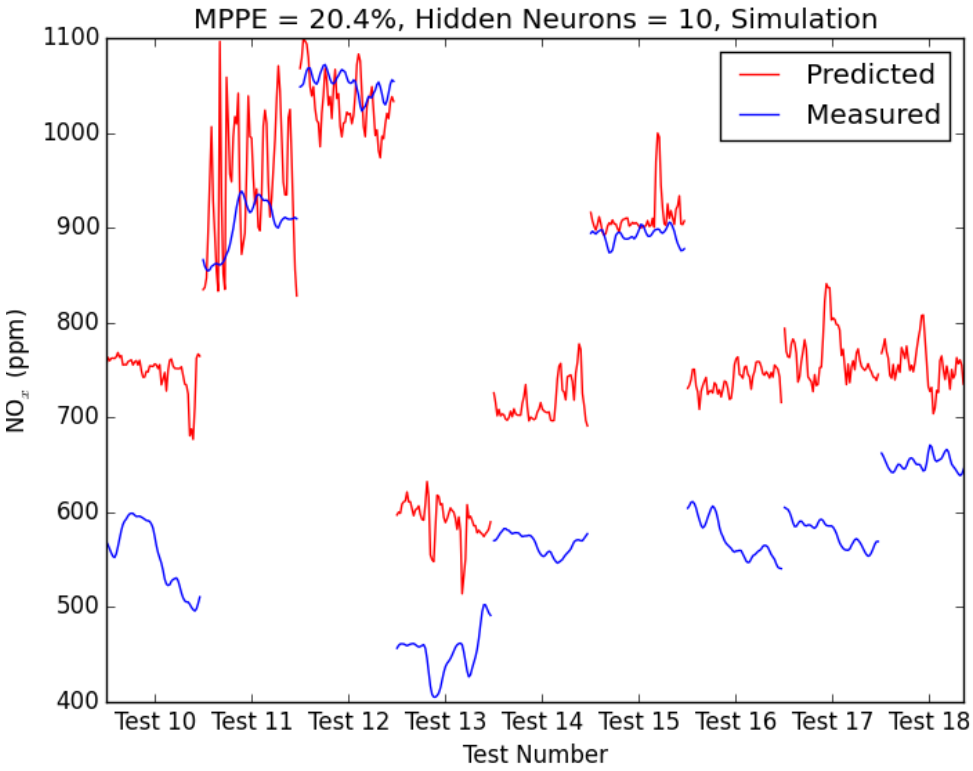

Figure 5.32: ANN prediction of NO_x - Validation - trained with RMS, PSD and RMS of the best wavelet coefficients with PCA - 10 hidden neurons

Figure 5.32 shows the NO_x prediction results of the best performing ANN with 10 hidden neurons, with a MPPE of 20.4 % for "unseen" data - Tests 10 to 18. The prediction MPPE has improved compared to case study 6 with increased number of training inputs to the ANN (from 8 to 72 tests) but has increased compared to 9.19 % seen for case study 5 (figure 5.28) for the same number of input tests. This means a poorer prediction result with the application of PCA, which points to some useful information in some of the inputs being stripped by the application of PCA.

Table 5.18 shows the O_2 prediction results for case study 7 (Table 5.14) for the various ANNs trained with different number of hidden neurons ranging between 10 to 25, with the application of PCA to reduce the dimensionality of the input to train the ANN. The training and testing phase of the ANNs were carried out at least 5 times for each of the different number of hidden neurons being evaluated and the best performing network, based on the least MPPE was chosen. As before in case study 4, the input features were the same - RMS, PSD

Table 5.18: Comparison of performance of O_2 prediction results for ANN trained with RMS, PSD & Wavelet coefficients together with PCA

Hidden Neurons	MPPE (%)	
	Training	Validation
10	23	23.2
12	22	20.5
15	21	24.3
20	18	27.4
25	17	24.2

and RMS of the best wavelet coefficients of the three photodiodes, except for the application of PCA. The input to the ANNs for training were Test 1 to 9, 19 to 54 and 64 to 90 and Tests 10 to 18 were utilised to test the performance of the trained model (these tests not presented for training the network).

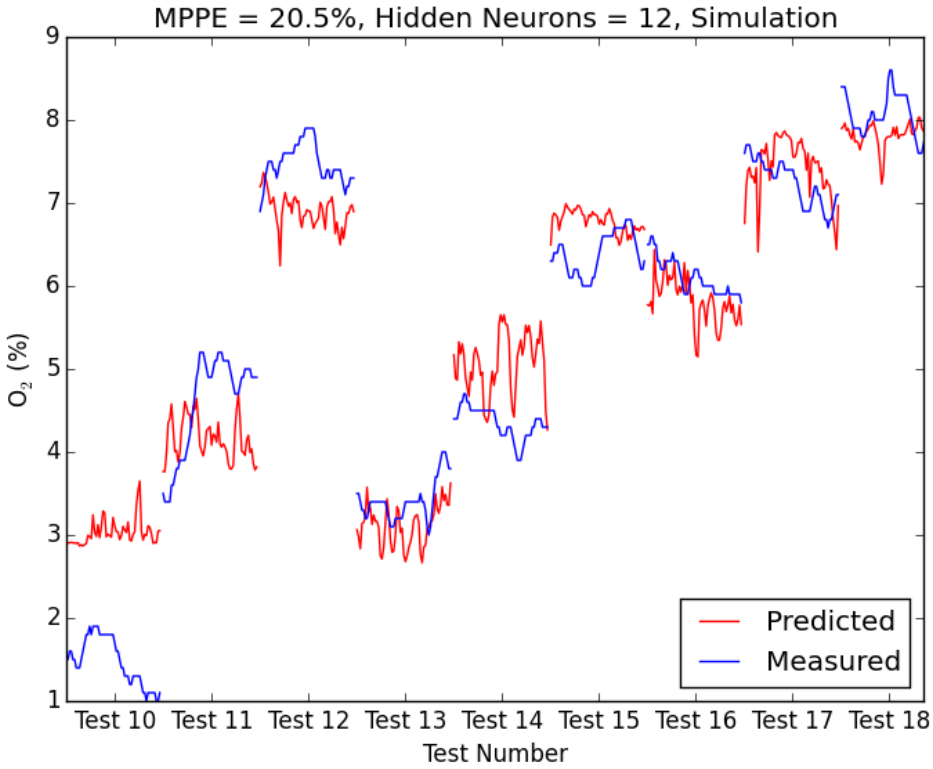

Figure 5.33: ANN prediction of O_2 - Validation - trained with RMS, PSD and RMS of the best wavelet coefficients with PCA - 12 hidden neurons

Figure 5.33 shows the O_2 prediction results of the best performing ANN with 12 hidden neurons, with a MPPE of 20.5 % for "unseen" data - Tests 10 to 18. The prediction MPPE has improved compared to 26.1 % seen for case study 5 (figure 5.29) for the same number of input tests but deteriorated compared to 21.1 % observed for case study 6 when the number of tests used for the training phase was increased. This points to the generalisation capability of the model decreasing with many inputs being used to train the network. Overall, with the application of PCA the prediction accuracy has dropped for NO_x and marginally

increased for O_2. The slight improvement in O_2 prediction has to be taken with caution for the application as there has been significant unmetered leakage through observation ports and increased purge air percentage at low thermal loads, and hence the O_2 recorded may not be very reliable to train ANNs for flame stability. So total airflow to the burner was considered, as the the primary and secondary air to the burner were continuously recorded at the CTF as part of the plant control system. Two additional case studies - 8 and 9 (Table 5.19) were carried out to check the viability of total airflow prediction instead of prediction O_2.

Table 5.19: Additional case studies to evaluate total airflow predictions

Case study	Number of features	Input features	Training tests	Validation tests
8	9	RMS, PSD and RMS of the best wavelet coefficient of UV, VIS and IR sensors	1 to 5 & 7 to 9	6
9			1 to 9, 19 to 54 & 64 to 90	10 to 18

Table 5.20: Comparison of performance of total airflow prediction results for ANN trained with RMS, PSD & Wavelet coefficients

Hidden Neurons	MPPE (%)	
	Training	Validation
10	0.48	1.69
12	0.54	1.6
15	0.58	8.39
20	0.72	8.94
25	0.72	9.3

Table 5.20 shows the total airflow prediction results for case study 8 (Table 5.19) for the various ANNs trained with different number of hidden neurons ranging between 10 to 25. The training and testing phase of the ANNs were carried out at least 5 times for each of the different number of hidden neurons being evaluated and the best performing network, based on the least MPPE was chosen. As before in case study 4, the input features were the same - RMS, PSD and RMS of the best wavelet coefficients of the three photodiodes. The input to the ANNs for training were Tests 1 to 5 and 7 to 9 and Test 6 was utilised to test the performance of the trained model (test not presented for training the network).

Figure 5.34 shows the total airflow prediction result of the best performing ANN with 12 hidden neurons, with a MPPE of 1.6 % for "unseen" data - Test 6. The prediction MPPE has vastly improved compared to 24.6 % seen for case study 4 (figure 5.27) for the same number of input tests and 21.1 % for case

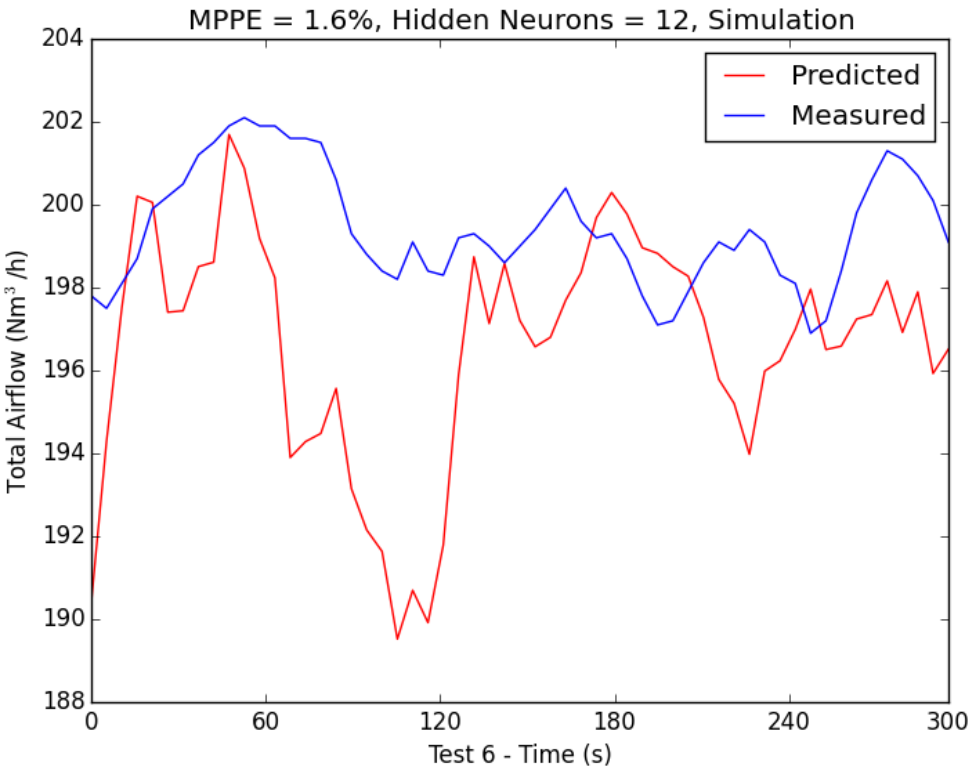

Figure 5.34: ANN prediction of total airflow - Validation - trained with RMS, PSD and RMS of the best wavelet coefficients with PCA - 12 hidden neurons

study 6 with the application of PCA to eliminate redundant inputs that don't contribute very much to the entire input variation.

Table 5.21: Comparison of performance of total airflow prediction results for ANN trained with RMS, PSD & Wavelet coefficients

Hidden Neurons	MPPE (%)	
	Training	Validation
10	2.3	5.81
12	2.2	6.14
15	2.1	6.03
20	1.8	5.68
25	1.7	5.31

Table 5.21 shows the total airflow prediction results for case study 9 (Table 5.19) for the various ANNs trained with different number of hidden neurons ranging between 10 to 25. The training and testing phase of the ANNs were carried out at least 5 times for each of the different number of hidden neurons being evaluated and the best performing network, based on the least MPPE was chosen. As before in case study 5, the input features were the same - RMS, PSD and RMS of the best wavelet coefficients of the three photodiodes. The input to the ANNs for training were Tests 1 to 9, 19 to 54 and 64 to 90 and Tests 10 to 18 were utilised to test the performance of the trained model (these tests not presented for training the network).

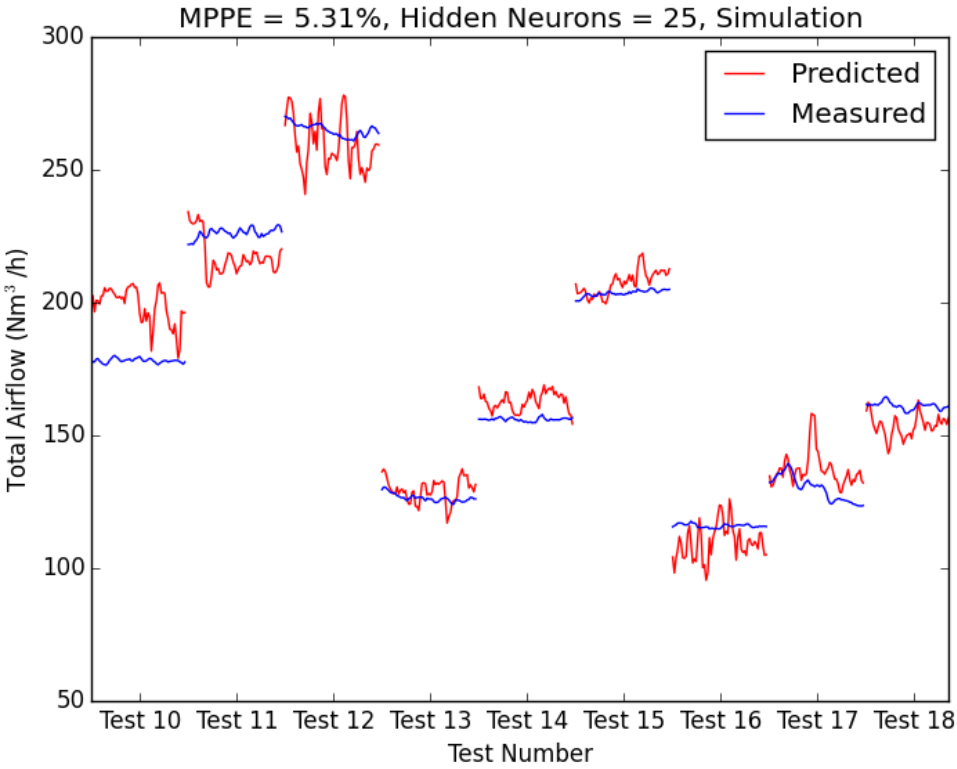

Figure 5.35: ANN prediction of total airflow - Validation - trained with RMS, PSD and RMS of the best wavelet coefficients with PCA - 25 hidden neurons

Figure 5.35 shows the total airflow prediction result of the best performing ANN with 25 hidden neurons, with a MPPE of 5.31 % for "unseen" data - Tests 10

to 18. The prediction MPPE has deteriorated with increased number of input tests used for training the network compared to case study 8.

The neural network modelling has so far been carried out to predict O_2 in the stack, NO_x emissions in the stack and total airflow to the burner. The neural network modelling until now seems to be producing better predictions for NO_x and total airflow to the burner than oxygen. This can be explained by the significant amount of excess purge air in the system, which was used for cooling of the lens assembly and to avoid accumulation of dust on the lens (the same purge air amounts were used for all thermal loads, leading to higher dilution with lower thermal load as well). The oxygen concentration measured by the flue gas analyser at two different locations did not represent the actual level of excess air participating in the combustion process. Furthermore, fluctuations of oxygen were more evident than the measured airflow as can be seen in figures 5.29 and 5.35.

5.2.6 Evaluation of Other Methods for Flame Stability Detection

Until now prediction of NO_x and O_2 with the use of processed data from the three sensors applied to a trained ANN formed the basis for prediction of the stability of the flame. This so far has yielded some results, but then the percentage error seems to increase with increases in the number of test conditions used and especially unseen data. This can potentially impact the prediction accuracy while being used online for flame stability as the coal, even from the same mine can have slight variations over the day in huge power plants as they tend to combust tonnes of coal. Also the prediction is relative and not the absolute values of NO_x or O_2 and also depends on the accuracy of the measurement devices used while training the neural network. In this case the O_2 measurements may not accurately identify the combustion conditions at the end of the combustion chamber as there was a lot of air ingress around the monitoring ports and side viewing panel; and also the cooling & purge air contributing a much higher percentage to this while having low thermal loads compared to higher thermals loads due to the amount of carrier / primary and secondary air being fed to the burner.

It was felt that a different type of signal processing and / or ANN needed to be evaluated to identify changes to flame stability instead of the focus on prediction of NO_x, O_2 or air flow rates. This was also considered due to the time taken for training feed-forward ANNs with BR with multiple signal processing inputs from the three sensors, which might affect the usability of such a system for running online for control actions to be suggested.

5.3 Self-organising Map

Self-organising Map (SOM) have been applied widely for identification or monitoring of complex processes, where the data has been difficult to interpret or visualise relationships. SOM's can smoothly map data with high-dimensional input to lower dimensional outputs, this clusters the input information and makes

it easy to map the input relationships [176]. SOM could be utilized to classify the condition of the flame based on the sensor data and to do corrective actions to achieve a good combustion state of the burner.

5.3.1 WVD Preliminary Analysis

Wigner-Ville Distribution (WVD) maps a time variant signal to the two dimensions of time and frequency, with the same resolution in both domains Section 4.3.2. As initially ascertained using FFT (Section 4.2), there weren't much recognisable trends with changes in combustion conditions like change in secondary air.

WVD was applied for the various conditions as explained in Section 4.3.2. WVD has the best resolution in both time and frequency domain compared to other Cohen's class time frequency methods [143], even though it could produce cross correlation features between the various frequencies present (results are very similar to Gabor – 0 order, as the order increases, resolution drops away and starts moving away from WVD results in terms of resolution). The results, especially when they are averaged over a short period of time, such as between 3 to 30 s, visualises the results which aided in detecting trends.

Once the continuously varying air flow experiments – Tests 91 to 99 (Tables 3.8 and 3.9) were processed, a very clear trend of varying intensity and frequency spread could be noticed in these experiments. Again, these changes are not proportional to the changes in air flow and also have similar output for different air flow and thermal load conditions. This time instead of applying a supervised ANN, an unsupervised one was tried to see if it classified the condition instead of trying to predict absolute NO_x, CO or air flow.

5.3.2 WVD Result Analysis for Experiments with Varying Secondary Air

This sort of processing was felt would be of particular benefit in detecting flame instability problems and by inference the same technique would be of benefit in classifying normal burner operation. Therefore this Section will focus on only the flame stability tests. As the 500 kW CTF had quartz viewing windows on the entire length of the combustion chamber, it was possible to image the flame under various conditions although as is normal with the combustion of coal and biomass these windows became quickly covered by fly ash, significantly worsening the visibility. As an example, selected frames from Test 98 (flame instability test) are presented in figures 5.36 – 5.38. Figure 5.36 shows a flame for "normal" conditions (secondary air flow – 160 Nm^3/h). The flame is stable and attached to the burner. When the secondary air flow was decreased down to 50 Nm^3/h, the flame lengthened, and became unstable and distanced from the burner, as shown in figure 5.37. After increasing the secondary air flow up to 280 Nm^3/h, the flame was much shorter and became very unstable, close to being blown-off, as shown in figure 5.38.

[———Flame length————————————————————————Burner

Figure 5.36: Test 98 – “normal conditions”, secondary air flow: 160 Nm^3/h

————Flame length————————————————————————] Burner

Figure 5.37: Test 98 – “decreased excess air”, secondary air flow: 50 Nm^3/h

[——Flame length–Burner

Figure 5.38: Test 98 – “increased excess air”, secondary air flow: 280 Nm^3/h

Figures 5.39, 5.42, 5.43, 5.46, 5.47 and 5.49 show the WVD output of the IR

sensor signal from six experiments (Table 3.9). Similarly, figures 5.40, 5.42, 5.44, 5.46, 5.48 and 5.50 show the recorded NO_x and CO emissions in parts per million (ppm) as well as the total air flow (in Nm^3/h) to the CTF, for the respective WVD output results (Figures 5.39, 5.42, 5.43, 5.46, 5.47 and 5.49). It can be noted that in figures 5.40, 5.42 and 5.44, the CO emissions towards the end of the test increases to 999, the saturation point of the sensor.

It could be observed that the energy of the IR signal in the range of 30 to 120 Hz increases as secondary air is decreased for the experiment shown in figure 5.39 using 100 % coal. The trend is exactly the same for the UV and VIS sensors for the same experiment, the results simply differing in the absolute intensity of the signals and these are presented in Appendix C.

The same trend of the IR sensor signal could be noted in the other two experiments, in figures 5.42 and 5.43, where the fuel composition was altered by adding 10 % and 20 % biomass to the coal by weight respectively while decreasing secondary air to the combustion chamber. Even though the outputs are quite similar, the variation is not linear nor does it increase or decrease proportionally to the secondary air flow or fuel composition.

Figures 5.39 to 5.44 illustrate the WVD results and the respective NO_x, CO emissions and the total air flow to the combustion chamber when secondary air is being decreased for differing biomass content. The following figures 5.46 to 5.50 illustrate the results and recorded data when secondary air flow is being increased from stable combustion. As previously encountered in decreasing excess air, the flame remains stable for a longer time with 100 % coal compared to 10 % and 20 % biomass substituted coal.

Figure 5.47 though quite devoid of very distinguishable features compared to other WVD results, it does contain information which is not easily viewable at the current colour map settings. The reason to use the same colour map settings across all WVD results (for each sensor) is to easily distinguish intensity changes in the flames from one test relative to another, which wouldn't be possible to compare if different scales are employed.

Similar WVD analysis was carried out on the VIS and UV spectral data. These WVD results were then applied to train a SOM. A set of two or three tests from stable burner conditions at various thermal loads and excess air levels was used to train the SOM, such as Tests 1 to 3 or 10 to 12. The SOM was then tested by generating predictions on unseen data.

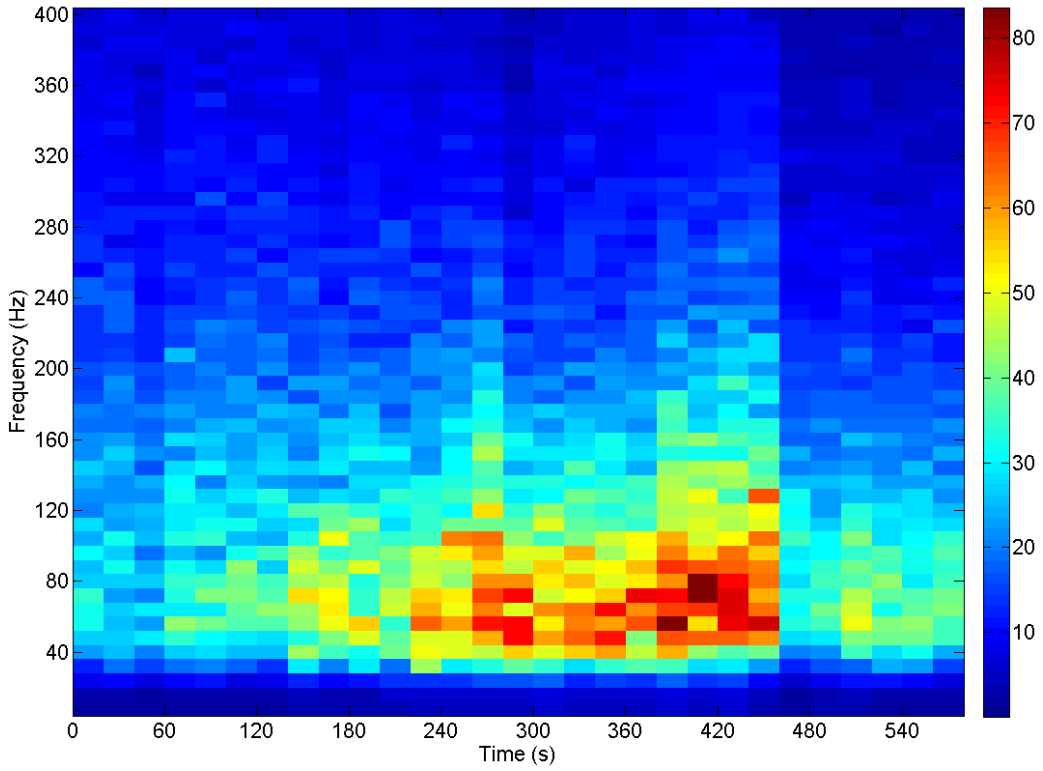

Figure 5.39: WVD of the IR sensor signal for the test (Test 97a) with decreasing secondary air with 100 % coal

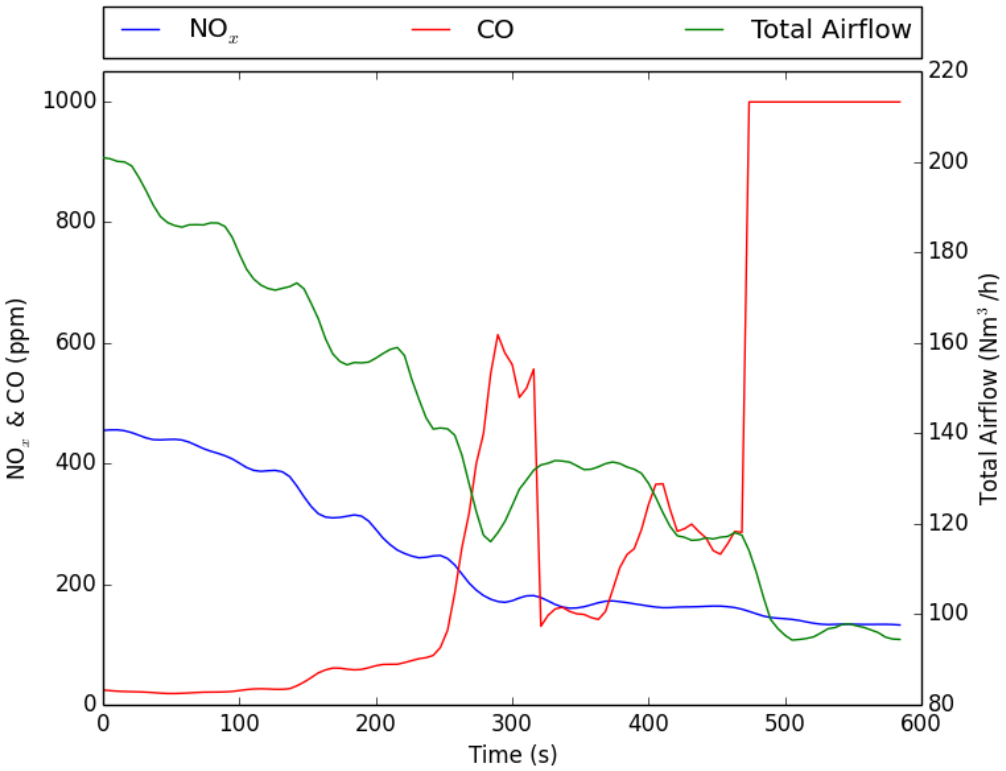

Figure 5.40: NO_x / CO Emissions and Total Airflow recorded for the test (Test 97a) with decreasing secondary air with 100 % coal

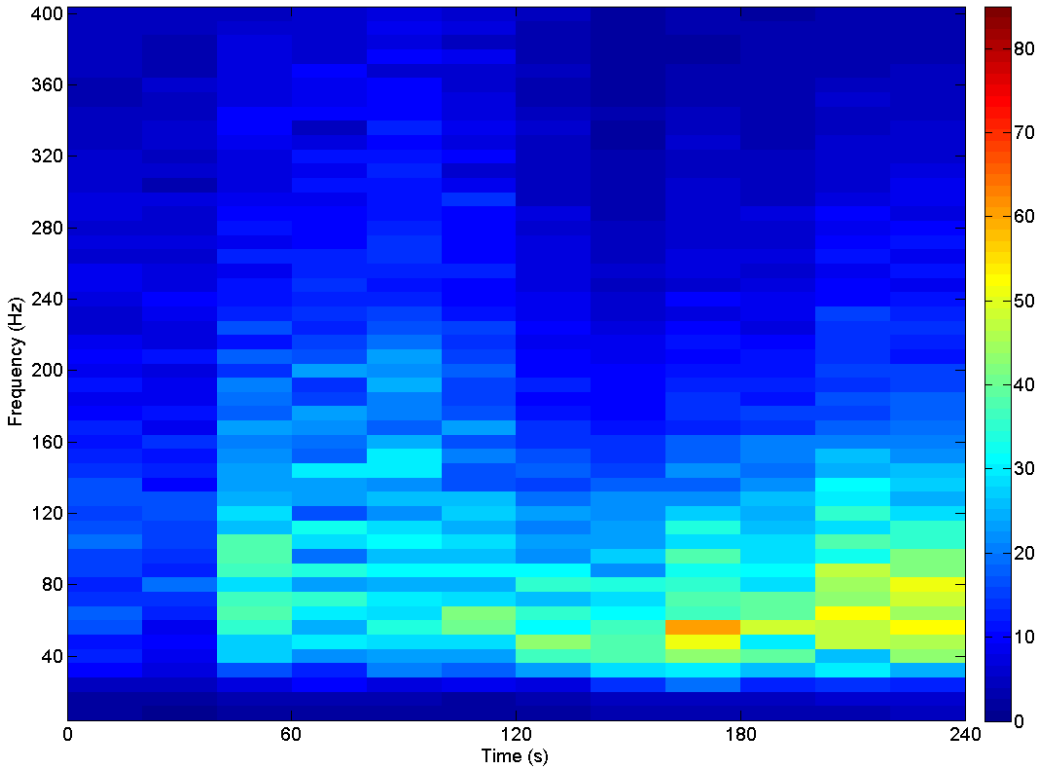

Figure 5.41: WVD of the IR sensor signal for the test (Test 98a) with decreasing secondary air with 90 % coal & 10 % biomass

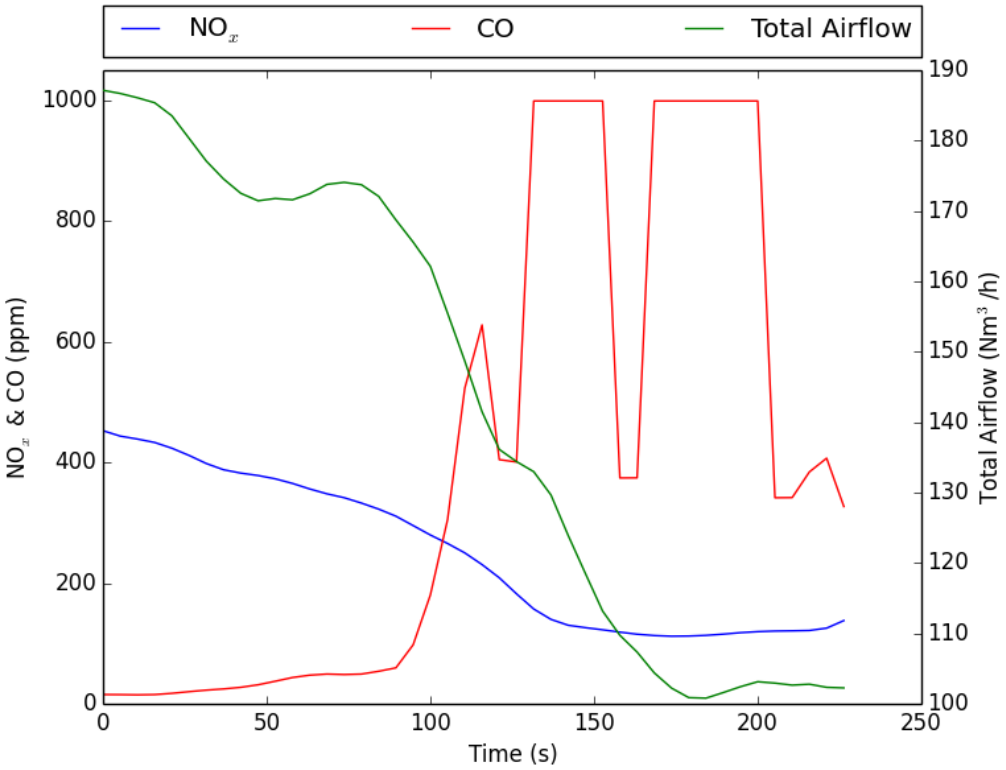

Figure 5.42: NO_x / CO Emissions and Total Airflow recorded for the test (Test 98a) with decreasing secondary air with 90 % coal & 10 % biomass

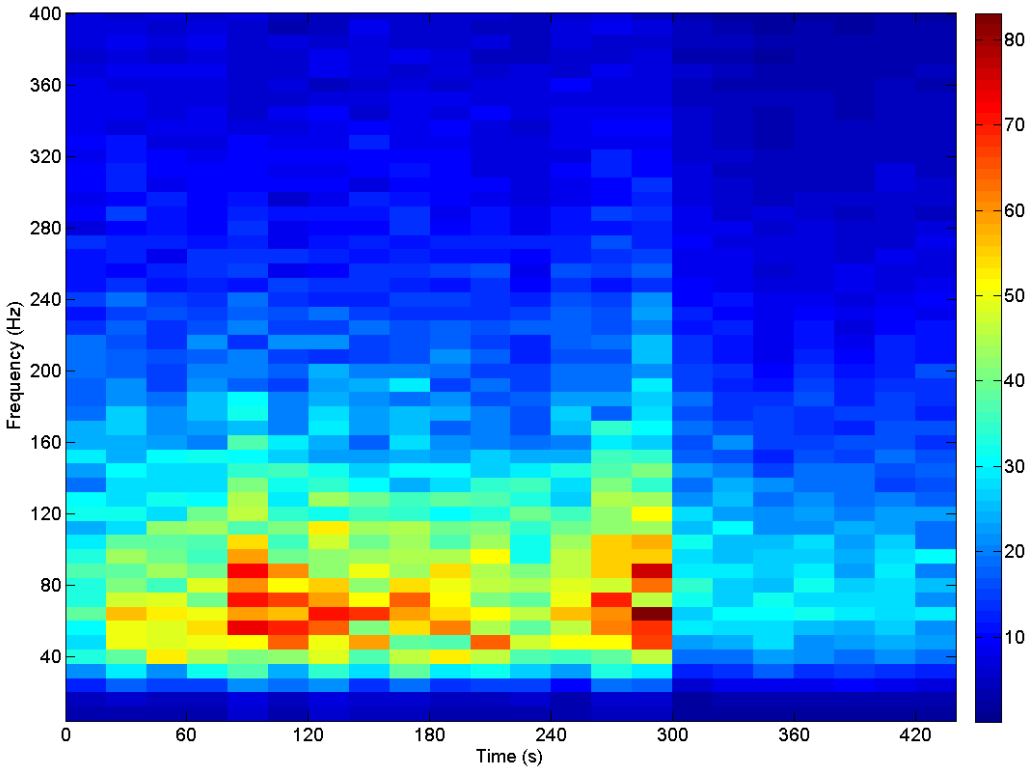

Figure 5.43: WVD of the IR sensor signal for the test (Test 99a) with decreasing secondary air with 80 % coal & 20 % biomass

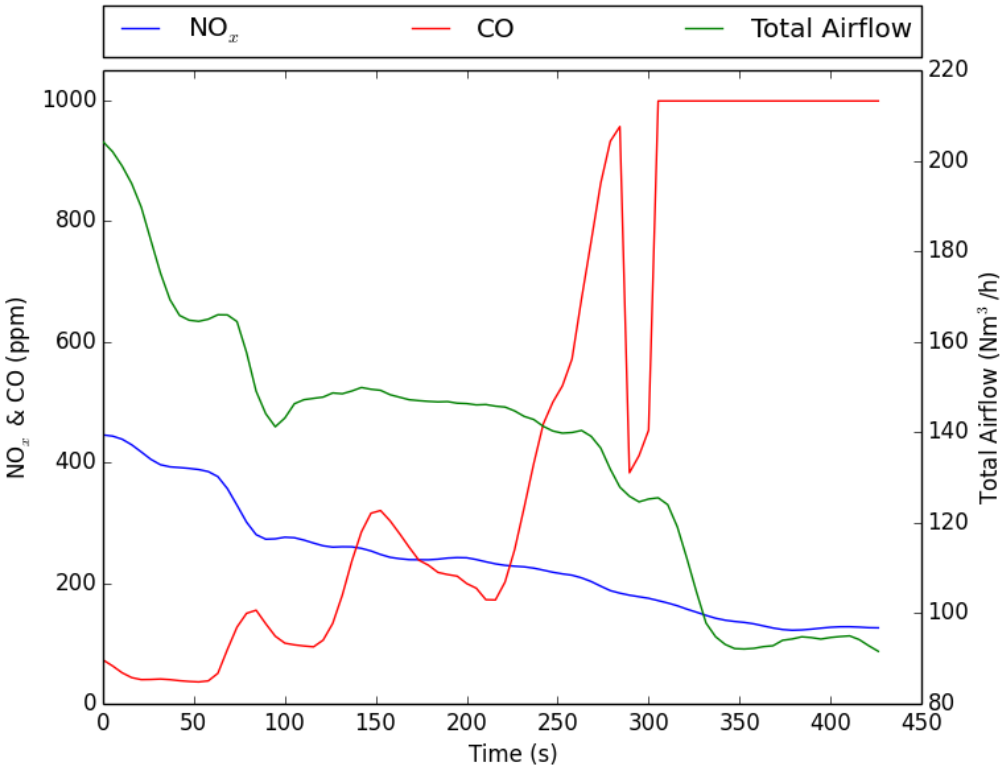

Figure 5.44: NO_x / CO Emissions and Total Airflow recorded for the test (Test 99a) with decreasing secondary air with 80 % coal & 20 % biomass

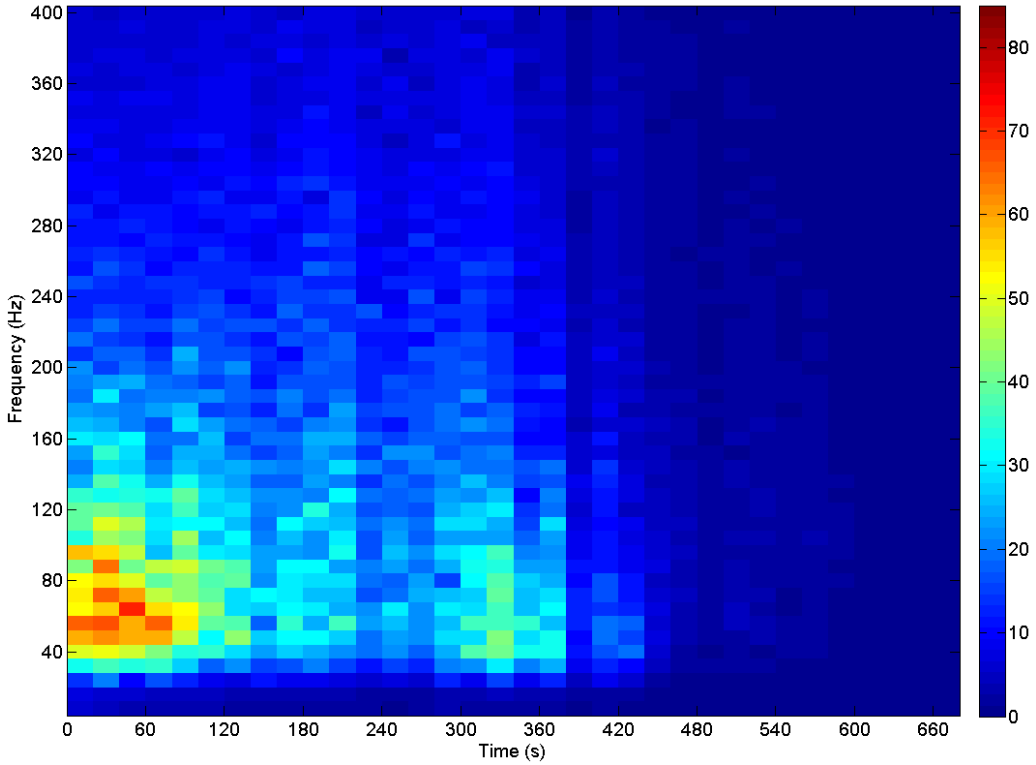

Figure 5.45: WVD of the IR sensor signal for the test (Test 97b) with increasing secondary air with 100 % coal

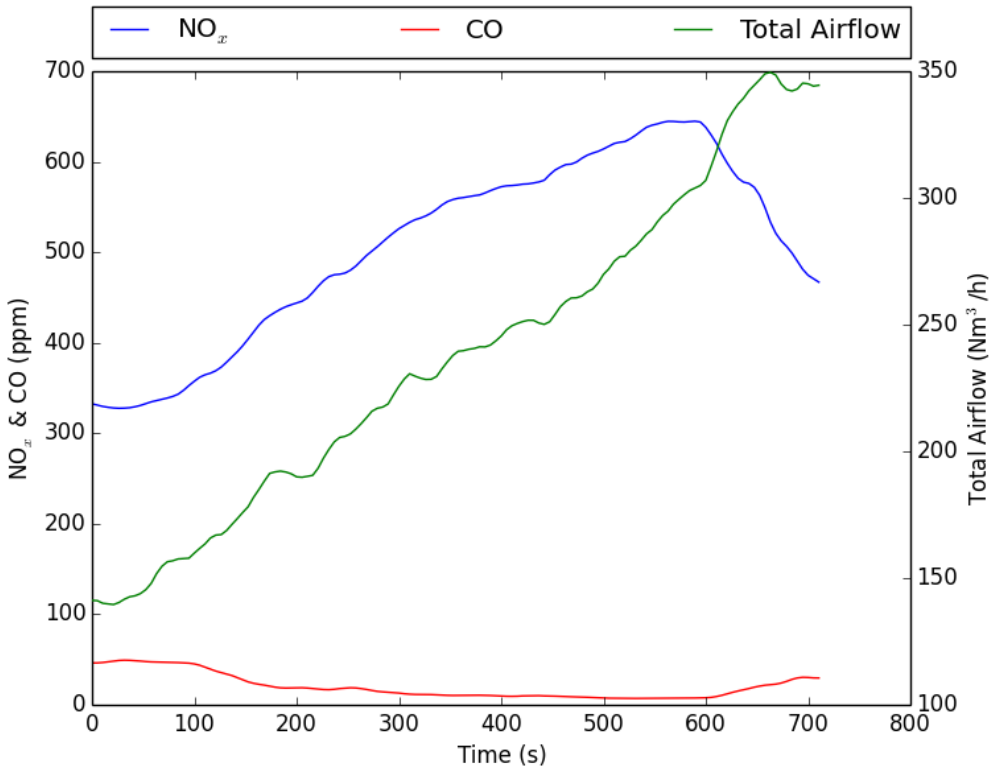

Figure 5.46: NO_x / CO Emissions and Total Airflow recorded for the test (Test 97b) with increasing secondary air with 100 % coal

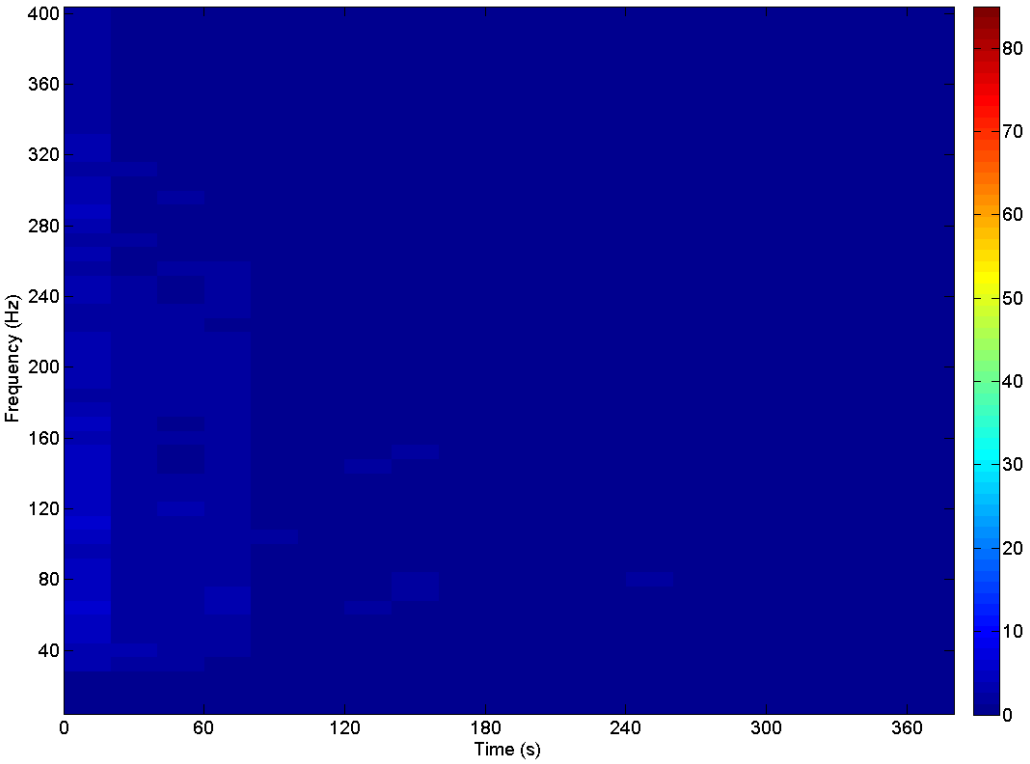

Figure 5.47: WVD of the IR sensor signal for the test (Test 98b) with increasing secondary air with 90 % coal & 10 % biomass

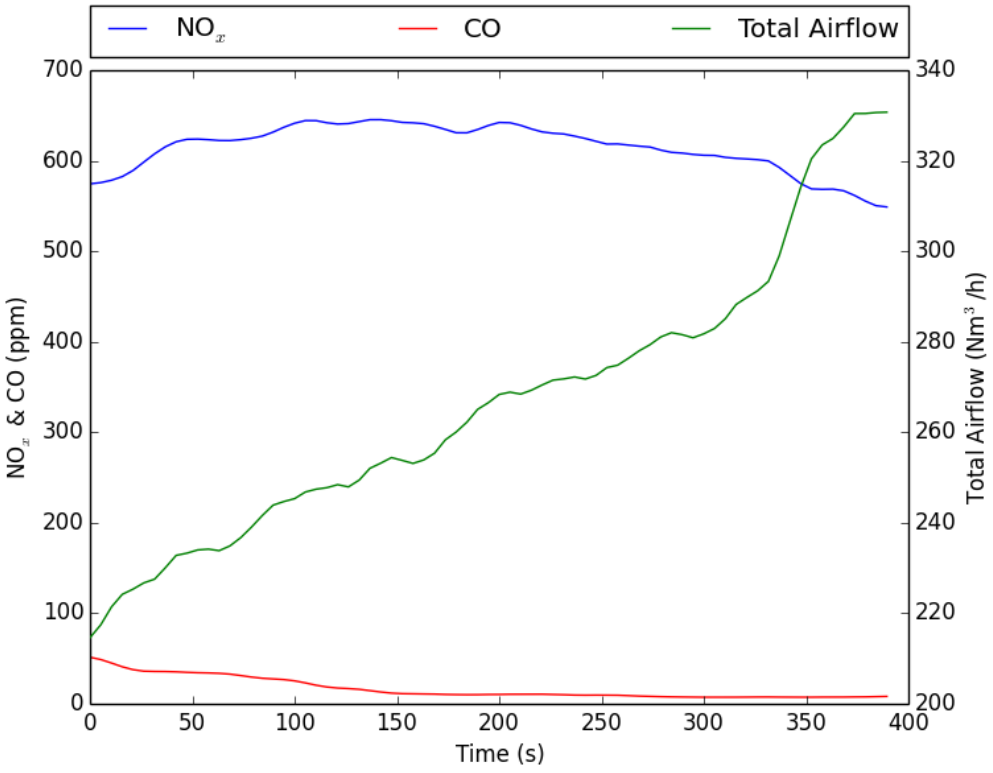

Figure 5.48: NO_x / CO Emissions and Total Airflow recorded for the test (Test 98b) with increasing secondary air with 90 % coal & 10 % biomass

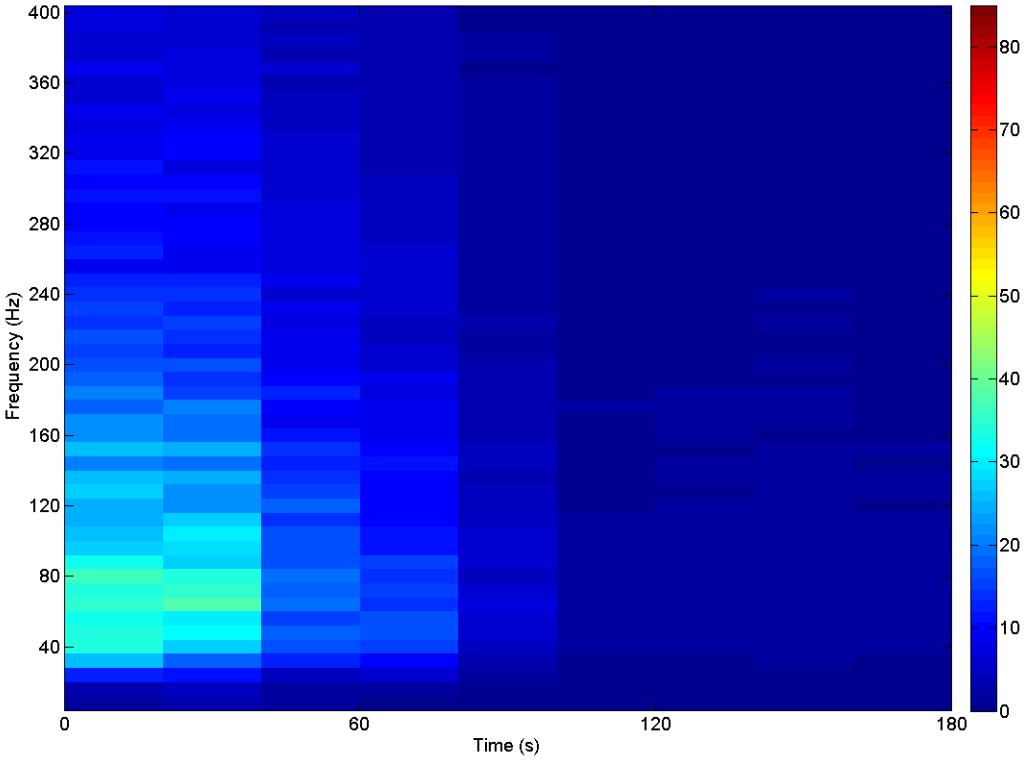

Figure 5.49: WVD of the IR sensor signal for the test (Test 99b) with increasing secondary air with 80 % coal & 20 % biomass

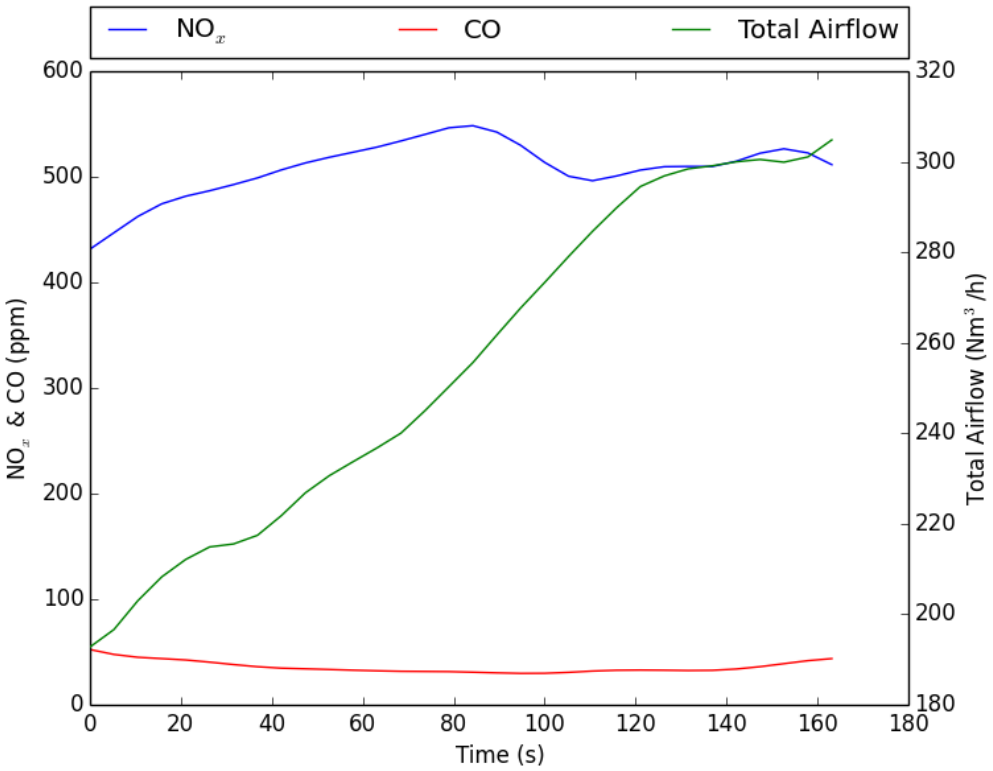

Figure 5.50: NO_x / CO Emissions and Total Airflow recorded for the test (Test 99b) with increasing secondary air with 80 % coal & 20 % biomass

In summary, changing from stationary signal features to a more complex Joint Time Frequency (JTF) approach would appear to yield a more consistent approach to visualising and understanding the complexities in the data.

5.3.3 SOM Based Control System Using WVD

As attempts to predict absolute values of NO_x and airflow had quite high errors this section will investigate the use of SOMs to classify the data. The experiments involved a wide range of operating conditions (Table 3.7) such as variations in thermal loads and excess air levels. Hence, a model capable of identifying the patterns in the various sets of data from multiple sensor sources and WVD output is necessary. A set of three or more tests based on relatively stable burner conditions at various thermal loads and excess air levels were used to train the SOM. The SOM model was subsequently tested with totally unseen data from a test in which the secondary air was continually increased or decreased until the combustion appeared to become unstable.

As mentioned before, during low thermal load and low excess air conditions, the percentage of purged air used to cool the sensors was significantly higher as a proportion than at optimal conditions, hence a measure of excess air calculated from the flue gases was not appropriate to be used for the SOM training. As a result, the total airflow was used in the prediction instead of excess air.

In this case, features from 0 Hz to 200 Hz extracted from the WVD data for the UV, VIS and IR photodiodes were used to train the SOM. PSD and WVD outputs showed no significant frequency changes beyond 100 Hz, but a higher margin of 200 Hz was used to avoid losing any features which weren't observed earlier. Hence 25 features of the frequency bins, each 8 Hz, which yields the range of 0 Hz to 200 Hz, were used to train the SOM, together with the respective total airflow to the CTF.

A SOM model with 20 by 20 neurons, selected as the best performing from the 10 * 10, 12 * 12, 15 * 15, and 25 * 25 networks tested, was trained using a set of experimental data with a consistently stable flame and optimal combustion parameters for 100 % coal (and similar SOM models for other thermal load conditions), one with a low secondary air condition but without the flame blowout and another with very high secondary air when the flame pulsated further and became detached from the burner quarl. This was used to predict the potential unstable flame condition normally encountered during low secondary air conditions, which also gets aggravated in conditions where biomass is mixed with coal. Similarly, two other models were also trained using experimental data collected from 10 % and 20 % biomass substitutions.

Figures 5.51 to 5.56 illustrate the SOM predictions of likely instabilities in the experiments with varying total airflows. The predicted values were smoothed out by averaging every 60 s (running mean). Separate SOMs were trained for different fuel compositions and the predictions are based on the experiments that were used to train the SOM model. Three photodiodes, namely UV, VIS and IR were used to train the SOM as preliminary SOM trials using just one sensor did not yield very good predictions, especially fluctuating between stable and unstable flame conditions during the transition. This might stem from the fact that the sensor intensity variation with different thermal conditions for the various sensors

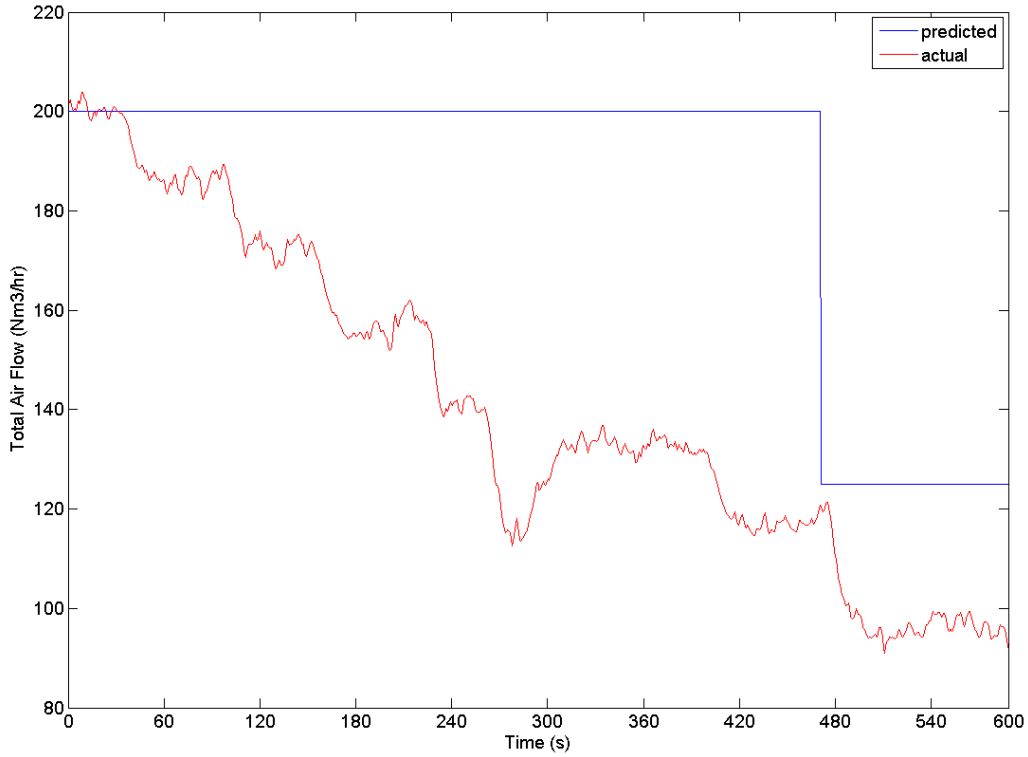

Figure 5.51: Total airflow vs instability prediction - 100 % Coal - decreasing secondary air from stable condition

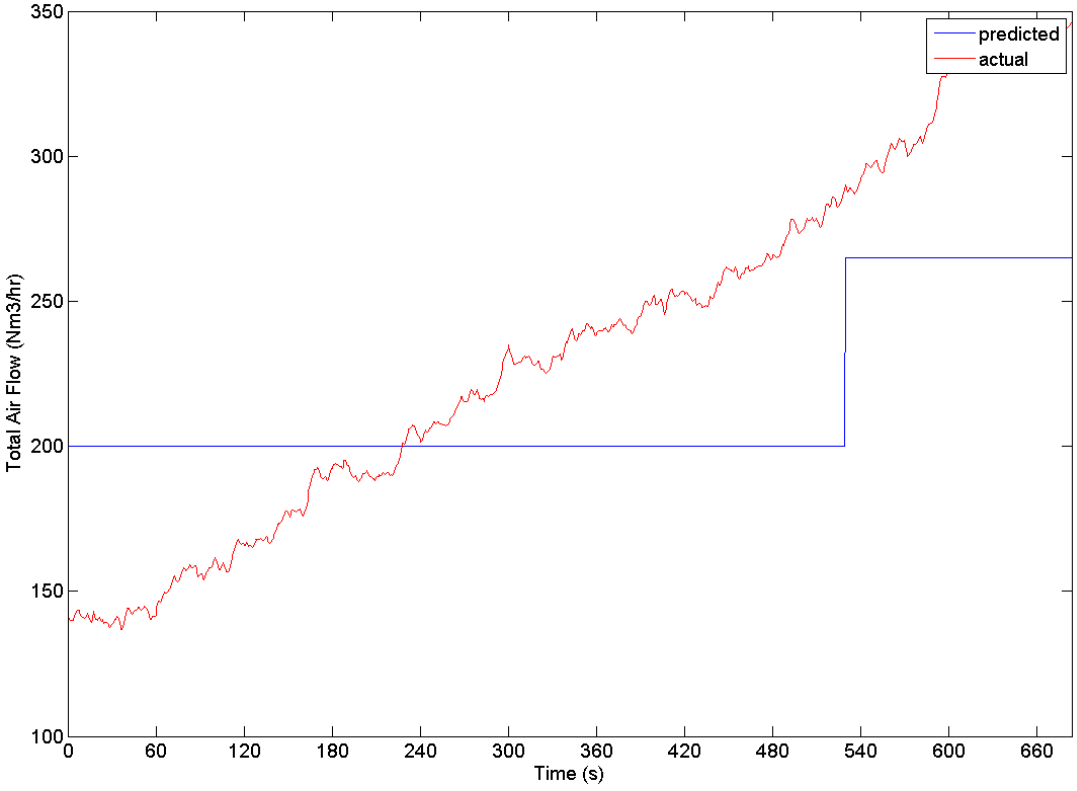

Figure 5.52: Total airflow vs instability prediction - 100 % Coal - increasing secondary air from stable condition

is neither linear nor proportional.

The experimental data used for training the model for the predictions shown in Figures 5.51 & 5.52 for 100 % coal were three tests with total airflows of 265 (Test 3), 200 (Test 1) and 125 (Test 7) Nm^3/h. As can be seen in figure 5.51 for 100 % coal, the classified value (among the three experiments used to train the SOM) stays well within the normal burner conditions until ≈450 s, beyond which the prediction drops to a lower airflow region, indicating that the SOM detects sensor signals very near burner instability. If this were to be represented as a cluster, the first 480 s of the test would be very near the centre of the cluster and would gradually deviate as the potential flame instability sets in. This prediction coincides with the observations made during the experiment using the sighting panel on the side of the combustion chamber.

The same trend can be observed in the classified values of other SOM models trained with experiments having total airflows of 270 (Test 11), 200 (Test 15) and 120 (Test 16) Nm^3/h, and 235 (Test 84), 170 (Test 90) and 120 (Test 88) Nm^3/h for fuels that consisted of 10 % and 20 % biomass substitution as shown respectively in figures 5.53 & 5.54 and figures 5.55 & 5.56. As can be seen in figure 5.53, the burner instabilities set in around 45 s into the tests as predicted by the SOMs and the flames become unstable quite quickly when having 10 % and 20 % biomass substitution as compared to firing without biomass substitution. Although the decrease in secondary air amongst these tests is not linear, the results show that the flame starts to get unstable around 160 to 180 Nm^3/h range when co-firing with biomass substitutions as compared to 140 Nm^3/h or lower without biomass.

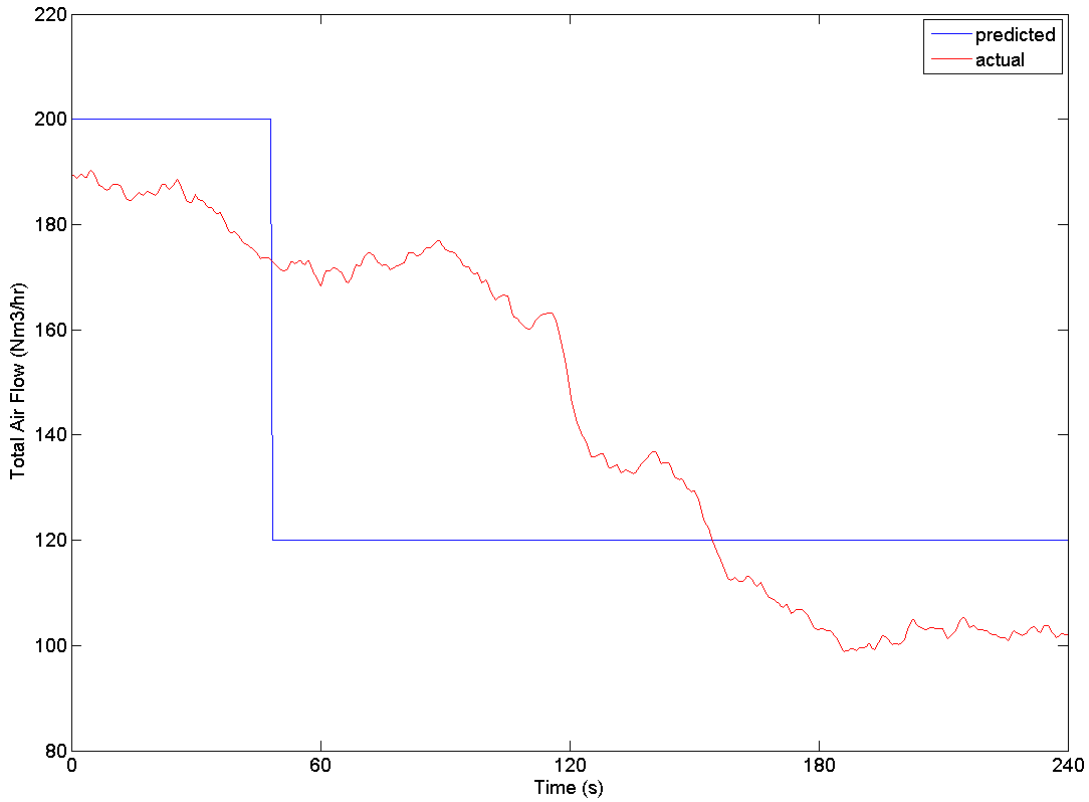

Figure 5.53: Total airflow vs instability prediction - 90 % Coal & 10 % Biomass - decreasing secondary air from stable condition

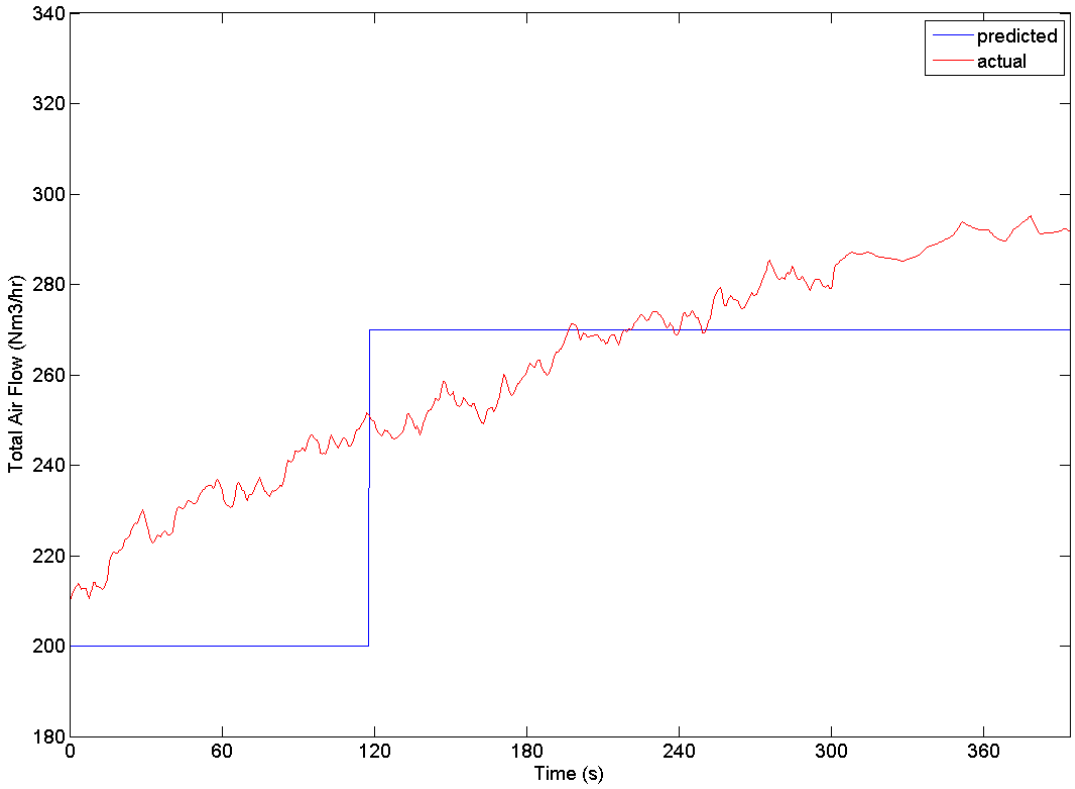

Figure 5.54: Total airflow vs instability prediction - 90 % Coal & 10 % Biomass - increasing secondary air from stable condition

On the other hand, figures 5.53 & 5.54 show that the predictions of the burner stability are quite similar to the actual secondary airflow to thereabouts of 250 Nm^3/h, the average of high secondary air conditions used to train the three SOM models. This trend would have continued until the end of the test with higher secondary airflow if the tests used for training had such high secondary airflows. The predictions for 10 % and 20 % biomass substitution shows the flame characteristics deviate further from optimal condition much earlier than without biomass substitution on careful observation. This is consistent with decreasing secondary air conditions discussed earlier (figures 5.51 & 5.53) where biomass inclusion affects the flame stability much earlier than just firing with 100 % coal. This reinforces the reason for the need of a capable monitoring system that is able to identify flame instability and potential flame blowout conditions with increases in biomass substitution.

In addition to predicting instability conditions, high excess conditions could be predicted as well, provided that sufficient training data is available to represent the highest secondary airflow conditions. This prediction could possibly be enhanced by using more controlled tests at various thermal loads and total airflow conditions representative of the entire optimal range of the burner in question for training as opposed to just three test conditions as discussed above. This would enable the SOM to predict higher secondary airflow or excess air quite accurately as well as aid in reducing NO_x emissions.

It is clear that the SOM can detect total airflow conditions which are representative of burner instability conditions. The processing of the experiments

conducted using the WVD algorithm show the potential of SOM to be able to detect the onset of burner instabilities resulting from changes to the total airflow to a burner. A system based on this would be of value in operating large coal burners where air flow to individual burners cannot be metered.

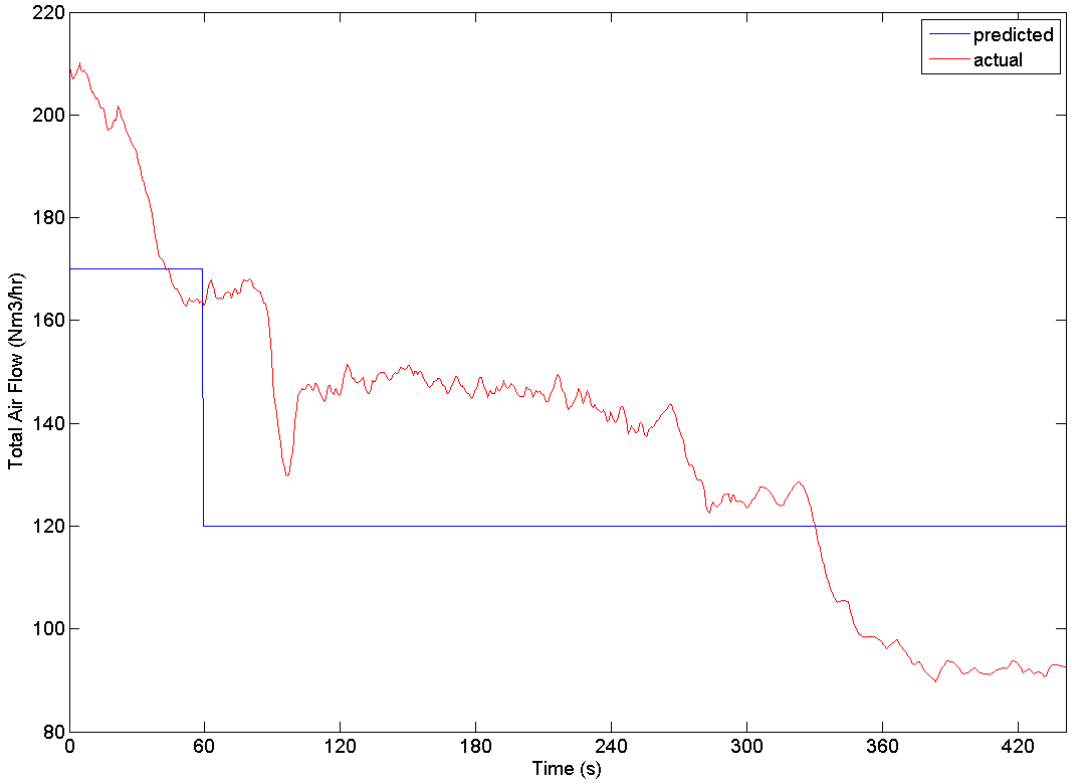

Figure 5.55: Total airflow vs instability prediction - 80 % Coal & 20 % Biomass - decreasing secondary air from stable condition

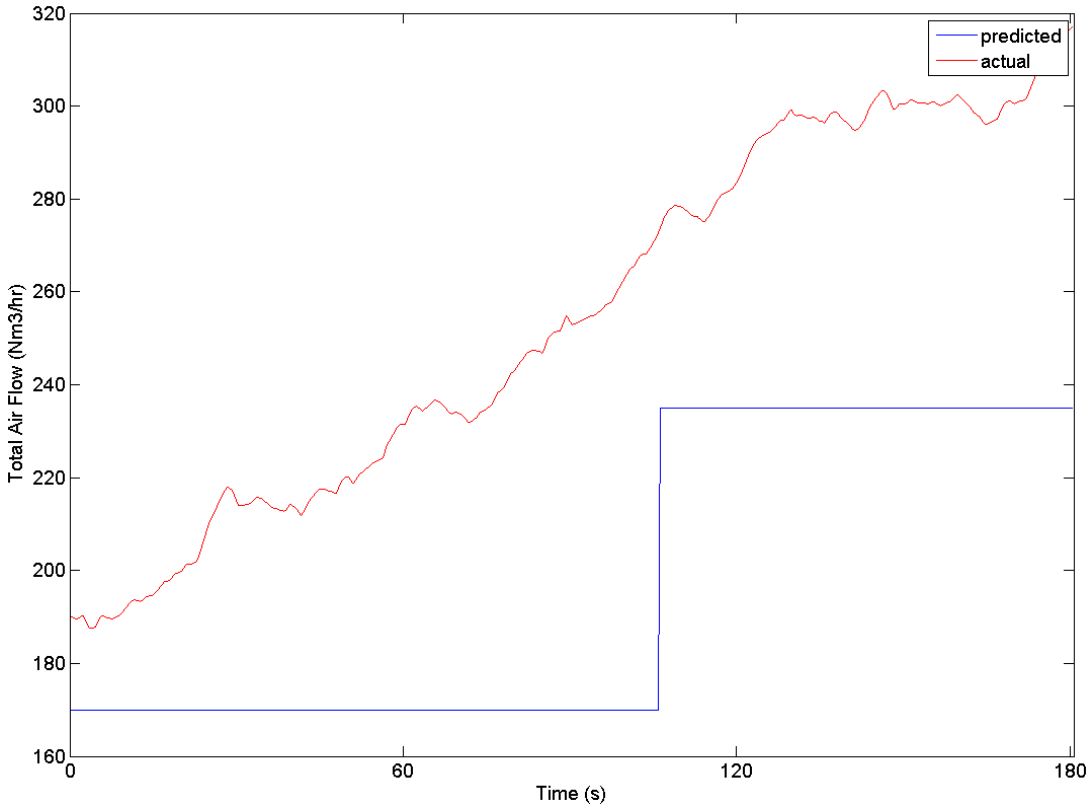

Figure 5.56: Total airflow vs instability prediction - 80 % Coal & 20 % Biomass - increasing secondary air from stable condition

5.3.4 SOM for NO_x Classification

In the previous Section 5.3.3, results were presented where an unsupervised SOM was tested for detecting burner instability. This procedure has been extended to test the ability of a SOM to predict NO_x and CO emissions.

The experimental data used for training the models for NO_x classification shown in the figures 5.57 & 5.58 for 100 % coal were three tests with total airflows of 265 (Test 3), 200 (Test 1) and 125 (Test 7) Nm^3/h having average NO_x emissions of 1066, 659 and 619 ppm respectively. It is to be noted that the prediction in the decreasing excess air test (figure 5.57) follows the trend (with reference to the values used to train) and shows the lowest value used to train as the prediction for *unseen values which were much lower* than the tests used to train the SOM model. The prediction is based on the values used to train the system, in this case the normal and low values used to train were 659 and 619 ppm, where by the system has correctly predicted the trend of lower NO_x but the predicted value is based on the values the system was used to train (in this case 619 ppm). Similarly the increasing excess air test (figure 5.58) shows the trend and predicts the higher values with the highest value used to train the model.

Models for 90 % coal & 10 % biomass and 80 % coal & 20 % biomass were each trained with three tests with total airflows of 270 (Test 11), 200 (Test 15) and 120 (Test 16) Nm^3/h, and 235 (Test 84), 170 (Test 90) and 120 (Test 88) Nm^3/h having average NO_x emissions of 900, 572 and 453 ppm and 812, 703 and 491 ppm re-

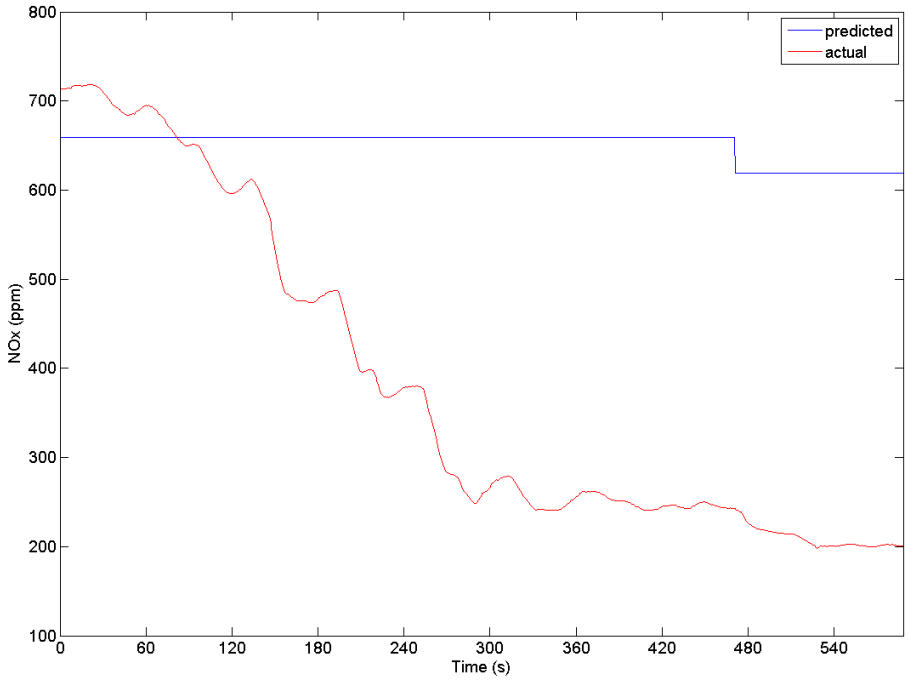

Figure 5.57: NO_x measured vs prediction - 100 % Coal - decreasing secondary air from stable condition

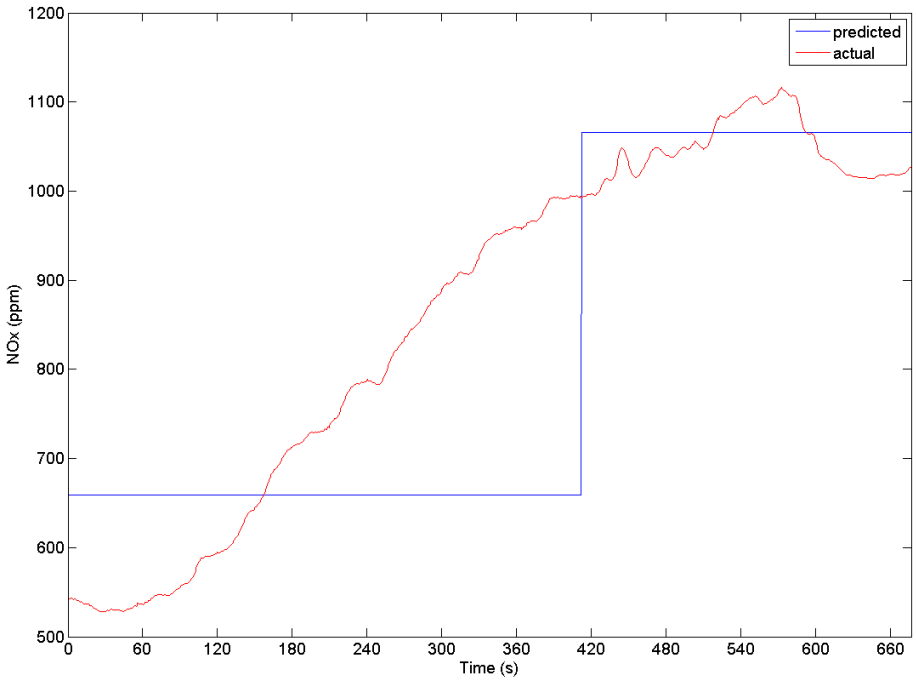

Figure 5.58: NO_x measured vs prediction - 100 % Coal - increasing secondary air from stable condition

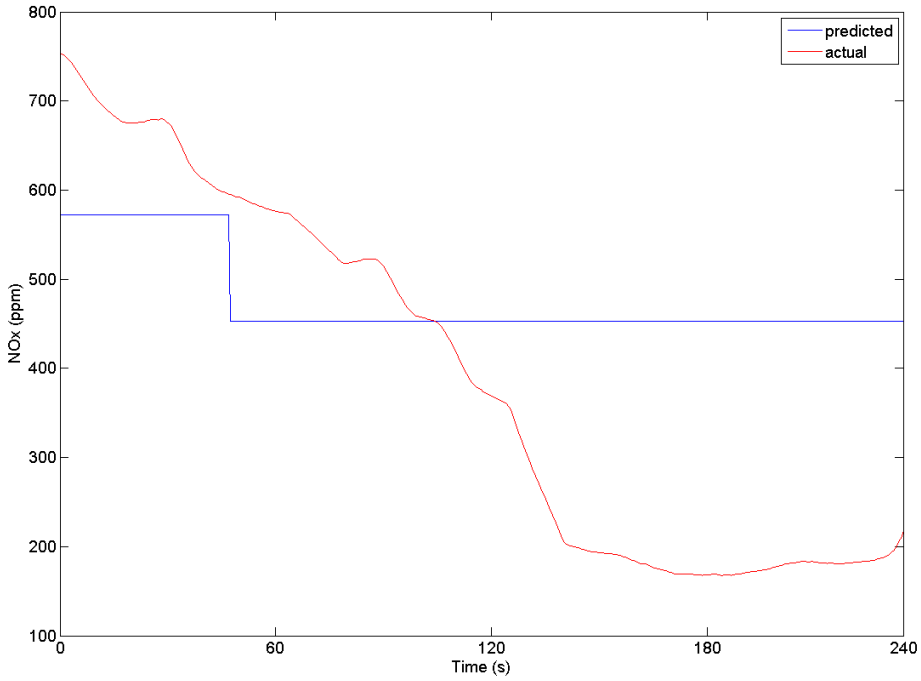

Figure 5.59: NO_x measured vs prediction - 90 % Coal & 10 % Biomass - decreasing secondary air from stable condition

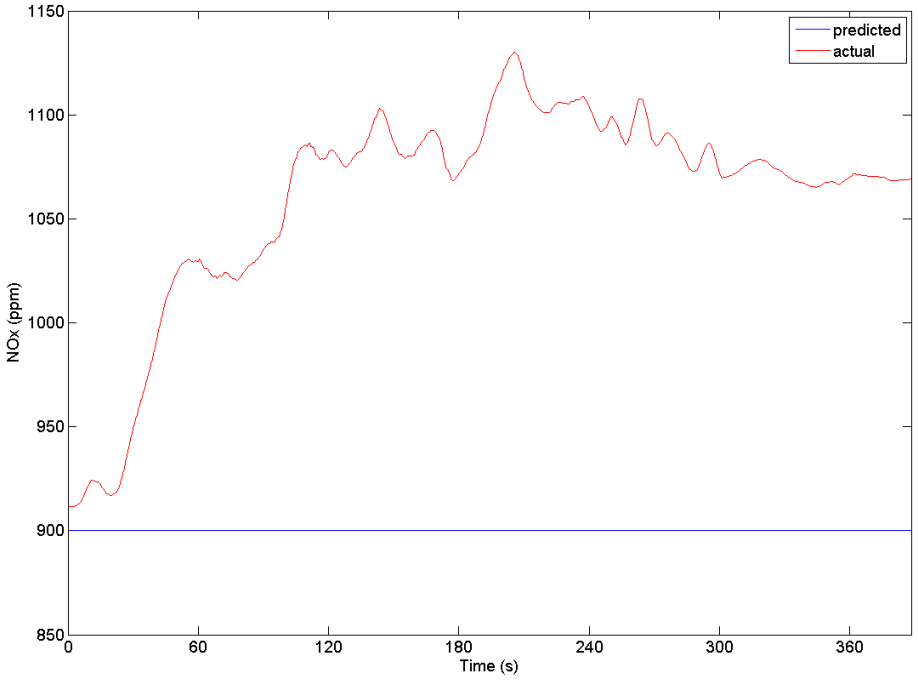

Figure 5.60: NO_x measured vs prediction - 90 % Coal & 10 % Biomass - increasing secondary air from stable condition

spectively. The test with increasing excess air for coal biomass blend of 90 %/10 % (figure 5.60) had high NO_x emissions at the start of the test and the SOM classified it correctly. These were done at the CTF where very precise controls of the inputs couldn't be maintained or attained for a long period and hence some tests may not have the expected range to test out the predictions as just mentioned. The predictions for the coal biomass blend of 80 %/20 % are fairly good. All the classifications that were discussed were averaged over a period of 60 s to avoid spontaneous changes in flame which might affect these values, and hence you can notice that the system takes a short while before it notices or changes the predicted values (this duration over which is averaged can be modified for faster response with increased spontaneous fluctuation but then power station boiler inputs are usually changed gradually).

5.3.5 SOM for CO Classification

As with the NO_x predictions in the previous Section 5.3.4, CO prediction models were trained with three tests each for 100 % coal, 90 % coal & 10 % biomass substitution and 80 % coal & 20 % biomass substitution with total air flow rates of 265 (Test 3), 200 (Test 1) and 125 (Test 7) Nm^3/h, 270 (Test 11), 200 (Test 15) and 120 (Test 16) Nm^3/h, and 235 (Test 84), 170 (Test 90) and 120 (Test 88) Nm^3/h having average CO emissions of 9, 90 and 57 ppm, 11, 11 and 102 ppm and 31, 39 and 164 ppm respectively. Compared to NO_x predictions, the predictions for CO are not very consistent for two reasons:

1. The training data used from the CO sensor contained a number of saturated values when the concentration exceeded the upper limit of the analyser.

2. The nature of CO concentrations to fluctuate compared to relatively stable NO_x emissions for the same flame condition. This is expected due to the fluctuation of the flame front across the line of sight of the sensors.

Some of the training tests contain higher values, but only the average value of CO was taken to avoid huge fluctuations in classifications and the saturated values were substituted with the highest value previously measured by the sensor for the test.

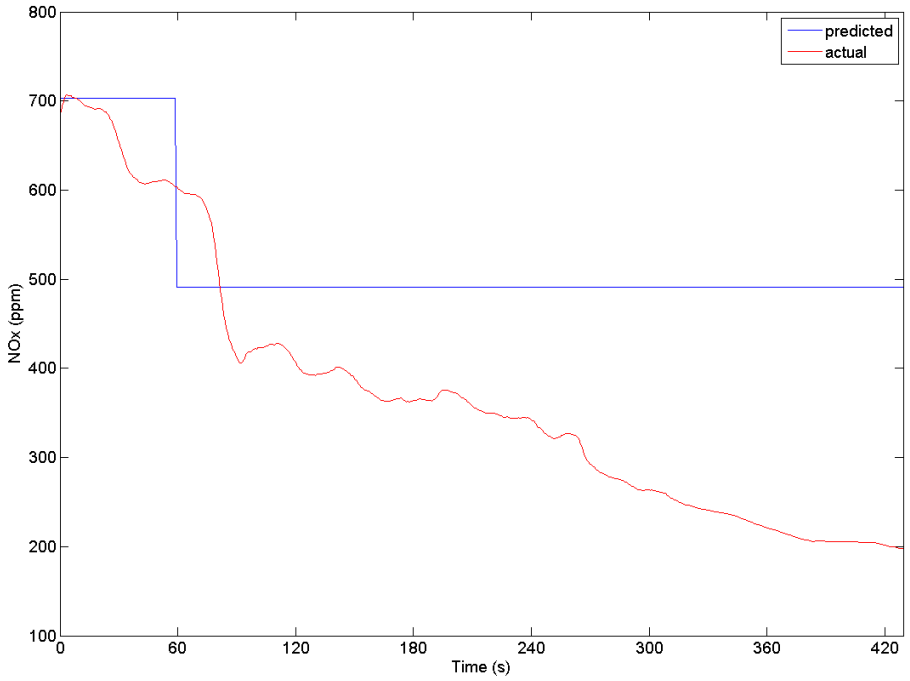

Figure 5.61: NO_x measured vs prediction - 80 % Coal & 20 % Biomass - decreasing secondary air from stable condition

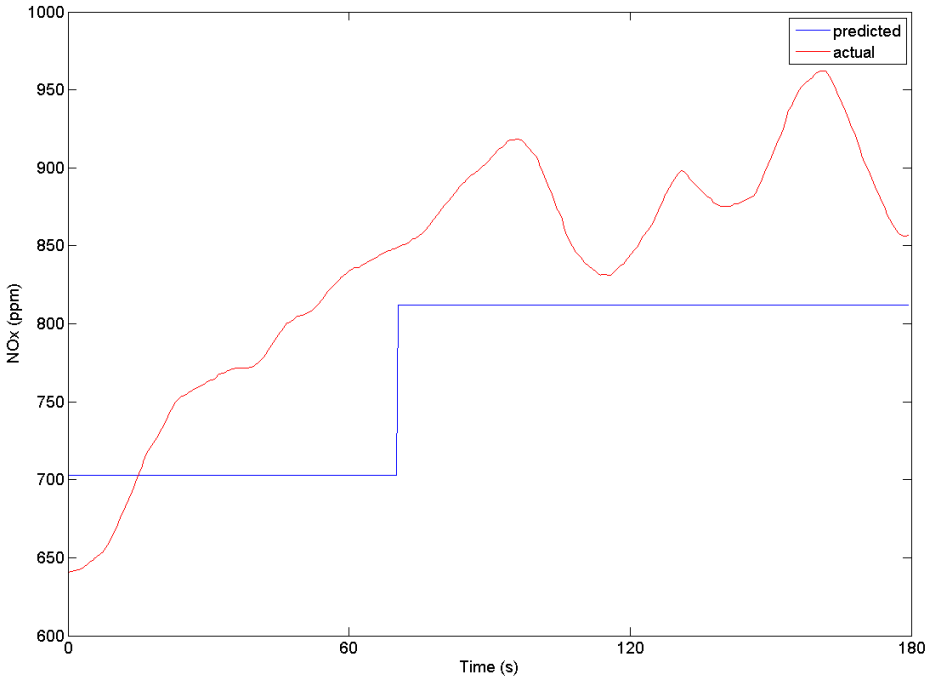

Figure 5.62: NO_x measured vs prediction - 80 % Coal & 20 % Biomass - increasing secondary air from stable condition

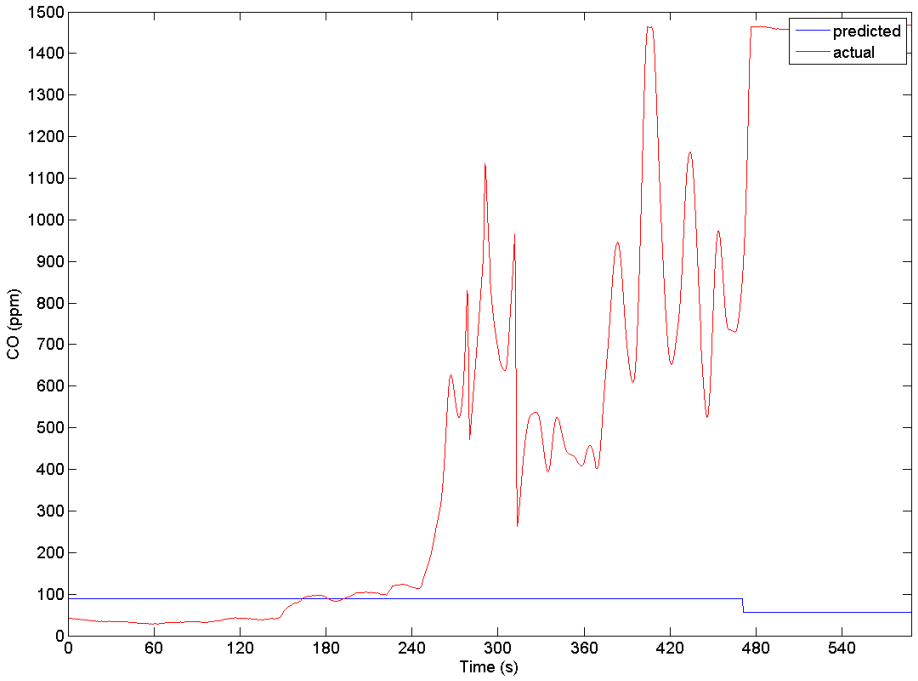

Figure 5.63: CO measured vs prediction - 100 % Coal - decreasing secondary air from stable condition

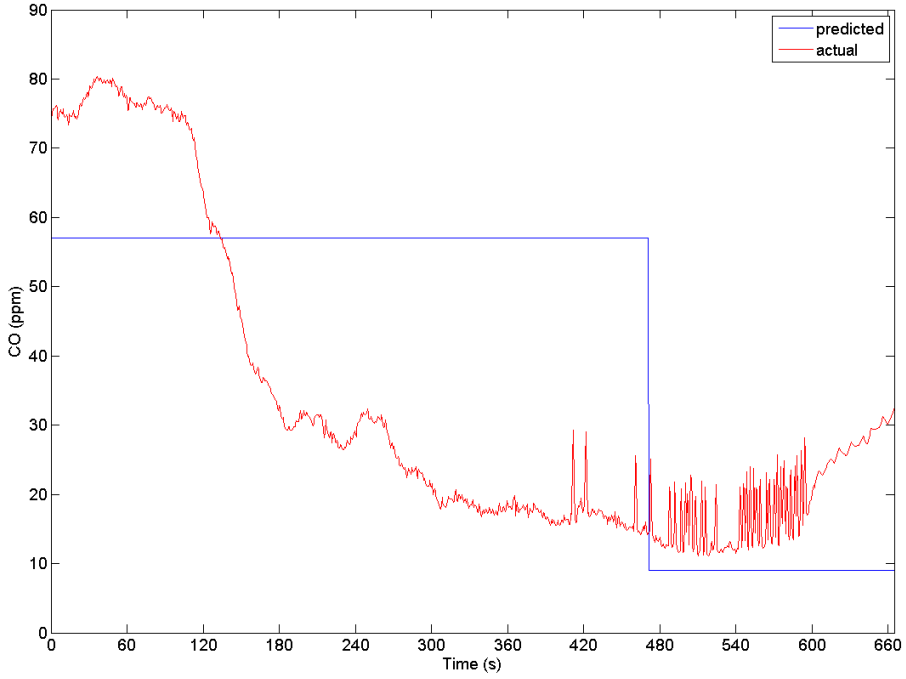

Figure 5.64: CO measured vs prediction - 100 % Coal - increasing secondary air from stable condition

The test for 100 % coal with decreasing excess air (figure 5.63) shows a lower value than the highest value used to train at the very end of the test as the actual value itself saturated and the sensor couldn't accurately give a value and it was near flame blow out condition. Even at the earlier part of the test, the values classified are beyond the normal range of the burner for normal total air flow levels and hence the SOM correctly predicts it as a high CO condition. The coal biomass blends of 90 %/10 % and 80 %/20 % exhibit similar conditions at the start of the decreasing excess air test as in 100 % coal test and this is due to the reason that the test rig wasn't able to sustain or regain a similar condition to normal optimal conditions in quick successions when doing multiple tests. The CO classifications would have been better if the tests were much more controllable and the recorded data used for training didn't have fluctuating values and more representative values higher in the range than now used. This can be avoided in the full control system by having good representative values and training with a number of optimal and slightly unstable to highly unstable conditions than just the 3 (high, normal & low excess air conditions) used in these evaluations.

In figure 5.65, the CO values used to train the SOM, experiments 270 (Test 11), 200 (Test 15) and 120 (Test 16) Nm^3/h were 11, 11 and 102 ppm respectively. Since the highest value used to train the SOM for the results shown in figures 5.65 & 5.66 is just 102 ppm, the system correctly classifies higher CO concentrations from the flame.

Similar scenarios exist for classifications shown for 80 % coal & 20 % biomass in figures 5.67 & 5.68, where by the highest CO value used during training the SOM was 164 ppm, that's the maximum value displayed during classification, even though the CO concentrations were higher. So the trends of classifications are very promising to be used in a control system using such a method of signal processing and application of SOM for CO prediction.

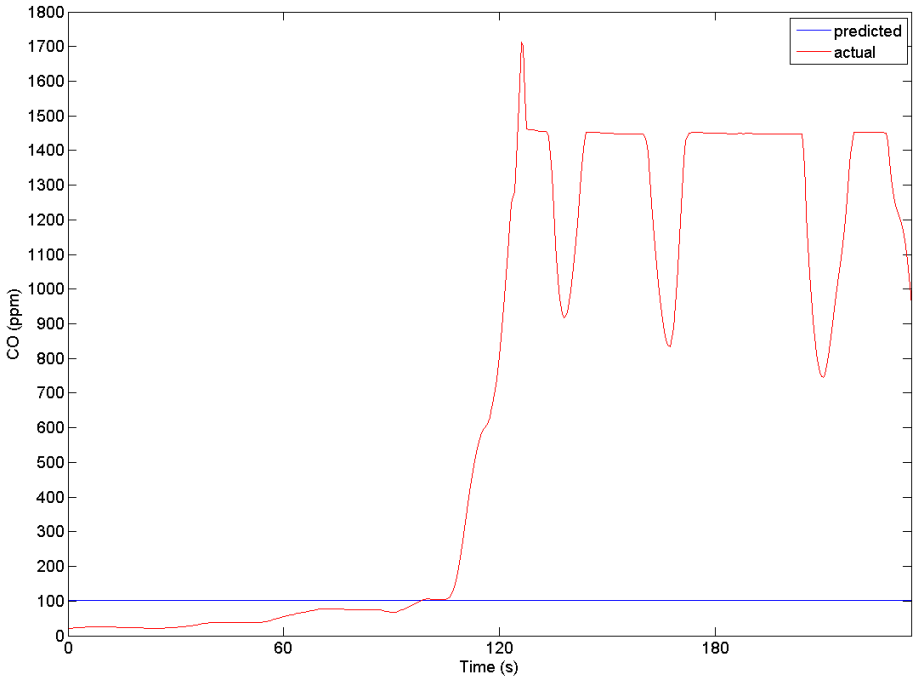

Figure 5.65: CO measured vs prediction - 90 % Coal & 10 % Biomass - decreasing secondary air from stable condition

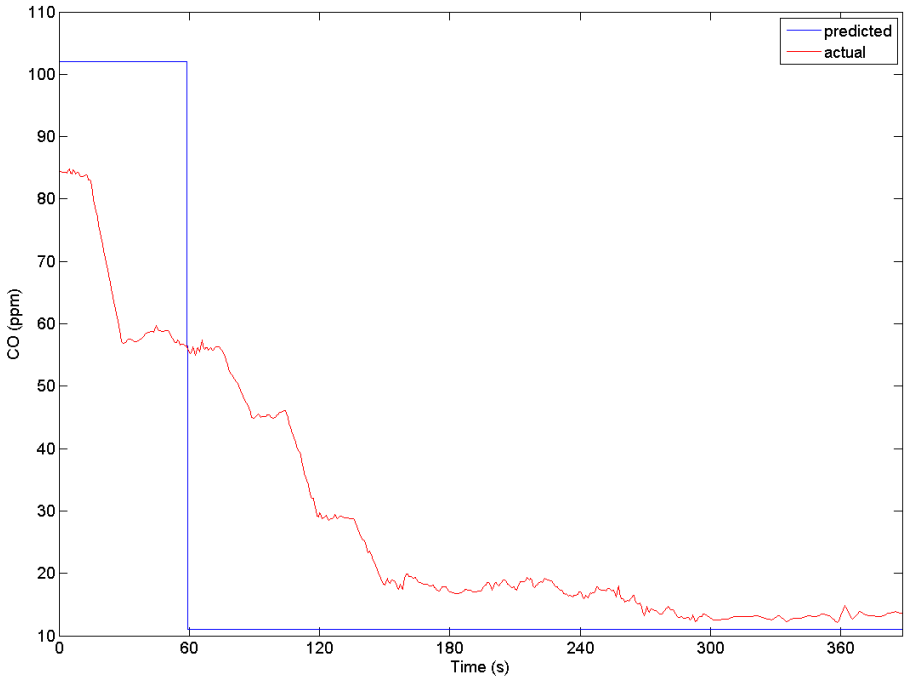

Figure 5.66: CO measured vs prediction - 90 % Coal & 10 % Biomass - increasing secondary air from stable condition

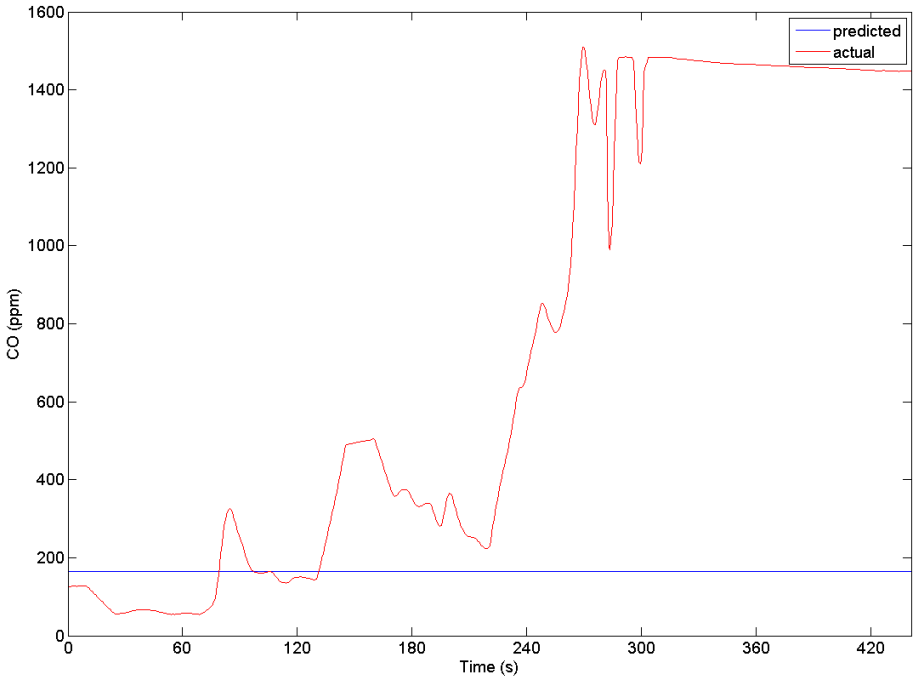

Figure 5.67: CO measured vs prediction - 80 % Coal & 20 % Biomass - decreasing secondary air from stable condition

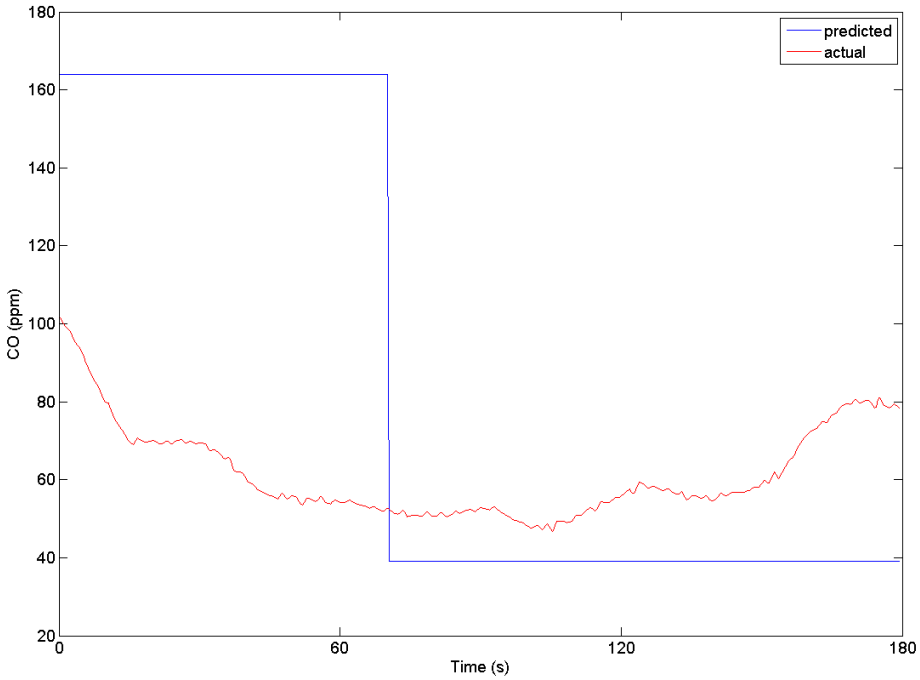

Figure 5.68: CO measured vs prediction - 80 % Coal & 20 % Biomass - increasing secondary air from stable condition

5.4 Control System – Training and Application of SOM Model

The methodologies for training and applying the control system are illustrated in the flow charts shown in figures 5.69 & 5.70 below. In figure 5.69, initially the various test conditions are set in the burner and the resulting data recorded using the three sensors. This data is processed using WVD before it is used to train the SOM model for each thermal load, with at least three excess air conditions. This process is repeated for each thermal load. The training process also needs data from flue gas measurements made during the various test conditions for training NO_x and CO prediction models and total airflow data when training air flow prediction models.

This process involves some manual handling of data and running scripts / programs in MATLAB© / LabVIEW© as the systems used to record the 3 (UV, VIS and IR) sensors are different to the one used to record other plant data and flue gas measurements. Once the data from the 3 sensors namely UV, VIS and IR are recorded, it is processed using a custom developed LabVIEW© program to derive WVD data. Then the WVD data for frequencies 0 Hz to 200 Hz for each of the test conditions used for training is extracted together with the respective NO_x, CO or total air flow data. It is then used to train the SOM model in MATLAB©. The trained SOM model is then used by the control program as described in figure 5.70.

The control system as described in figure 5.70 above uses LabVIEW© similar to the training program to acquire the 3 sensor data using DAQs but encapsulates everything needed to operate without any manual handling except for starting and stopping the program. After acquisition is completed, WVD is calculated for all the sensors and the control is passed on automatically to SOM scripts in MATLAB© and the result obtained is passed back to LabVIEW©. This prediction of CO and NO_x is then used in the rule based algorithm to give predictions to decrease, increase or maintain constant, the secondary air flow to the burner. Table 5.22 below shows the simple rule based algorithm used for control of the air flow.

Table 5.22: Simple rule based algorithm for control of airflow (AF = Air Flow)

CO / NO_x	High	Medium	Low
High	Check settings /sensor	AF↓	AF↓↓
Medium	AF↑	AF↓↑	AF↓
Low	AF↑↑	AF↑	No change

The control program is designed to run continuously averaging the last 5 predictions (3 minutes worth of data) until stopped. This could be varied very easily to adapt to different burners depending on the dynamics and speed of change possible for each burner.

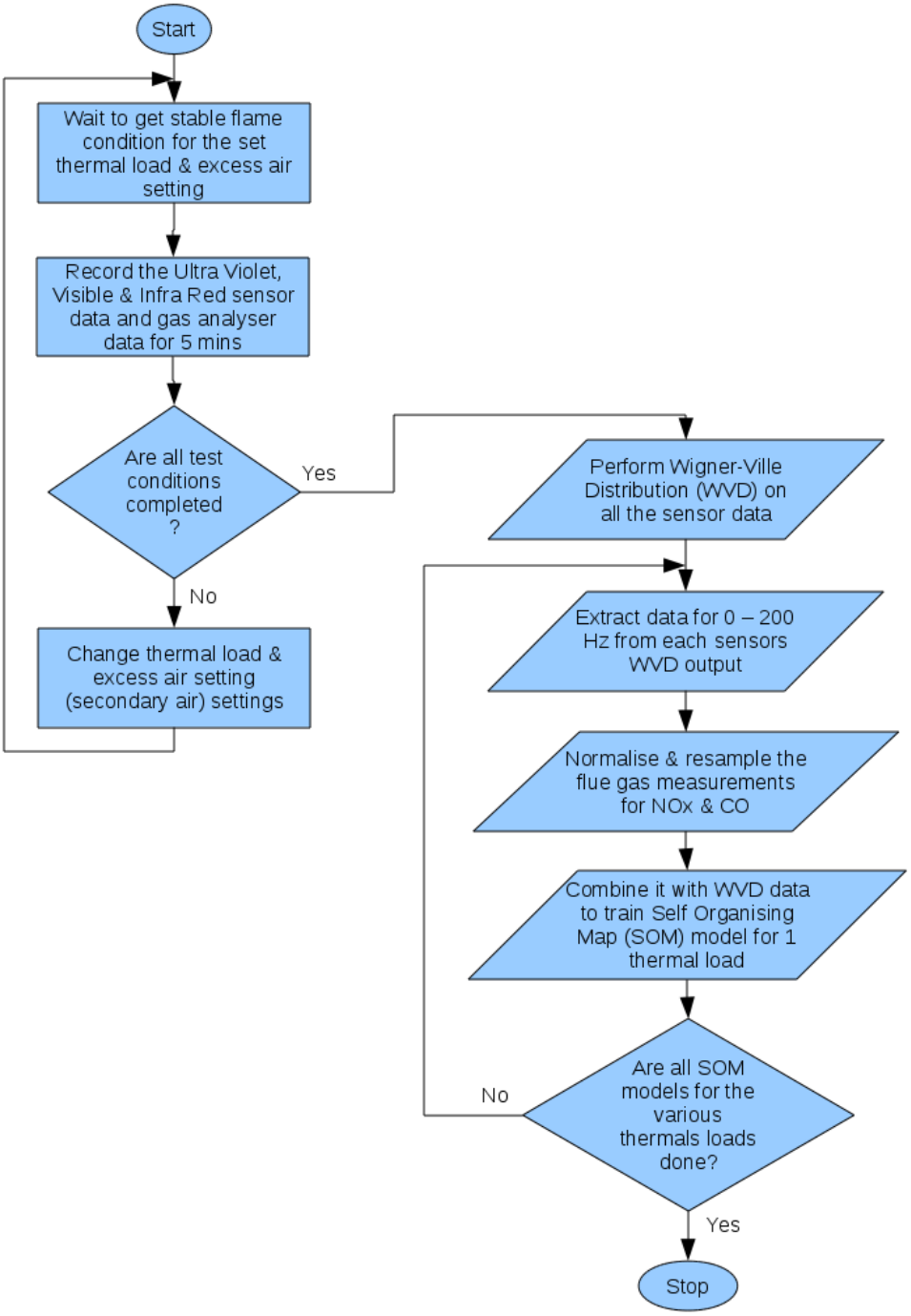

Figure 5.69: Algorithm for training the SOM model

The algorithm can be adapted with more control steps provided the initial training data is obtained with more combustion conditions than just the 3 different airflows employed here. Only three were applied during the training tests at IEn Poland due to limited capability of the test rig. The arrows represent the trend to increase or decrease secondary air flow in our case being a single

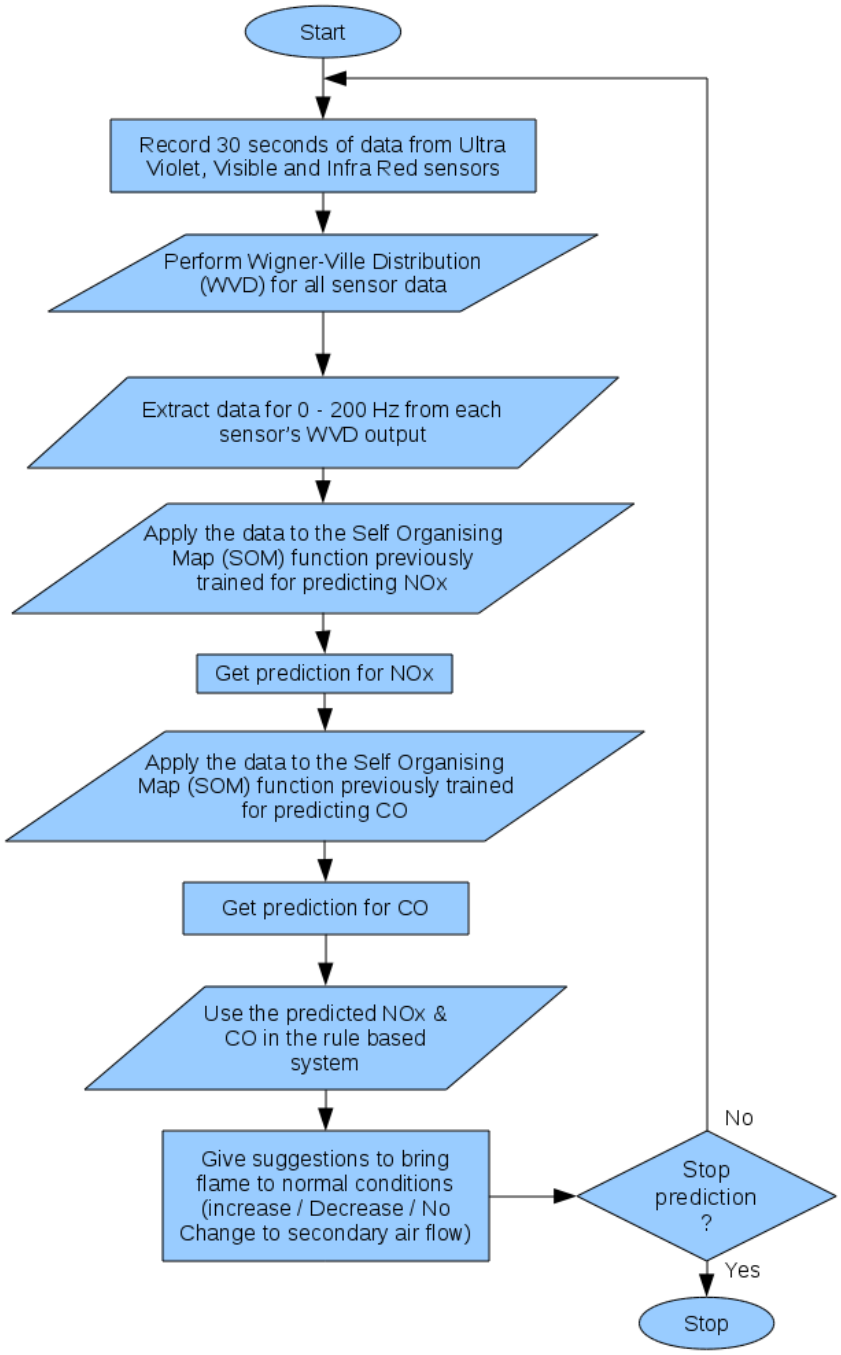

Figure 5.70: Algorithm for application of the SOM model

arrow representing 2 units, two arrows being 4 units and the up & down arrow being either increase or decrease. The unit here represents the air flow rate in Nm^3/h that can reliably be changed every time on the burner controls. 'Check settings / sensor' is used when NO_x and CO are both high as all the training tests used until now to train the system do not have this condition and when the

low conditions for both NO_x and CO, no change is need to the secondary air to the burner.

5.5 Summary

This chapter outlined the process in the selection of the detection algorithm that is used to process the sensor data to make predictions of the current state of combustion and suggest changes to rectify that if required. Initially, one of the most commonly used networks, BR back propagation ANN was utilised with varying number of hidden neurons to check the suitability of such a network for making NO_x and O_2 predictions. This first 3 case studies, showed that the number of features chosen wasn't enough for getting good predictions from the networks trained. This prompted the application of all the three signal processing methods - namely the RMS, PSD and RMS of the wavelet coefficients to be applied as inputs to train the back propagation ANN which showed some promise in terms of NO_x but had high MPPE for O_2 predictions.

Case study 4 showed some promise for NO_x predictions but had high MPPE for O_2. This case study still only utilised a small subset for testing out the detection algorithm. Hence case study 5 was carried out to include the entire set of experiments to train the ANN, the prediction of NO_x improved almost twofold compared to case study 4 with a subset of input experiments. O_2 prediction performance dipped even further, in addition to the network taking considerable time o be trained.

Case studies 6 and 7 were carried out to evaluate the application of the PCA to the ANN inputs to reduce the dimensionality by stripping principal components that contributed less than 2 %. This in turn reduced the training time, but it affected the prediction errors; adversely affecting NO_x and slightly improving the O_2, but despite this improvement the MPPE for O_2 was still above 20 %. So case studies 8 and 9 were evaluated to check if the prediction of some other parameter, total airflow to the burner could be better as it was better controlled than O_2. Total airflow prediction had much better performance than O_2 prediction but the overall MPPEs were still high and a different approach was tried out. Instead of trying to predict NO_x, O_2 or total airflow, the input data was applied to an unsupervised ANN to be classified to the nearest matching condition, changing it to a classification problem instead of a prediction.

Results obtained from the SOM seems to classify the combustion condition much better than the back propagation network previously employed. Training the map was simple, the features from the signal processing method was applied from a few (3 in this case) conditions from the steady state experiments and the classification was very good. This prompted the validation of the map with tests that had continuously varying airflow conditions and the performance of the SOM was promising and was presented in this chapter together with the workings of such a demonstration system that would be capable of doing this in real time to give suggestion to correct unfavourable combustion conditions. The next chapter (Chapter 6) would discuss the results from the application of this monitoring and control system in the pilot and full scale burners in an online basis.

Chapter 6

MONITORING AND CONTROL SYSTEM - TESTING AND RESULTS

This chapter discusses the performance of the Monitoring, Control and Optimisation (MCO) during testing at the pilot scale 500kW$_{th}$ Combustion Test Facility (CTF) located at the Institute Energitky - Institute of Power Engineering (IEn), Poland and the full scale tests at the Dolna Odra power plant, Poland.

6.1 Pilot Scale Testing

This section will present the testing of the MCO system at the pilot scale CTF at IEn. The layout of the burner, the sensor selection and placement, and signal analysis algorithms employed to process the acquired data have been presented in Chapters 3 and 4. Signals recorded from the three low cost photodiode sensors were processed using the Wigner-Ville Distribution (WVD) joint time-frequency signal processing algorithm and the 0 to 200 Hz (25 features) generated were then used to train an unsupervised Self-organising Map (SOM) as described in Section 5.4.

6.1.1 Experiments

Table 6.1 summarises all the experiments carried out to test the MCO system at the CTF. Each row covers one experiment and shows the initial start condition of the total airflow to the burner, followed by the fuel used for the test, and finally the fuel used to train the MCO system prior to its testing. It is important to note that the code & algorithms used in the burner MCO system was the same for the various thermal loads regardless of the variation in conditions used during the training phase and the results obtained vary in response to the knowledge the intelligent system has learnt from the training data. This testing was in fact spread over two testing periods, separated by a few months. There were some operational issues, as would be expected, that mainly resulted from slag build up. In order to facilitate the explanation Figure 6.1 shows a schematic of the MCO system, following the flowcharts shown in figures 5.69 & 5.70, in the previous chapter.

Table 6.1: MCO system testing at pilot scale CTF

Test Number	Initial condition (Airflow)	Fuel for testing the MCO system *	Fuel used to train the MCO system *
P1	High	90 % J + 10 % B	100 % J
P2	Low	90 % J + 10 % B	100 % J
P3	High	100 % R	100 % R
P4	Low	100 % J	100 % J
P5	High	100 % J	100 % J
P6	Low	90 % J + 10 % B	90 % J + 10 % B
P7	Low	100 % E	100 % J
P8	High	90 % E + 10 % B	100 % J

∗R - Russian coal J - Janina (Polish) coal
E - Ekogroszek (Polish) coal
B - Biomass in the form of agricultural straw

The MCO system collects the time series data from the optical sensors in the Ultra Violet (UV), Visible (VIS) and Infrared (IR) bands and processes this information with the WVD algorithm to yield the 25 features - the frequency bins between 0 to 200 Hz. These features are then passed to the SOM to classify whether the data collected belongs to a 'good' burner condition, where the flame is stable and the airflow to and the emissions from the burner are acceptable. This classification of the burner state was averaged over four minutes to ensure stochastic variations are minimised and then if the burner condition was not in this 'good' state corrective action was taken that was determined through a series of rules that provided a control action for nine different possible states (Table 5.22). Once these corrective actions were implemented manually to effect the desired change to the burner, the MCO system then repeated the above steps until the burner condition was returned to a 'good' state.

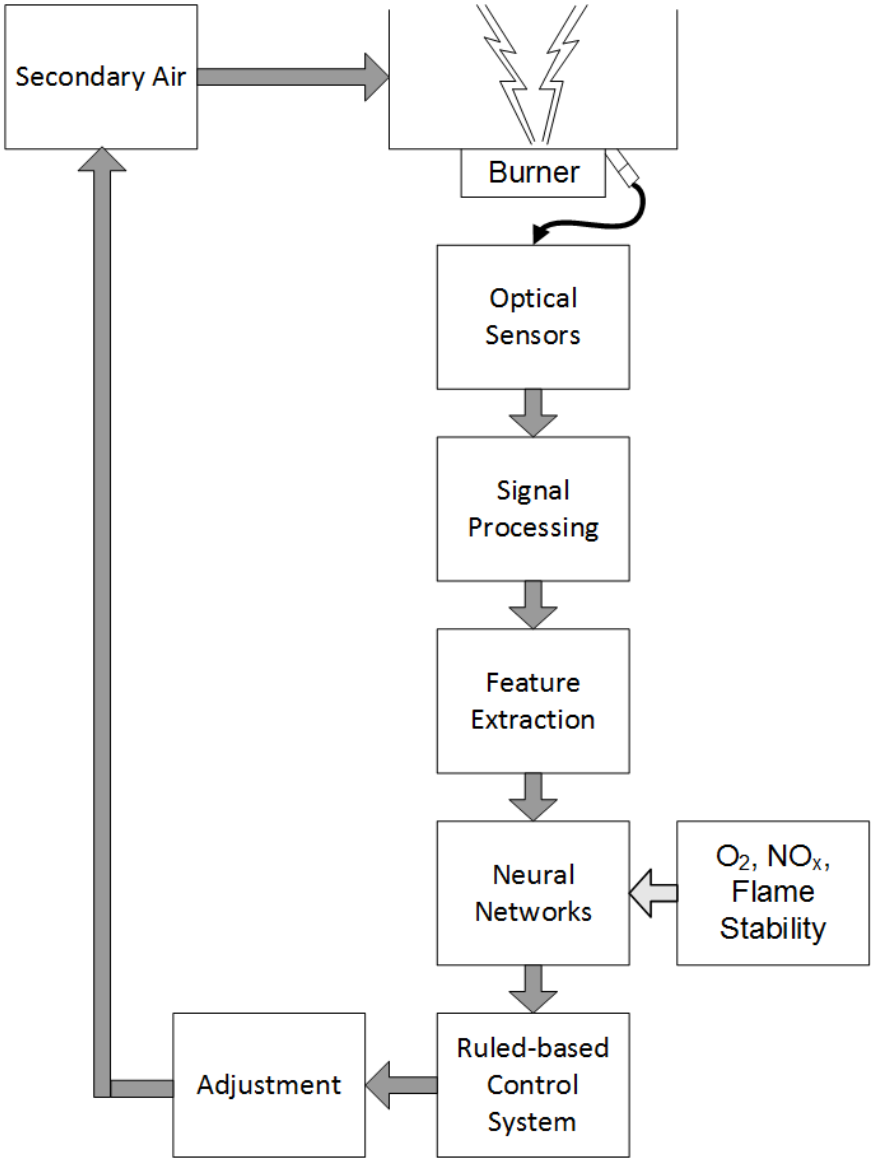

Figure 6.1: Schematic of the MCO system

6.1.2 Results & Discussion

The results from the pilot scale testing will be discussed by comparing the actual NO_x and CO measurements in the exhaust together with the predictions made by the intelligent MCO system during the range of experiments listed in Table 6.1.

Figure 6.2 shows the predicted NO_x and the actual measurements made by the gas analysers during Test P1 (Table 6.1) at the CTF in IEn, Poland. At the start of the experiment (left hand side of the graph) the total airflow of the burner was set much higher than the optimal condition and the objective of the experiment was to observe whether the MCO system could reduce the airflow to bring the emissions back to acceptable levels. As would be expected with a high airflow rate to the burner (hence high excess air) the NO_x emissions are higher than desired with the NO_x as measured in ppm in the exhaust being shown in blue in Figure 6.4. Each sample interval represents four minutes, over which the measurements and predictions were averaged, with the error bars presenting

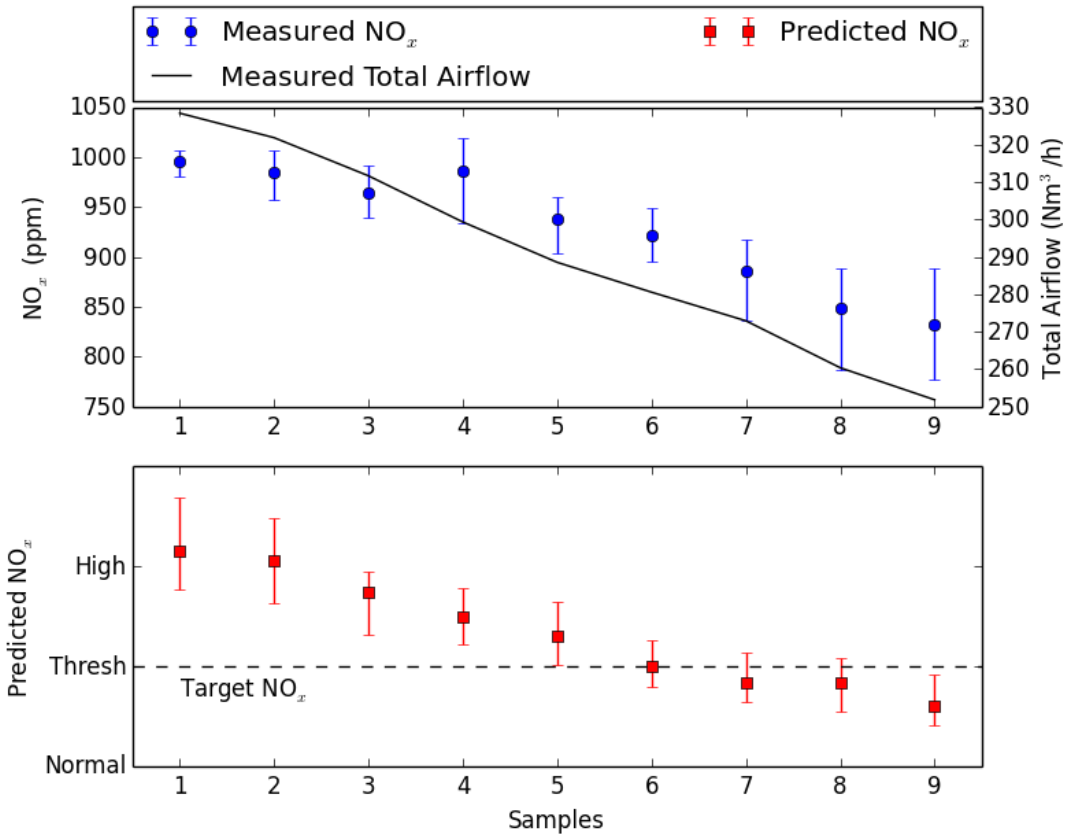

Figure 6.2: Comparison of Actual Vs Predicted NO_x in relation to Total airflow for 90 % Janina Coal + 10 % Biomass (Test P1 of Table 6.1)

the range of the variation during that time period. Similarly, the red squares represent the predicted NO_x during the same duration and the error bars showing the range of the predictions.

One criterion of the MCO system was to maintain the NO_x emissions below the acceptable upper limit for the combustion system, which is indicated by the dotted line. Therefore, for the MCO system, if the red square at any control step falls outside of the dotted threshold line, then a control action would need to take place and vice versa. Following the graph from left to right it can be seen that the predicted NO_x falls outside of the optimal range and so the MCO system reduces the airflow thereby reducing the NO_x. This process is repeated over six control steps before the NO_x is brought within the desired range through the reductions in airflow.

The MCO system used predictions of the CO (figure 6.3) together with the NO_x predictions to control the burner. Figure 6.3 shows the same experiment as Figure 6.2, but this time the data relating to CO is plotted together with the airflow. Again the start of the experiment is on the left hand side of the graph and as would be expected with a high airflow rate to the burner the CO measurements were very low. In fact CO readings were in general low suggesting good combustion but an arbitrary limit of just over 20 ppm was set to demonstrate the operation of the MCO system. As can be seen moving from left to right on the graph as the airflow was reduced the CO emissions increase (as would be expected) with the emissions reaching the target band after the eight control

steps.

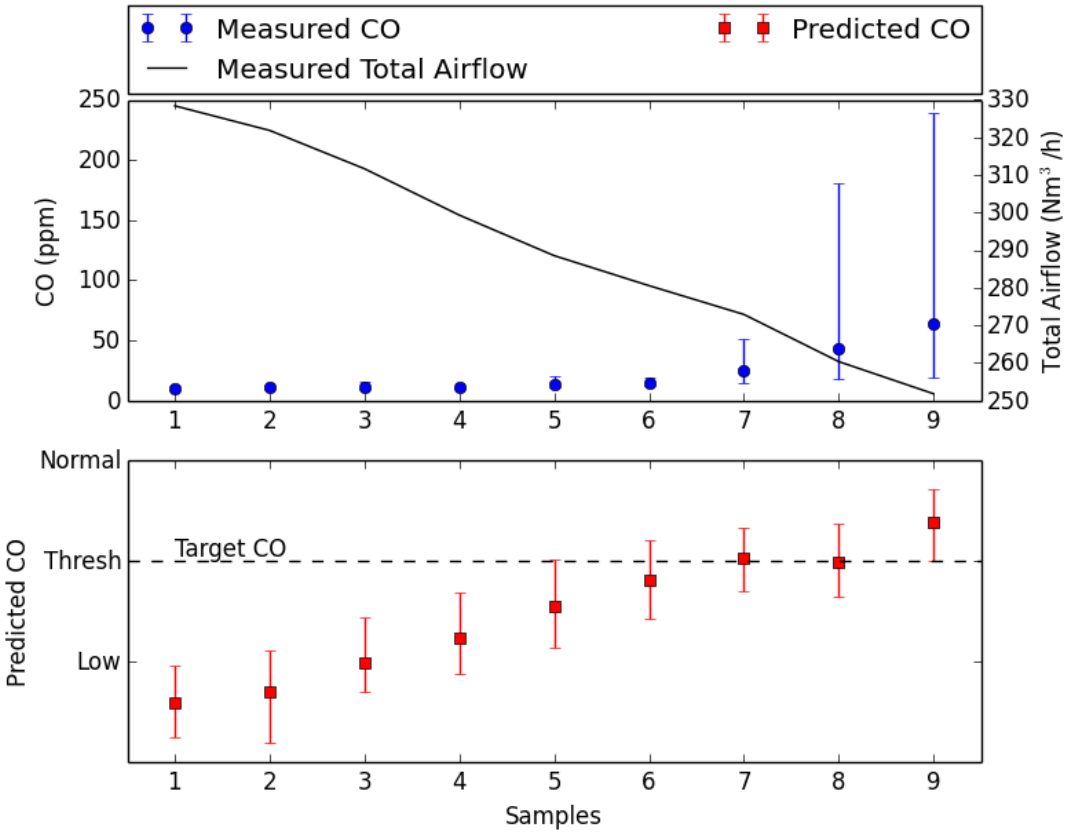

Figure 6.3: Comparison of Actual Vs Predicted CO in relation to Total airflow for 90 % Janina Coal + 10 % Biomass (Test P1 of Table 6.1)

This combination of reducing the airflow to enable the NO_x emissions to be reduced whilst also ensuring the competing objective of ensuring good combustion, as measured by the CO emissions, was achieved. It allowed the MCO system to optimise the flame and hence the combustion at the burner. The measured CO in ppm is represented by the blue circles whilst the red squares represent the predicted CO together with the respective error bars (Figure 6.3). The CO readings fluctuated towards samples 8 and 9 as the CO increased with decreasing airflow to the burner, the error bar shows the lowest and highest measured value in that time period. In the same way the dotted threshold line in the figure shows the optimal range for the predicted CO. The optimal region for both NO_x and CO varies for different fuels as well as thermal loads and has been arbitrarily set for this experiment to demonstrate the capability of the MCO system based on plant operator input. The important point to note for this experiment is that the experimental data used to train the MCO system were from the tests with 100 % Janina coal. However, the predictions shown in Figures 6.2 & 6.3 for the MCO system testing were for a mixture of 90 % Janina coal with 10 % biomass, so the predictions are unseen data from a new fuel blend for the SOM. This demonstrates that the MCO system was able to generalise enough information pertaining to the flame condition to be able to correctly classify the flame conditions to enable control, even though the system has not been presented with this fuel combination previously.

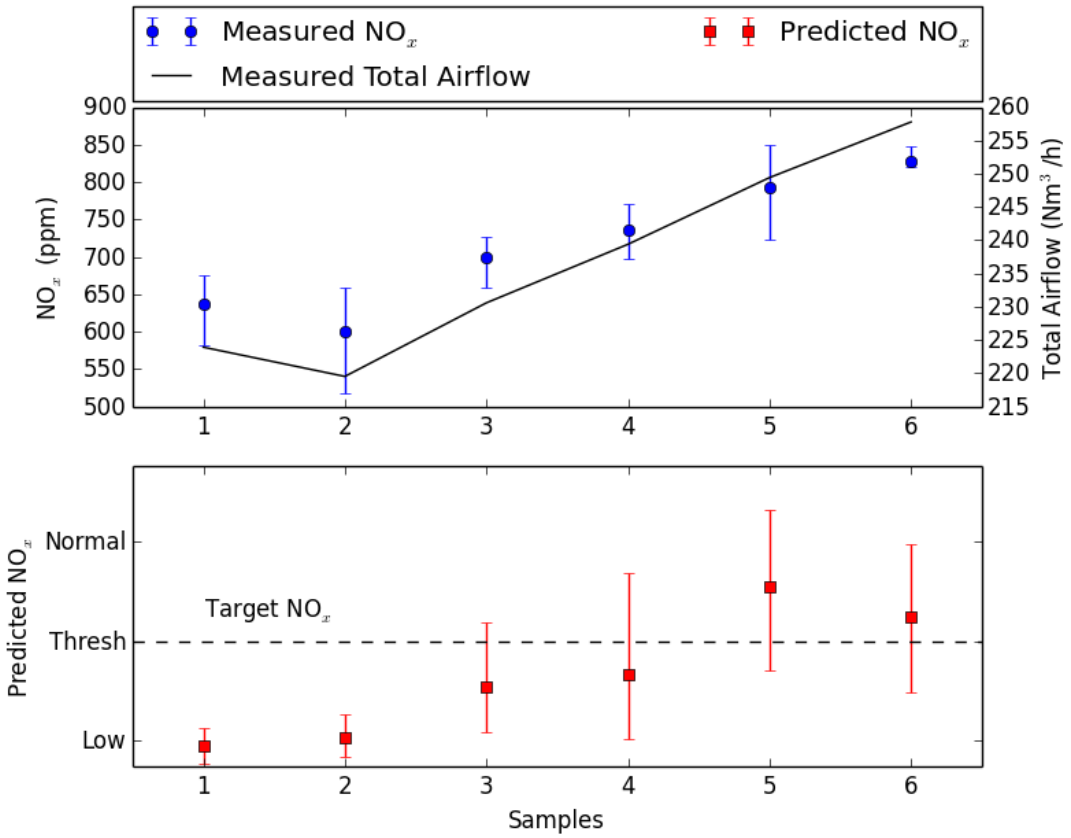

Figure 6.4: Comparison of Actual Vs Predicted NO_x in relation to Total airflow for 90 % Janina Coal + 10 % Biomass (Test P2 of Table 6.1)

Figures 6.4 & 6.5 present the results of the next experiment (Test P2 of Table 6.1) and are similar to the data presented in figures 6.2 & 6.3. The measured NO_x and CO are compared to the values predicted by the MCO system, but in this case, the airflow was increased from the initial low starting value until optimal conditions were reached. The above results demonstrate the performance of the MCO system when controlling the combustion of 90 % Janina coal with 10 % biomass, when the system has been trained with 100 % Janina coal. Taking figures 6.4 & 6.5 together, on the left hand side of the graphs the airflow is low with a corresponding low NO_x level but high CO. Then as the airflow is increased the NO_x increases and the CO reduces until after four control steps (sample 5 onwards in figures 6.4 & 6.5) the MCO system brings both the NO_x and CO to within the desired bands and maintains them there.

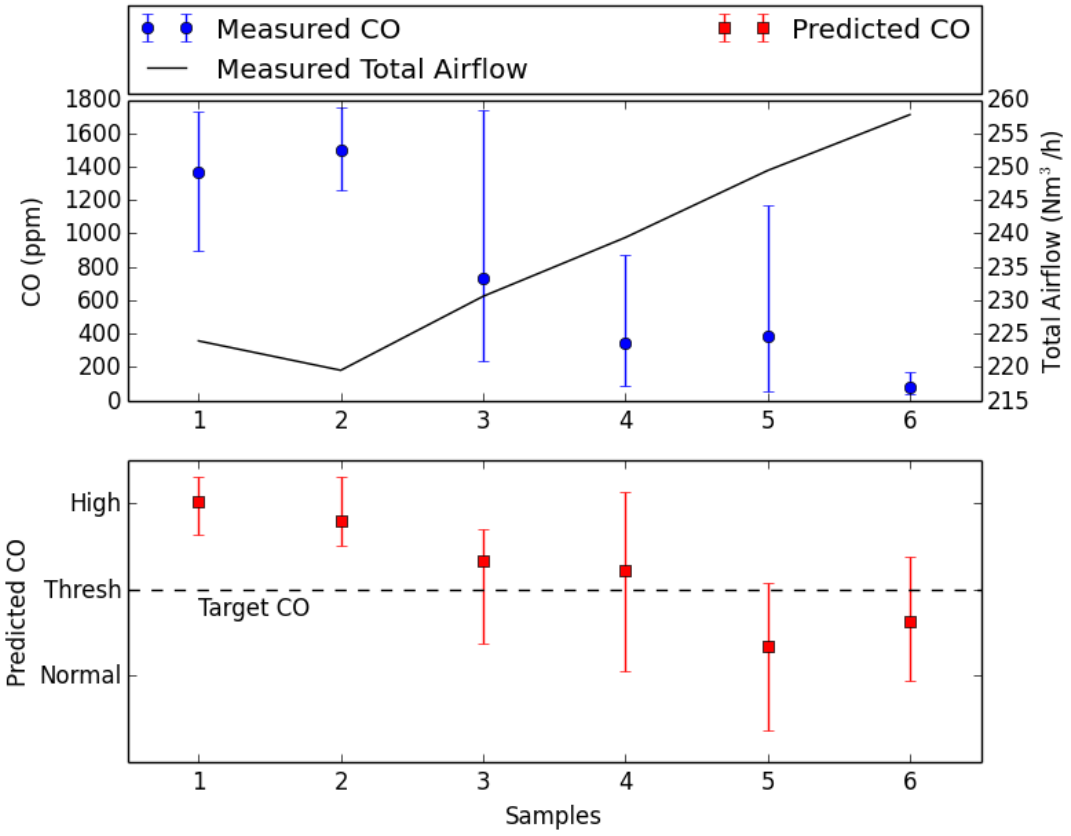

Figure 6.5: Comparison of Actual Vs Predicted NO_x in relation to Total airflow for 90 % Janina Coal + 10 % Biomass (Test P2 of Table 6.1)

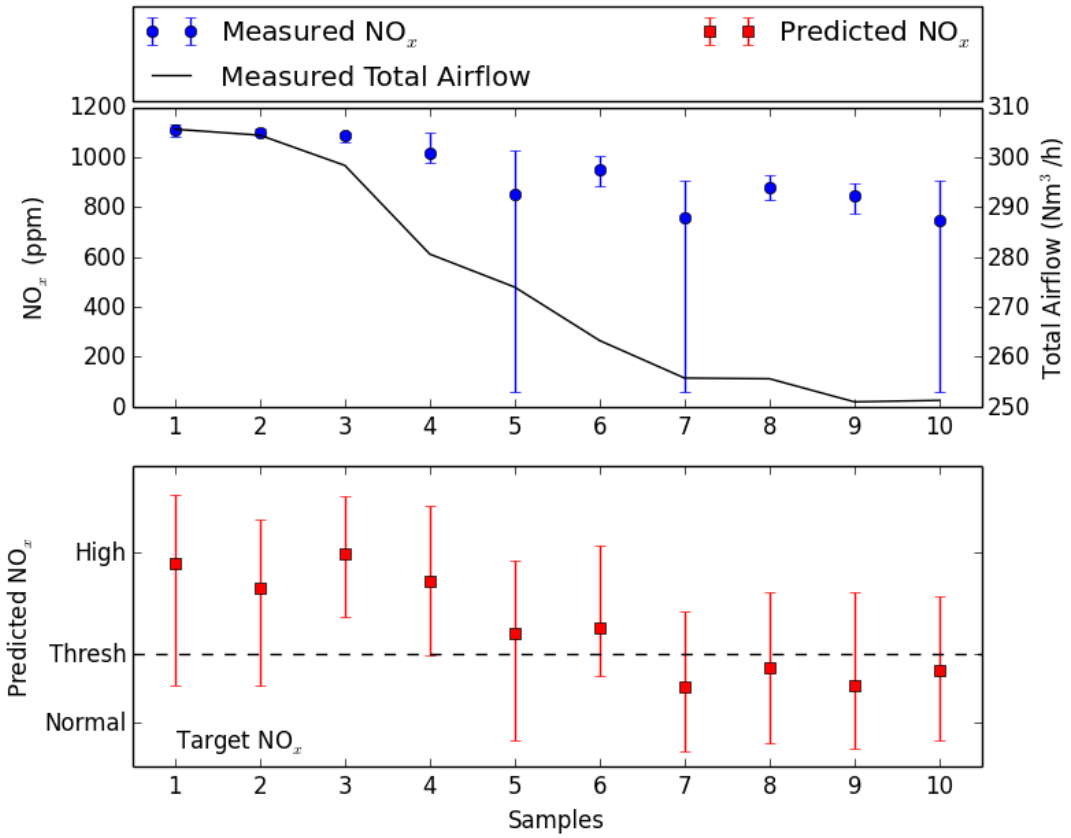

Figure 6.6: Comparison of Actual Vs Predicted NO_x in relation to Total airflow for 100 % Russian Coal (Test P3 of Table 6.1)

Figures 6.6 & 6.7 present the results with 100 % Russian coal (Test P3 of Table 6.1). In a similar manner to Test P1 the airflow was initially set to an overall high flow rate. The above results reflect the performance of the MCO system when controlling the combustion of 100 % Russian coal, when the system was trained with 100 % Russian coal. Taking figures 6.6 & 6.7 together, on the left hand side of the graphs the airflow is high with a corresponding high NO_x and low CO concentration. Then as the airflow is decreased the NO_x decreases and the CO increases until after sample 6. Sample 7 onwards in figures 6.6 & 6.7 the MCO system brings both the NO_x and CO within the desired bands and maintains them there. The error bars represent the smallest and largest values encountered during the measurement period for a sample, in this case samples 5, 7 and 10 generally had small deviations except for a few moments when it registered a small value and though to be of spurious nature and hence shows a very large error bar. It has to be noted that the NO_x values didn't usually fluctuate too much compared to CO measurements.

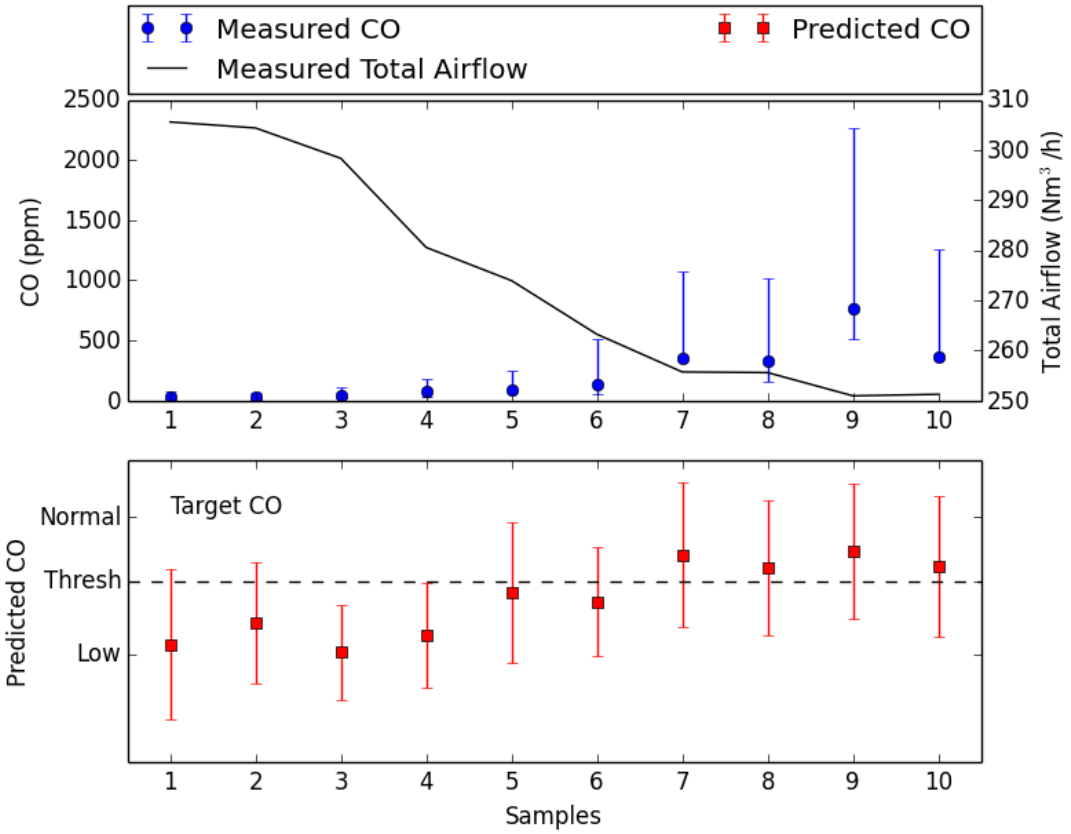

Figure 6.7: Comparison of Actual Vs Predicted NO_x in relation to Total airflow for 100 % Russian Coal (Test P3 of Table 6.1)

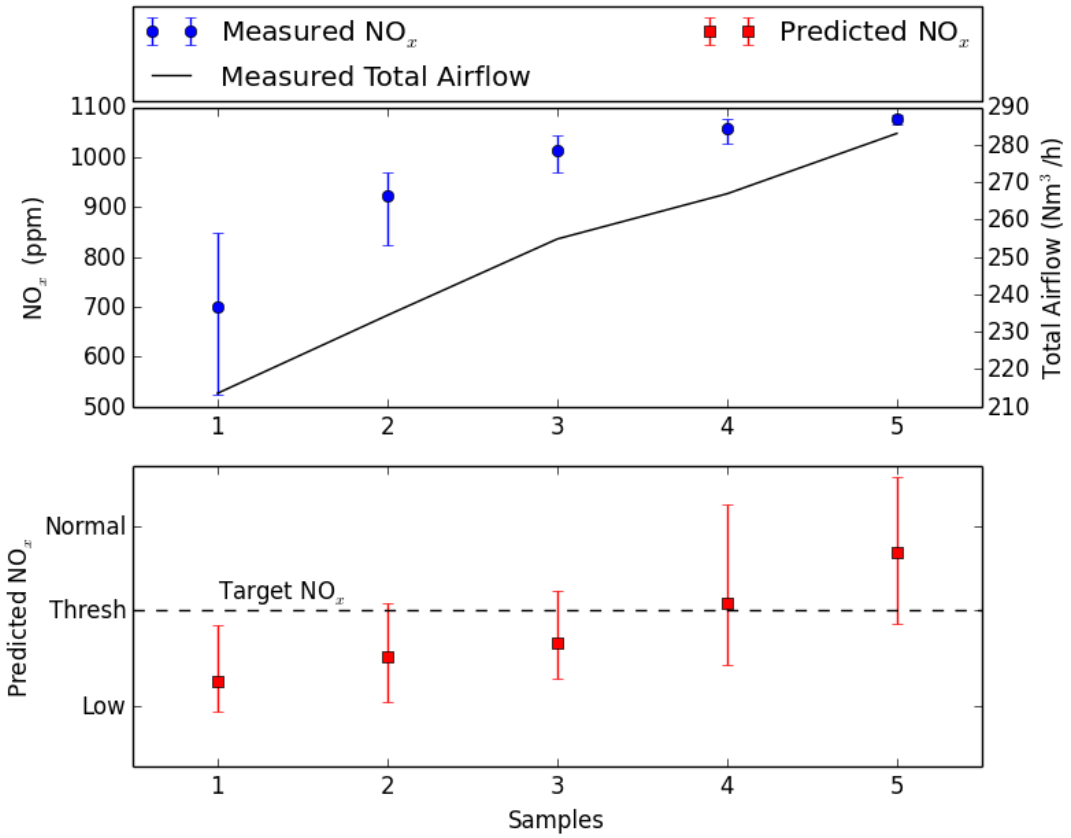

Figure 6.8: Comparison of Actual Vs Predicted NO_x in relation to Total airflow for 100 % Russian Coal (Test P4 of Table 6.1)

Figures 6.8 & 6.9 present the results with 100 % Janina coal (Test P4 of Table 6.1). In a similar manner to Test P2 the airflow was initially set to an overall low flow rate. The above results reflect the performance of the MCO system when controlling the combustion of 100 % Janina coal, when the system was trained with 100 % Janina coal. Taking figures 6.8 & 6.9 together, on the left hand side of the graphs the airflow is low with a corresponding low NO_x and high CO concentration. Then as the airflow is increased the NO_x increases and the CO decreases until after sample 4 onwards in figures 6.8 & 6.9 the MCO system brings both the NO_x and CO within the desired bands and maintains them there.

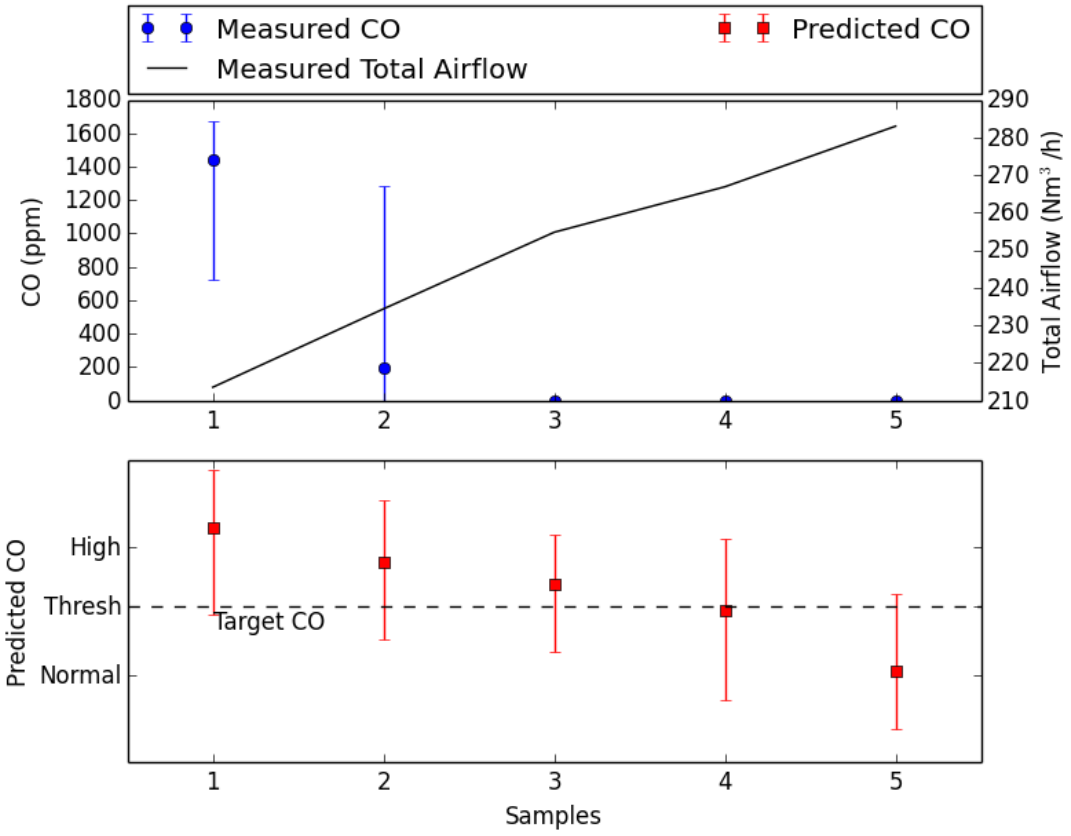

Figure 6.9: Comparison of Actual Vs Predicted NO_x in relation to Total airflow for 100 % Russian Coal (Test P4 of Table 6.1)

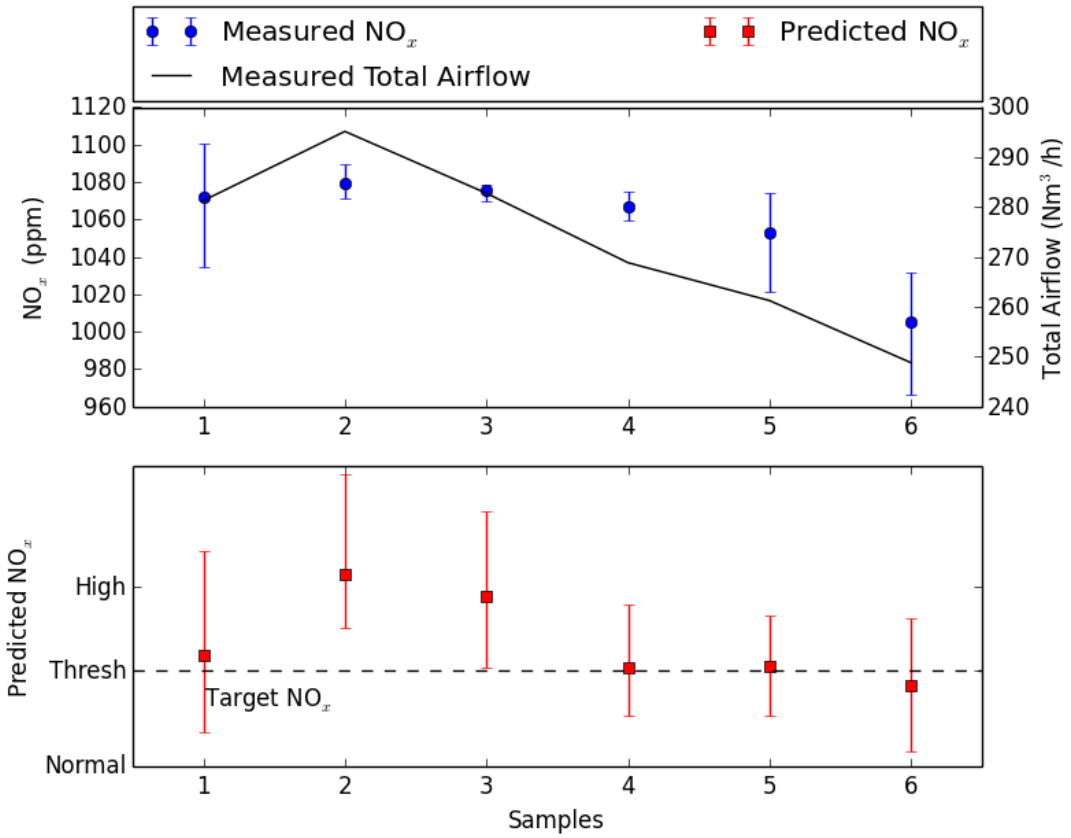

Figure 6.10: Comparison of Actual Vs Predicted NO_x in relation to Total airflow for 100 % Russian Coal (Test P5 of Table 6.1)

Figures 6.10 & 6.11 present the results with 100 % Janina coal (Test P5 of Table 6.1). In a similar manner to Test P1 the airflow was initially set to an overall high flow rate. The above results reflect the performance of the MCO system when controlling the combustion of 100 % Janina coal, when the system was trained with 100 % Janina coal. Taking figures 6.10 & 6.11 together, on the left hand side of the graphs the airflow is high with a corresponding high NO_x and low CO concentration. Then as the airflow is decreased the NO_x decreases and the CO increases until after sample 4 onwards in figures 6.10 & 6.11 the MCO system brings both the NO_x and CO within the desired bands and maintains them there. The CO readings saturated and the analyser didn't recover fast enough for further measurements so only the last known large value and the system saturation level have been noted in figure 6.11.

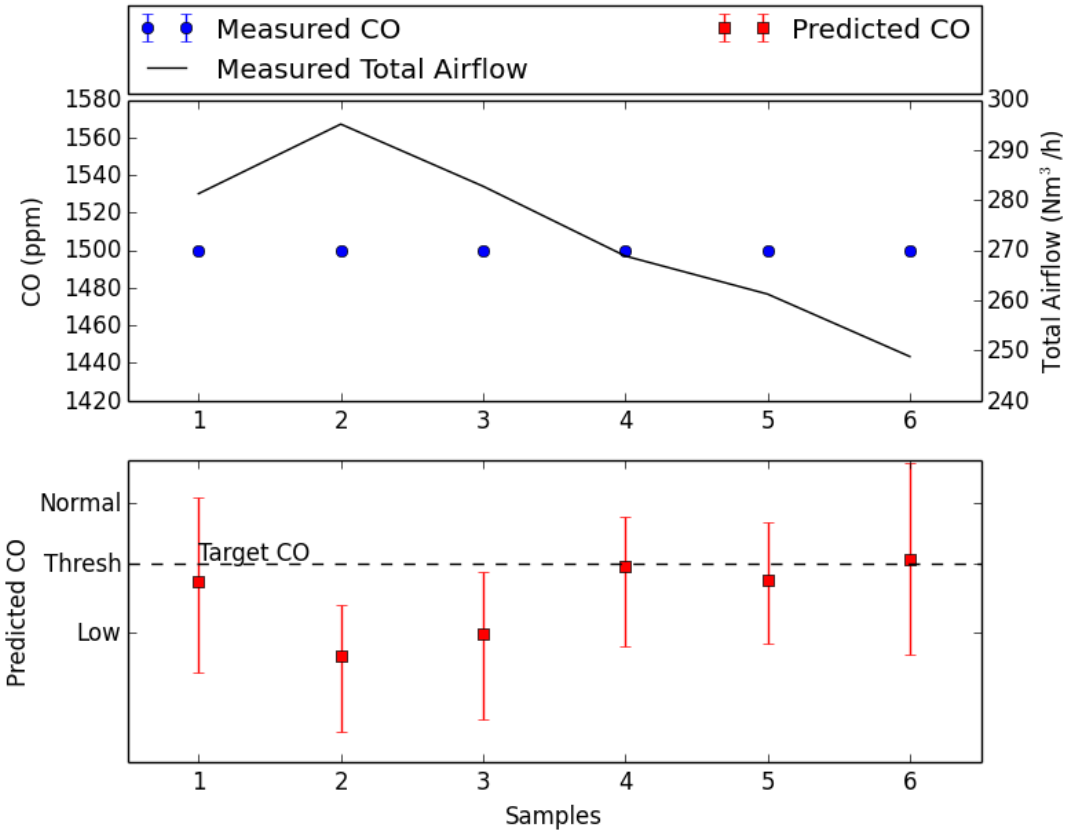

Figure 6.11: Comparison of Actual Vs Predicted NO_x in relation to Total airflow for 100 % Russian Coal (Test P5 of Table 6.1)

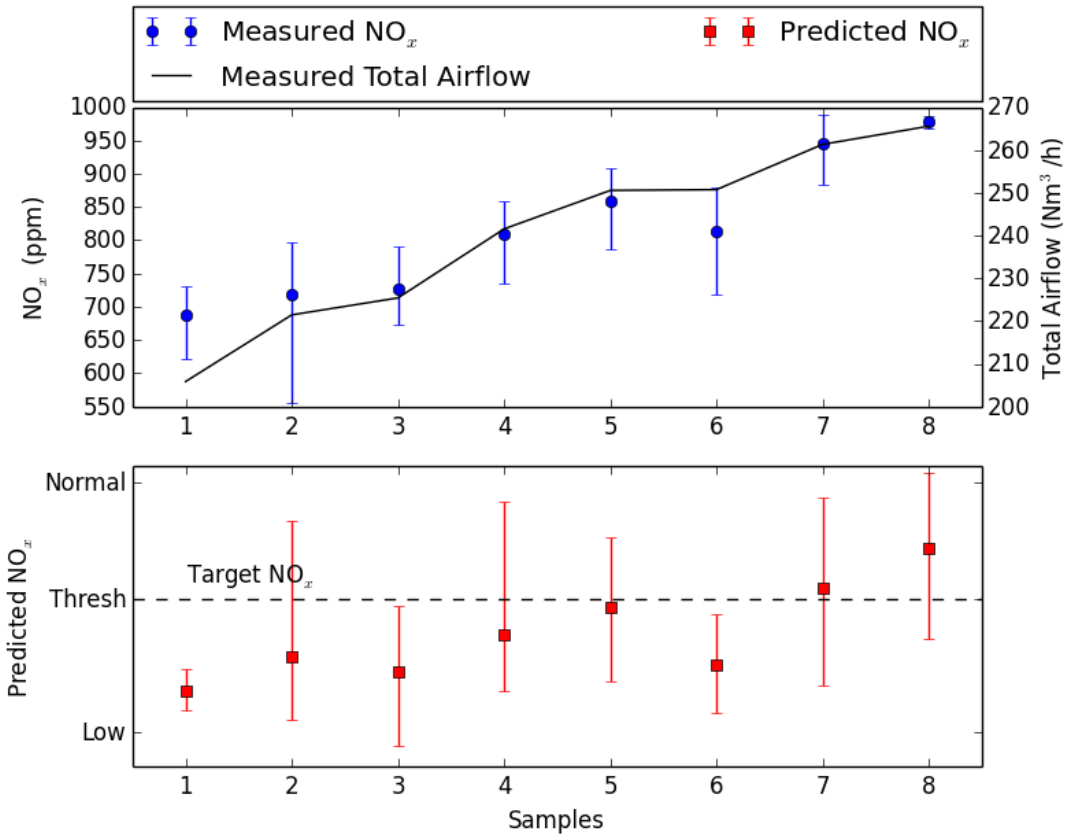

Figure 6.12: Comparison of Actual Vs Predicted NO_x in relation to Total airflow for 100 % Russian Coal (Test P6 of Table 6.1)

Figures 6.12 & 6.13 present the results with 90 % Janina coal and 10 % biomass (Test P6 of Table 6.1). In a similar manner to Test P2 the airflow was initially set to an overall low flow rate. The above results reflect the performance of the MCO system when controlling the combustion of 90 % Janina coal and 10 % biomass, when the system was trained with 90 % Janina coal and 10 % biomass. Taking figures 6.12 & 6.13 together, on the left hand side of the graphs the airflow is low with a corresponding low NO_x and high CO concentration. Then as the airflow is increased the NO_x increases and the CO decreases until after sample 7 onwards in figures 6.12 & 6.13 the MCO system brings both the NO_x and CO within the desired bands and maintains them there.

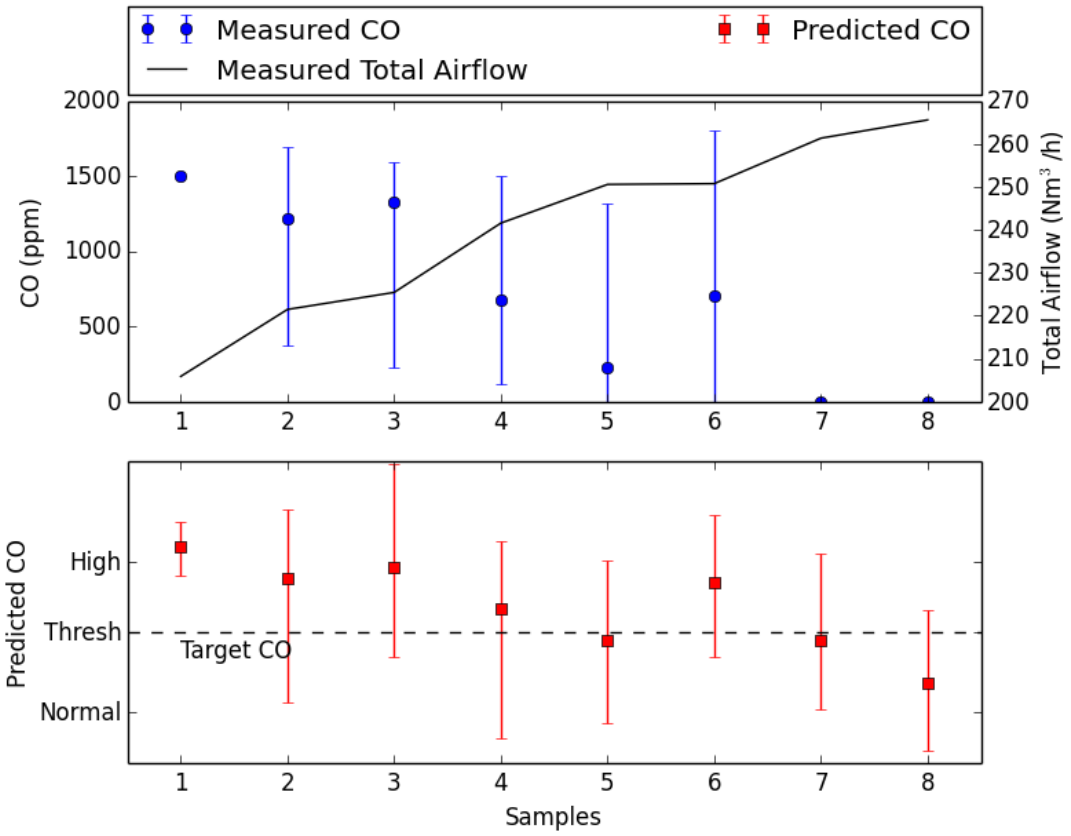

Figure 6.13: Comparison of Actual Vs Predicted NO_x in relation to Total airflow for 100 % Russian Coal (Test P6 of Table 6.1)

The tests when burning 100 % Russian coal, 100 % Janina coal and 90 % Janina coal /10 % biomass clearly demonstrated the capability and performance of the MCO system (figures 6.2 to 6.13). Other results on 100 % Ekogroszek coal (Test P7) or 90 % Ekogroszek coal / 10 % biomass (Test P8) when trained with 100 % Janina coal are not presented, as the MCO system was only able to predict the correct NO_x and CO trends but the absolute predictions didn't allow the MCO system to consistently take corrective actions to bring the combustion to normal range with emissions in the trained band. It is likely that the coal properties differed too widely (Table 3.1). In fact a visual observation detected that the coal burnt with a flame colour which had a bright orange tinge. The MCO system relies on the ability of the SOM to be able to categorise the flame information. In this case, the wide variation in coal properties between those used to train the system and those used during the MCO system tests resulted in incorrect predictions. The solution to this, in a practical application, would be to conduct a short commissioning run of the MCO system whenever the coal properties have varied beyond a certain range from those of the training conditions.

6.2 Full Scale Testing

This section will present the testing of the MCO system at the Dolna Odra power station in Poland. The layout of the burner, the sensor placement, and signal analysis algorithms employed to process the acquired data have been presented in previous chapters. Signals recorded from the three low cost sensors were processed using the WVD joint time-frequency signal processing algorithm and the features generated were used to train SOM as described in Section 5.4.

6.2.1 Experiments

In a similar manner to the experiments at the CTF, as demonstrated in the previous section (Section 6.1), it was decided to use three different thermal loads during the full scale experiments at the Dolna Odra power plant. In the case of this boiler, this resulted in fuel flow rates of 15 000, 20 000 and 25 000 kg/h to the monitored burners on the lowest level. This fuel flow was the total fuel supplied to the four burners on this level with the corresponding airflows being; low, optimal and high. The data from these experiments were used to train the MCO system, as can be seen in Table 3.10. Overall combustion was staged during normal operation of the boiler, and this lowest level of burners were operated sub-stoichiometrically to maintain NO_x below Polish and European Union (EU) regulatory limits. The implication of this was that the burners did not have a condition where the CO levels were ever low and this necessitated the training of the MCO system with just normal and high total airflow rates instead of the low, normal and high as carried out for the testing at the pilot scale in IEn.

A number of other factors that may affect the results are as follows:

1. Oil was combusted at higher levels in the boiler during the data gathering for training as well as testing of the MCO system (not continuously or all higher levels, but as and when needed) to allow the boiler to load balance, and cope with flame out conditions or when having problem with other fuel feeders.

2. Different numbers of the various burner levels were active during the tests due to varying electricity production demands.

3. Unavailability of the same type of coal to be used for MCO system testing experiments as the training experiments were carried out in different month to the MCO system testing.

4. Different coals being used throughout the experiments on a day to day basis as per normal operating procedures during the tests due to the amount of coal being burnt in a large power plant.

5. Over fire air to reduce NO_x emissions was also used at Dolna Odra compared to none used at the pilot scale burner at IEn.

6. Varying overall thermal load due to differing demand for electricity throughout the day.

Table 6.2: MCO system testing at full scale at Dolna Odra, Poland

Test Number	Total Airflow Initial condition**	Thermal Load**	Fuel used to test the MCO system*	Fuel used to train the MCO system*
F1	High	Low	F	B
F2	High	Medium	E	A
F3	High	Low	H	D

* with reference to Table 3.5
** with reference to Table 3.10

Table 6.2 summarises all the experiments carried out to test the MCO system at Dolna Odra. Each row summarises the initial start condition of the total airflow to the boiler, followed by the fuel used for testing and the fuel used to train the MCO system prior to testing. The MCO system performance and training tests at Dolna Odra were carried out a few months apart, hence the predictions varying only based on the training data obtained a few months before (and wasnt retrained with new training data). From Table 3.10 it is important to note that the coal used in the boiler had considerable variation in its calorific value with some changes occurring during the same day due to the quantity of coal being used within an hour. Table 6.2 relates the coal being used by the identification tag as assigned to each coal as listed out in the Table 3.5, under coal properties.

6.2.2 Results & Discussion - Single Burner

Very encouragingly the results obtained from the work conducted at Dolna Odra are quite similar to the results obtained from applying the MCO system in the CTF in IEn. The prediction of NO_x is accurate enough for the MCO system to be able to make decisions as to the correct course of action. Due to the bank of burners being operated sub-stoichiometrically the CO predictions were not as accurate and at times were inconsistent due to the inability of the gas analysers to measure values above 2500 ppm or values below 0.1 %. Also there were large difference in values between the low total airflow compared to the optimal or high total airflows. CO was measured using two gas analysers, one capable of measuring in multiples of 1 ppm up to 2500 ppm and the other capable of measuring in multiples of 0.1 % with approximate accuracy of 0.1 to 1 %, which leads to inaccuracies when the value measured is between 2500 ppm or 0.25 % to 1 %. This necessitated changing the rule based algorithm for control at Dolna Odra, where only the NO_x was taken into consideration for making a prediction. A sample of the CO prediction for 15 000 kg/h thermal load is shown in figure 6.15.

In a similar manner to the pilot scale tests, figures 6.14 & 6.16 compare the NO_x predictions to the actual values measured with reference to the total airflow to the burner at fuel flow rates of 15 000 and 20 000 kg/h (low and medium) when burning 100 % coal (Tests F1 and F2 respectively of Table 6.2). At the start of the experiment (left hand side of the graph) the total airflow of the

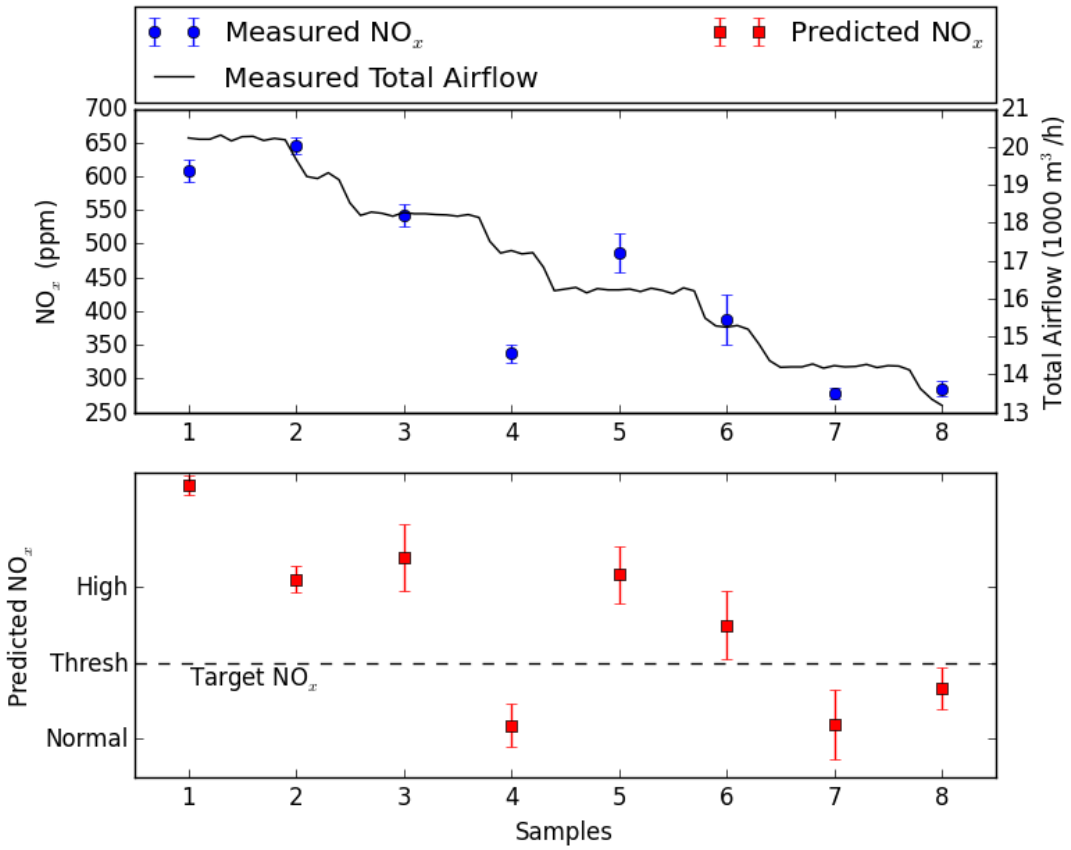

Figure 6.14: Comparison of Actual Vs Predicted NO_x in relation to Total airflow for 100 % Coal F at thermal load of 15 000 kg/h (to the lowest level of burners)(Test F1 of Table 6.2)

burner was set much higher than the optimal condition and the objective of the experiment was to observe whether the MCO system could reduce the airflow to bring the emissions back to acceptable levels. Blue dots in figures 6.14 & 6.16 represent the averaged actual measured NO_x in ppm from the gas sampler, the error bars represent the variation during the measurement period of 4 minutes. Similarly, red squares represent the predicted NO_x while maintaining the same burner conditions as actual measured values. If the predictions (red squares) fall within the normal band, above the dotted threshold line (representing the stable / optimal value of NO_x for the particular condition), no control action is required and vice versa. The actual measured NO_x (blue dots) are plotted against the measured total airflow to the burner which is represented by the black line and is expressed in units of 1000 m^3/h.

Figures 6.14 & 6.16 clearly show the decreasing NO_x trend, both for the measurements and the predictions as the total airflow to the burner is decreased, as would be expected. Similar success at predicting the NO_x and controlling the airflow to the burner is shown in figure 6.17 for a test with 90 % coal & 10 % biomass for a medium firing rate. In figures 6.14, 6.16 & 6.17 it is also possible to observe the manner with which the MCO system reduced the airflow with the steps being clearly visible in the solid black line. Reduced performance was observed for the tests at the maximum coal feed rate (25 000 kg/h). This might have resulted from changes in the flame length that would be expected to occur

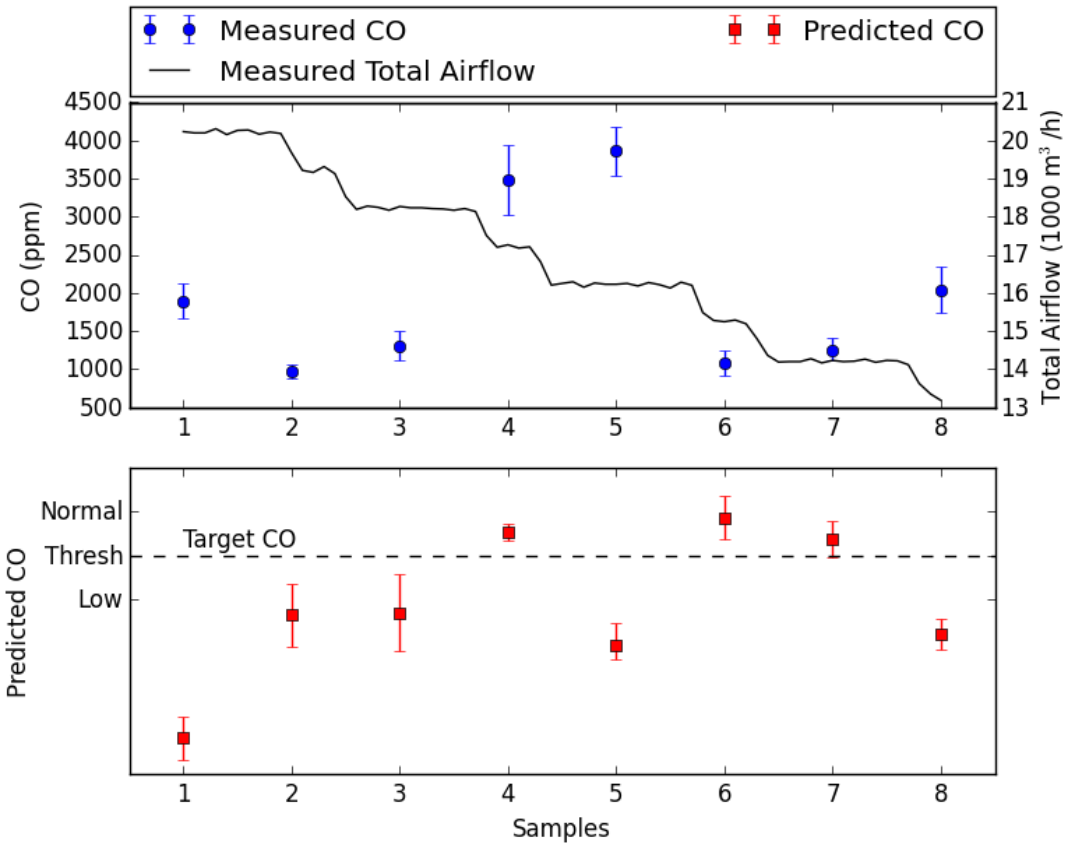

Figure 6.15: Comparison of Actual Vs Predicted CO in relation to Total airflow for 100 % Coal F at thermal load of 15 000 kg/h (to the lowest level of burners)(Test F1 of Table 6.2)

with different coal feed rates. The longer flame meant that due to the fixed viewing angle of the observation port, the MCO system imaged a different part of the flame.

The MCO system was able to predict reasonably well even though the coal biomass blend was different to the one used to train the MCO system. This result demonstrates that the MCO system can be trained with one coal / coal biomass blend but as long as the properties of the coal biomass blend is not too different, it is still possible to control the burner. If the coal properties vary more widely, then retraining of the MCO system is necessary as observed from the pilot scale testing results as discussed earlier in Section 6.1.2.

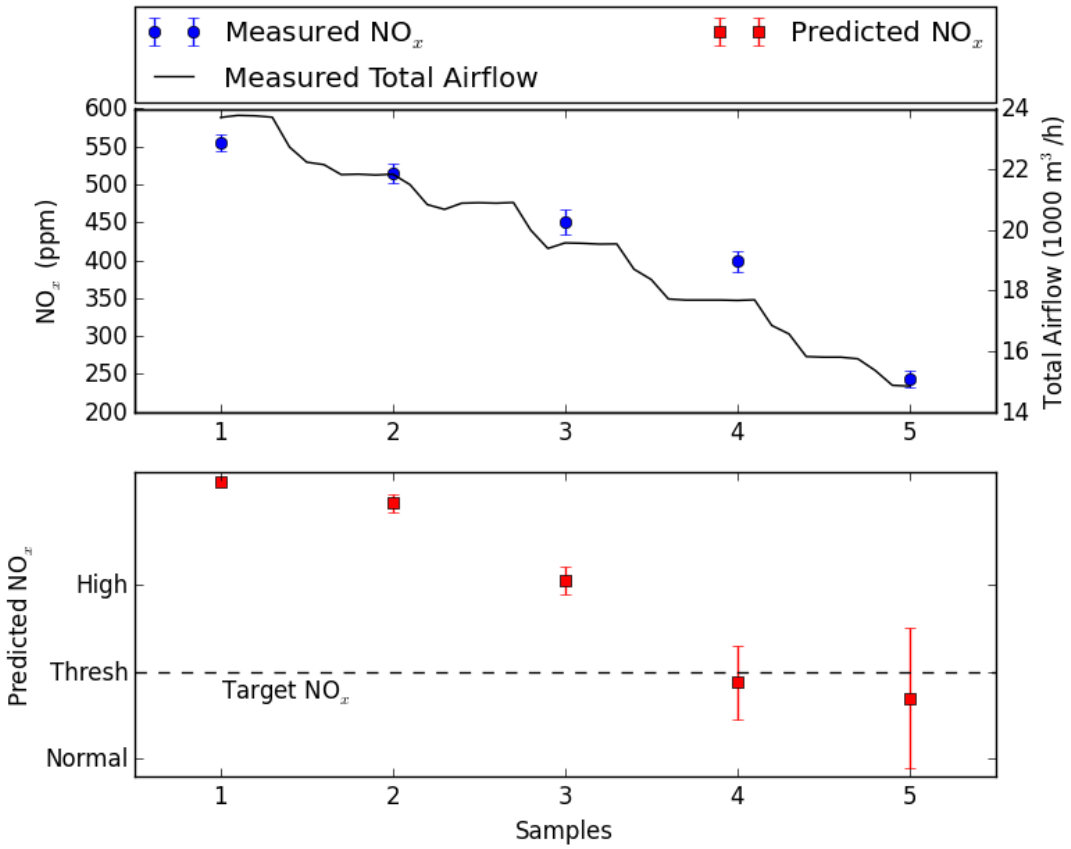

Figure 6.16: Comparison of Actual Vs Predicted NO_x in relation to Total airflow for 100 % Coal E at thermal load of 20 000 kg/h (to the lowest level of burners)(Test F2 of Table 6.2)

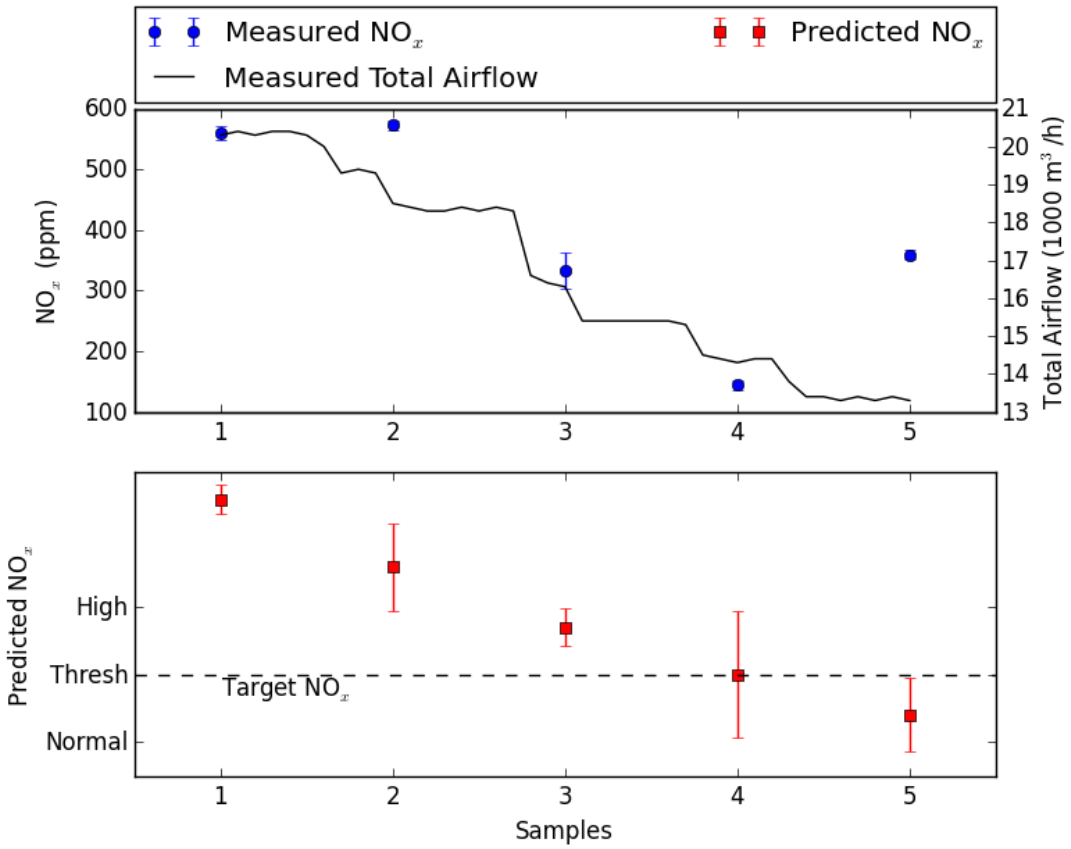

Figure 6.17: Comparison of Actual Vs Predicted NO_x in relation to Total airflow for 90 % Coal H + 10 % Biomass at thermal load of 15 000 kg/h (to the lowest level of burners)(Test F3 of Table 6.2)

6.2.3 Results & Discussion - Multi-Burner Balancing

All the experiments for training the MCO system at Dolna Odra were performed on two burners and the MCO system was able to quite accurately predict the NO_x values as discussed above in Section 6.2.2. The MCO system was then able to suggest appropriate changes to be effected to return the burner to optimal conditions (in the case of Dolna Odra, reducing total airflow to run the lowest level of burners at sub-stiochiometric conditions).

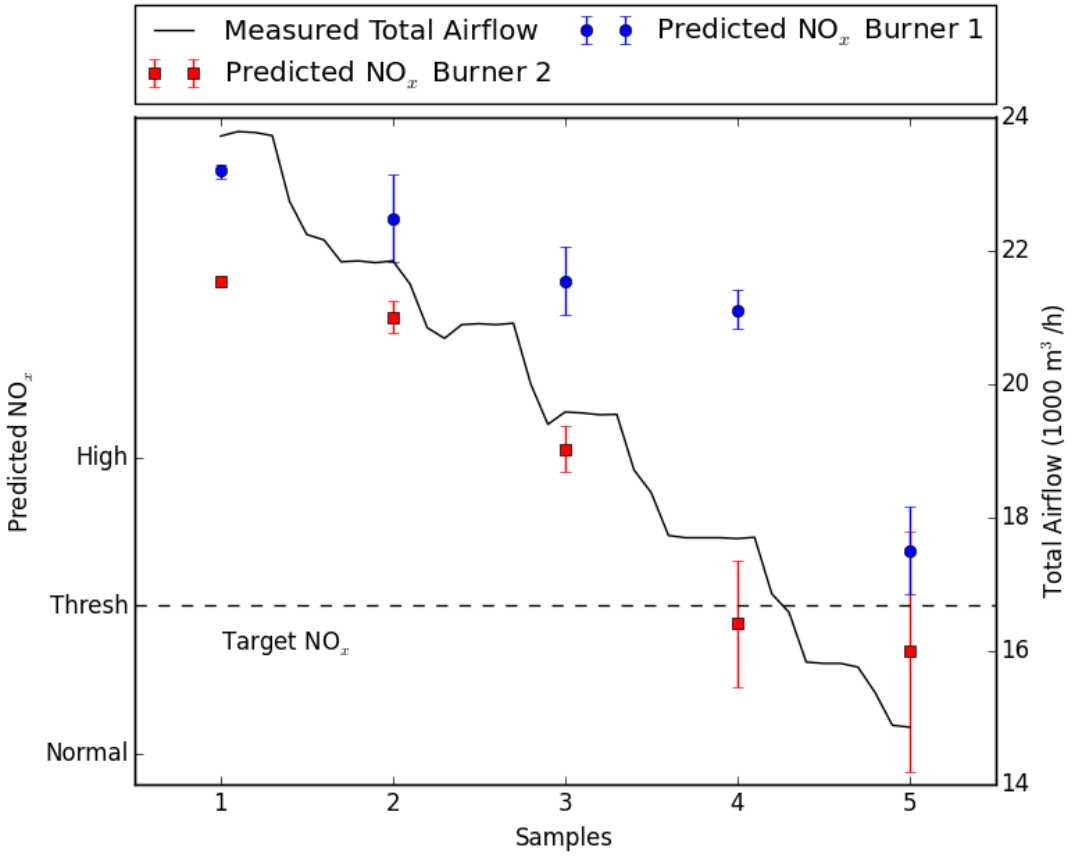

Figure 6.18: Comparison of predicted NO_x in burners 1 and 2 in relation to Total airflow for 100 % Coal at thermal load of 20 000 kg/h (to the lowest level of burners)(Test F2 of Table 6.2)

Figure 6.18 shows a comparison between the predicted NO_x for burners 1 and 2 for a coal feed rate of 20 000 kg/h together with the measured total airflow to the burners when burning 100 % coal. During the tests at Dolna Odra it was not possible to separately control the airflow to the burners in a bank. This means during the application of the MCO system, the system had to attempt to determine the best compromise in airflow to optimise both burners. Figure 6.18 shows the predictions that were generated by the MCO system by using the algorithm as discussed in previous chapter (Section 5.4), except that the prediction was performed once for each of the burners being monitored. Once the predictions for both the burners were obtained, the corrective action was based on the median of the two predictions of NO_x. At the start of the experiment (Sample 1) the predicted NO_x values are very similar, then as the experiment progresses (Samples 3 & 4) although the prediction trend is correct the predictions for burner 1

are much higher than those for burner 2. This would appear to indicate that there were differences between the combustion of the two burners that the MCO system has identified. The objective of the experiment was to reduce a high total airflow, which caused suboptimal NO_x emissions, to a more optimal condition and balance the NO_x emissions from the two burners. The interesting part of the figure occurs at sample 4, where the NO_x predictions for burner 2 are within the optimal emission band whereas those for burner 1 are higher than optimal at the same time. Following the subsequent corrective control action suggested by the MCO system (sample 5 of figure 6.18) burner 2 is still within the optimal emission band and burner 1 is very near optimal target band. Any further reductions in airflow to the bank of burners would have probably resulted in the NO_x emissions for burner 2 falling outside of the optimal band. Therefore the experiment was stopped at this point. It has therefore been demonstrated that the MCO system can balance burners, although separate control of the airflow to individual burners would result in the ability to individually tune burners to ensure that the emissions are optimal.

6.3 Summary

This chapter outlined the results from the performance testing of the MCO system being applied at pilot and full scale plants. At pilot scale, a number of tests to check the capability of the developed MCO system was carried out with various fuels, especially when the system was trained with data from different fuel composition providing the system with unseen data. The prediction capability of the system was very good with identification of abnormal combustion conditions and correctly suggesting changes to secondary air to get the emissions to the target region. This capability of the system to make predictions and suggest changes was tried out on many fuel blends, but the capability degraded when the changes in coal (fuel) properties was quite large between the conditions used to train the system and the currently used fuel. In practical usage, this would mean a retraining (or continuous training) of the system whenever the fuel properties vary by a large margin.

The MCO system was tested at the Dolna Odra power plant for the full scale tests, while they were operating and producing electricity. The tests used for training and the performance testing of the MCO system were carried out a few months apart and the coal properties varied on day to day basis. Two low NO_x burners of the lowest level of a tangentially fired boiler were monitored for these full scale tests. These burners were chosen because of availability and accessibility of ports on the lowest level. Also the high CO concentrations affected the CO measurement as this level of burners were run at sub-stoichiometrically to keep lower NO_x with over fire air. Hence the performance testing only looked at NO_x emissions due this issue.

The results from the performance testing at full scale again shows the capability of the MCO system to make predictions and suggestions based on a rule based system to correct these abnormal combustion conditions. This has been demonstrated with different fuel blends over multiple days and with various thermal loads as well on an online real-time basis.

Chapter 7

CONCLUSIONS AND FURTHER WORK

7.1 Conclusions

One short term approach to utilise biomass is to co-fire in Pulverised Coal (PC) boilers built for coal combustion, with minimal cost and modifications to existing facilities. So the system developed as part of this research is capable of identifying abnormal conditions leading to unstable flames that might affect utilisation of biomass whilst co-firing in existing boilers.

As part of the research, a novel three broadband sensors in Ultra Violet (UV), Visible (VIS) and Infrared (IR) range were utilised for monitoring co-firing flames. The sensors were capable of monitoring co-firing flames with suitable signal processing algorithms, this was initially developed and tested at pilot scale and was eventually demonstrated at full scale in Dolna Odra plant. In this research this was demonstrated with a computer running the signal processing algorithms, but this could be miniaturised to a single board / instrumentation as discussed in section 7.2.

A number of experiments were initially carried out to select an appropriate signal processing algorithm for this research where only one parameter was varied. From these experiments, it wasn't possible to extract any consistent features from the three sensors that correlated with the input to the burners or to NO_x, CO or total airflow to the burner from simpler signal processing methods in either the time or frequency domains.

Further to this, advanced signal processing methods from the Joint Time Frequency (JTF) domain were considered and these fared slightly better in showing some trends in the sensor readings. Again, similar to earlier signal processing methods lacked sufficient information to be utilised on its own in a set points based system to identify a specific combustion condition, they weren't systematic with the changes made to the operating conditions, especially with varying thermal loads. The trends were however much clearer with JTF methods for the same experiments compared to the other signal processing methods used in this research.

Coal combustion is a complex process and other researchers have handled monitoring such a complex process using Artificial Neural Network (ANN) as illustrated in the literature review. In this research, ANN with back propagation

was utilised to predict emissions based on the three sensor data as these could be related and measured. ANN with back propagation based processing of the three sensor data using the simpler time and frequency domain signal processing methods weren't capable of gleaning enough information for the system to learn to predict NO_x, CO or total airflow to the burner correctly. Varying number of hidden neurons were tried before selection of the best performing network based on the least mean percentage prediction error (MPPE) when applied with the processed data from the three sensors.

Since ANN with back propagation based on simpler signal processing didn't yield good results, more computationally intensive JTF methods were tried. The results were promising for some of the experiments, but validation with completely unseen data resulted in poor prediction accuracy meaning generalisation capability of the trained network was poor for the given sensor data. Prediction of O_2 using ANN with back propagation was not effective in this research as the O_2 measurements weren't very near the burner and hence weren't representative of the combustion condition in the burner.

With reference to the prediction results obtained using ANN with back propagation, it was not possible to have a system capable of monitoring and control of co-firing flames that could adapt to varying thermal loads and slight changes to fuel properties as is expected in a power station boiler. So the problem was approached in a slightly different angle, instead of trying to predict values of emission or total airflow, classification of the combustion condition using Self-organising Map (SOM), which is a type of ANN with unsupervised learning. Again, similar to the previous ANN predictions with simpler time or frequency methods, the SOM ones weren't performing very well as these signal processing methods didn't produce many features that the neural network could learn from. SOM with Wigner-Ville Distribution (WVD) processed data from the three sensors was able to classify the conditions correctly and during validation, the system was even able to identify conditions which were similar or in-between conditions used to train correctly. Then a simple rule based algorithm was used to suggest changes to the burner inputs, which the burner operator could follow to get the desirable condition.

The SOM based system was initially trialled in real-time at the pilot scale plant trained with three conditions, namely the ideal condition that the operator wants to operate and two conditions with higher and lower total airflow to the burner that are most likely to be encountered. The system identified the presented conditions correctly and suggested the changes as required for the burner operator, where the fuel used for training and testing were the same. To test the generalisation of the system, conditions with varying total airflow and thermal load to the burner were presented and the system performed very well in identifying these changes and classified correctly.

To further evaluate the generalisation capability of the developed monitoring and control system, different coals were carried out. The results showed the system was capable of identifying the conditions correctly as long as the coal/biomass blend used is similar to the one used for training the system. If it varied too widely, then the system needed to be retrained with the new fuel type. This training needs to be done only once per fuel, and could be reused whenever the fuel is reused.

Once the system was successfully demonstrated at pilot scale, the Monitoring, Control and Optimisation (MCO) was trialled at full scale plant at Dolna Odra. The system was again trained with at least three conditions and successfully predicted the conditions presented to it when the fuel used was same or similar between the training and testing phases. As noted before, the system needed retraining if the fuel properties used for testing varied too much from the fuel used for training.

The generalisation capability of the SOM reduces the need for retraining whenever fuel properties vary only slightly. This project has showed that such a system would be a promising means to aid boiler operators to optimise co-firing coal and biomass flames when higher biomass content in such fuels push the stable operating envelope. Finally, for such a system to be of practical use, long term testing and demonstration using multiple fuels would be required, which is beyond the scope of the current research.

7.2 Recommendations for Further Work

The results from the current research was encouraging and could be extended as follows in a number of areas:

1. Additional tests of longer term nature should be carried out to validate the systems' capability to 'learn' and generalise.

2. For long terms tests or regular usage, a miniaturised system which fits into a smaller box or tube with an embedded processor and all sensor associated electronics would be desirable, similar to off-the-shelf flame detectors.

3. The learning phase of the SOM in this research was carried out on a computer, this would either need a embedded processor (such as Micorchip Inc.'s 32MX family) to have all the necessary custom code to directly learn on demand from some of the data monitored by the system or a recording function within the embedded system that could be easily downloaded to be carried out on a computer.

4. Another related area of interest might be the specific wavelength monitoring of OH^*, CH^* and their ratios for condition monitoring, though the cost of such sensors (Photo-Multiplier Tubes) are much higher than the broadband sensors used here.

5. The system could be developed with some standard interfaces so that it could be easily integrated with the existing plant control system to extend its usability, this might help utility operators to fire higher ratios of biomass.

6. Hybrid or multiple types of ANNs could be investigated to see if the prediction capability could be improved with additional parameters being predicted to enhance combustion efficiency and optimise other operational parameters such as temperature and un-burnt carbon (UBC).

Bibliography

[1] International Energy Agency. *Power Generation from Coal - Measuring and Reporting Efficiency Performance and CO_2 Emissions*. Tech. rep. Paris, France, 2010.

[2] R. Heinberg. *Blackout: Coal, Climate and the Last Energy Crisis*. United Kingdom: Clairview Books, 2009.

[3] Anthony F Armor. "Advanced Fossil Fuel Power Systems". In: *Energy Conservation*. CRC Press, 2007. Chap. 13, pp. 13-1 –13-29. URL: http://www.crcnetbase.com/isbn/9781420044324 (visited on 21st July 2015).

[4] Department of Energy & Climate Change. *Energy Trends*. Dec. 2015. URL: https://www.gov.uk/government/uploads/system/uploads/attachment_data/file/487870/ET_Dec_15.pdf (visited on 14th Mar. 2016).

[5] BP. *Statistical Review of World Energy*. June 2015. URL: http://www.bp.com/content/dam/bp/pdf/energy-economics/statistical-review-2015/bp-statistical-review-of-world-energy-2015-full-report.pdf (visited on 14th Mar. 2016).

[6] International Energy Agency. *India Energy Outlook*. Tech. rep. Paris, France, 2015. URL: http://www.worldenergyoutlook.org/media/weowebsite/2015/IndiaEnergyOutlook_WEO2015.pdf (visited on 14th Mar. 2016).

[7] BP. *What drives energy demand?* June 2016. URL: http://www.bp.com/en/global/corporate/energy-economics/energy-outlook-2035/drivers-of-energy-demand.html (visited on 14th Mar. 2016).

[8] Sunggyu Lee, James G Speight and Sudarshan K Loyalka. *Handbook of Alternative Fuel Technologies*. Boca Raton, CRC Press, 2007, pp. 1–23.

[9] M Sami, K Annamalai and M Wooldridge. "Co-firing of coal and biomass fuel blends". In: *Progress in Energy and Combustion Science* 27.2 (2001), pp. 171–214.

[10] M J Cooke. *Coal R&D Successes in the UK*. Tech. rep. Cheltenham, UK: The Coal Research Forum, June 1996. URL: http://www.coalresearchforum.org/crfsuccesses.pdf (visited on Jan. 2014).

[11] European Environment Agency. *Atmospheric greenhouse gas concentrations (CSI 013)*. Jan. 2012. URL: http://www.eea.europa.eu/data-and-maps/indicators/atmospheric-greenhouse-gas-concentrations-2/assessment (visited on Jan. 2015).

[12] Boyan Kavalov and S. D. Peteves. *The Future of Coal*. Tech. rep. Luxembourg, 2007. URL: http://publications.jrc.ec.europa.eu/repository/handle/JRC36671.

[13] *Kyoto Protocol to the United Nations Framework Convention on Climate Change*. Tech. rep. Kyoto, Japan, United Nations, 1998. URL: http://unfccc.int/resource/docs/convkp/kpeng.pdf (visited on 15th July 2015).

[14] European Commission. *Paris Agreement*. Dec. 2015. URL: http://ec.europa.eu/clima/policies/international/negotiations/paris/index_en.htm (visited on 14th Mar. 2016).

[15] Massoud Kayhanian, George Tchobanoglous and Robert C Brown. "Biomass Conversion Process for Energy Recovery". In: *Energy Conversion*. CRC Press, 2007, pp. 22-37–22-50. URL: http://www.crcnetbase.com/isbn/9781420044324.

[16] Ralph P Overend and Lynn L Wright. "Biomass Energy". In: *Energy Conversion*. CRC Press, 2007, pp. 3-1 –3-18. URL: http://www.crcnetbase.com/isbn/9781420044324.

[17] *Directive 2009/28/EC of the European Parliament and of the Council of 23 April 2009 on the promotion of the use of energy from renewable sources and amending and subsequently repealing Directives 2001/77EC and 2003/30/EC*. Tech. rep. Strasbourg, France, EU, 2009. URL: http://eur-lex.europa.eu/legal-content/EN/TXT/PDF/?uri=CELEX:32009L0028&from=EN (visited on 20th July 2015).

[18] *Biomass Co-firing : Technology Brief*. Tech. rep. International Energy Agency - Energy Technology Systems Analysis Programme (IEA-ETSAP) and International Renewable Energy Agency (IRENA), Jan. 2013.

[19] J Domac, K Richards and S Risovic. "Socio-economic drivers in implementing bioenergy projects". In: *Biomass and Bioenergy* 28.2 (Feb. 2005), pp. 97–106. URL: http://www.sciencedirect.com/science/article/pii/S0961953404001485.

[20] Amy O'Mahoney, Fiona Thorne and Eleanor Denny. "A cost-benefit analysis of generating electricity from biomass". In: *Energy Policy* 57 (June 2013), pp. 347–354. URL: http://www.sciencedirect.com/science/article/pii/S0301421513000906 (visited on 14th July 2015).

[21] Gang Lu, Yong Yan, Steve Cornwell, Michael Whitehouse and Gerry Riley. "Impact of fo-firing coal and biomass on flame characteristics and stability". In: *Fuel* 87.7 (2008), pp. 1133–1140.

[22] KRG Hein and JM Bemtgen. "EU clean coal technology – Co-combustion of coal and biomass". In: *Fuel Processing Technology* 54 (1998), pp. 159–169.

[23] Anna Maciejewska, H. Veringa, J. Sanders and S.D. Peteves. *Co-Firing Of Biomass With Coal: Constraints And Role Of Biomass Pre-Treatment*. Tech. rep. Luxembourg, 2006.

[24] A Demirbas. "Sustainable cofiring of biomass with coal, Energy Conversion and Management". In: *Energy Conversion and Management* (Jun 2003), Vol. 44, Iss. 9, Iss. 9.

[25] Renewable Energy Focus. *Alstom plans two new biomass facilities in the UK*. Mar. 2015. URL: http://www.sciencedirect.com/science/article/pii/S1755008415300387 (visited on 14th Apr. 2016).

[26] Colin Henderson. *Cofiring of biomass in coal-fired power plants - European experience*. Jan. 2015. URL: http://www.iea-coal.org.uk/documents/83524/9188/Henderson---Cofiring-of-biomass-in-coal-fired-power-plants-%E2%80%93-European-experience (visited on 22nd July 2015).

[27] International Energy Agency. *Profiles: Cofiring high ratios of biomass with coal*. Feb. 2012. URL: http://www.iea-coal.org.uk/documents/82864/8366/Cofiring-high-ratios-of-biomass-with-coal,-CCC/194 (visited on 14th Apr. 2016).

[28] R Isermann. "Supervision, fault-detection and fault-diagnosis methods — An introduction". In: *Control Engineering Practice* 5.5 (May 1997).

[29] S -L Jämsä-Jounela, M Vermasvuori, P Endén and S Haavisto. "A process monitoring system based on the Kohonen self-organizing maps". In: *Control Engineering Practice* 11.1 (Jan. 2003), pp. 83–92. URL: http://www.sciencedirect.com/science/article/pii/S0967066102001417.

[30] Francisco Rodri´guez, Enrique Tova, Vicente Cortés and Luis Cañadas. "OPTICOM: Advanced automatic monitoring system of local combustion conditions for improving boiler performance in PC power plants". In: *Fuel* 81.5 (Mar. 2002), pp. 637–645.

[31] Joe Kay. "Monitoring - equipment and methods". In: 223 (1994), pp. 6–10.

[32] A R Jones. "Flame failure detection and modern boilers". In: *Journal of Physics E: Scientific Instruments* 21.10 (1988), pp. 921–928. URL: http://iopscience.iop.org/0022-3735/21/10/001 (visited on 16th Aug. 2010).

[33] Janos M Beér, Malcolm T Jacques and Derek J Teare. *Individual burner air/fuel ratio control optical adaptive feedback control system*. Tech. rep. MIT, 1982.

[34] Chee Keong Tan, Steven John Wilcox and John Ward. "Development of A Monitoring System for Near Burner Slag Formation". In: Proceedings of International Mechanical Engineering Congress & Exposition. New Orleans, Louisiana, USA, ASME, 2002, pp. 63–69.

[35] Katharina Kohse-Höinghausa, Robert S Barlow, Marcus Aldénc and Jürgen Wolfrum. "Combustion at the focus: laser diagnostics and control". In: *Proceedings of the Combustion Institute* 30 (2005), pp. 89–123.

[36] Shee Meng Thai, Steven John Wilcox, C.K. Tan, Alex Z.S. Chong, John Ward and Graham Andrews. "Monitoring regenerative steel reheating burners using an intelligent flame disgnostic system". In: *Journal of Energy Institute* 87 (2014), pp. 48–58.

[37] Nicolas Docquier and Sébastien Candel. "Combustion control and sensors: a review". In: *Progress in Energy and Combustion Science (28)* (2002), pp. 107–150.

[38] A.G. Gaydon. *The Spectroscopy of Flames*. London, Chapman and Hall, 1957.

[39] G Lu, Y Yan, M.J.F. Colechin and R Hill. "Monitoring of oscillatory characteristics of pulverised coal flames through image processing and spectral analysis". In: *IEEE Transactions on Instrumentation and Measurement* 55.1 (Feb. 2006), pp. 226–231.

[40] L Arias, S Torres, D Sbarbaro and P Ngendakumana. "On the spectral bands measurements for combustion monitoring". In: *Combustion and Flame* 158 (2011), pp. 423–433.

[41] J A Broadbent. "Fundamental flame flicker monitoring for power plant boilers". In: Advanced Sensors and Instrumentation Systems for Combustion Processes (Ref. No. 2000/080) IEE Seminar. Birmingham, IET, 2000, pp. 4/1–4/4.

[42] A Sanz, J Ballester, R Hernandez and L. M. Cerecedo. "Advanced monitoring of industrial burners based on fluctuating flame signals". In: *Fuel* 87 (2008), pp. 1063–1075.

[43] Soteris A. Kalogiru. "Artificial intelligence for the modelling and control of combustion processes: a review". In: *Progress in Energy and Combustion Science* 29.6 (2003), pp. 515–566.

[44] Chee Keong Tan, Steven John Wilcox and John Ward. "Use of artificial intelligence techniques for optimisation of co-combustion of coal with biomass". In: *Journal of the Energy Institute* 79.1 (2006), pp. 19–25.

[45] Jerzy Chomiak. *Combustion: A Study in Theory, Fact and Application*. Ed. by A K Gupta and D G Lilley. Montreux, Switzerland: Abacus Press / Gordon & Breach Science Publishers, 1990.

[46] H B Vuthaluru. "Thermal behaviour of coal/biomass blends during co-pyrolysis". In: *Fuel Processing Technology* 85.2 - 3 (Feb. 2004), pp. 141–155. URL: `http://www.sciencedirect.com/science/article/pii/S0378382003001127`.

[47] Steven John Wilcox, L Dominquez, Javier Ballester, F.J. de Celis Sanchez and K Jagiello. *The intelligent control and optimisation of power station boilers firing pulverised coal and coal/biomass blends*. Luxembourg, Luxembourg: Publications Office of the European Union, 2013, 2013. ISBN: 978-92-79-28949-1.

[48] *Clean Coal Technologies: Accelerating Commercial and Policy Drivers for Deployment*. Tech. rep. Paris, France, International Energy Agency, 2008.

[49] *Toward a Clean, Clever and Competitive Energy Future*. Tech. rep. Paris, France, 2007.

[50] Brian Ricketts. *Focus on Clean Coal*. Tech. rep. International Energy Agency, 2006.

[51] *Coal Medium-Term Market Report 2013*. Tech. rep. Paris, France, 2013.

[52] *The future of coal: options for a carbon-constrained world*. Tech. rep. 77 Massachusetts Avenue, Cambridge MA 02139-4307. Cambridge, MA, USA, Massachusetts Institute of Technology, 2007.

[53] *World Energy Outlook 2007*. Paris, France: International Energy Agency, 2007.

[54] *Fact Sheet: Electricity Generation*. 2006. URL: https://www.iea.org/publications/freepublications/publication/fact-sheet-electricity-generation.html (visited on 14th Apr. 2015).

[55] Eugene L Keating. *Applied Combustion*. 2nd ed. CRC Press, 2007.

[56] W Wojcik, T Golec, A Kotyra, A Smolarz, P Komada and M Kalita. "Concept of application of signals from fibre-optic system for flame monitoring to control separate pulverised coal burner". In: ed. by Ryszard S. Romaniuk. Vol. 5484. Proceedings of SPIE. Bellingham, WA, 2004, pp. 427–431.

[57] *Fossil Fuel Power Generation R, D & D Needs*. Tech. rep. 2004.

[58] *Cleaner Coal*. Tech. rep. London, UK, Parliamentary Office of Science and Technology, 2005. URL: http://researchbriefings.files.parliament.uk/documents/POST-PN-253/POST-PN-253.pdf (visited on 17th July 2015).

[59] *Energy Technology Perspectives 2014 - Executive Summary*. Tech. rep. Paris, France, 2014.

[60] *Fossil Fuel Power Generation: State-of-the-art*. Tech. rep. 2004.

[61] Javier Ballester, J Barroso, L M Cerecedo and R Ichaso. "Comparative study of semi-industrial-scale flames of pulverized coals and biomass". In: *Combustion and Flame* 141.3 (May 2005), pp. 204–215. URL: http://www.sciencedirect.com/science/article/pii/S0010218005000180.

[62] M. Shimoda, A. Sugano, T. Kimura, Y. Watanabe and Ishiyama K. "Prediction method of unburnt carbon for coal fired utility boiler using image processing technique of combustion flame". In: *Energy Conversion, IEEE Transactions on* 5.4 (Dec. 1990), pp. 640–645.

[63] *Low Carbon Technologies for Energy-Intensive Industries*. Tech. rep. London, UK, Parliamentary Office of Science and Technology, 2012. URL: http://researchbriefings.files.parliament.uk/documents/POST-PN-403/POST-PN-403.pdf (visited on 16th July 2015).

[64] *Carbon Footprint of Electricity Generation*. Tech. rep. London, UK, Parliamentary Office of Science and Technology, 2006, pp. 1–4. URL: http://www.parliament.uk/documents/post/postpn268.pdf (visited on 2012).

[65] Honglu Yu and John F MacGregor. "Monitoring flames in an industrial boiler using multivariate image analysis". In: *AIChE Journal* 50.7 (July 2004), pp. 1474–1483.

[66] S De and M Assadi. "Impact of cofiring biomass with coal in power plants - A techno-economic assessment". In: *Biomass and Bioenergy* 33.2 (Feb. 2009), pp. 283–293.

[67] *Emissions Trading System*. Oct. 2013. URL: http://ec.europa.eu/clima/publications/docs/factsheet_ets_en.pdf (visited on 16th July 2015).

[68] *Global Carbon Trading*. Tech. rep. London, UK, Parliamentary Office of Science and Technology, 2010. URL: http://researchbriefings.files.parliament.uk/documents/POST-PN-354/POST-PN-354.pdf (visited on 20th July 2015).

[69] Fouad Al-Mansour and Jaroslaw Zuwala. "An evaluation of biomass co-firing in Europe". In: *Biomass and Bioenergy* 34.5 (May 2010), pp. 620–629.

[70] Lars Storm Pedersen, Hanne Philbert Nielsen, Søren Kiil, Lone Aslaug Hansen, Kim Dam-Johansen, Finn Kildsig, Jan Christensen and Peer Jespersen. "Full-scale co-firing of straw and coal". In: *Fuel* 75.13 (Oct. 1996), pp. 1584–1590. URL: http://www.sciencedirect.com/science/article/pii/0016236196826421 (visited on July 2015).

[71] Larry Baxter. "Biomass-coal Co-combustion: Oppotunity for Affordable Renewable Energy". In: *Fuel* 84.10 (July 2005), pp. 1295–1302.

[72] *Renewable energy roadmap: renewable energies in the 21st century; building a sustainable future*. Jan. 2007. URL: http://ec.europa.eu/energy/energy_policy/doc/03_renewable_energy_roadmap_en.pdf.

[73] *Framework Convention on Climate Change*. 2014. URL: http://unfccc.int/kyoto_protocol/items/2830.php (visited on 15th July 2015).

[74] *Energy Policy*. URL: http://www.biomassenergycentre.org.uk/portal/page?_pageid=77,20911&_dad=portal&_schema=PORTAL (visited on 24th Apr. 2015).

[75] *A Strategy for Developing Carbon Abatement Technologies for Fossil Fuel Use*. Tech. rep. Department of Trade and Industry, Department for Environment, Food & Rural Affairs, 2005. URL: http://www.apgtf-uk.com/index.php/publications/publications-2005/doc_view/8-a-strategy-for-developing-carbon-abatement-technologies-for-fossil-fuel-use (visited on 20th July 2015).

[76] *Future Electricity Networks*. Tech. rep. London, UK, Parliamentary Office of Science and Technology, 2011. URL: http://researchbriefings.files.parliament.uk/documents/POST-PN-372/POST-PN-372.pdf (visited on 17th July 2015).

[77] *Coal Research Needs in the UK*. Tech. rep. Cheltenham, UK, 2004.

[78] Nicolas Docquier, Francois Lacas and Sebastien Candel. "Operating point control of gas turbine combustor". In: vol. AIAA 2001-0485. 39th AIAA Aerospace Sciences Meeting & Exhibit. Reno, NV, American Institute of Aeronautics and Astronautics, 2001.

[79] *Clean Coal Technology: Reducing emissions of nitrogen oxides via low-NOx burner technologies*. Tech. rep. Germantown, MD, USA, 1996.

[80] *Overview - The Clean Air Act Amendments of 1990*. Aug. 2013. URL: http://epa.gov/air/caa/caaa_overview.html (visited on 6th July 2015).

[81] Janos M Beér, Malcolm T Jacques and W F Farmayan. *Control of NOx by combustion process modifications*. Tech. rep. Cambridge, Massachusetts, MIT, 1981.

[82] Gary L Borman and Kenneth W Ragland. *Combustion Engineering*. Boston, USA: WCB / McGraw-Hill, 1998.

[83] Li-Gang Zheng, Hao Zhou, Ke-Fa Cen and Chun-Lin Wang. "A comparative study of optimization algorithms for low NOx combustion modification at a coal-fired utility boiler". In: *Expert Systems with Applications* 36.2, Part 2 (Mar. 2009), pp. 2780–2793. URL: http://www.sciencedirect.com/science/article/pii/S0957417408000730.

[84] *Large Combustion Plants Directive*. Oct. 2001. URL: http://eur-lex.europa.eu/LexUriServ/site/en/consleg/2001/L/02001L0080-20011127-en.pdf%20(http://ec.europa.eu/environment/air/pollutants/stationary/lcp/legislation.htm) (visited on 7th July 2015).

[85] *Large Combustion Plants Directive*. Apr. 2015. URL: http://ec.europa.eu/environment/industry/stationary/lcp/legislation.htm (visited on 7th July 2015).

[86] *Directive 2001/77/EC of the European Parliament and of the Council of 27 September 2001 on the promotion of electricity produced from renewable energy sources in the internal electricity market*. Tech. rep. Strausburg, France, EU, 2001. URL: http://eur-lex.europa.eu/legal-content/EN/TXT/PDF/?uri=CELEX:32001L0077&from=EN (visited on 23rd July 2015).

[87] *Green Paper - Towards a European strategy for the security of energy supply*. Tech. rep. TREN, 2000. URL: http://eur-lex.europa.eu/legal-content/EN/TXT/?uri=URISERV:l27037 (visited on 23rd July 2015).

[88] Peter M Connor. "UK renewable energy policy: a review". In: *Renewable and Sustainable Energy Reviews* 7.1 (Feb. 2003), pp. 65–82. URL: http://www.sciencedirect.com/science/article/pii/S1364032102000540 (visited on 24th July 2015).

[89] Bishnu Raj Upreti and Dan van der Horst. "National renewable energy policy and local opposition in the UK: the failed development of a biomass electricity plant". In: *Biomass and Bioenergy* 26.1 (Jan. 2004), pp. 61–69. URL: http://www.sciencedirect.com/science/article/pii/S0961953403000990 (visited on 23rd July 2015).

[90] *The UK Renewable Energy Strategy*. Tech. rep. London, UK, Department of Energy & Climate Change, 2009. URL: https://www.gov.uk/government/publications/the-uk-renewable-energy-strategy (visited on Nov. 2015).

[91] *UK Renwable Energy Roadmap*. Tech. rep. London, UK, Department of Energy & Climate Change, 2011. URL: https://www.gov.uk/government/uploads/system/uploads/attachment_data/file/48128/2167-uk-renewable-energy-roadmap.pdf (visited on 24th July 2015).

[92] Stijn Cornelissen, Michèle Koper and Yvonne Y Deng. "The role of bioenergy in a fully sustainable global energy system". In: *Biomass and Bioenergy* 41 (June 2012), pp. 21–33. URL: http://www.sciencedirect.com/science/article/pii/S0961953411006684 (visited on 23rd July 2015).

[93] Prabir Basu, James Butler and Mathias A Leon. "Biomass co-firing options on the emission reduction and electricity generation costs in coal-fired power plants". In: *Renewable Energy* 36.1 (Jan. 2011), pp. 282–288.

[94] Ying Gang Pan, Enrique Velo and Luis Puigjaner. "Pyrolysis of blends of biomass with poor coals". In: *Fuel* 75.4 (Mar. 1996), pp. 412–418.

[95] *Why use biomass?* URL: http://www.biomassenergycentre.org.uk/portal/page?_pageid=76,15068&_dad=portal&_schema=PORTAL (visited on 24th Apr. 2015).

[96] *Co-firing*. URL: http://www.biomassenergycentre.org.uk/portal/page?_pageid=75,41175&_dad=portal&_schema=PORTAL (visited on 24th Apr. 2015).

[97] Enrico Biagini, Federica Lippi, Luigi Petarca and Leonardo Tognotti. "Devolatilization rate of biomasses and coal–biomass blends: an experimental investigation". In: *Fuel* 81.8 (May 2002), pp. 1041–1050. URL: http://www.sciencedirect.com/science/article/pii/S0016236101002046 (visited on June 2015).

[98] H Spliethoff, W Scheurer and K R G Hein. "Effect of Co-Combustion of Sewage Sludge and Biomass on Emissions and Heavy Metals Behaviour". In: *Process Safety and Environmental Protection* 78.1 (Jan. 2000), pp. 33–39. URL: http://www.sciencedirect.com/science/article/pii/S0957582000708421 (visited on 28th July 2015).

[99] A Gonzalez-Cencerrado, B Pena and A Gil. "Experimental analysis of biomass co-firing flames in a pulverized fuel swirl burner using a CCD based visualisation system". In: *Fuel Processing Technology* 130 (2015), pp. 299–310. DOI: 10.1016/j.fuproc.2014.10.041.

[100] M V Gil, D Casal, C Pevida, J J Pis and F Rubiera. "Thermal behaviour and kinetics of coal/biomass blends during co-combustion". In: *Bioresource Technology* 101.14 (July 2010), pp. 5601–5608. URL: http://www.sciencedirect.com/science/article/pii/S0960852410002798.

[101] S G Sahu, N Chakraborty and P Sarkar. "Coal–biomass co-combustion: An overview". In: *Renewable and Sustainable Energy Reviews* 39 (Nov. 2014), pp. 575–586. URL: http://www.sciencedirect.com/science/article/pii/S1364032114005589.

[102] European Central Bank. *Determination of the euro conversion rates*. Dec. 1998. URL: http://www.ecb.europa.eu/press/pr/date/1998/html/pr981231_2.en.html (visited on 11th Apr. 2016).

[103] *Industrial Emissions (Integrated Pollution Prevention and Control)*. Nov. 2010. URL: http://eur-lex.europa.eu/legal-content/EN/TXT/PDF/?uri=CELEX:32010L0075&from=EN%20(http://ec.europa.eu/environment/industry/stationary/ied/legislation.htm) (visited on 1st Sept. 2016).

[104] Luis Arias, Sergio Torres, Daniel Sbarbaro and Oscar Farias. "Photodiode-based sensor for flame sensing and combustion-process monitoring". In: *Applied Optics* 47.29 (Oct. 2008), pp. 5541–5549.

[105] Robert S Barlow. "Laser diagnostics and their interplay with computations to understand turbulent combustion". In: *Proceedings of the Combustion Institute* 31 (2007), pp. 49–75.

[106] A Leipertz, R Obertacke and F Wintrich. "Industrial Combustion Control Using UV Emission Tomography". In: *Symposium (International) on Combustion* 26.2 (1996), pp. 2869–2875.

[107] P M Willson and T E Chappell. "Pulverized fuel flame monitoring in utility boilers". In: *Journal of the Institute of Energy* 58 (Mar. 1985), pp. 12–19. ISSN: 0144-2600.

[108] Carlos Romero, Xianchang Li, Shahla Keyvan and Rodney Rossow. "Spectrometer-based combustion monitoring for flame stoichiometry and temperature control". In: *Applied Thermal Engineering* 25.5-6 (Apr. 2005), pp. 659–676.

[109] Shee Meng Thai, Steven John Wilcox, Chee Keong Tan, John Ward and Graham Andrews. "Development of an intelligent flame monitoring system for steel reheating burners". In: *Proceedings of the Institution of Mechanical Engineers, Part A: Journal of Power and Energy* 226.8 (Sept. 2012), pp. 1014–1031.

[110] A.G. Gaydon and H.G. Wolfhard. *Flames: Their Structure, Radiation, and Temperature*. London, Chapman and Hall, 1978.

[111] Hyeon Bae, Sungshin Kim, Bo-Hyeun Wang, Man Hyung Lee and Fumio Harashima. "Flame Detection for the Stem Boiler Using Neural Networks and Image Information in the Ulsan Steam Power Generation Plant". In: *IEEE Transactions on Industrial Electronics* 53.01 (Feb. 2006), pp. 338–348.

[112] Giorgio Zizak. *Flame Emission Spectroscopy: Fundamentals and Applications*. Cairo, Egypt, Nov. 2000.

[113] R Obertacke, H Wintrich, F Wintrich and A Leipertz. "A New Sensor System for Industrial Combustion Monitoring and Control using UV Emission Spectroscopy and Tomography". In: *Combustion Science and Technology* 121.1-6 (1996), pp. 133–151.

[114] Javier Ballester and Tatiana García-Armingol. "Diagnostic techniques for the monitoring and control of practical flames". In: *Progress in Energy and Combustion Science (36)* (2010), pp. 375–411.

[115] Sébastien Candel. "Combustion dynamics and control: Progress and challenges". In: *Proceedings of the Combustion Institute* 29.1 (2002), pp. 1–28.

[116] Mark Khesin. "Demonstration of new frequency-based flame monitoring system". In: *Proceedings of the American Power Conference* 58 (1996), pp. 1010–1013.

[117] Gang Lu, Yong Yan, Gerry Riley and Harrish Chandr Bheemul. "Concurrent Measurement of Temperature and Soot Concentration of Pulverised Coal Flames". In: *Instrumentation and Measurement, IEEE Transactions on* 51.5 (Oct. 2002), pp. 990–995.

[118] A González-Cencerrado, B Peña and A Gil. "Coal flame characterization by means of digital image processing in a semi-industrial scale PF swirl burner". In: *Applied Energy* 94 (June 2012), pp. 375–384.

[119] Javid J Huseynov and Shankar B Baliga. "Optical infrared flame detection system with neural networks". In: *Proc. SPIE 6697: Advanced Signal Processing Algorithms, Architectures, and Implementations XVII* (Sept. 2007).

[120] Yong Yan, Gang Lu and M.J.F. Colechin. "Monitoring and characterisation of pulverised coal flames using digital imaging techniques". In: *Fuel* 81.5 (2002), pp. 647–655.

[121] F Wang, X J Wang, Z Y Ma, J H Yan, Y Chi, C Y Wei, M J Ni and K F Cen. "The research on the estimation for the NO_x emissive concentration of the pulverized coal boiler by the flame image processing technique". In: *Fuel* 81.16 (Nov. 2002), pp. 2113–2120. ISSN: 0016-2361. DOI: http://dx.doi.org/10.1016/S0016-2361(02)00145-Xfaf. URL: http://www.sciencedirect.com/science/article/pii/S001623610200145X (visited on 7th Feb. 2014).

[122] Junghui Chen, Yu Hsiang Chang, Yi Cheng Cheng and Chen Kai Hsu. "Design of image-based control loops for industrial combustion processes". In: *Applied Energy* 94 (2012), pp. 13–21. DOI: 10.1016/j.apenergy.2011.12.080.

[123] Sing-Tze Bow. "Dimensionality Reduction and Feature Selection". In: *Pattern Recognition and Image Preprocessing*. CRC Press, 2002. Chap. 7, pp. 168–195. ISBN: 978-0-8247-0659-3. URL: http://www.crcnetbase.com/isbn/9780824706593 (visited on 21st July 2015).

[124] Norm O'Rourke and Larry Hatcher. "Principal Component Analysis". In: *A Step-by-Step Approach to Using SAS for Factor Analysis and Structural Equation Modelling*. SAS Institute, 2014. Chap. 1, pp. 1–56. ISBN: 978-1-61290-387-3.

[125] Gang Lu, Yong Yan and Colechin M. "A digital imaging based multifunctional flame monitoring system". In: *Instrumentation and Measurement, IEEE Transactions on* 53.4 (Aug. 2004), pp. 1152–1158.

[126] M G Abdul Rahman, J R Gibbins and A K Forrest. *Combustion in Power Station Boilers – Advanced Monitoring Using Imaging*. Tech. rep. London, UK, Imperial College of Science, Technology and Medicine, 2004.

[127] Mark Khesin, Bill Strohecker and Rob Girvan. "Application of a New Burner Diagnostic System for Coal-Fired Utility Boilers". In: *Instrumentation, Controls and Automation in the Power Industry* 40 (1997), pp. 127–136. ISSN: 1067-6988.

[128] Jack A Bryant. "Update your flame-monitoring know-how". In: *Power - Instrumentation and control* 124.8 (Aug. 1980), pp. 21–25.

[129] Lijun Xu and Yong Yan. "An Improved Algorithm for the Measurement of Flame Oscillation Frequency". In: *Instrumentation and Measurement, IEEE Transactions on* 56.5 (2007), pp. 2087–2093.

[130] C.J. Lawn. "Distribution of Instantaneous Heat Release by the Cross-Correlation of Chemiluminescent emissions". In: *Combustion and Flame* 123.1–2 (Oct. 2000), pp. 227–240.

[131] Tatiana García-Armingola, Javier Ballester and Andrzej Smolarz. "Chemiluminescence-based sensing of flame stoichiometry: Influence of the measurement method". In: *Measurement* 43 (2013), pp. 3084–3097.

[132] B Higgins, M.Q. McQuay, F Lacas, J.C. Rolon, N Darabiha and S Candel. "Systematic measurements of OH chemiluminescence for fuel-lean, high-pressure, premixed, laminar flames". In: *Fuel* 80 (2001), pp. 67–74.

[133] Venkata N. Nori and Jerry M. Seitzman. "CH* chemiluminescence modeling for combustion diagnostics". In: *Proceedings of the Combustion Institute* 32 (2009), pp. 895–903.

[134] Nicolas Docquier, Sami Belhalfaoui, Francois Lacas, Nasser Darabiha and Carlos Rolon. "Experimental and numerical study of chemiluminescence in methane/air high-pressure flames for active control applications". In: *Proceedings of the Combustion Institute* 28 (2000), pp. 1765–1774.

[135] Ooi Hong Tan, Steven John Wilcox, John Ward and M Lewitt. "The development of a monitoring and control system for pulverised coal flames using neural networks". In: ASME international mechanical engineers congress. Washington, DC, USA, ASME, 2003, pp. 91–98.

[136] Javid Huseynov, Zvi Boger, Gary Shubinsky and Shankar Baliga. "Optical flame detection using large-scale artificial neural networks". In: vol. 3. Proceedings of IEEE International Joint Conference on Neural Networks, 2005. Montreal, Quebec, Canada, IEEE, 2005, pp. 1959–1964. DOI: 10.1109/IJCNN.2005.1556180.

[137] Jose V Pastor, Jose M Garcia and Santiago Molina. "Analysis methodology of diesel spray and flame by means of in-cylinder endoscopic imaging". In: IEE Seminar on Advanced Sensors and Instrumentation Systems for Combustion Processes. Birmingham, UK, IET, 2000, pp. 13/1–13/4.

[138] Ooi Hong Tan, Steven John Wilcox, G C Premier, Chee Keong Tan and John Ward. "Monitoring pulverised coal flames". In: *Journal of the Energy Institute* (Jan. 2007), pp. 131–139.

[139] Shahla Keyvan, Rodney Rossow, Carlos Romero and Xianchang Li. "Comparison between visible and near-IR flame spectra from natural gas-fired furnace for blackbody temperature measurements". In: *Fuel* 83.9 (June 2004), pp. 1175–1181. URL: http://www.sciencedirect.com/science/article/pii/S0016236103004113 (visited on 23rd July 2015).

[140] T Yamaguchi, K T V Grattan, H Uchiyama and T Yamada. "A practical fiber optic air-ratio sensor operating by flame color detection". In: *Review of Scientific Instruments* 68.1 (1997), pp. 197–202. URL: http://search.ebscohost.com/login.aspx?direct=true&db=a9h&AN=5327726&site=ehost-live (visited on 8th Jan. 2016).

[141] Zhiyue Lin. "An introduction to time-frequency signal analysis". In: *Sensor Review* 17.1 (1997), pp. 46–53. URL: http://dx.doi.org/10.1108/02602289710163364 (visited on 26th Nov. 2014).

[142] Qian Shie and Dapang Chen. "Understanding the nature of signals whose power spectra change with time - Joint analysis". In: 16.2 (Mar. 1999), pp. 52–67.

[143] T Thayaparan and S Kennedy. *Application of Joint Time-Frequency Representations to a Maneuvering Air Target in Sea-Clutter: Analysis Beyond FFT*. Tech. rep. Ottawa, Canada, Defence Research & Development Canada, Mar. 2003.

[144] Azeemsha Thacham Poyil and K M Nasimudeen. "Multi resolution signal analysis using improved Wigner Ville Distribution". In: Communication, Information Computing Technology (ICCICT), 2012 International Conference on. IEEE, 2012, pp. 1–4. URL: http://ieeexplore.ieee.org/xpl/articleDetails.jsp?arnumber=6398197 (visited on 10th Aug. 2015).

[145] L Cohen. "Time-frequency distributions – a review". In: *Proceedings of the IEEE 77* (1989), pp. 941–981.

[146] Haldun M Ozaktas, Zeev Zalevsky and M. Alper Kutay. *The Fractional Fourier Transform: with Applications in Optics and Signal Processing*. Chichester, West Sussex England: John Wiley & Sons Ltd., 2001.

[147] Azeddine Beghdadi and Razvan Iordache. "Image quality assessment using the joint spatial / spatial-frequency representation". In: *EURASIP Journal on Advances in Signal Processing* 2006.ID 80537 (May 2006), pp. 1–8. DOI: 10.1155/ASP/2006/80537.

[148] F. Hlawatsch and G.F. Boudreaux-Bartels. "Linear and quadratic time-frequency signal representations". In: *Signal Processing Magazine, IEEE* 9.2 (Apr. 1992), pp. 21–67.

[149] E.P. Wigner. "On the quantum correction for the thermodynamic equilibrium". In: *Physics Reviews* 40.5 (June 1932), pp. 749–759.

[150] J Ville. "Theorie ef applications de la notion de signal analytique". In: *Cables et Transmission 2A* (1948). Ville, J.. Theory and Applications of the Notion of Complex Signal. Santa Monica, CA: RAND Corporation, 1958. http://www.rand.org/pubs/translations/T92, pp. 61–74.

[151] T. A. C. M. Claasen and W. F. G. Mecklenbrauker. "The Wigner distribution – a tool for time-frequency analysis. Part 1: continuous time signals". In: *Philips Journal of Research 35* (1980), pp. 217–250.

[152] T. A. C. M. Claasen and W. F. G. Mecklenbrauker. "The Wigner distribution – a tool for time-frequency analysis. Part 2: discrete time signals". In: *Philips Journal of Research 35* (1980), pp. 276–300.

[153] T. A. C. M. Claasen and W. F. G. Mecklenbrauker. "The Wigner distribution – a tool for time-frequency analysis. Part 3: relations with other time-frequency transformations". In: *Philips Journal of Research 35* (1980), pp. 372–389.

[154] W. J. Staszewski, K. Worden and G. R. Tomlinson. "Time-frequency analysis in gearbox fault detection using the Wigner-Ville distribution and pattern recognition". In: *Mechanical Systems and Signal Processing* 11.5 (1997), pp. 673–692.

[155] C. L. Nikias and A. P. Petropulu. *Higher-Order Spectra Analysis: A Non-Linear signal Processing Framework*. Englewood Cliffs, New Jersey, Prentice-Hall, 1993.

[156] Patrick Flandrin. "Time-frequency and time-scale". In: *Fourth Annual ASSP Workshop on Spectrum Estimation and Modeling* (1988), pp. 77–80. DOI: 10.1109/SPECT.1988.206166.

[157] Stephen Marsland. *Machine Learning: An Algorithmic Perspective*. Second. CRC Press, 2015. ISBN: 978-1-4665-8328-3.

[158] R. J. Schalkoff. *Pattern Recognition: Statistical, Structural and Neural Approaches*. New York, John Wiley, 1991.

[159] James A Freeman and David M Skapura. *Neural Networks: Algorithms, Applications, and Programming Techniques*. Addison-Wesley Publishing Company Inc, 1991.

[160] Simon Haykin. *Neural Networks: A Comprehensive Foundation*. Second. Upper River Saddle, New Jersey, USA, USA: Prentice Hall, 1999.

[161] A K Jain, Jian Chang Mao and K M Mohiuddin. "Artificial neural networks: a tutorial". In: *Computer* 29.3 (Mar. 1996), pp. 31–44.

[162] R Rohwer, M Wynne-Jones and F F. Wysotzki. "Neural Networks". In: *Machine Learning, Neural and Statistical Classification*. 1994. Chap. 6, pp. 84–106.

[163] Richard D De Veaux and Lyle H Ungar. *Penn Data Mining Group: Publications*. 1997. URL: http://www.cis.upenn.edu/~ungar/Datamining/Publications/nnet-intro.pdf (visited on Jan. 2015).

[164] Ben Krose and Patrick van der Smagt. *An introduction to Neural Networks*. Eighth. Amsterdam, The Netherlands: University of Netherlands, 1996. URL: http://lia.univ-avignon.fr/chercheurs/torres/livres/book-neuro-intro.pdf (visited on 10th Aug. 2015).

[165] Henryk Rusinowski and Wojciech Stanek. "Neural modelling of steam boilers". In: *Energy Conversion and Management* 48.11 (Nov. 2007), pp. 2802–2809.

[166] B Martín and A Sanz. *Neural Networks and Fuzzy Systems*. Madrid, RAMA, 2001.

[167] I.W. Mayes. "Generic NOx control intelligent system (GNOCIS)". In: Artificial Intelligence-Based Applications for the Power Industry (Ref. No. 1999/065), IEE Colloquium on. IET, 1999, pp. 9/1–9/4.

[168] Soteris A Kalogirou. "Applications of artificial neural-networks for energy systems". In: *Applied Energy* 67.1 - 2 (July 2000), pp. 17–35. URL: http://www.sciencedirect.com/science/article/pii/S0306261900000052.

[169] I. A. Basheer and M Hajmeer. "Artificial neural networks: fundamentals, computing, design, and application". In: *Journal of Microbiological Methods* 43.1 (Dec. 2000), pp. 3–31.

[170] George F. Luger. *Artificial Intelligence: Structures and Strategies for Complex Problem Solving*. Sixth. Pearson Education, 2009. ISBN: 978-0-13-209001-8.

[171] Jiawei Han, Micheline Kamber and Jian Pei. *Data Mining: Concepts and Techniques*. Third. Elsevier, 2012. ISBN: 978-0-12-381479-1.

[172] Stuart Russell and Peter Norvig. *Artificial Intelligence: A Modern Approach*. Third. Pearson Education, 2016. ISBN: 9781292153964.

[173] Constantine Kotropoulos and Ioannis Pitas. "Self-Organizing Maps and Their Applications in Image Processing, Information Organization, and Retrieval". In: *Nonlinear Signal and Image Processing: Theory, Methods, and Applications*. Boca Raton, Florida USA: CRC Press, 2003, pp. 387–444. URL: http://www.crcnetbase.com/isbn/9780849314278 (visited on 30th July 2015).

[174] Olli Simula, Juha Vesanto, Esa Alhoniemi and Jakko Hollmen. *Analysis and Modelling of Complex Systems Using the Self-Organising Map*. Tech. rep. Helsinki, Finland: Helsinki University of Technology.

[175] Teuvo Kohonen. "The Self-organising map". In: *Neurocomputing* 21.1-3 (1998), pp. 1–6.

[176] Teuvo Kohonen, Erkki Oja, Olli Simula, Ari Visa and Jari Kangas. "Engineering Applications of the Self-Organizing Map". In: *Proceedings of the IEEE* 84.10 (Oct. 1996), pp. 1358–1384.

[177] Jari Kangas and Teuvo Kohonen. "Developments and applications of the self-organizing map and related algorithms". In: *Mathematics and Computers in Simulation* 41.1 - 2 (June 1996), pp. 3–12. URL: http://www.sciencedirect.com/science/article/pii/0378475496882231 (visited on July 2015).

[178] Ron Wehrens and Lutgarde M C Buydens. "Self- and Super-organizing Maps in R: The kohonen Package". In: *Journal of Statistical Software* 21.5 (Oct. 2007). DOI: 10.18637/jss.v021.i05. (Visited on 12th Jan. 2016).

[179] *Bibliography of SOM papers*. Oct. 2011. URL: http://www.cis.hut.fi/research/som-bibl/ (visited on 10th Oct. 2015).

[180] *Roithner Lasertechnik - Photodiode - EPD440*. URL: http://www.roithner-laser.com/datasheets/pd/EPD-440-0_1_4.pdf (visited on 27th Nov. 2014).

[181] *Hamamatsu - Photodiode - S1226-18BK*. URL: http://www.hamamatsu.com/eu/en/product/category/3100/4001/4103/S1226-18BK/index.html (visited on 30th Mar. 2016).

[182] *Hamamatsu - Photodiode - G8376-05*. URL: http://www.hamamatsu.com/resources/pdf/ssd/g8376_series_kird1051e.pdf (visited on 30th Mar. 2016).

[183] Juho Vesanto, Johan Himberg, Esa Alhoniemi and Juha Parhankangas. *SOM Toolbox for Matlab 5*. Vol. Report A57. Helsinki, Finland: SOM Toolbox Team, Helsinki University of Technology, 2000. URL: http://www.cis.hut.fi/projects/somtoolbox/.

Appendices

Appendix A

DEVELOPED CODE

A.1 Supervised ANN

The following MATLAB code was used for training a neural network (dependency MATLAB Neural Network Toolbox):

```
clear all; clc; close all;

%LOAD DATA FILES
data= <'Read data from excel or csv files: where data is arranged by sensor in each coloumn'>;
a=1:285;
b=343:513;
t=[a b];  %the rows (experiments) being used for training the network
TPinput=[data(t,14:16)]';
TO2_target=data(t,1)'; %get the O2 / NOx or airflow data for training

%NORMALISE DATA
% to normalise the inputs and targets to have zero mean and unity standard
% deviation
[tpn,meanp,stdp,ttn,meant,stdt] = prestd(TPinput, TO2_target);

%TRAINING DATA SET
%1,2,4,5,6,8,9,10,12... getting 75% data for training and 25% for testing
Ptrain1=tpn(:,1:4:end);
Ttrain1=ttn(:,1:4:end);
Ptrain2=tpn(:,2:4:end);
Ttrain2=ttn(:,2:4:end);
Ptrain4=tpn(:,4:4:end);
Ttrain4=ttn(:,4:4:end);
Ptrain = [Ptrain1 Ptrain2 Ptrain4];
Ttrain = [Ttrain1 Ttrain2 Ttrain4];
```

```
26
27 %TESTING DATA SET
28 %3,7,11... getting 25% for testing
29 Ptest=tpn(:,3:4:end);
30 Ttest=ttn(:,3:4:end);
31
32 Test.P = Ptest; Test.T = Ttest;
33
34 %NEURAL NETWORK TRAINING
35 H= 25; %test for hidden neurons of 10 12 15 20 25 and
      30
36 net = newff((minmax(Ptrain)),[H 1],{'tansig' 'purelin'
      },'trainbr');
37 net.trainParam.epochs = 3000;
38 net.trainParam.show = 50;
39 net = init(net);
40 [net,tr] = train(net,Ptrain,Ttrain,[],[],[],Test);
41
42 %NEURAL NETWORK TESTING
43 Y=sim(net,Ptest);
44 Ytest=poststd(Y,meant,stdt);
45 target=poststd(Ttest,meant,stdt);
46
47 mppe_t=100*sum(abs(Ytest-target)./target)/length(Ytest)
      ;
48
49 %SAVE TRAINED NETWORK
50 savefilename = strcat('IEn_3_1_O2_psd_',num2str(hn),'
      _model.mat');
51 save(savefilename,'net', 'tr', 'meanp', 'stdp', 'meant'
      , 'stdt');
52
53 %PLOTTING
54 figure;
55 set(gca,'FontSize',16);
56 plot(1:length(target),target,'b',1:length(Ytest),Ytest,
      'r--','LineWidth',3);
57 txt=strcat('Testing;','MPPE=',num2str(mppe_t,2),'%;','
      Hidden Neuron=',num2str(H)); title(txt);
58 grid on; xlabel('Data Point (5s/Data Point)'); ylabel('
      O2 (%)');
59 legend('Measured O2','Predicted O2','Location','
      SouthOutside','Orientation','horizontal');
60
61 saveas(gca,strcat('ann_o2_psd_',num2str(hn),'
      neurons_t1tot5_t7tot9_training.fig'));
```

The following MATLAB code was used for testing the neural network model with new data:

```
62
63 %LOAD DATA FILES:
64 data= <'Read data from excel or csv files: where data
       is arranged by sensor in each coloumn'>;
65 x=286:342;
66 %y=2566:3078;
67 s=x;
68 SPinput=[data(s,14:16)]'; %UV, VIS & IR Photodiodes
69 SO2_target=data(s,1)';
70
71 %LOAD TRAINED NETWORK
72 load(savefilename) %variables: net,tr,meanp,stdp,meant,
       stdt
73
74 %NORMALISE DATA
75 %Preprocesses the network training set using the mean &
        standard deviation
76 %that were previously computed by 'prestd'
77 spn=trastd(SPinput,meanp,stdp);
78 stn=trastd(SO2_target,meant,stdt);
79
80 %NETWORK SIMULATION
81 Y=sim(net,spn);
82 Ytest=poststd(Y,meant,stdt);
83 target=poststd(stn,meant,stdt);
84
85 mppe_s=100*sum(abs(Ytest-target)./target)/length(Ytest)
       ;
86
87 %PLOTTING
88 figure(2);
89 set(gca,'FontSize',16);
90 plot(1:length(target),target,'b',1:length(Ytest),Ytest,
       'r--','LineWidth',3);
91 txt=strcat('Simulation;','MPPE=',num2str(mppe_s,3),'%;'
       ,'Hidden Neuron=',num2str(H)); title(txt);
92 grid on; xlabel('Data Point (5s/Data Point)'); ylabel('
       O2 (%)');
93 legend('Measured O2','Predicted O2','Location','
       SouthOutside','Orientation','horizontal');
94 saveas(gca,strcat('ann_o2_psd_',num2str(hn),'
       neurons_t6_simulation.fig'));
```

A.2 Supervised ANN with PCA

The following MATLAB code was used for training a neural network with Principal Component Analysis (PCA):

```
clear all; clc; close all;

%LOAD DATA FILES
data= <'Read data from excel or csv files: where data is arranged by sensor in each coloumn'>;
a=1:285;
b=343:513;
t=[a b];  %the rows (experiments) being used for training the network
TPinput=[data(t,3:5), data(t,14:16), data(t,25:27)]'; % UV, VIS & IR Photodiodes
TO2_target=data(t,1)'; %get the O2 / NOx or airflow data for training

%NORMALISE DATA
% to normalise the inputs and targets to have zero mean and unity standard
% deviation
[tpn,meanp,stdp,ttn,meant,stdt] = prestd(TPinput, TO2_target);
[ptrans,transMat] = prepca(tpn,0.02); %PCA

%TRAINING DATA SET
%1,2,4,5,6,8,9,10,12... getting 75% data for training and 25% for testing
Ptrain1=ptrans(:,1:4:end);
Ttrain1=ttn(:,1:4:end);
Ptrain2=ptrans(:,2:4:end);
Ttrain2=ttn(:,2:4:end);
Ptrain4=ptrans(:,4:4:end);
Ttrain4=ttn(:,4:4:end);
Ptrain = [Ptrain1 Ptrain2 Ptrain4];
Ttrain = [Ttrain1 Ttrain2 Ttrain4];

%TESTING DATA SET
%3,7,11... getting 25% for testing
Ptest=ptrans(:,3:4:end);
Ttest=ttn(:,3:4:end);

Test.P = Ptest; Test.T = Ttest;

%NEURAL NETWORK TRAINING
H= 25; %test for hidden neurons of 10 12 15 20 25 and 30
```

```
net = newff((minmax(Ptrain)),[H 1],{'tansig' 'purelin'},'trainbr');
net.trainParam.epochs = 3000;
net.trainParam.show = 50;
net = init(net);
[net,tr] = train(net,Ptrain,Ttrain,[],[],[],Test);

%NEURAL NETWORK TESTING
Y=sim(net,Ptest);
Ytest=poststd(Y,meant,stdt);
target=poststd(Ttest,meant,stdt);

mppe_t=100*sum(abs(Ytest-target)./target)/length(Ytest);

%SAVE TRAINED NETWORK
savefilename = strcat('IEn_3_1_O2_pca_',num2str(hn),'_model.mat');
save(savefilename,'net', 'tr', 'meanp', 'stdp', 'meant', 'stdt');

%PLOTTING
figure;
set(gca,'FontSize',16);
plot(1:length(target),target,'b',1:length(Ytest),Ytest,'r--','LineWidth',3);
txt=strcat('Testing;','MPPE=',num2str(mppe_t,2),'%;','Hidden Neuron=',num2str(H)); title(txt);
grid on; xlabel('Data Point (5s/Data Point)'); ylabel('O2 (%)');
legend('Measured O2','Predicted O2','Location','SouthOutside','Orientation','horizontal');

saveas(gca,strcat('ann_o2_pca_',num2str(hn),'neurons_t1tot5_t7tot9_training.fig'));
```

The following MATLAB code was used for testing the neural network with PCA model with new data:

```
%LOAD DATA FILES:
data= <'Read data from excel or csv files: where data is arranged by sensor in each coloumn'>;
x=286:342;
%y=2566:3078;
s=x;
SPinput=[data(s,3:5), data(s,14:16), data(s,25:27)]'; % UV, VIS & IR Photodiodes
SO2_target=data(s,1)';

%LOAD TRAINED NETWORK
load(savefilename) %variables: net,tr,meanp,stdp,meant,stdt

%NORMALISE DATA
%Preprocesses the network training set using the mean & standard deviation
%that were previously computed by 'prestd'
spn=trastd(SPinput,meanp,stdp);
stn=trastd(SO2_target,meant,stdt);
sptrans = trapca(spn,transMat);  %PCA Transformation

%NETWORK SIMULATION
Y=sim(net,sptrans);
Ytest=poststd(Y,meant,stdt);
target=poststd(stn,meant,stdt);

mppe_s=100*sum(abs(Ytest-target)./target)/length(Ytest);

%PLOTTING
figure(2);
set(gca,'FontSize',16);
plot(1:length(target),target,'b',1:length(Ytest),Ytest,'r--','LineWidth',3);
txt=strcat('Simulation;','MPPE=',num2str(mppe_s,3),'%;','Hidden Neuron=',num2str(H)); title(txt);
grid on; xlabel('Data Point (5s/Data Point)'); ylabel('O2 (%)');
legend('Measured O2','Predicted O2','Location','SouthOutside','Orientation','horizontal');
saveas(gca,strcat('ann_o2_pca_',num2str(hn),'neurons_t6_simulation.fig'));
```

A.3 Developed Algorithm

The following figures show the LabVIEW code used for the prediction algorithm:

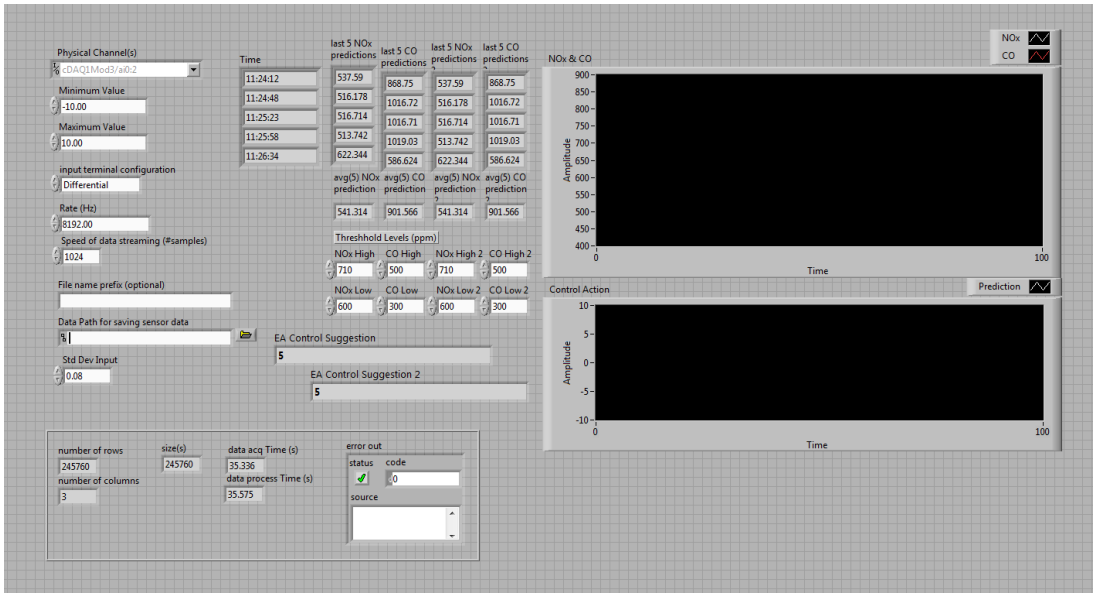

Figure A.1: MCO system front panel in LabVIEW

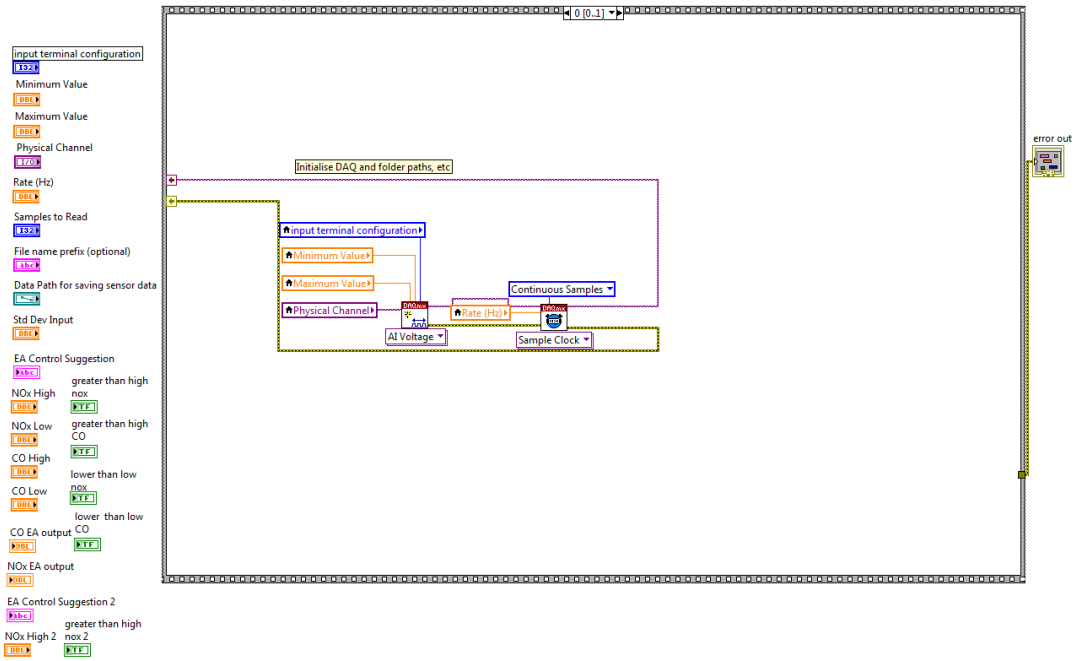

Figure A.2: MCO system DAQ initialisation

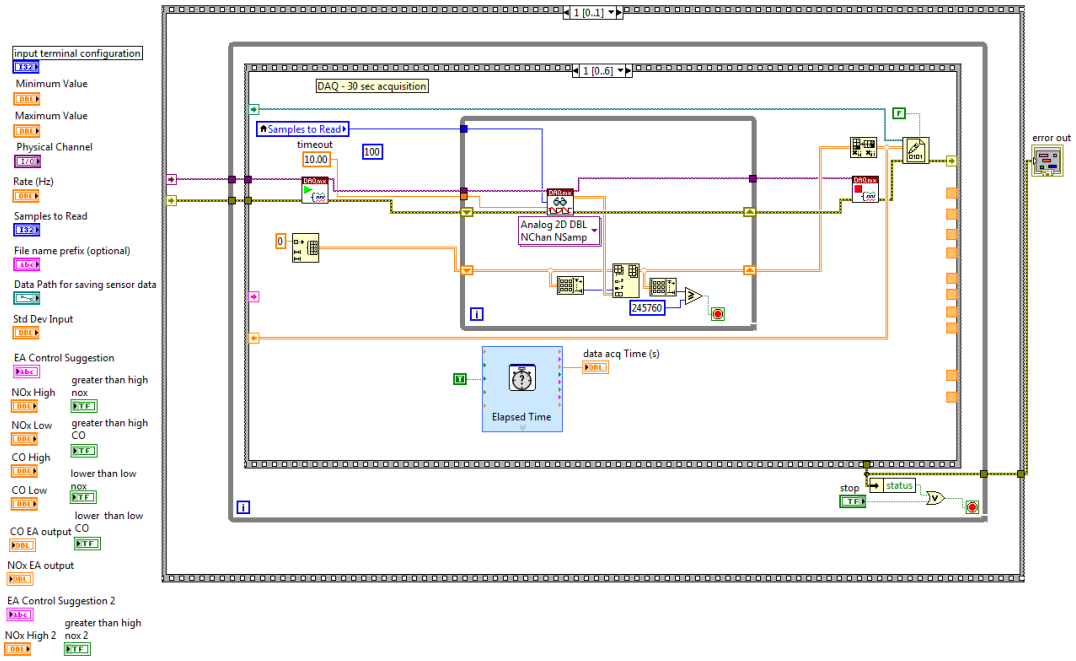

Figure A.3: MCO system DAQ recording for 30 s

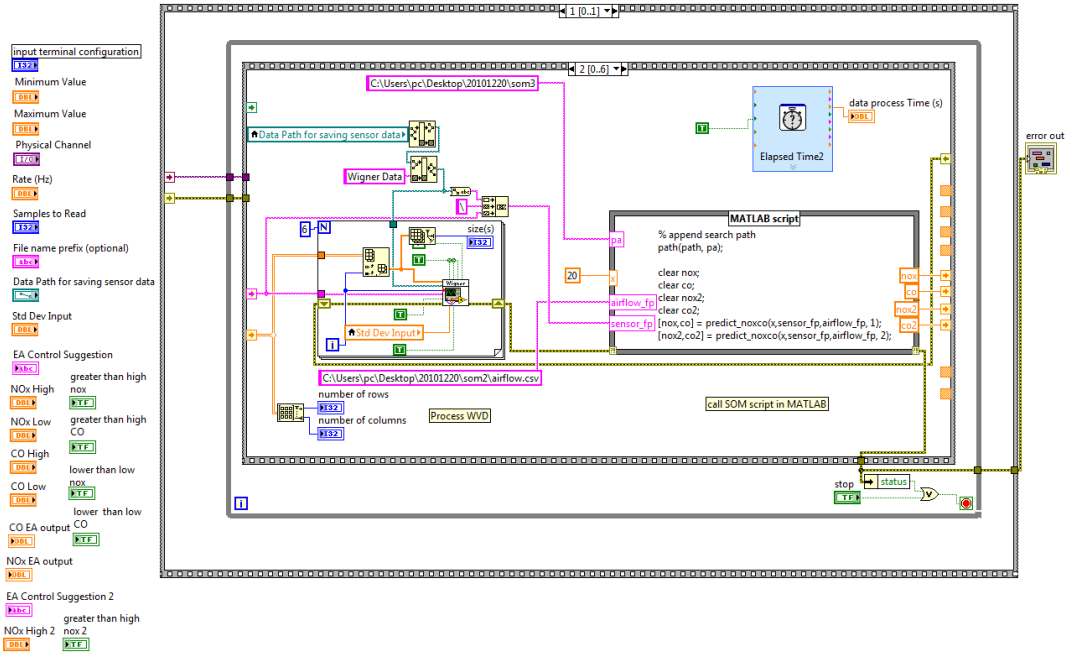

Figure A.4: Calculating the WVD for three sensor data and calling the SOM matlab function to do the prediction

Dependency - SOM toolbox [183] to be added to MATLAB path(s).
The following is the MATLAB function being called by the LabVIEW code do the SOM prediction - 'predict_noxco.m':

```
function[predictnox, predictco] = predict_noxco(x,
   sensordatafilepath, airflowdatafilepath, sensorset)

if sensorset == 2
    sensor = {'Ultra Violet2', 'Visible Light2', '
       Infrared2'};
else
    sensor = {'Ultra Violet', 'Visible Light', '
       Infrared'};
end
noxorco = 'nox';
somwig3s_b(sensordatafilepath,airflowdatafilepath,
   sensor,25,noxorco,sensorset); %
predictnox = mean(simsom_noxco_a(noxorco, sensorset));

noxorco = 'co';
somwig3s_b(sensordatafilepath,airflowdatafilepath,
   sensor,25,noxorco,sensorset); %
predictco = mean(simsom_noxco_a(noxorco, sensorset));
```

The following are the MATLAB functions being called by 'predict_noxco.m':
'somwig3s_b.m':

```
function[] = somwig3s_b(sensordatafilepath,
   airflowdatafilepath, sensorList, noFeaturesPerSensor
   , noxorco, sensorset, datafilefolderpath)

%SOM

%Load data
testpoints = 511;
TestData = somWigExtractData_c(sensordatafilepath,
   airflowdatafilepath, sensorList, noFeaturesPerSensor
   );
feat = length(sensorList)*noFeaturesPerSensor;

p = TestData(:,1:feat);
Tc = TestData(:,feat+1);

%data norm
[pn,minmaxp] = mapminmax(p');

sD_ts = som_data_struct(pn');

len = size(sD_ts.data);
for i=1:len(2)
```

```
    sD_ts.labels{i} = num2str(Tc(i));
end

%Save som net
if sensorset == 2
    if strcmp(noxorco,'nox')
        save somnox2_2.mat sD_ts minmaxp
    elseif strcmp(noxorco,'co')
        save somco2_2.mat sD_ts minmaxp
    end
else
    if strcmp(noxorco,'nox')
        save somnox_2.mat sD_ts minmaxp
    elseif strcmp(noxorco,'co')
        save somco_2.mat sD_ts minmaxp
    end
end
```

'somWigExtractData_c.m':

```
% this is for matlab - labview interface based program to access last data
% file to be used for predicting
function[x] = somWigExtractData_c(sensordatafilepath, airflowdatafilepath, sensorlist, nofeaturesPerSensor)

% Number of Points Per Test
noppt = 500;

% Number of Features per Sensor
    %assumption is nofps >= 1 [currently could be upto a maximum of 512]
nofps = nofeaturesPerSensor;

% Time between samples as recorded
tori = 1;
% Total samples for airflow
sori = 30;

lenS = length(sensorlist);
startRow = 0;

%needs to be removed and code to read the airflow directly from the plant
%has to be added if the comparison of actual vs predicted is to be shown in
%realtime
D = dlmread('airflow.csv');
```

```
testno = 102;

clear E;
clear F;

srlocal = startRow;
startRow = startRow + noppt;
for j = 1: lenS
    y = dlmread(strcat(sensordatafilepath,'_',
       sensorlist{j},'_data.csv'));
    x(srlocal+1:startRow,((j-1)*nofps)+1:j*nofps) = y
       (1:nofps,1:noppt)';
end
E = D(1:sori,testno);
E = interp1local(1:tori:sori, E, noppt);
x(srlocal+1:startRow,(lenS*nofps)+1) = E;
end
```

'simsom_noxco_a.m':

```
function[predict]=simsom_noxco_a(noxorco, sensorset)

save simsom_noxco_var.mat noxorco sensorset
%SOM predict
clear

load simsom_noxco_var.mat noxorco sensorset

%Load som network and the data to be used for
   prediction
if sensorset == 2
    if strcmp(noxorco,'co')
        load somco2.mat sM sD_tr
        load somco2_2.mat sD_ts
    elseif strcmp(noxorco,'nox')
        load somnox2.mat sM sD_tr
        load somnox2_2.mat sD_ts
    end
else
    if strcmp(noxorco,'co')
        load somco.mat sM sD_tr
        load somco_2.mat sD_ts
    elseif strcmp(noxorco,'nox')
        load somnox.mat sM sD_tr
        load somnox_2.mat sD_ts
    end
end

data = sD_ts.data;
```

```
29
30 %Convert map labels to numbers
31 labels = sM.labels;
32 i = strmatch('',labels,'exact');
33 labels = str2double(labels);
34 labels(i)=-1; %put -1 for empty labels
35
36 %neighbours
37 len = size(data);
38 for k=1:len(1)
39     bmus = som_bmus(sM,data(k,:),[1:20]);
40     sub_labels = labels(bmus);
41    predict2(k,:) = sub_labels;
42 end
43
44 predict = mode(predict2,2);
45 resamplesize = 100;
46 for i = 1:(length(predict)/resamplesize)
47     predict(((i-1)*resamplesize)+1:i*resamplesize) =
          mean(predict(((i-1)*resamplesize)+1:i*
          resamplesize));
48 end
```

The following code in file 'somwig3s_noxco_a.m' was used to train the SOM before the LabVIEW code above was used for continuous prediction: 'somwig3s_noxco_a.m':

```
1  function[] = somwig3s_noxco_a(noNodesx, noNodesy,
      trainFileList, testFileList, sensorList,
      noFeaturesPerSensor, datafilefolderpath,
      trainLabelList, noxorco, sensorset)
2  %this function based on somwig3s_noxco.m
3
4  testpoints = 511;
5
6  TrainData = somWigExtractData_c(trainFileList,
      sensorList, noFeaturesPerSensor, datafilefolderpath,
       noxorco);
7  TestData = somWigExtractData_c(testFileList, sensorList
      , noFeaturesPerSensor, datafilefolderpath, noxorco);
8
9  Ltr = size(TrainData,1);
10
11 %check trainfilelist and label list, if mismatched use
      actual airflow
12 if length(trainFileList) == length(trainLabelList)
13     %assumption, each test is 300s long
14     for i = 1:length(trainFileList)
15         TrainData(((i-1)*testpoints)+1:i*testpoints,(
```

```
            length(sensorList)*noFeaturesPerSensor)+1) =
             trainLabelList(i);
    end
end

feat = length(sensorList)*noFeaturesPerSensor;

p = [TrainData(:,1:feat); TestData(:,1:feat)];
Tc = [TrainData(:,feat+1); TestData(:,feat+1)];

%data norm
[pn,minmaxp] = mapminmax(p'); %p must be transposed
   before normalisation

%divide data for training and testing
ptr = pn(:,1:Ltr)';
pts = pn(:,Ltr+1:end)'; %ptr and pts are column vectors
ttr = Tc(1:Ltr);
tts = Tc(Ltr+1:end);

%som data struct
sD_tr = som_data_struct(ptr);
sD_ts = som_data_struct(pts);
len = size(sD_tr.data);
for i=1:len(1)
    sD_tr.labels{i} = num2str(ttr(i));
end

len = size(sD_ts.data);
for i=1:len(1)
    sD_ts.labels{i} = num2str(tts(i));
end

%som - train
sM = som_make(sD_tr,'msize',[noNodesx noNodesy]);
sM = som_autolabel(sM,sD_tr,'vote');

%save som net
if sensorset == 2
    if strcmp(noxorco,'nox')
        save somnox2.mat sM sD_tr sD_ts minmaxp
    elseif strcmp(noxorco,'co')
        save somco2.mat sM sD_tr sD_ts minmaxp
    end
else
    if strcmp(noxorco,'nox')
        save somnox.mat sM sD_tr sD_ts minmaxp
    elseif strcmp(noxorco,'co')
```

```
61          save somco.mat sM sD_tr sD_ts minmaxp
62      end
63  end
```

Appendix B

SIGNAL PROCESSING RESULTS

B.1 RMS results

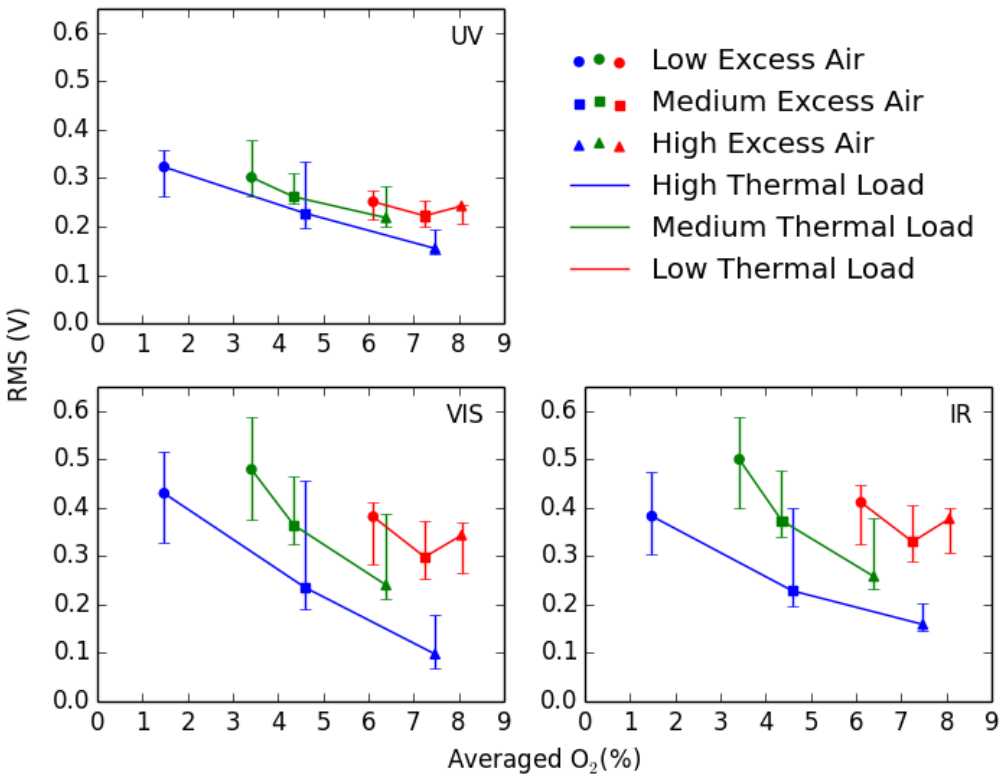

Figure B.1: RMS of UV, VIS & IR photodiode signals Vs averaged O_2 for Tests 10 to 18 - 90 % Coal & 10 % Straw - 50° Swirl

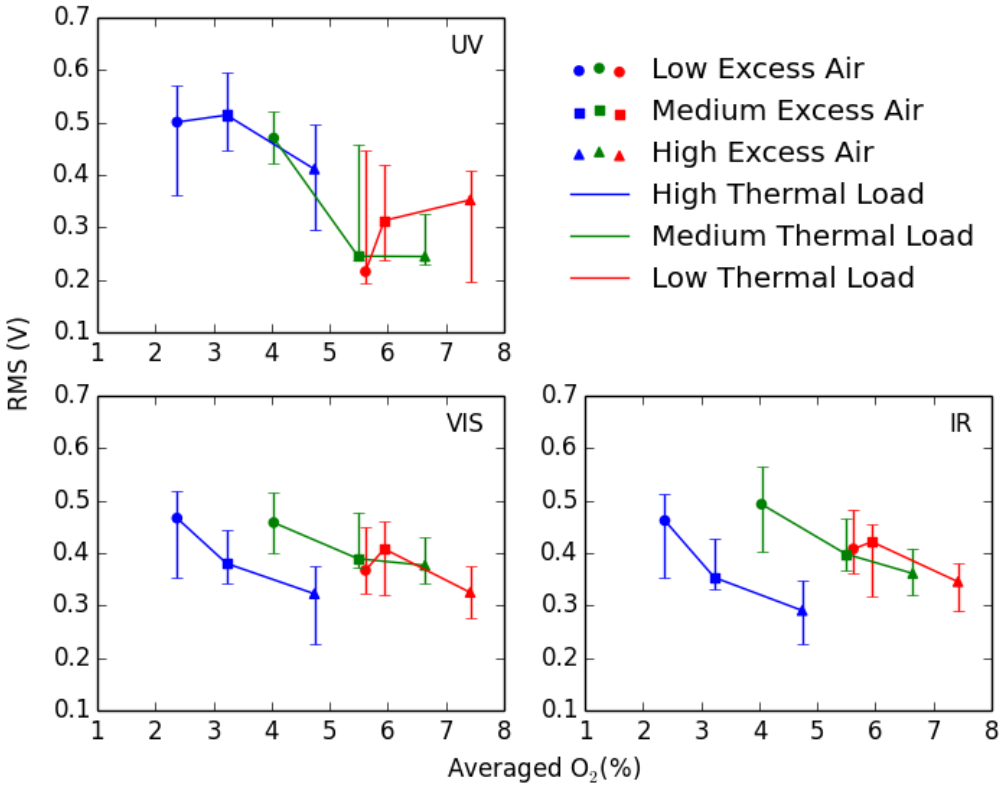

Figure B.2: RMS of UV, VIS & IR photodiode signals Vs averaged O_2 for Tests 82 to 90 - 80 % Coal & 20 % Straw - 50° Swirl

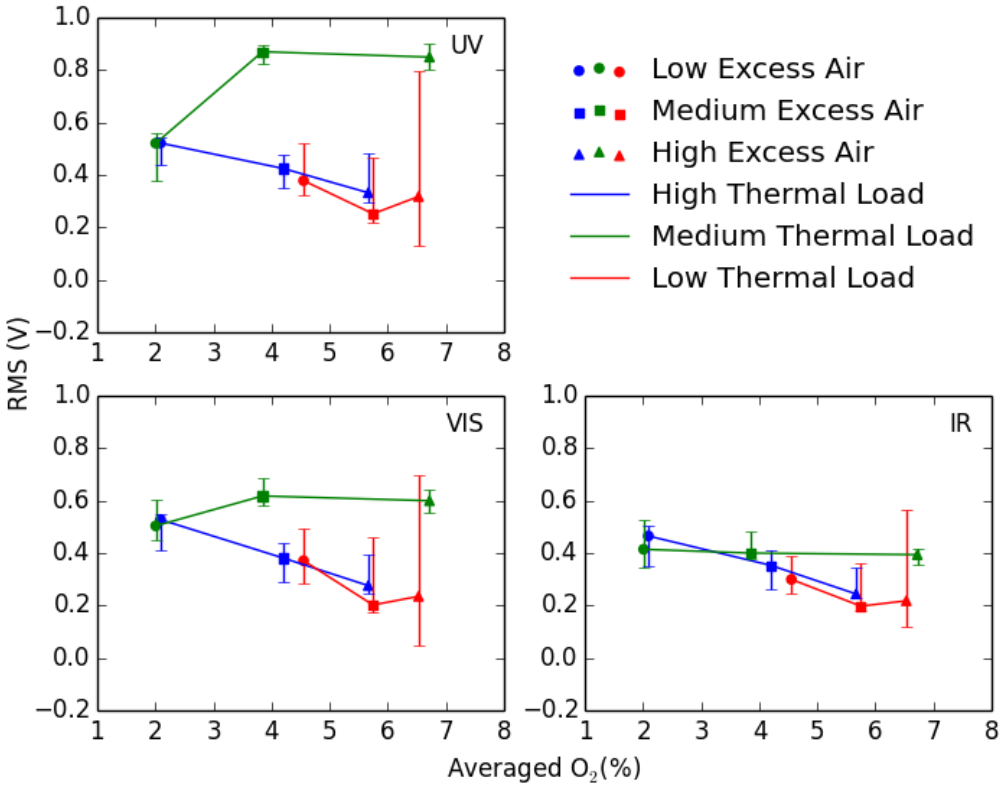

Figure B.3: RMS of UV, VIS & IR photodiode signals Vs averaged O_2 for Tests 55 to 63 - 70 % Coal & 30 % Straw - 60° Swirl

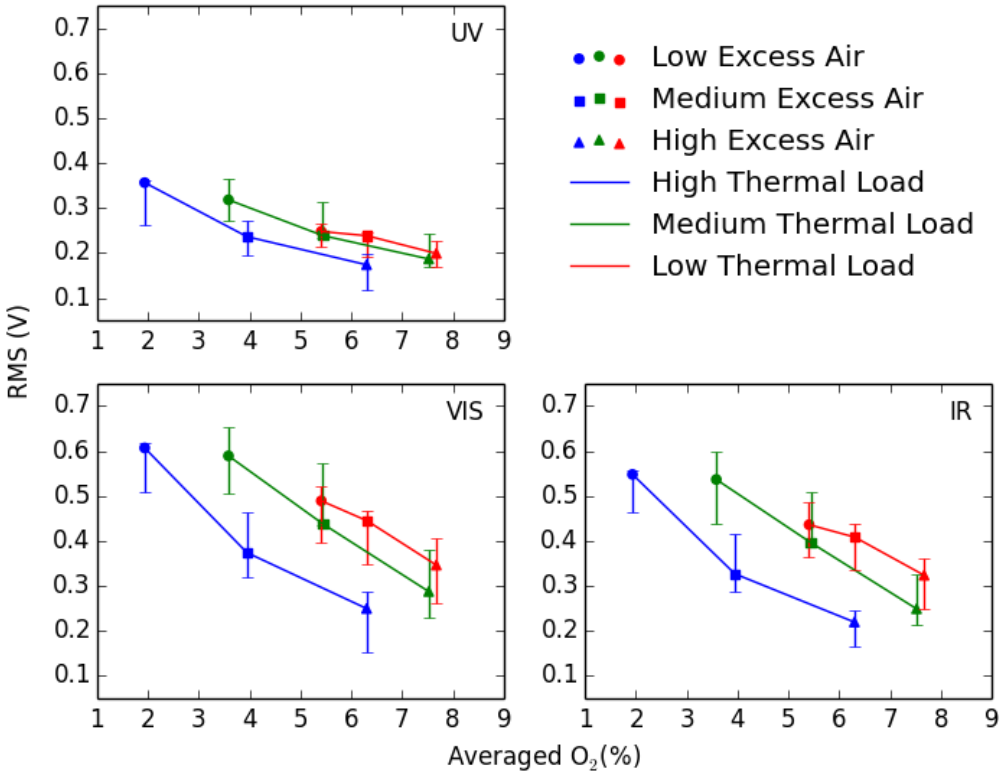

Figure B.4: RMS of UV, VIS & IR photodiode signals Vs averaged O_2 for Tests 37 to 45 - 100 % Coal - 60° Swirl

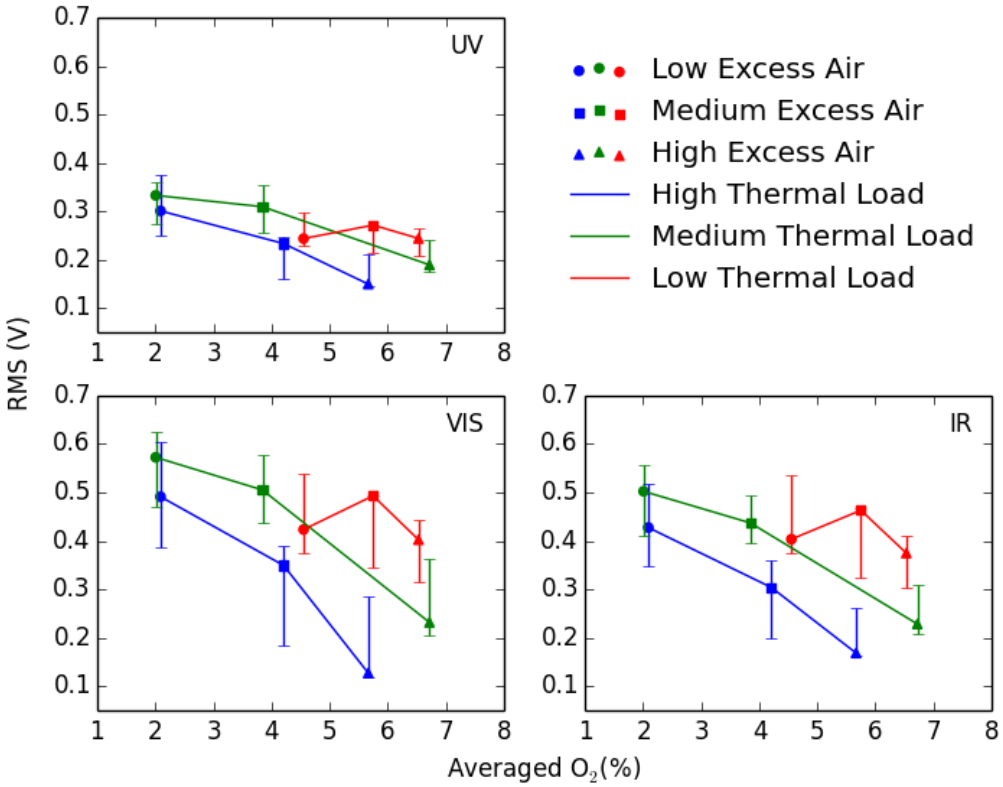

Figure B.5: RMS of UV, VIS & IR photodiode signals Vs averaged O_2 for Tests 46 to 54 - 90 % Coal & 10 % Straw - 60° Swirl

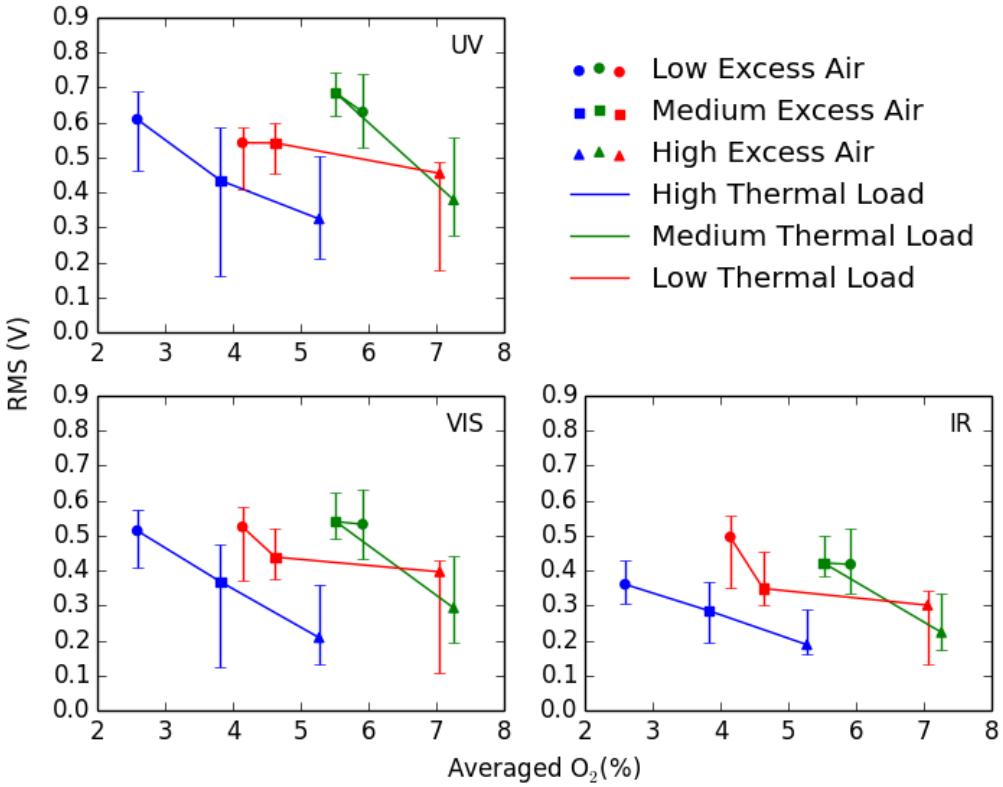

Figure B.6: RMS of UV, VIS & IR photodiode signals Vs averaged O_2 for Tests 64 to 72 - 80 % Coal & 20 % Straw - 60° Swirl

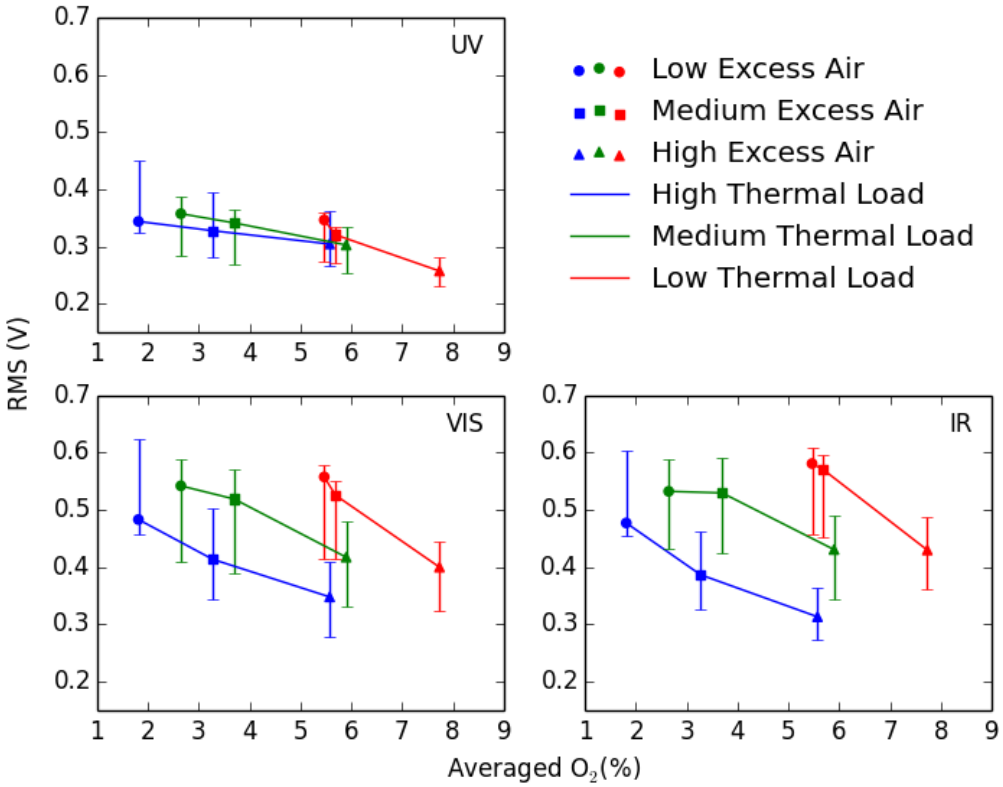

Figure B.7: RMS of UV, VIS & IR photodiode signals Vs averaged O_2 for Tests 28 to 36 - 100 % Coal - 40° Swirl

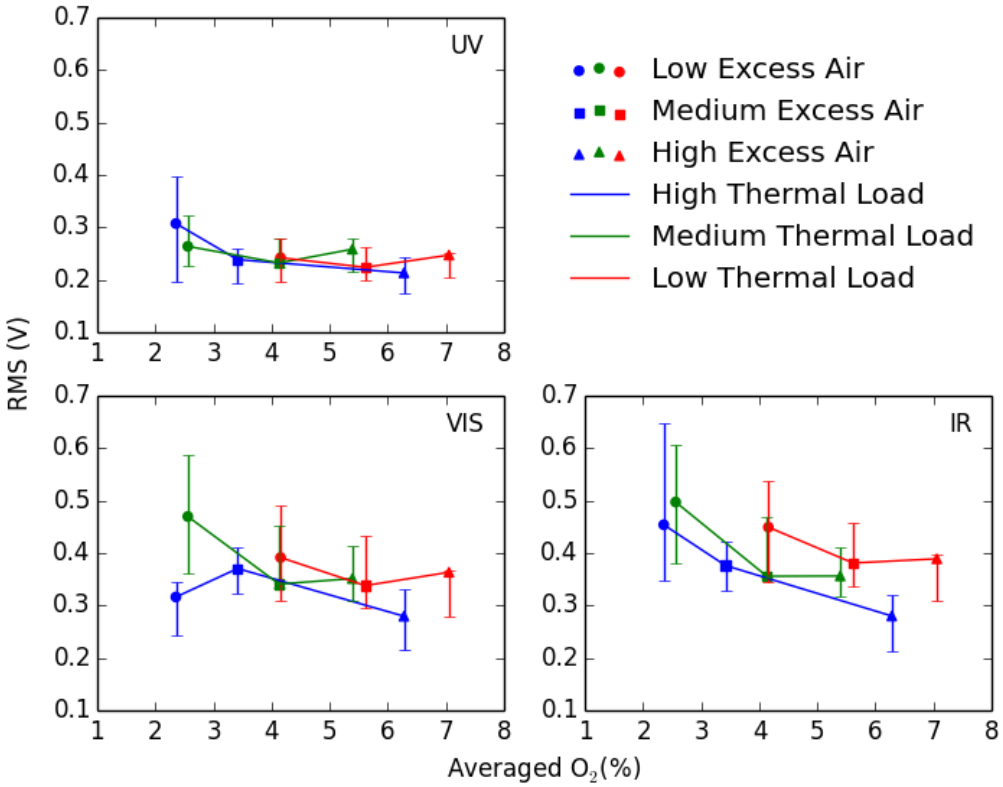

Figure B.8: RMS of UV, VIS & IR photodiode signals Vs averaged O_2 for Tests 19 to 27 - 90 % Coal & 10 % Straw - 40° Swirl

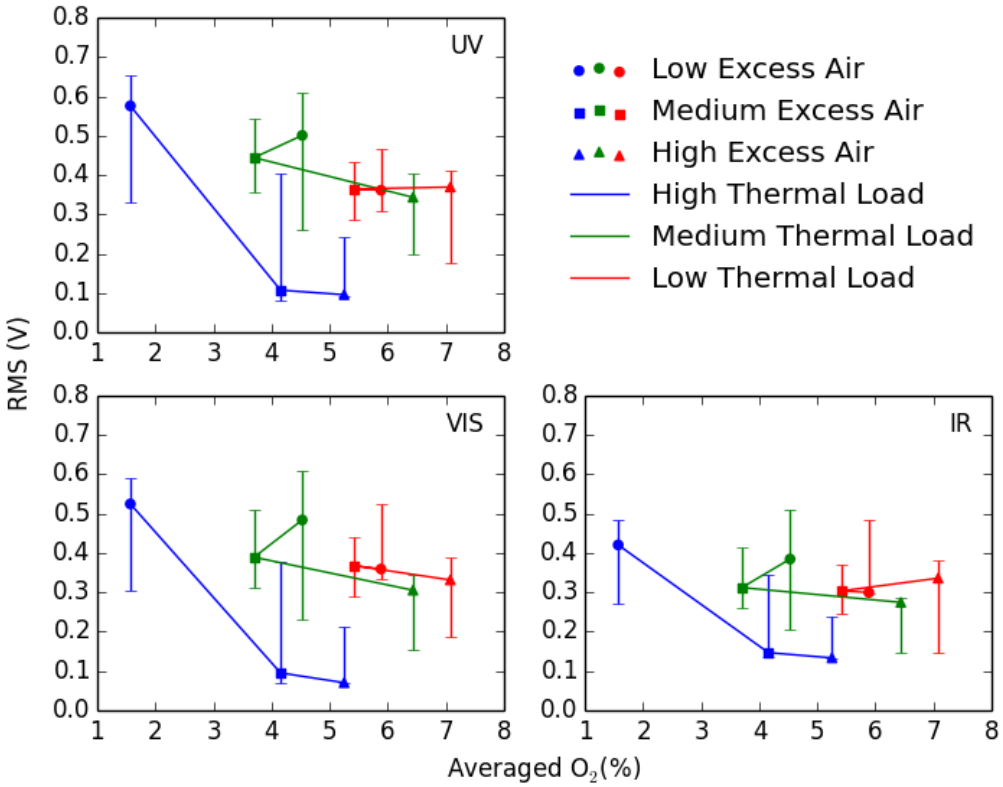

Figure B.9: RMS of UV, VIS & IR photodiode signals Vs averaged O_2 for Tests 73 to 81 - 80 % Coal & 20 % Straw - 40° Swirl

B.2 FFT results

All test numbers with reference to Table 3.7.

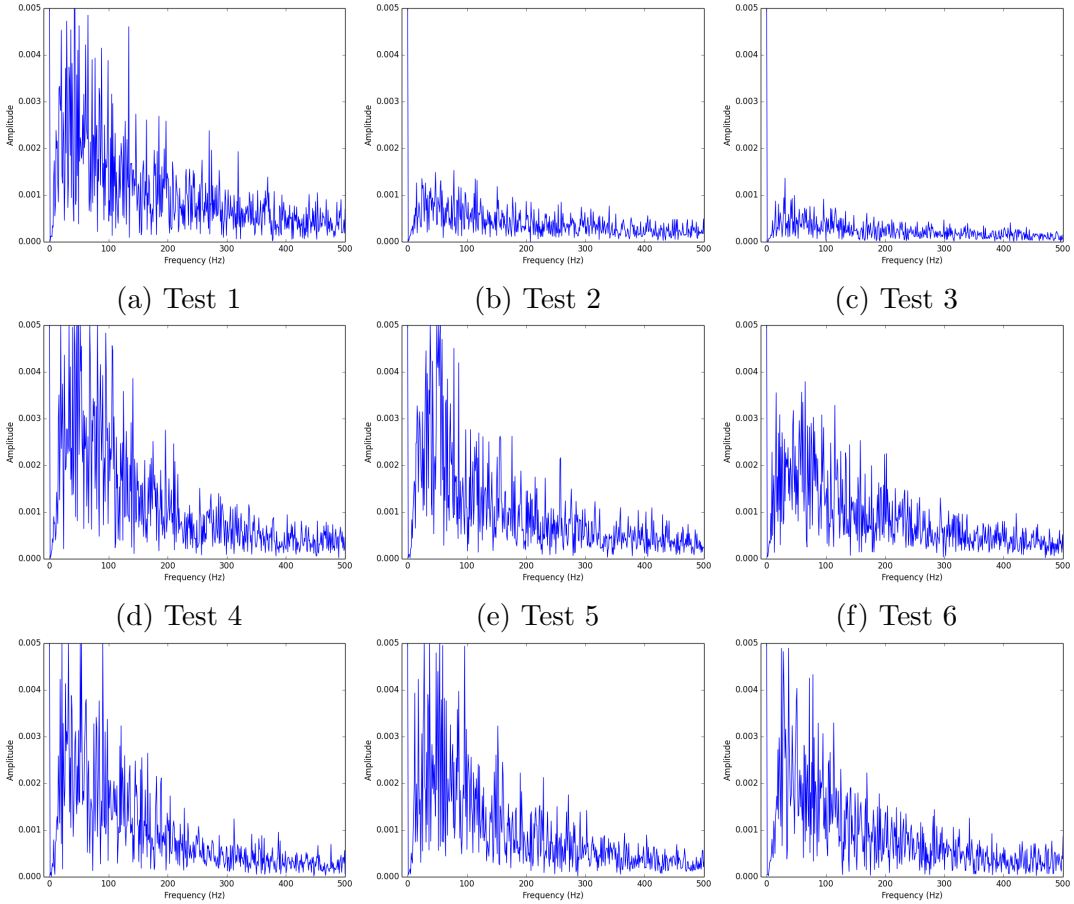

(a) Test 1 (b) Test 2 (c) Test 3

(d) Test 4 (e) Test 5 (f) Test 6

(g) Test 7 (h) Test 8 (i) Test 9

Figure B.10: FFT of VIS photodiode signal for Tests 1 to 9 - 100 % Coal - 50° Swirl

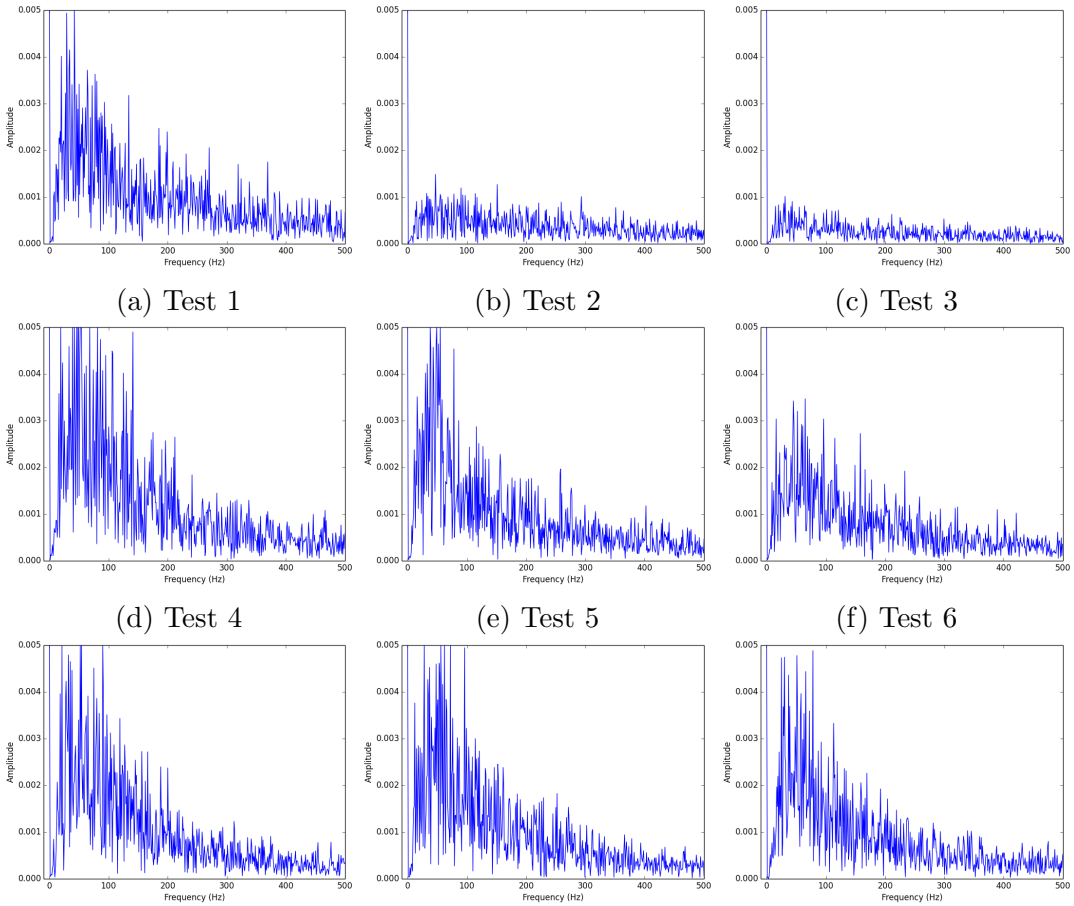

(a) Test 1 (b) Test 2 (c) Test 3

(d) Test 4 (e) Test 5 (f) Test 6

(g) Test 7 (h) Test 8 (i) Test 9

Figure B.11: FFT of IR photodiode signal for Tests 1 to 9 - 100 % Coal - 50° Swirl

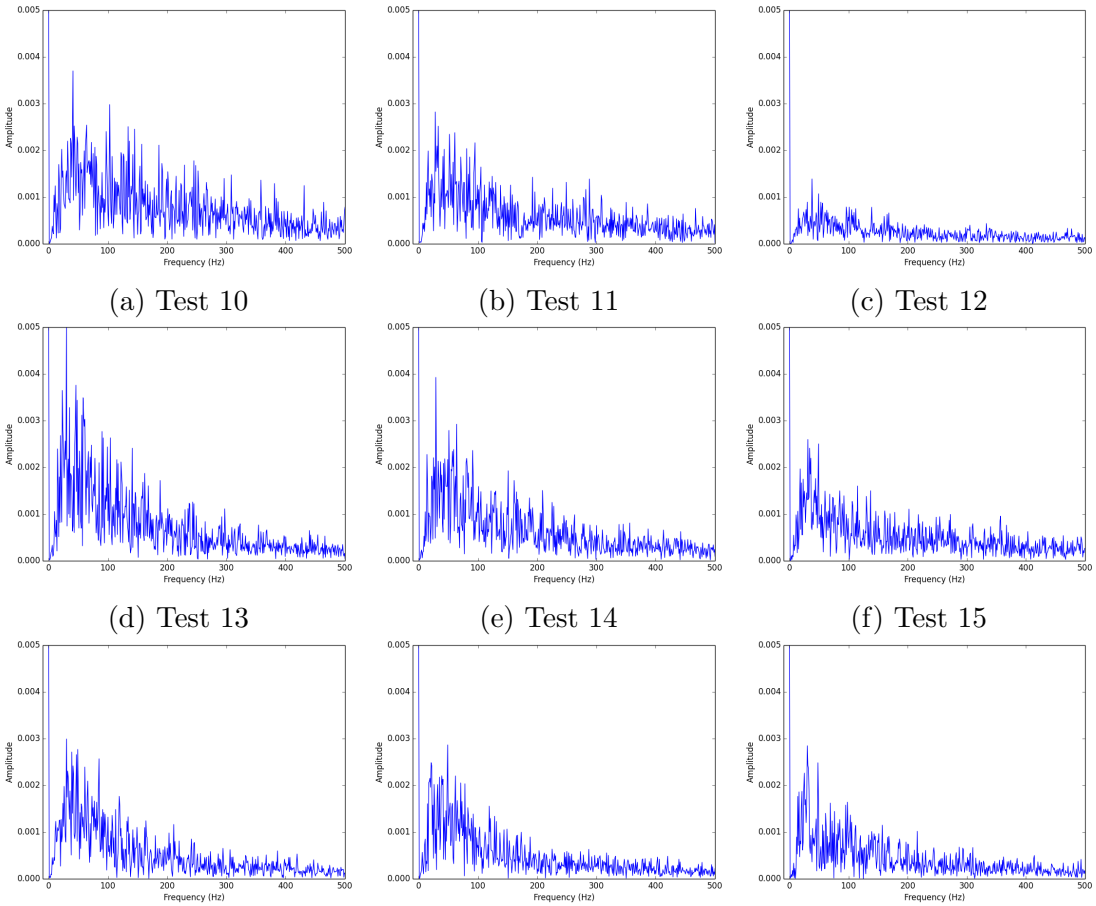

(a) Test 10 (b) Test 11 (c) Test 12

(d) Test 13 (e) Test 14 (f) Test 15

(g) Test 16 (h) Test 17 (i) Test 18

Figure B.12: FFT of UV photodiode signal for Tests 10 to 18 - 90 % Coal & 10 % Straw - 50° Swirl

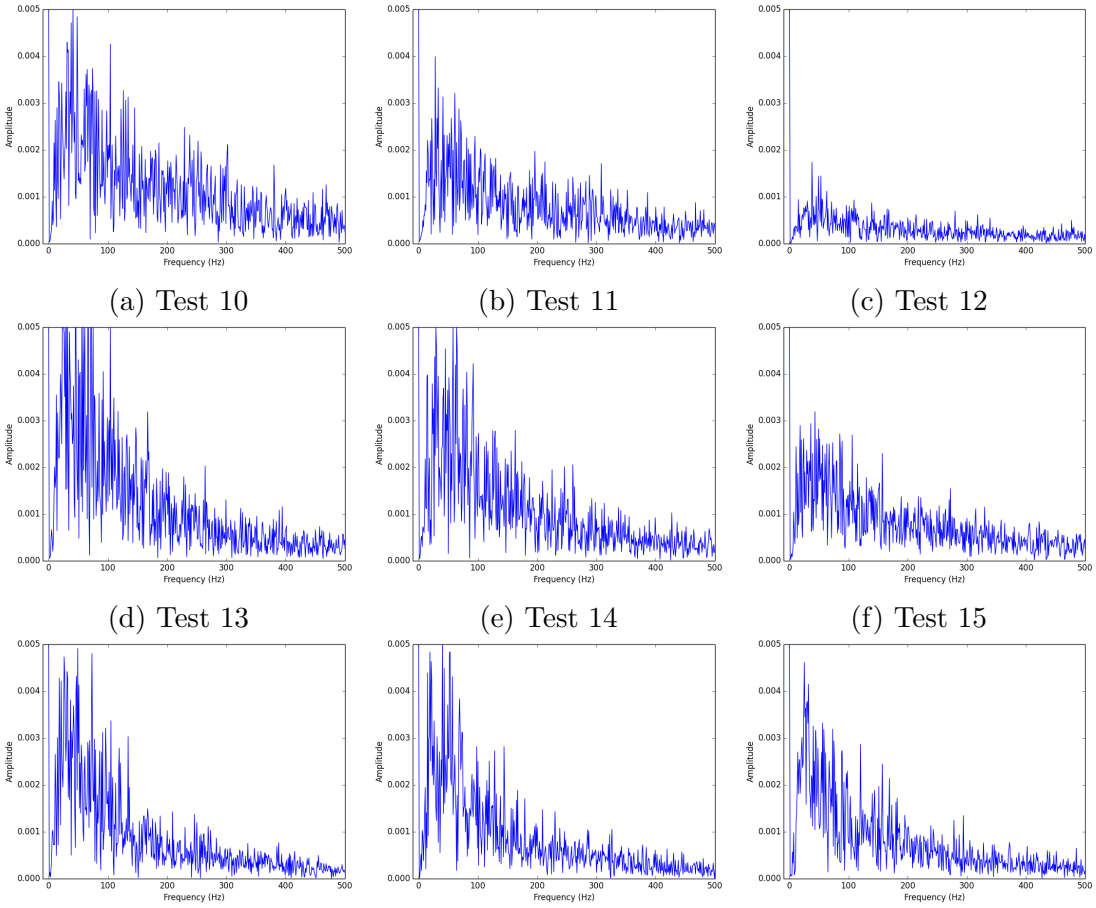

(a) Test 10 (b) Test 11 (c) Test 12

(d) Test 13 (e) Test 14 (f) Test 15

(g) Test 16 (h) Test 17 (i) Test 18

Figure B.13: FFT of VIS photodiode signal for Tests 10 to 18 - 90 % Coal & 10 % Straw - 50° Swirl

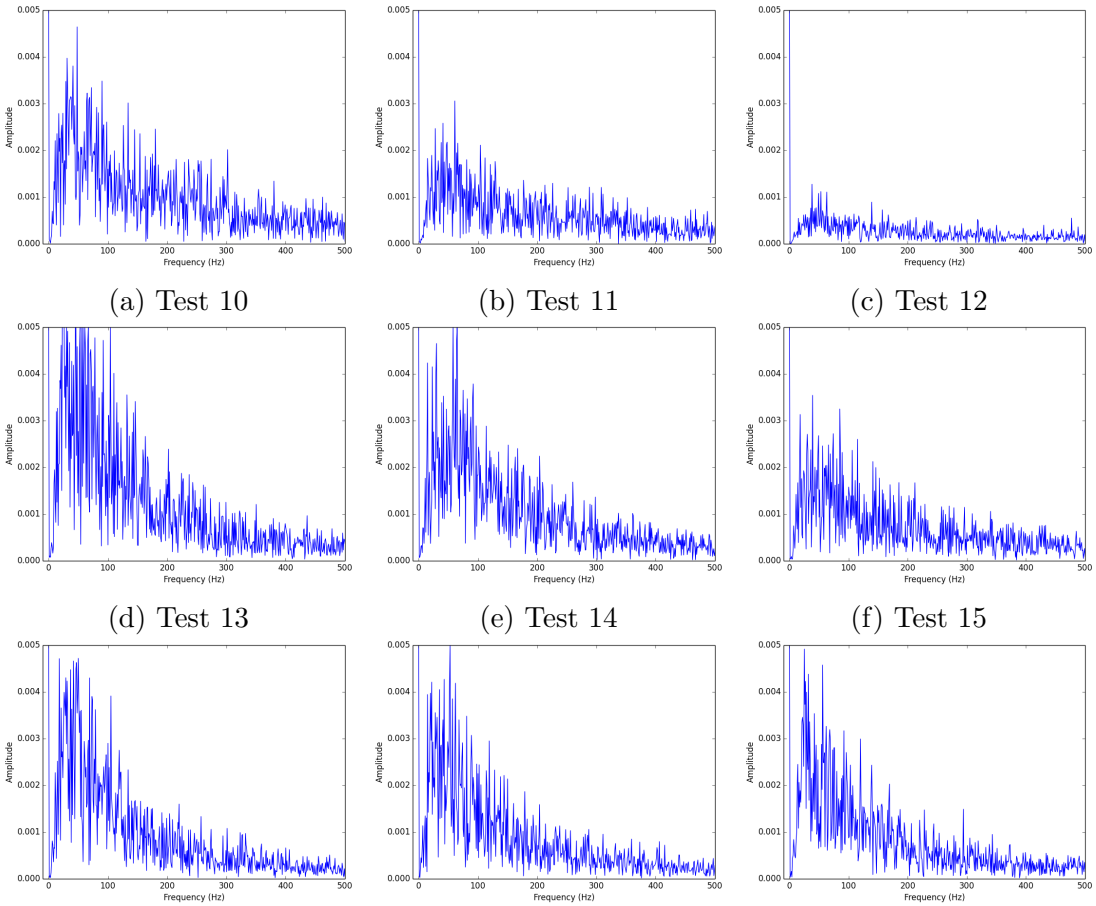

(a) Test 10 (b) Test 11 (c) Test 12

(d) Test 13 (e) Test 14 (f) Test 15

(g) Test 16 (h) Test 17 (i) Test 18

Figure B.14: FFT of IR photodiode signal for Tests 10 to 18 - 90 % Coal & 10 % Straw - 50° Swirl

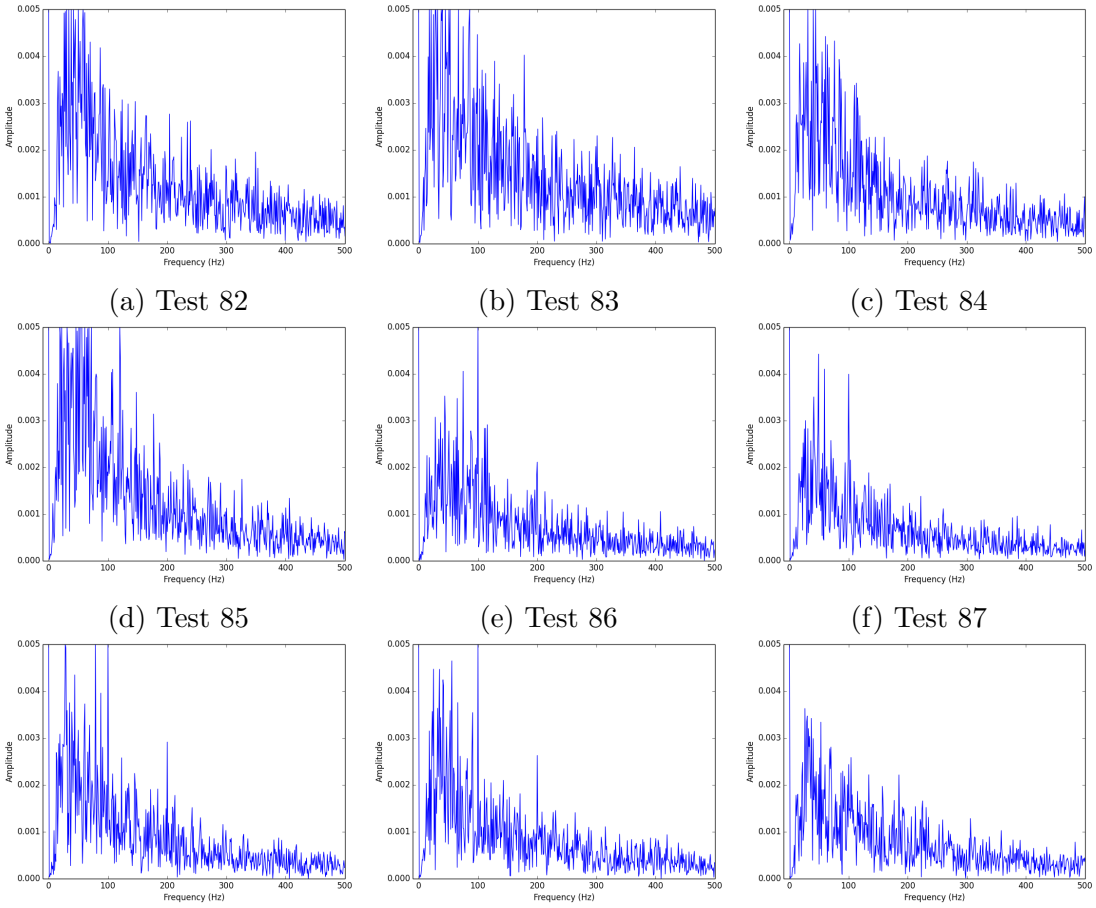

(a) Test 82 (b) Test 83 (c) Test 84

(d) Test 85 (e) Test 86 (f) Test 87

(g) Test 88 (h) Test 89 (i) Test 90

Figure B.15: FFT of UV photodiode signal for Tests 82 to 90 - 80 % Coal & 20 % Straw - 50° Swirl

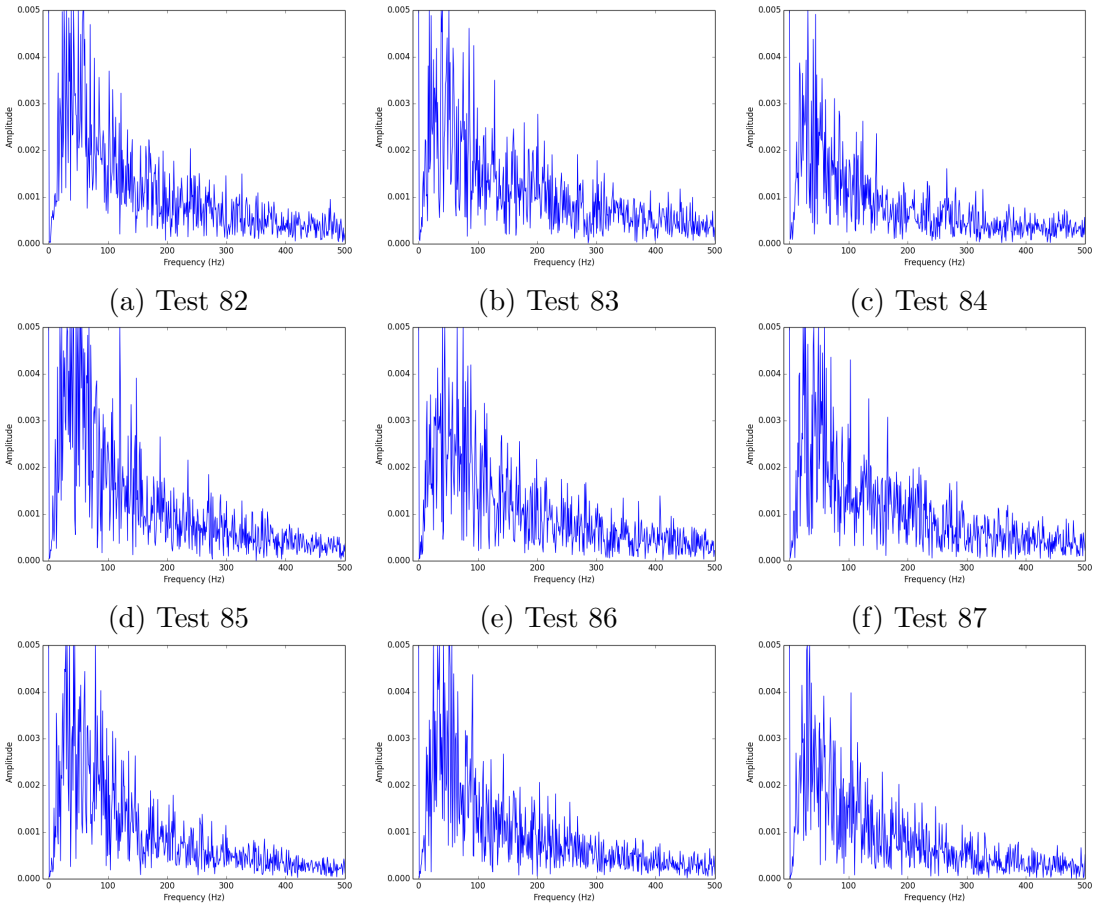

(a) Test 82 (b) Test 83 (c) Test 84

(d) Test 85 (e) Test 86 (f) Test 87

(g) Test 88 (h) Test 89 (i) Test 90

Figure B.16: FFT of VIS photodiode signal for Tests 82 to 90 - 80 % Coal & 20 % Straw - 50° Swirl

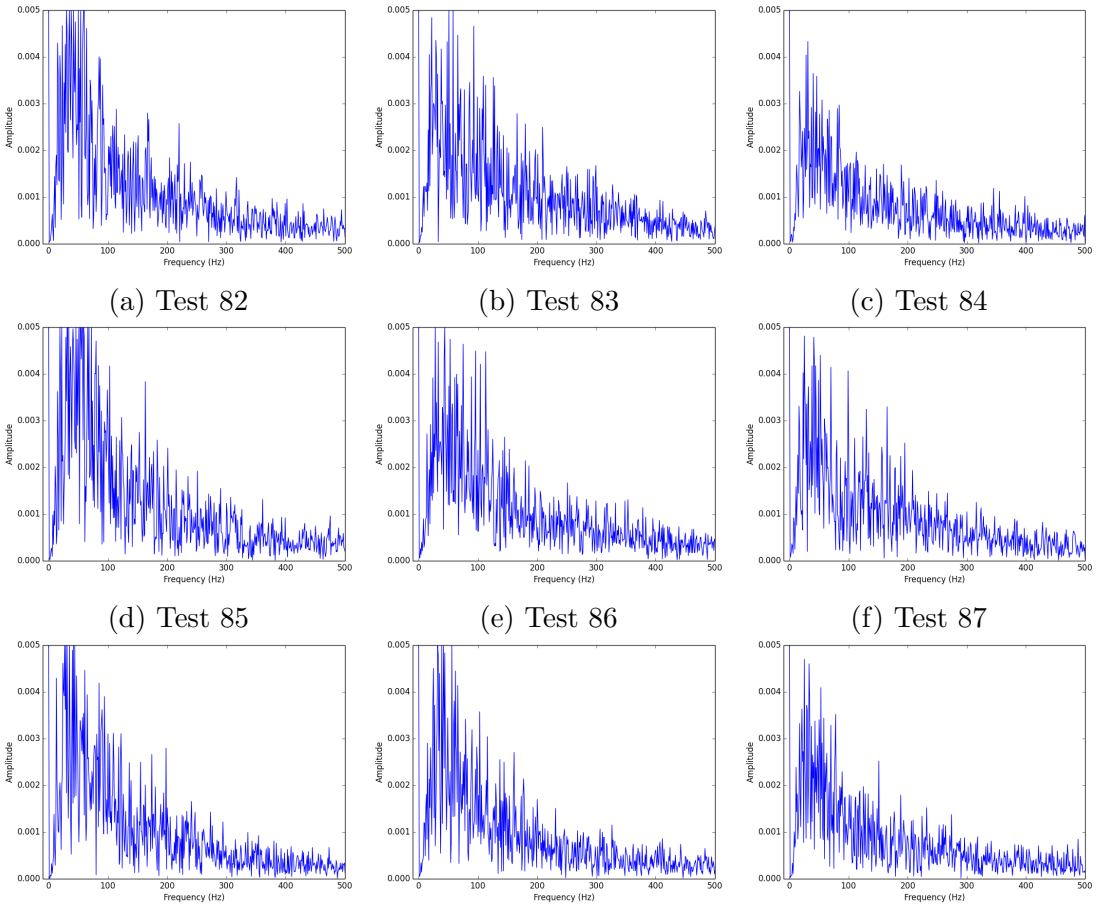

(a) Test 82 (b) Test 83 (c) Test 84

(d) Test 85 (e) Test 86 (f) Test 87

(g) Test 88 (h) Test 89 (i) Test 90

Figure B.17: FFT of IR photodiode signal for Tests 82 to 90 - 80 % Coal & 20 % Straw - 50° Swirl

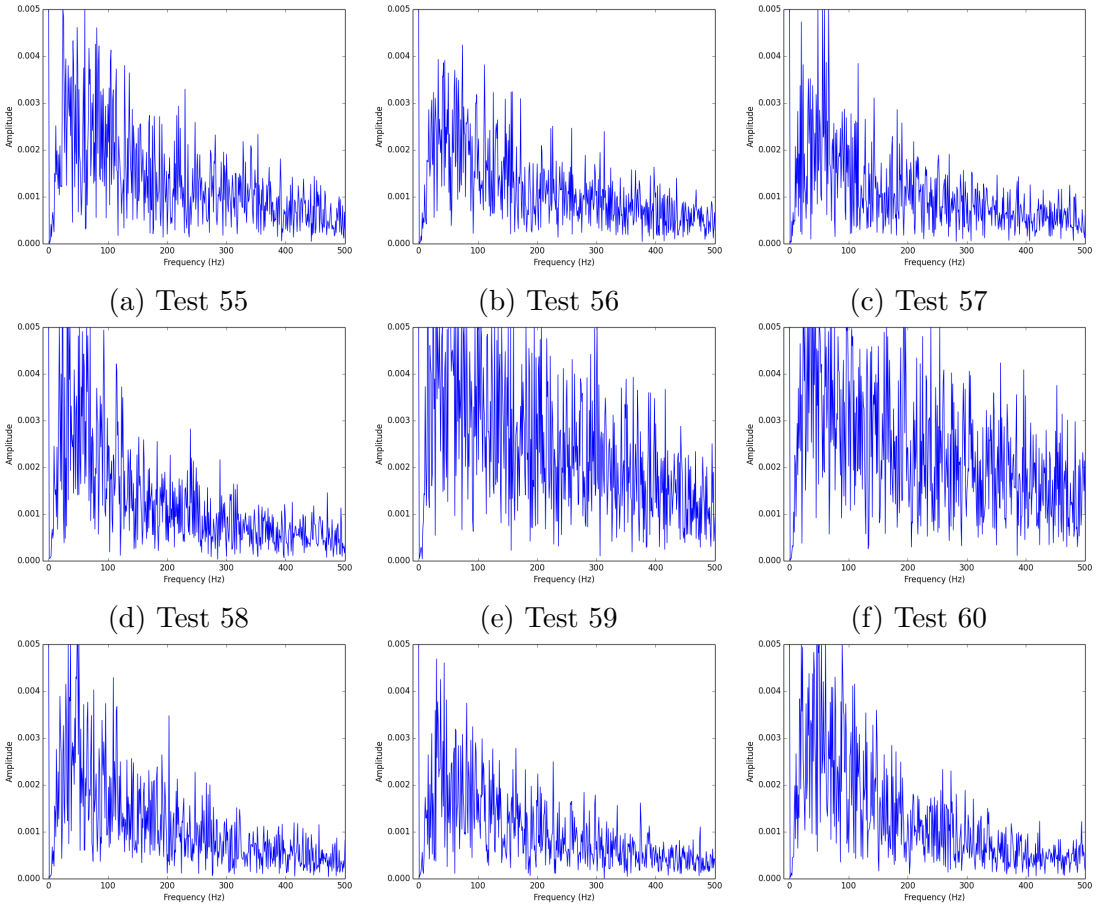

(a) Test 55 (b) Test 56 (c) Test 57

(d) Test 58 (e) Test 59 (f) Test 60

(g) Test 61 (h) Test 62 (i) Test 63

Figure B.18: FFT of UV photodiode signal for Tests 55 to 63 - 70 % Coal & 30 % Straw - 60° Swirl

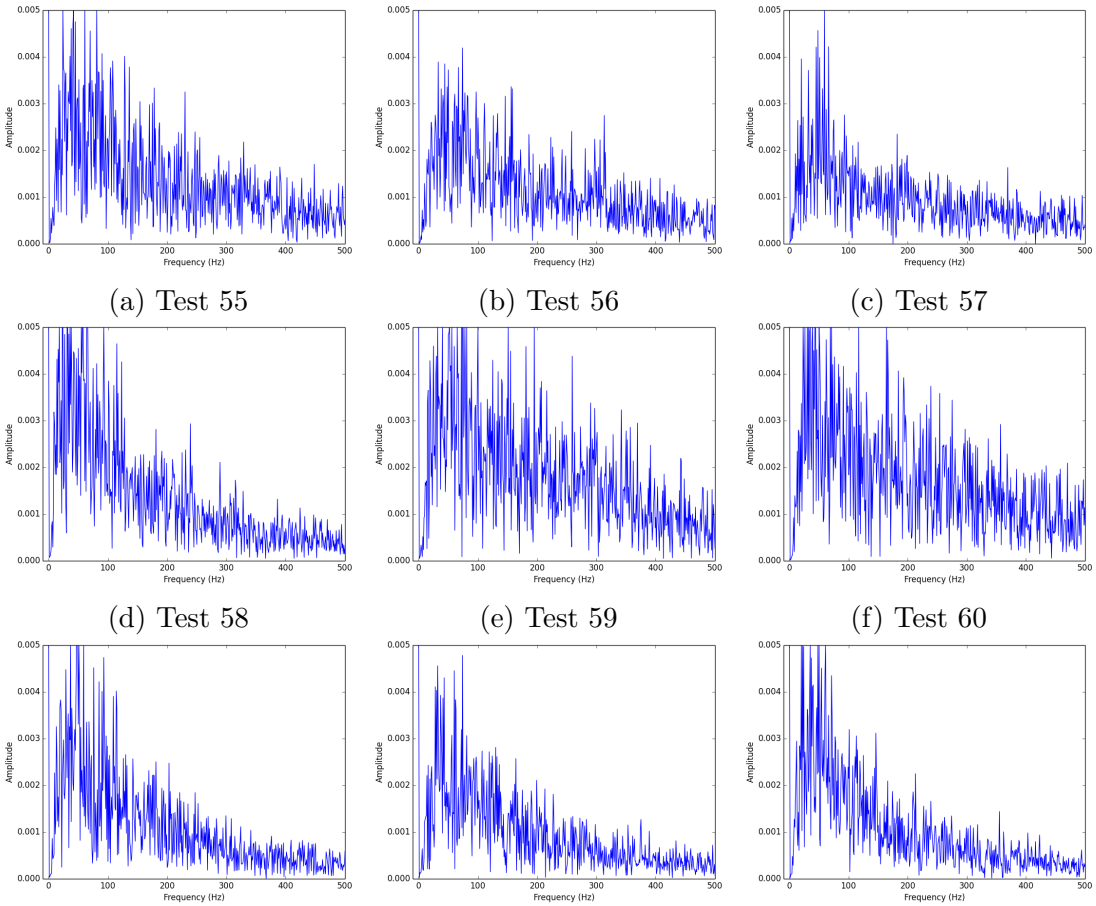

(a) Test 55 (b) Test 56 (c) Test 57

(d) Test 58 (e) Test 59 (f) Test 60

(g) Test 61 (h) Test 62 (i) Test 63

Figure B.19: FFT of VIS photodiode signal for Tests 55 to 63 - 70 % Coal & 30 % Straw - 60° Swirl

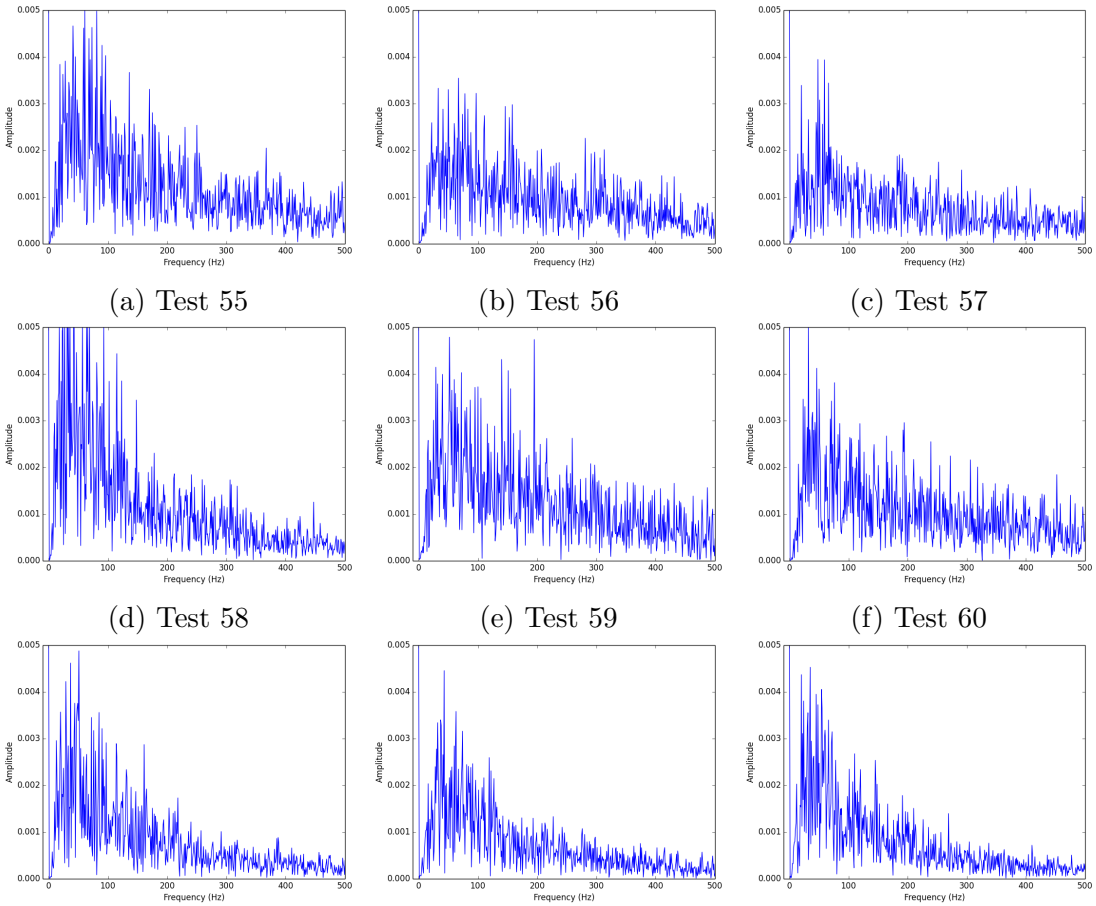

(a) Test 55 (b) Test 56 (c) Test 57

(d) Test 58 (e) Test 59 (f) Test 60

(g) Test 61 (h) Test 62 (i) Test 63

Figure B.20: FFT of IR photodiode signal for Tests 55 to 63 - 70 % Coal & 30 % Straw - 60° Swirl

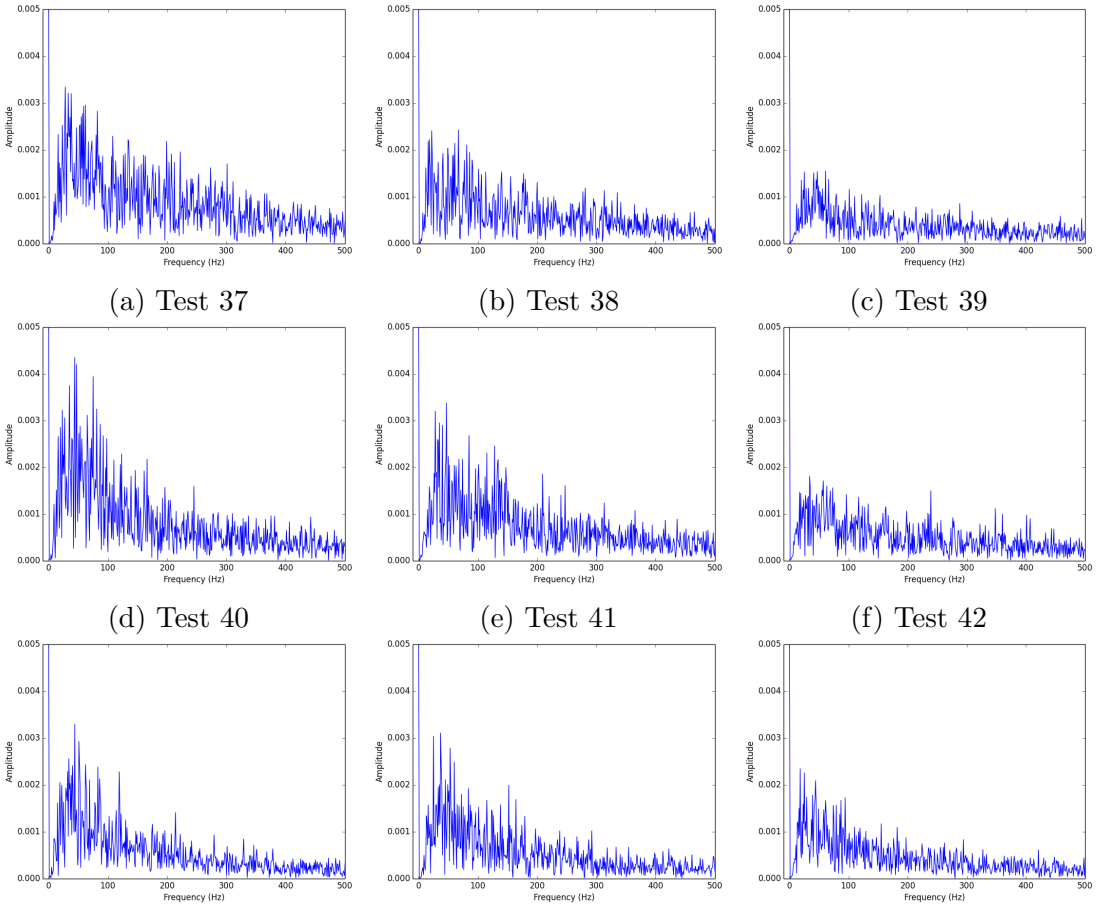

(a) Test 37 (b) Test 38 (c) Test 39

(d) Test 40 (e) Test 41 (f) Test 42

(g) Test 43 (h) Test 44 (i) Test 45

Figure B.21: FFT of UV photodiode signal for Tests 37 to 45 - 100 % Coal - 60° Swirl

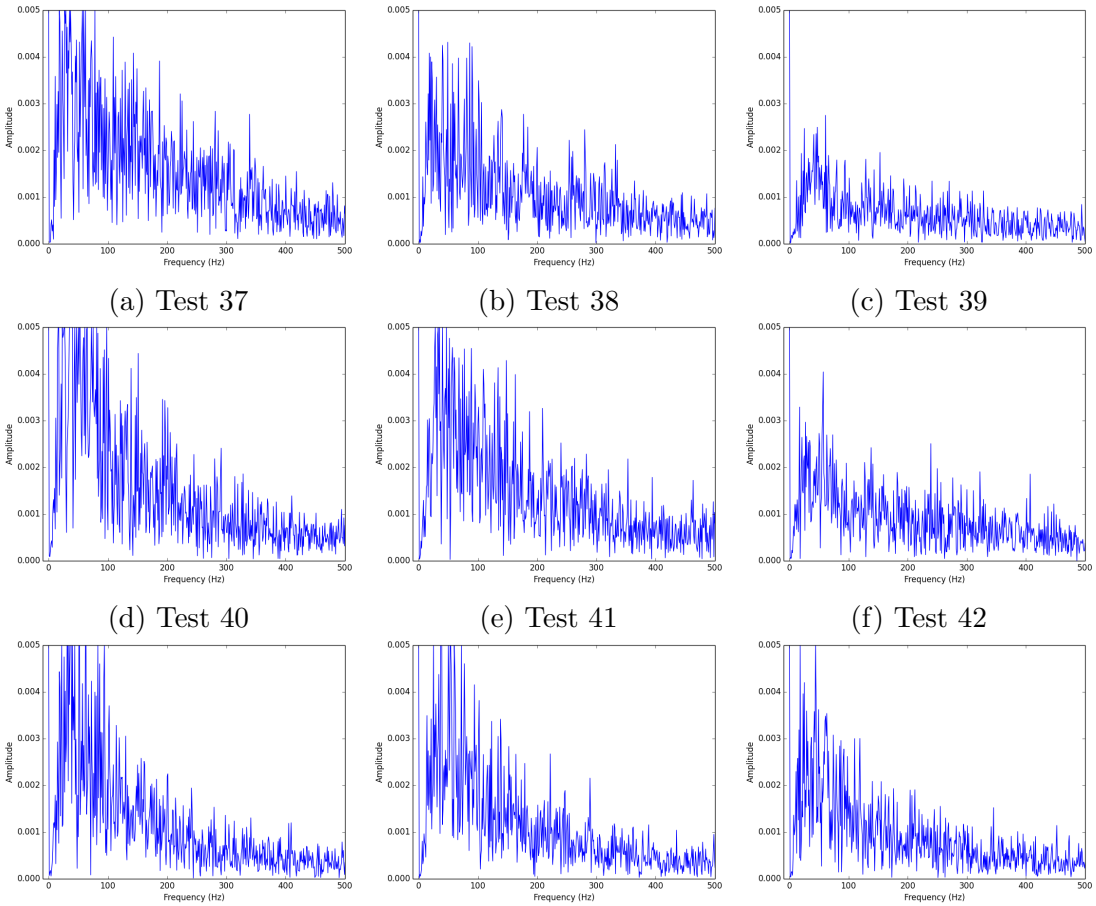

(a) Test 37 (b) Test 38 (c) Test 39

(d) Test 40 (e) Test 41 (f) Test 42

(g) Test 43 (h) Test 44 (i) Test 45

Figure B.22: FFT of VIS photodiode signal for Tests 37 to 45 - 100 % Coal - 60° Swirl

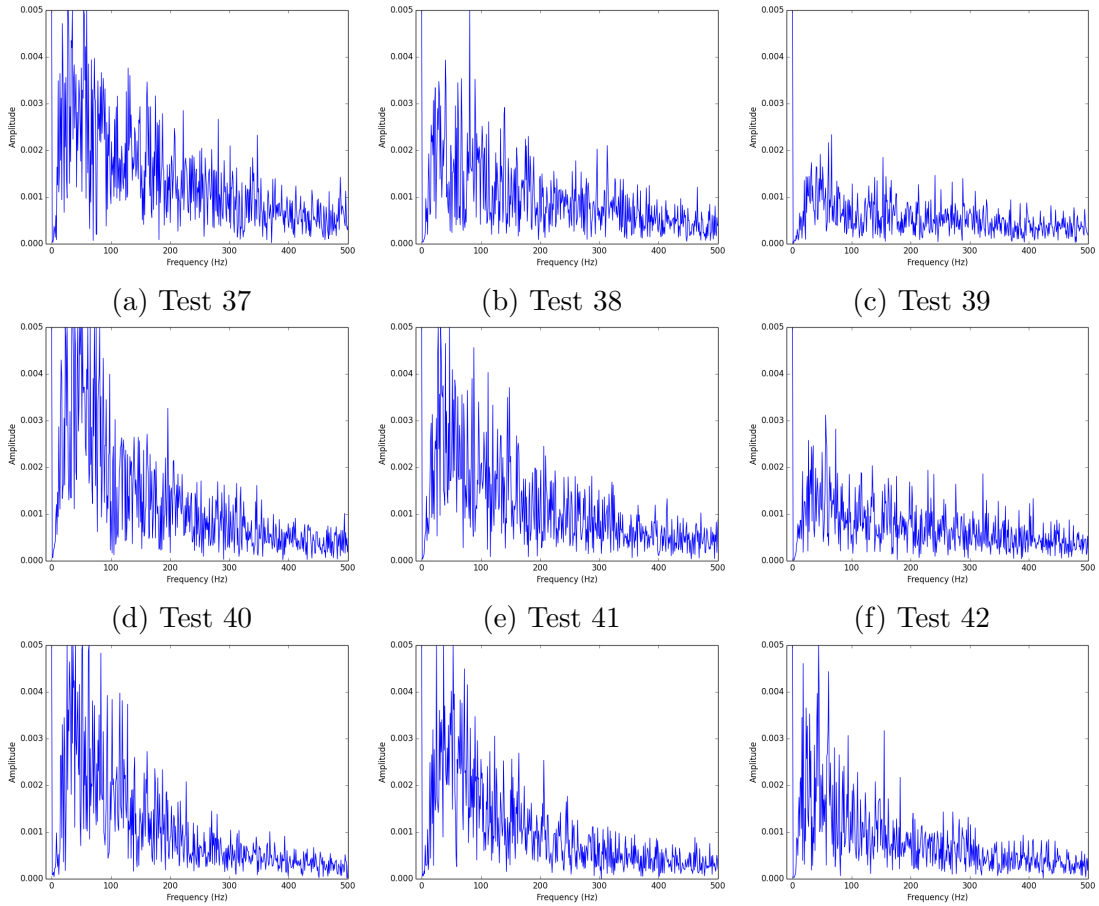

(a) Test 37 (b) Test 38 (c) Test 39

(d) Test 40 (e) Test 41 (f) Test 42

(g) Test 43 (h) Test 44 (i) Test 45

Figure B.23: FFT of IR photodiode signal for Tests 37 to 45 - 100 % Coal - 60° Swirl

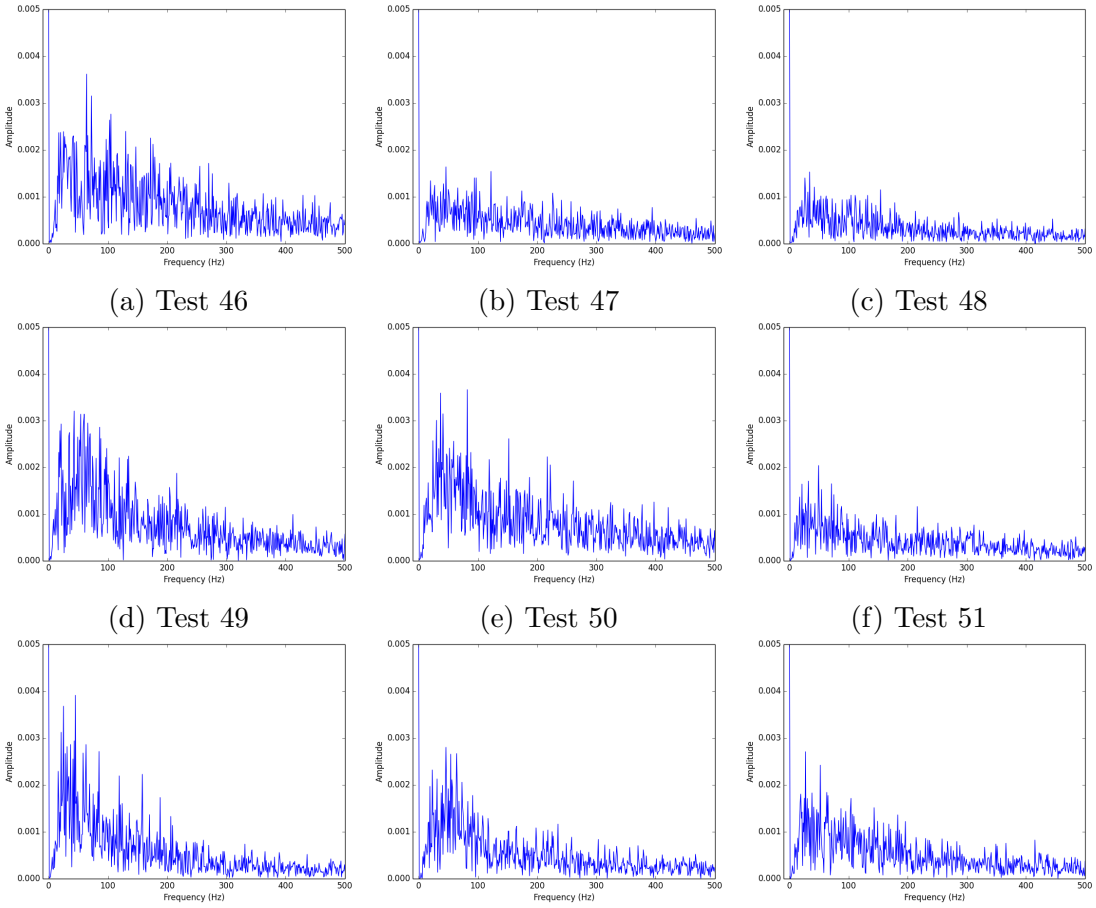

(a) Test 46 (b) Test 47 (c) Test 48

(d) Test 49 (e) Test 50 (f) Test 51

(g) Test 52 (h) Test 53 (i) Test 54

Figure B.24: FFT of UV photodiode signal for Tests 46 to 54 - 90 % Coal & 10 % Straw - 60° Swirl

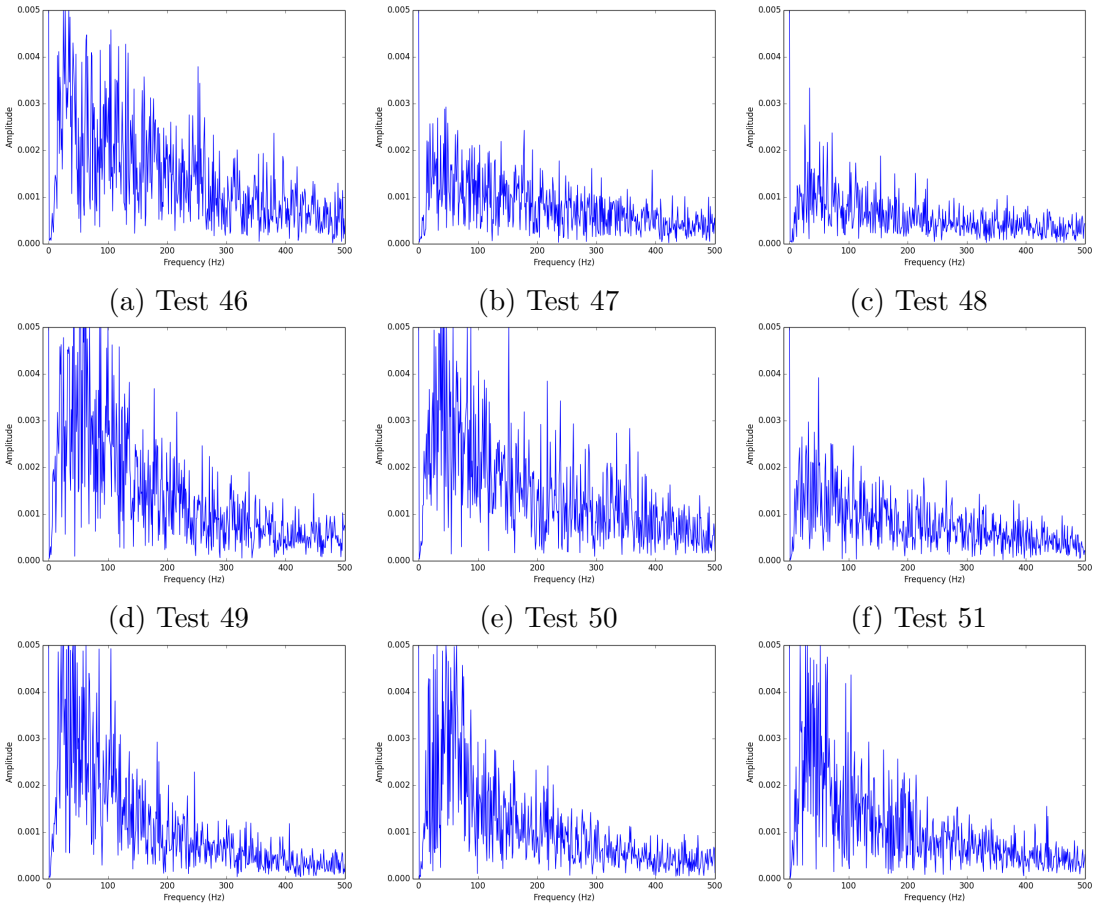

(a) Test 46 (b) Test 47 (c) Test 48

(d) Test 49 (e) Test 50 (f) Test 51

(g) Test 52 (h) Test 53 (i) Test 54

Figure B.25: FFT of VIS photodiode signal for Tests 46 to 54 - 90 % Coal & 10 % Straw - 60° Swirl

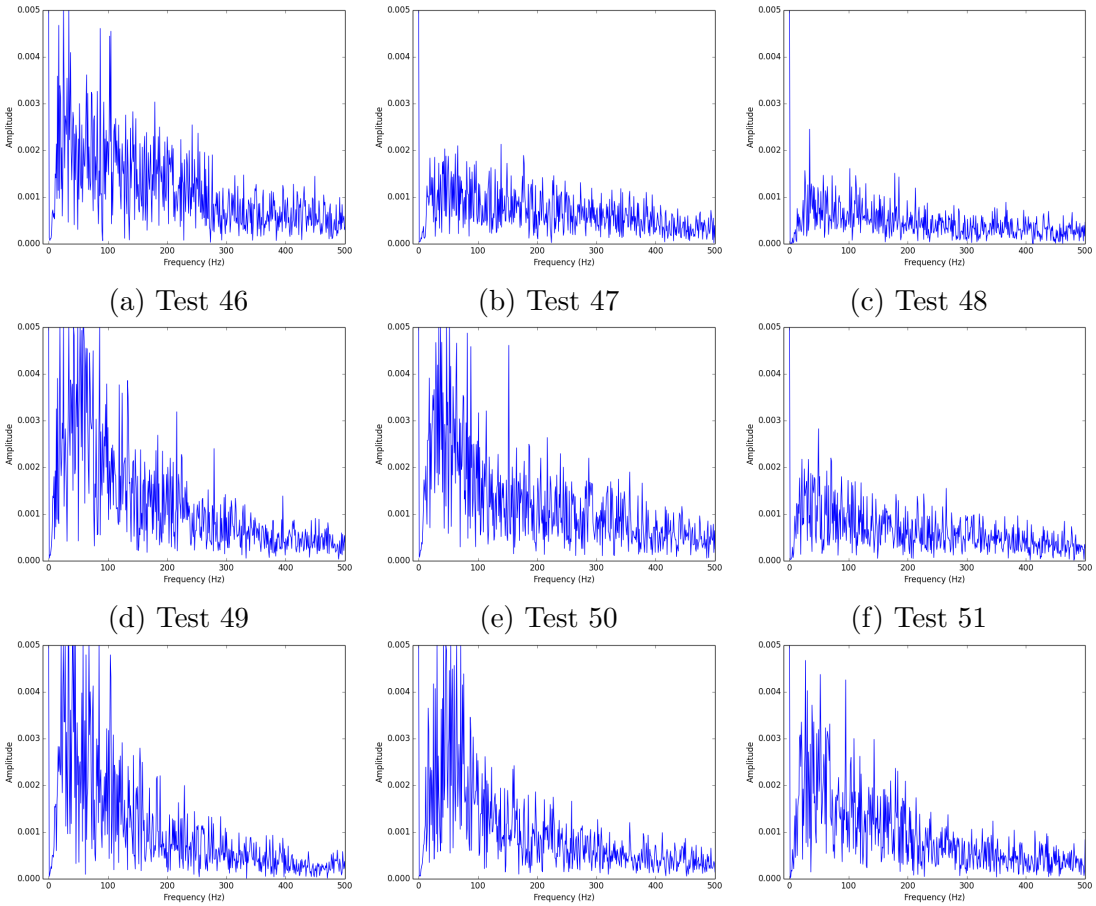

(a) Test 46 (b) Test 47 (c) Test 48

(d) Test 49 (e) Test 50 (f) Test 51

(g) Test 52 (h) Test 53 (i) Test 54

Figure B.26: FFT of IR photodiode signal for Tests 46 to 54 - 90 % Coal & 10 % Straw - 60° Swirl

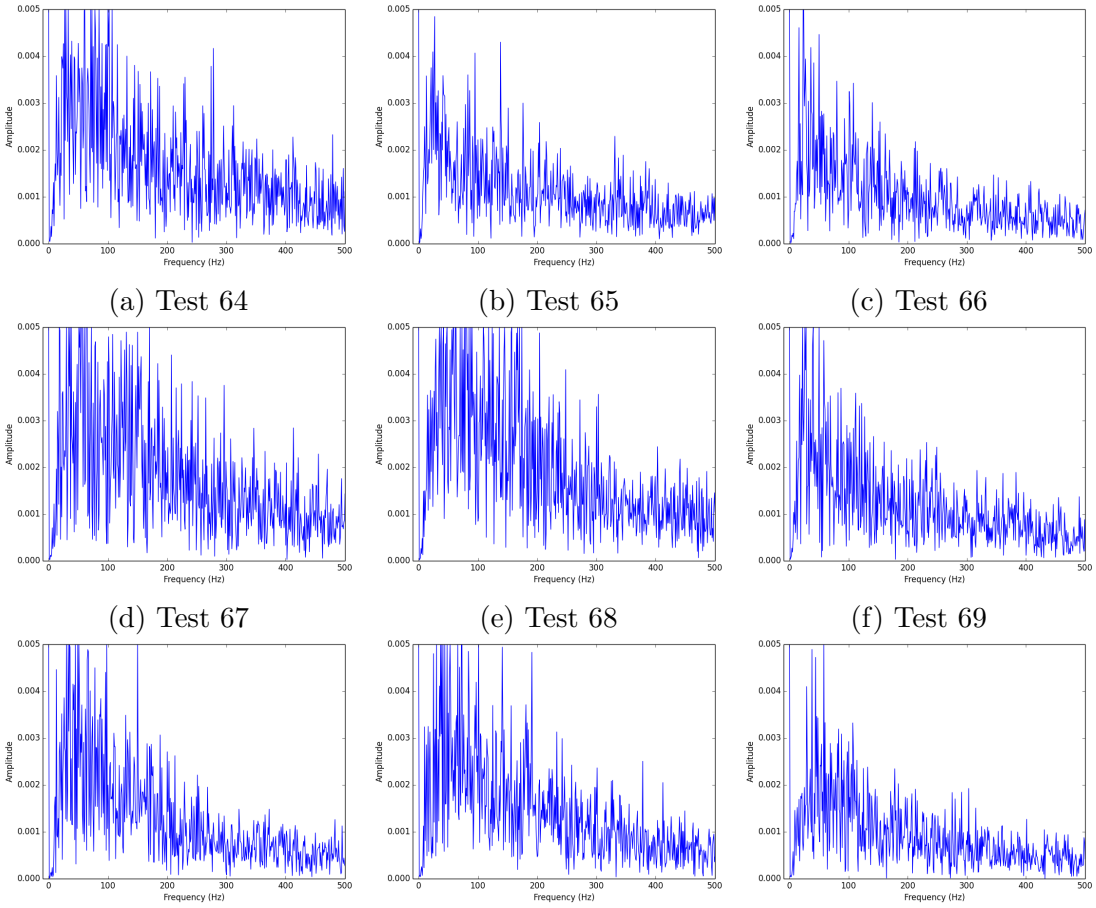

(a) Test 64 (b) Test 65 (c) Test 66

(d) Test 67 (e) Test 68 (f) Test 69

(g) Test 70 (h) Test 71 (i) Test 72

Figure B.27: FFT of UV photodiode signal for Tests 64 to 72 - 80 % Coal & 20 % Straw - 60° Swirl

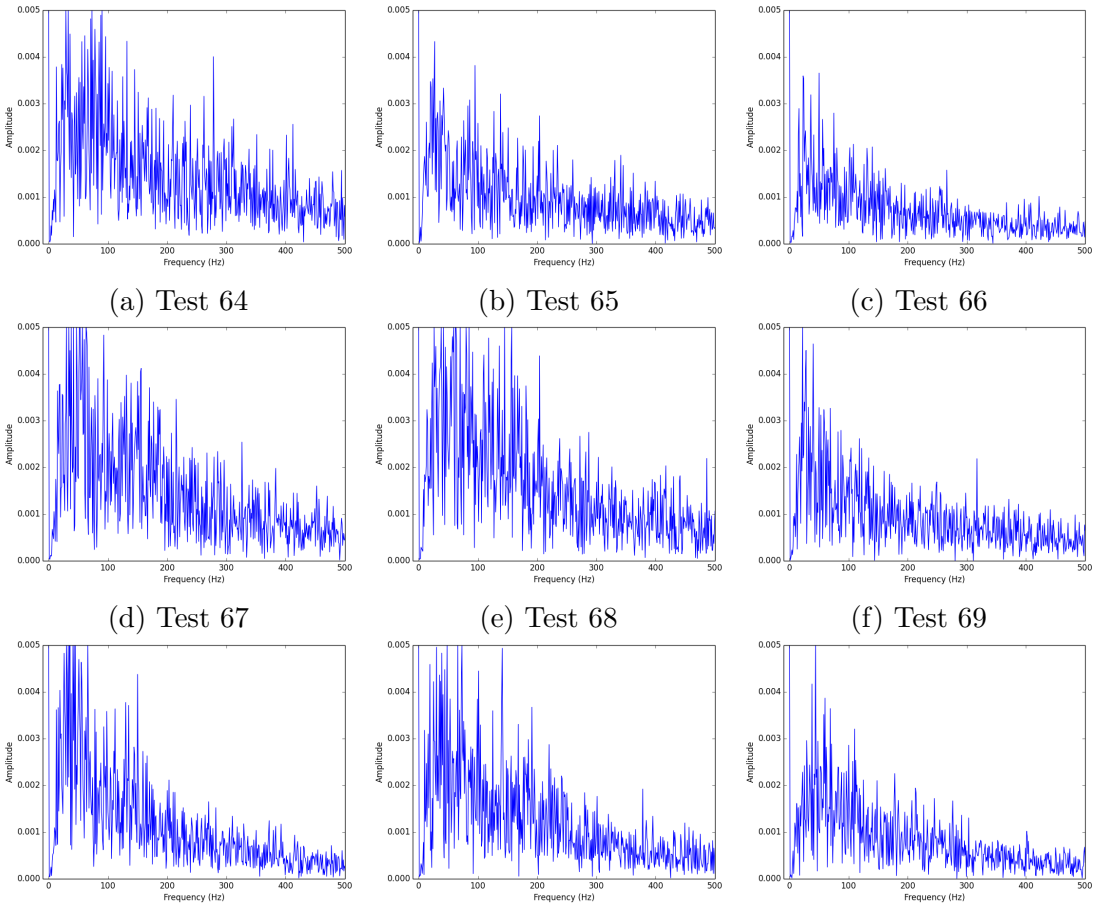

(a) Test 64 (b) Test 65 (c) Test 66

(d) Test 67 (e) Test 68 (f) Test 69

(g) Test 70 (h) Test 71 (i) Test 72

Figure B.28: FFT of VIS photodiode signal for Tests 64 to 72 - 80 % Coal & 20 % Straw - 60° Swirl

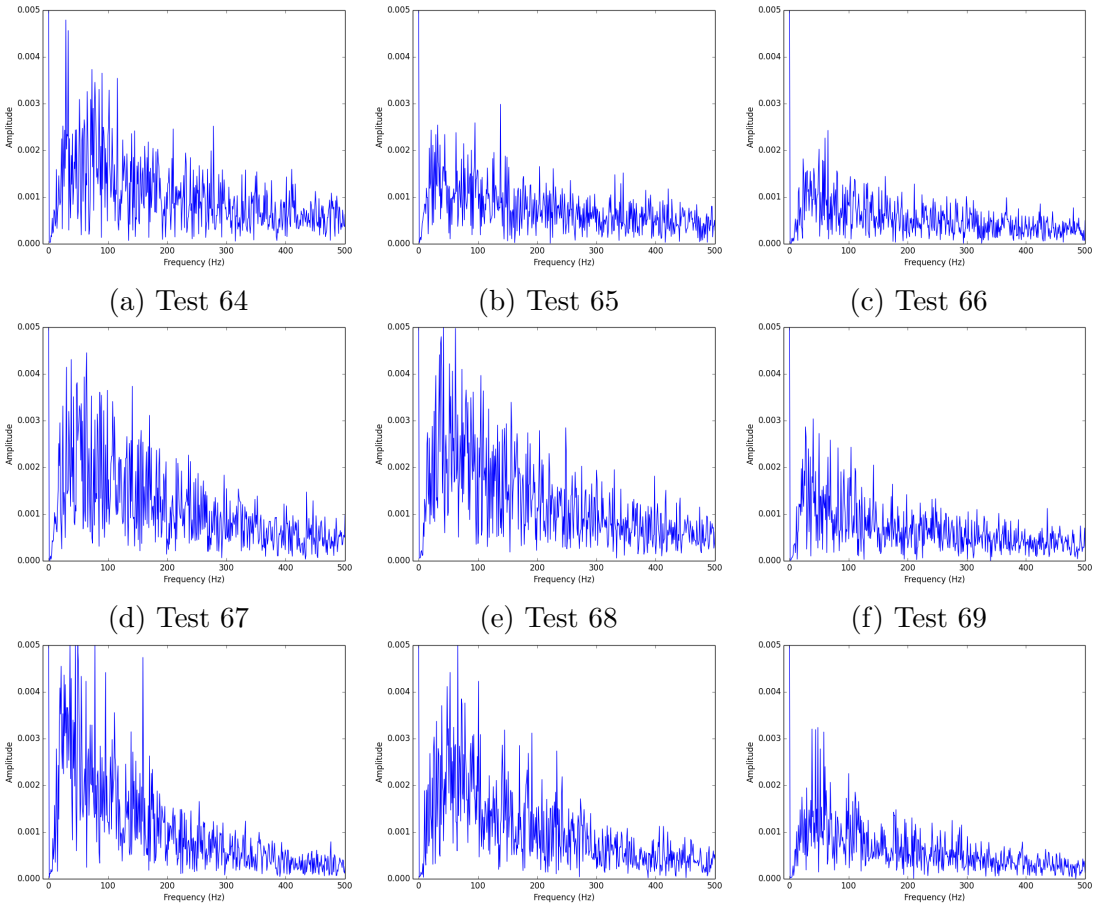

(a) Test 64 (b) Test 65 (c) Test 66

(d) Test 67 (e) Test 68 (f) Test 69

(g) Test 70 (h) Test 71 (i) Test 72

Figure B.29: FFT of IR photodiode signal for Tests 64 to 72 - 80 % Coal & 20 % Straw - 60° Swirl

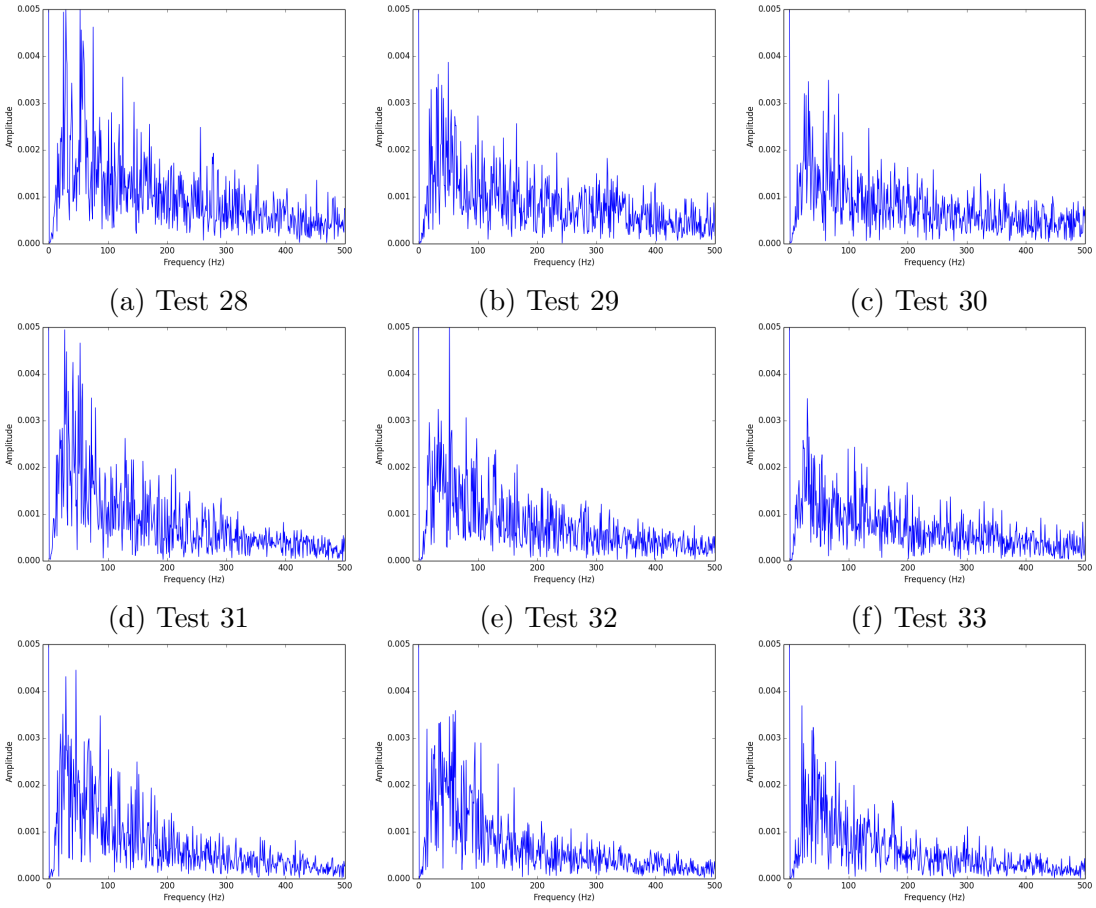

(a) Test 28 (b) Test 29 (c) Test 30

(d) Test 31 (e) Test 32 (f) Test 33

(g) Test 34 (h) Test 34 (i) Test 36

Figure B.30: FFT of UV photodiode signal for Tests 28 to 36 - 100 % Coal - 40° Swirl

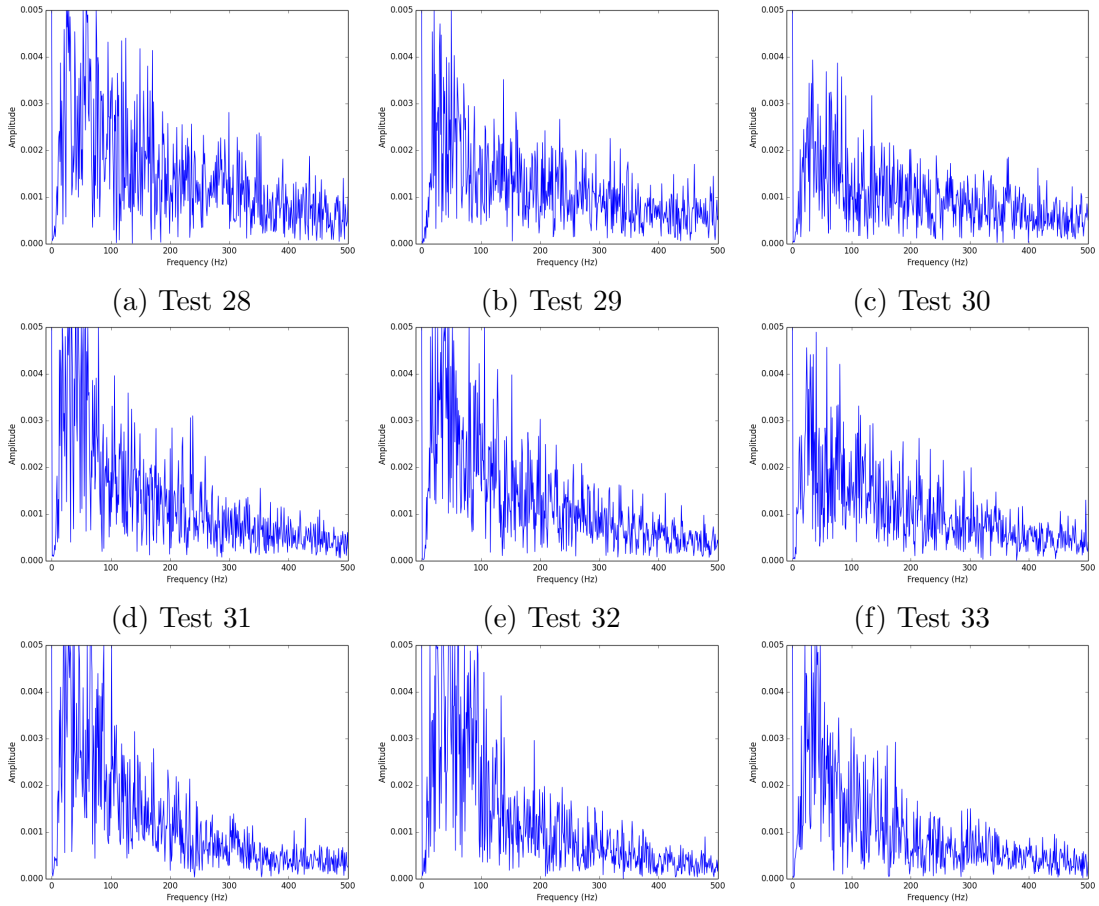

(a) Test 28 (b) Test 29 (c) Test 30

(d) Test 31 (e) Test 32 (f) Test 33

(g) Test 34 (h) Test 34 (i) Test 36

Figure B.31: FFT of VIS photodiode signal for Tests 28 to 36 - 100 % Coal - 40° Swirl

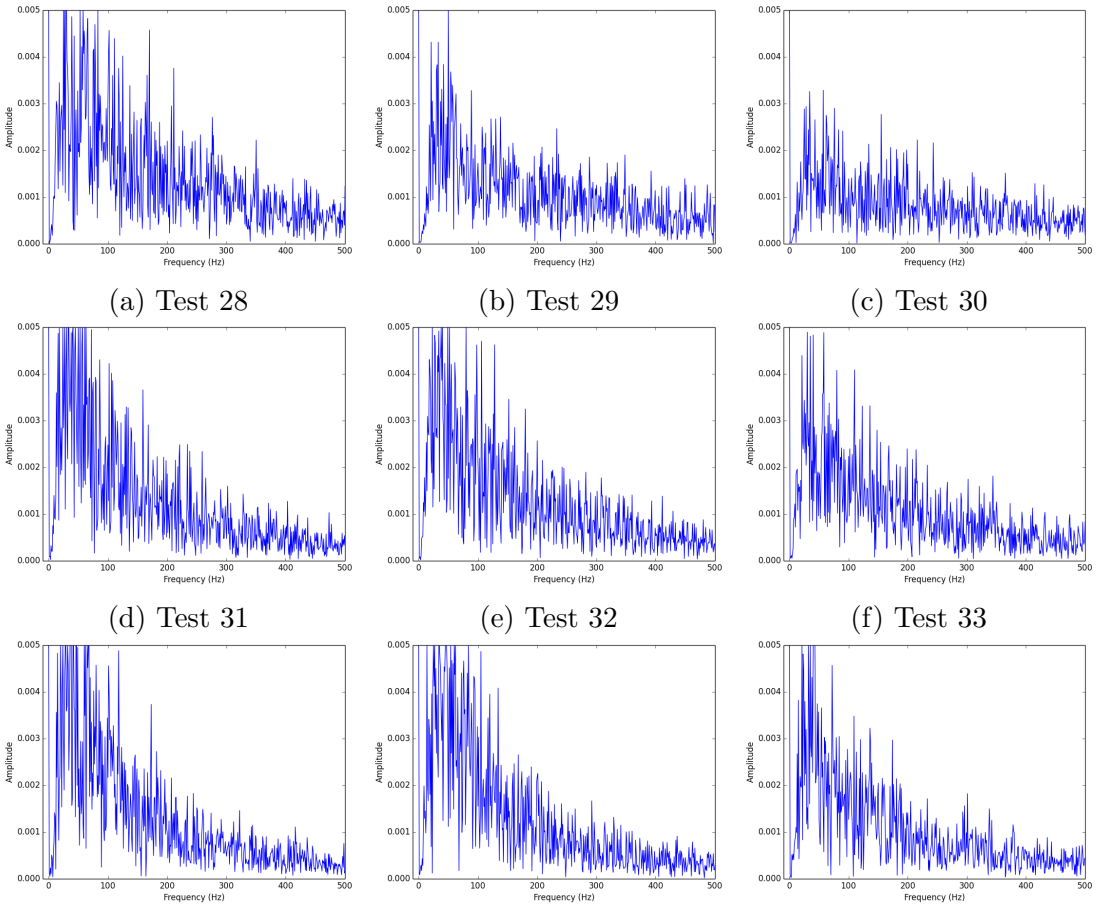

(a) Test 28 (b) Test 29 (c) Test 30

(d) Test 31 (e) Test 32 (f) Test 33

(g) Test 34 (h) Test 34 (i) Test 36

Figure B.32: FFT of IR photodiode signal for Tests 28 to 36 - 100 % Coal - 40° Swirl

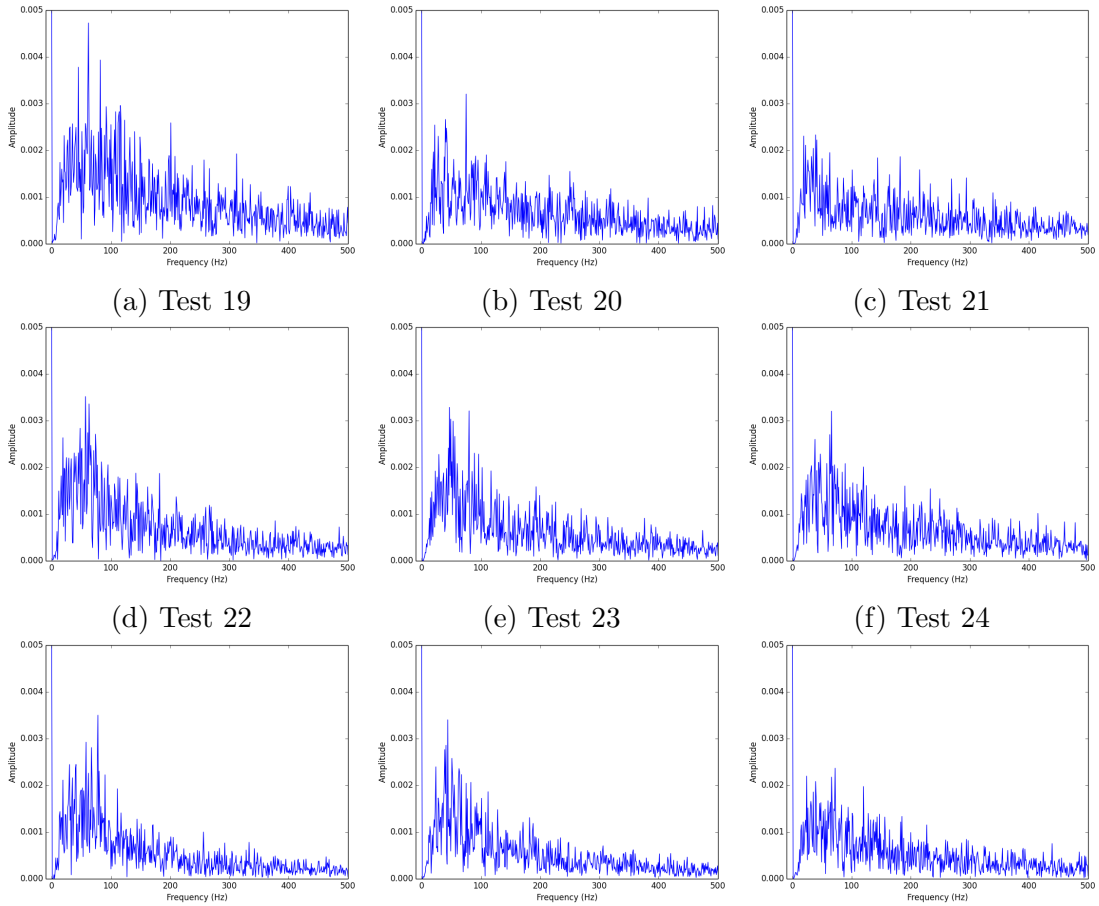

(a) Test 19 (b) Test 20 (c) Test 21

(d) Test 22 (e) Test 23 (f) Test 24

(g) Test 25 (h) Test 26 (i) Test 27

Figure B.33: FFT of UV photodiode signal for Tests 19 to 27 - 90 % Coal & 10 % Straw - 40° Swirl

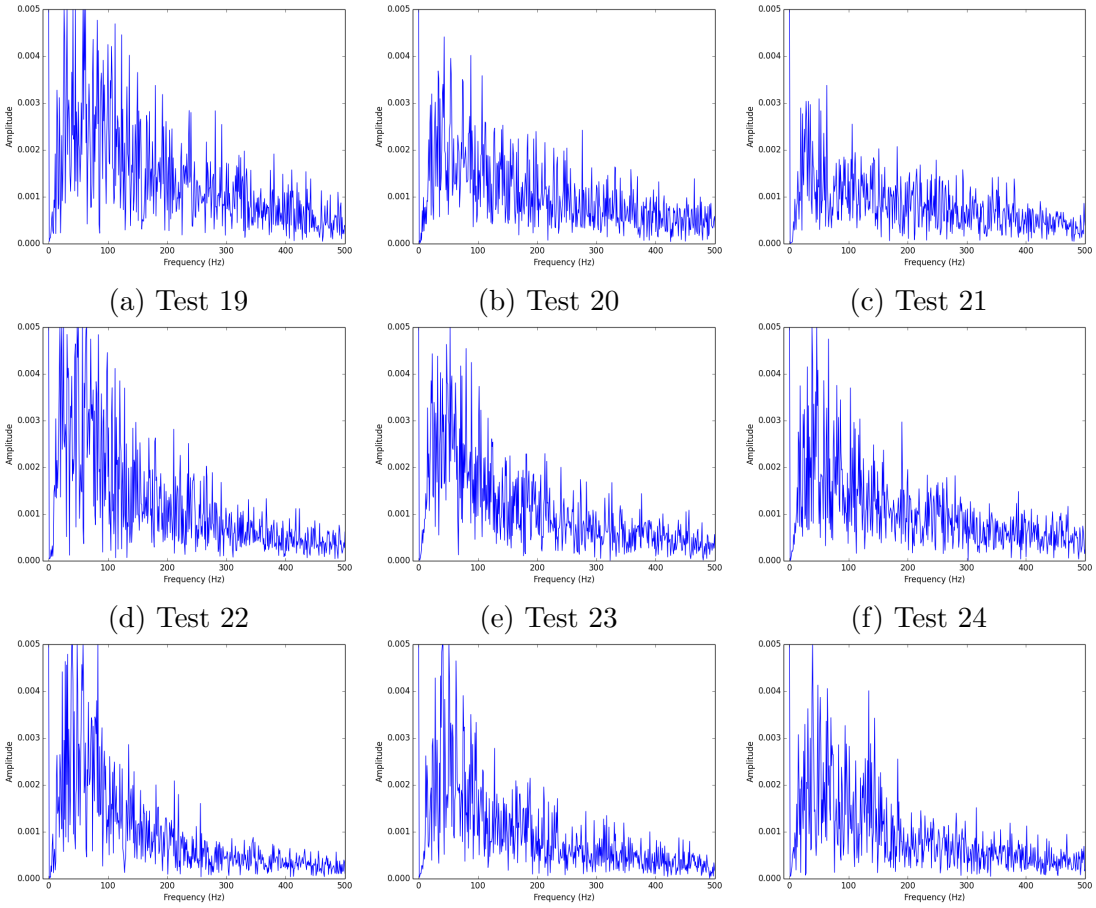

(a) Test 19 (b) Test 20 (c) Test 21

(d) Test 22 (e) Test 23 (f) Test 24

(g) Test 25 (h) Test 26 (i) Test 27

Figure B.34: FFT of VIS photodiode signal for Tests 19 to 27 - 90 % Coal & 10 % Straw - 40° Swirl

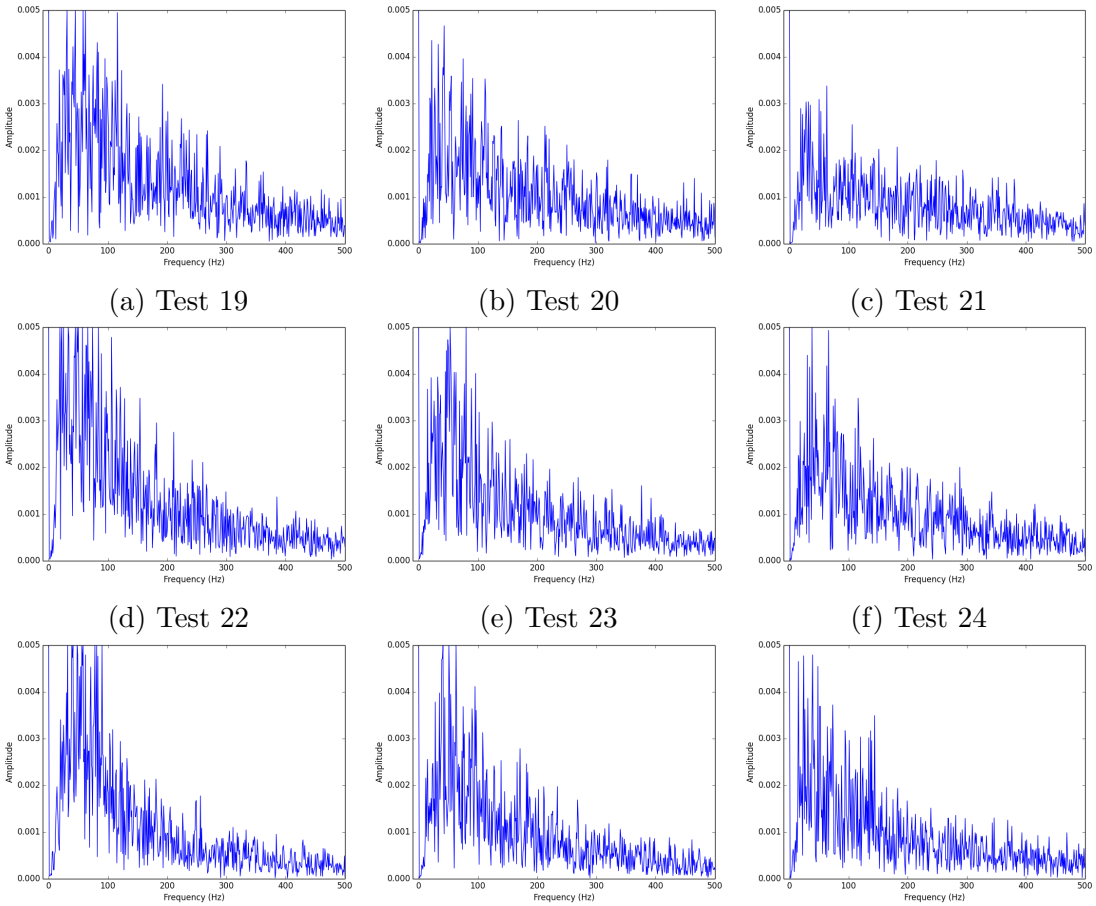

(a) Test 19 (b) Test 20 (c) Test 21

(d) Test 22 (e) Test 23 (f) Test 24

(g) Test 25 (h) Test 26 (i) Test 27

Figure B.35: FFT of IR photodiode signal for Tests 19 to 27 - 90 % Coal & 10 % Straw - 40° Swirl

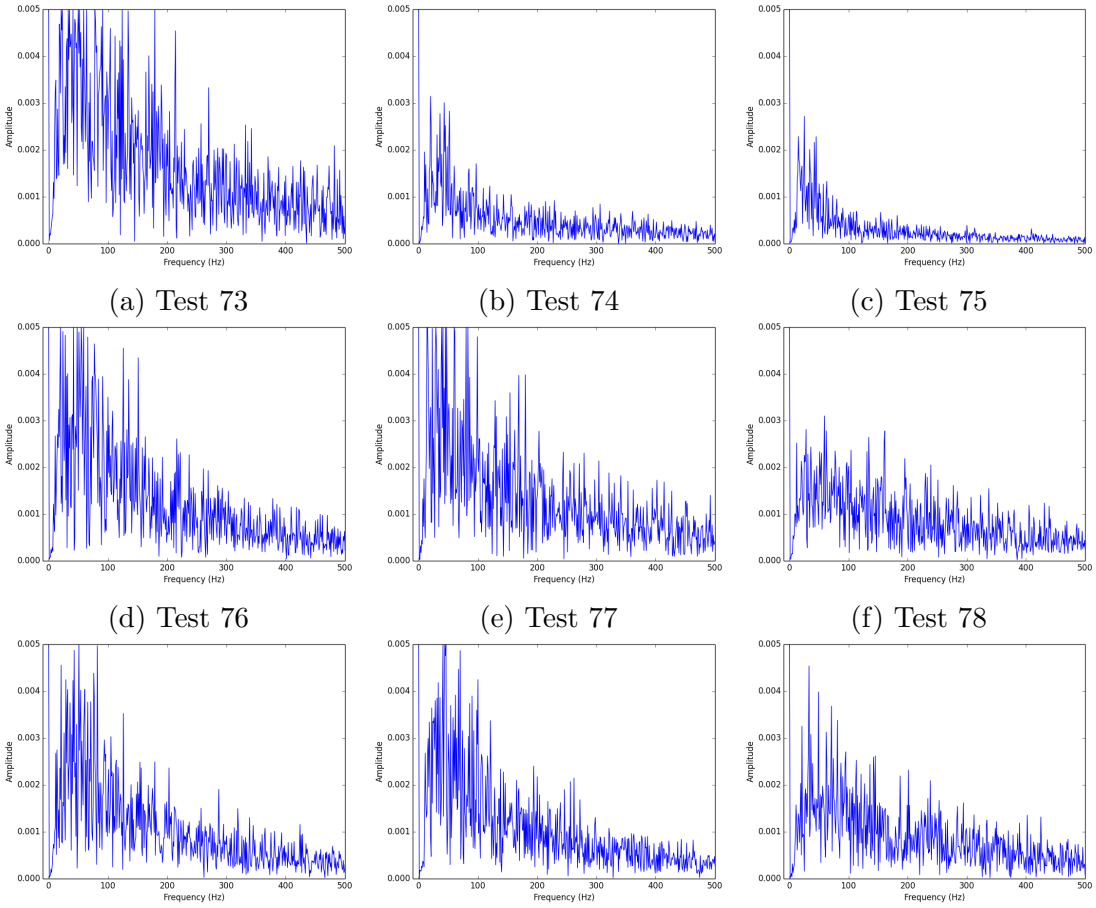

(a) Test 73 (b) Test 74 (c) Test 75

(d) Test 76 (e) Test 77 (f) Test 78

(g) Test 79 (h) Test 80 (i) Test 81

Figure B.36: FFT of UV photodiode signal for Tests 73 to 81 - 80 % Coal & 20 % Straw - 40° Swirl

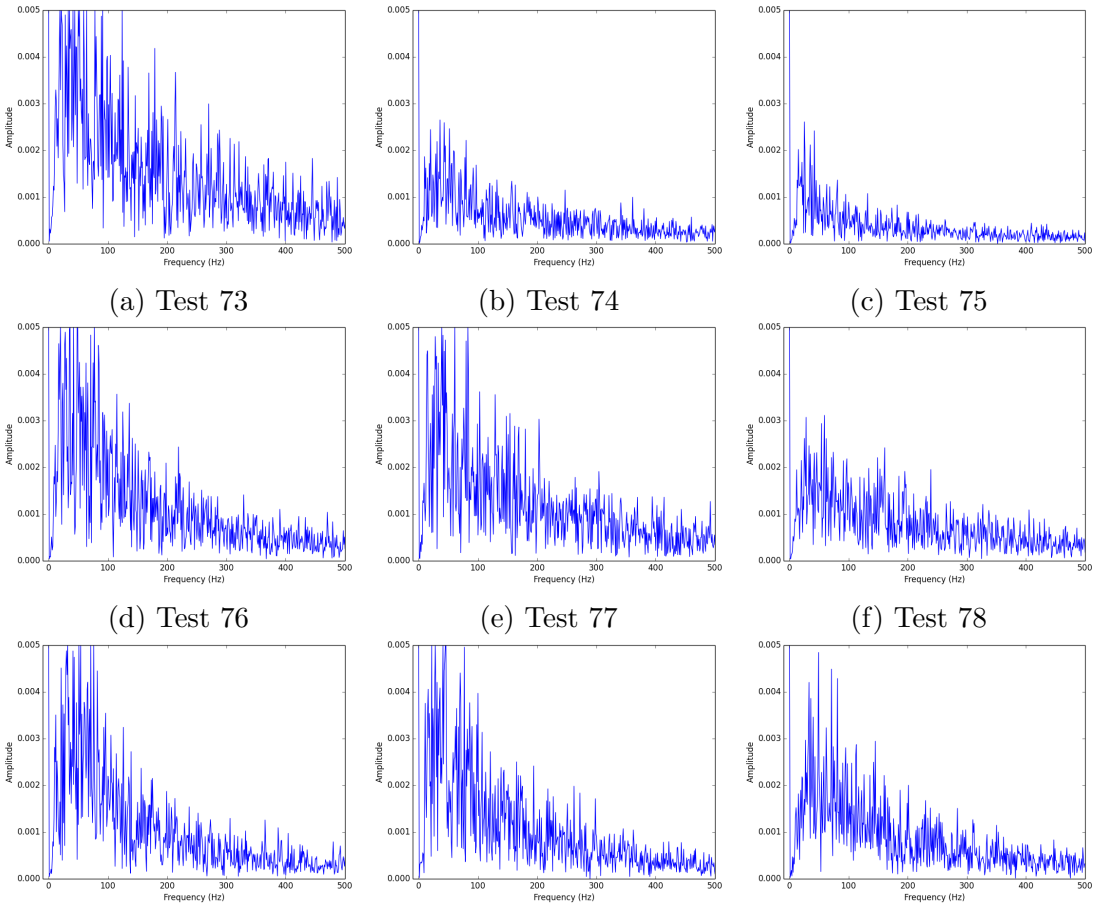

(a) Test 73 (b) Test 74 (c) Test 75

(d) Test 76 (e) Test 77 (f) Test 78

(g) Test 79 (h) Test 80 (i) Test 81

Figure B.37: FFT of VIS photodiode signal for Tests 73 to 81 - 80 % Coal & 20 % Straw - 40° Swirl

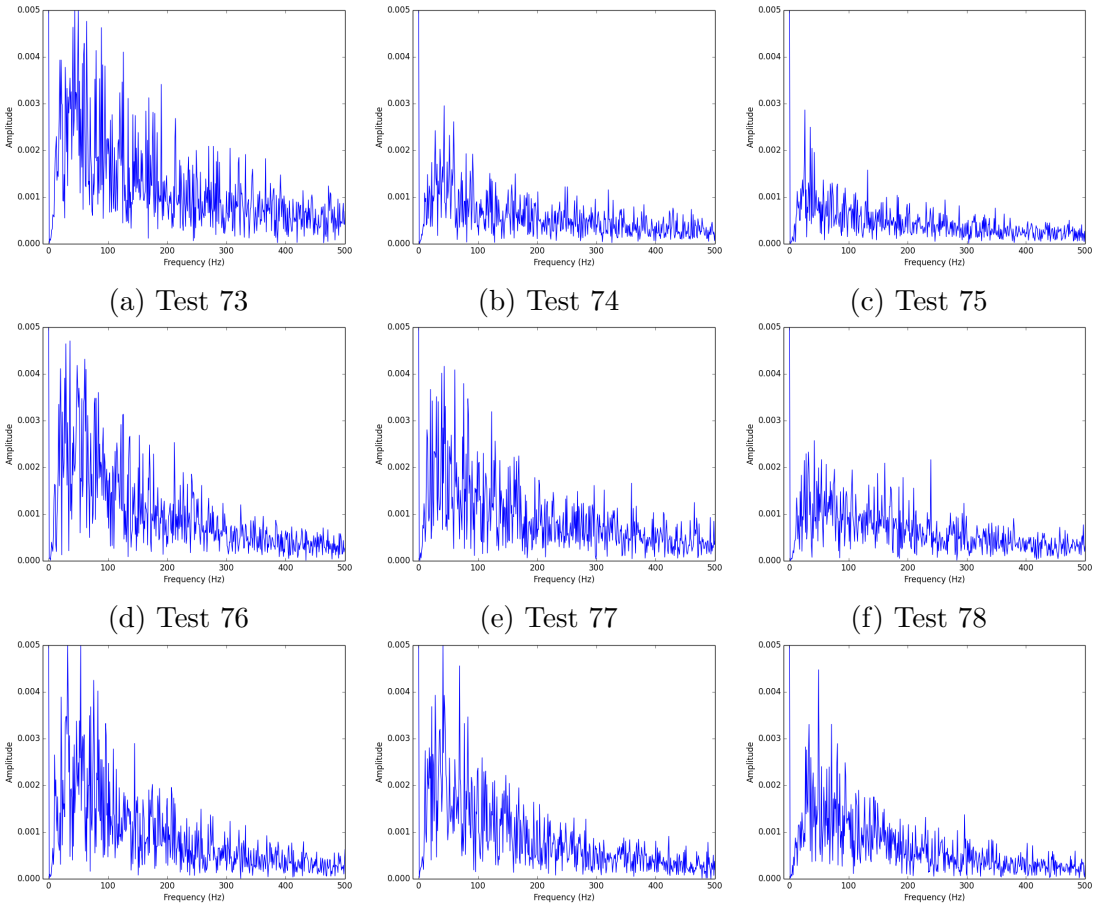

(a) Test 73 (b) Test 74 (c) Test 75

(d) Test 76 (e) Test 77 (f) Test 78

(g) Test 79 (h) Test 80 (i) Test 81

Figure B.38: FFT of IR photodiode signal for Tests 73 to 81 - 80 % Coal & 20 % Straw - 40° Swirl

B.3 PSD results

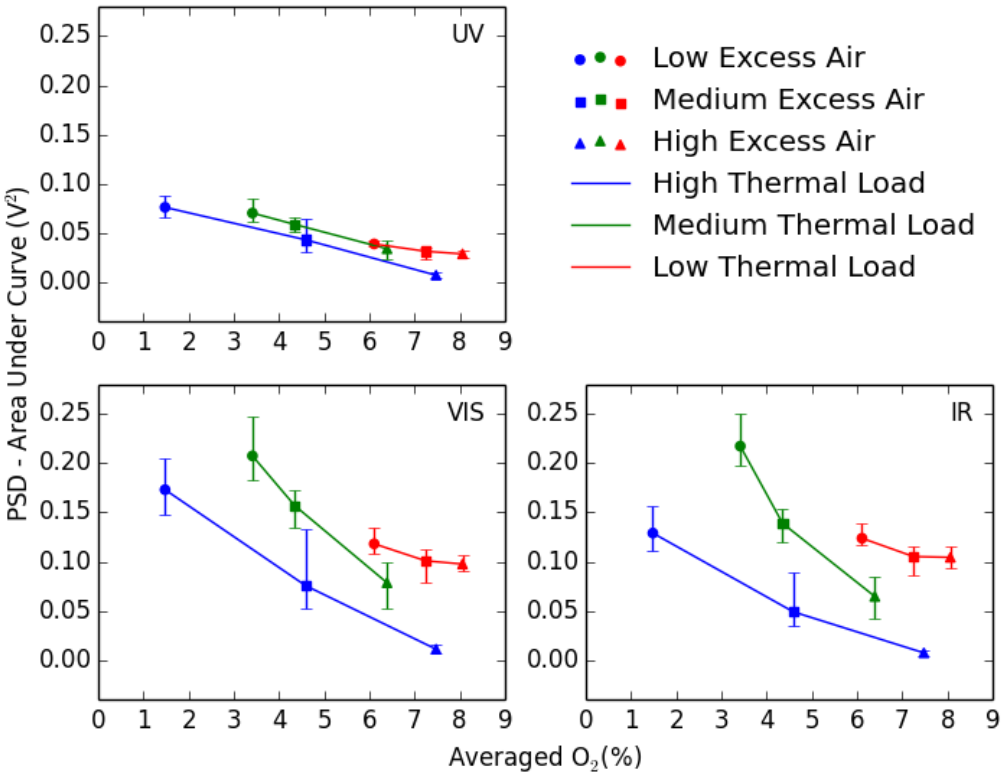

Figure B.39: PSD of UV, VIS & IR photodiode signals Vs averaged O_2 for Tests 10 to 18 - 90 % Coal & 10 % Straw - 50° Swirl

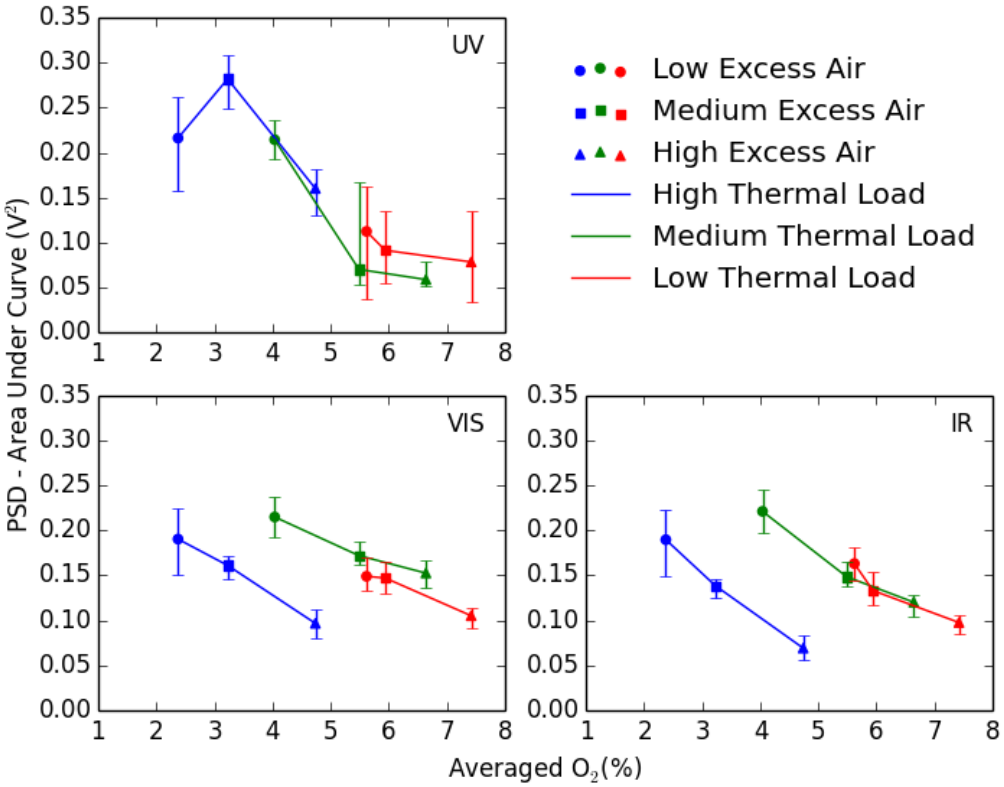

Figure B.40: PSD of UV, VIS & IR photodiode signals Vs averaged O_2 for Tests 82 to 90 - 80 % Coal & 20 % Straw - 50° Swirl

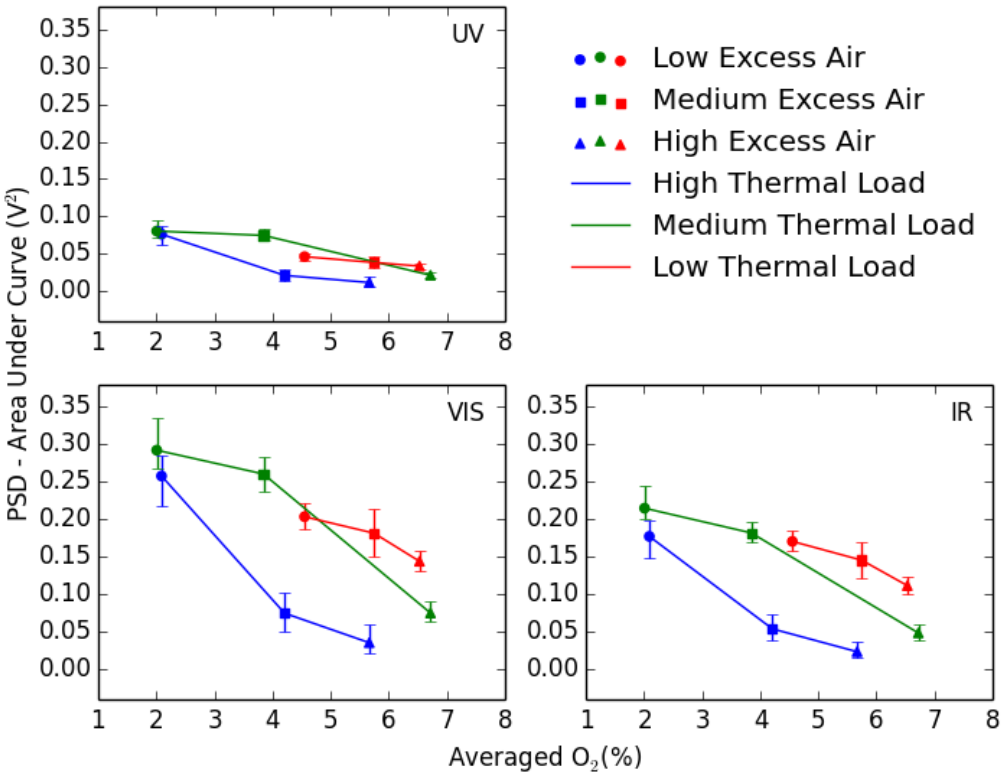

Figure B.41: PSD of UV, VIS & IR photodiode signals Vs averaged O_2 for Tests 55 to 63 - 70 % Coal & 30 % Straw - 60° Swirl

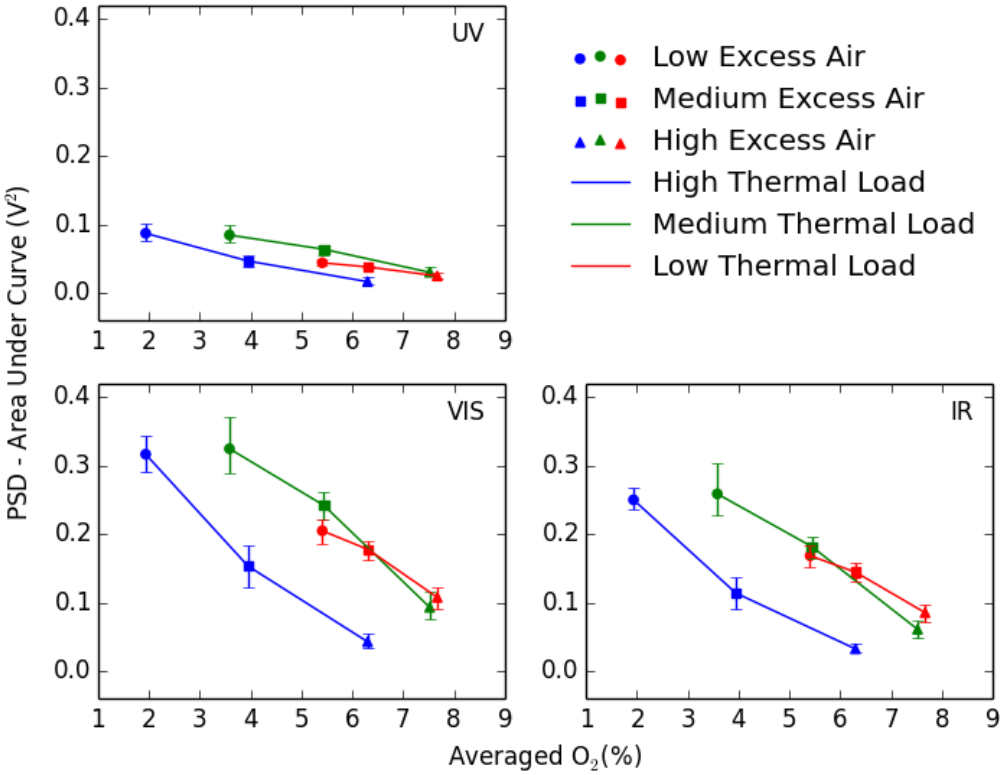

Figure B.42: PSD of UV, VIS & IR photodiode signals Vs averaged O_2 for Tests 37 to 45 - 100 % Coal - 60° Swirl

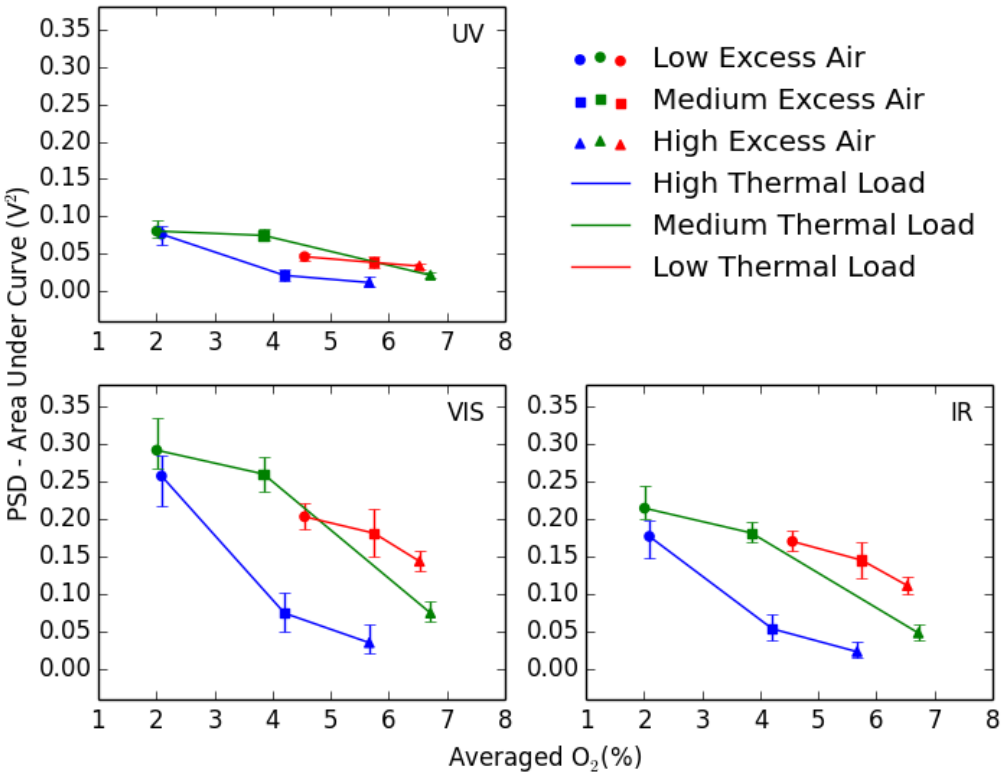

Figure B.43: PSD of UV, VIS & IR photodiode signals Vs averaged O_2 for Tests 46 to 54 - 90 % Coal & 10 % Straw - 60° Swirl

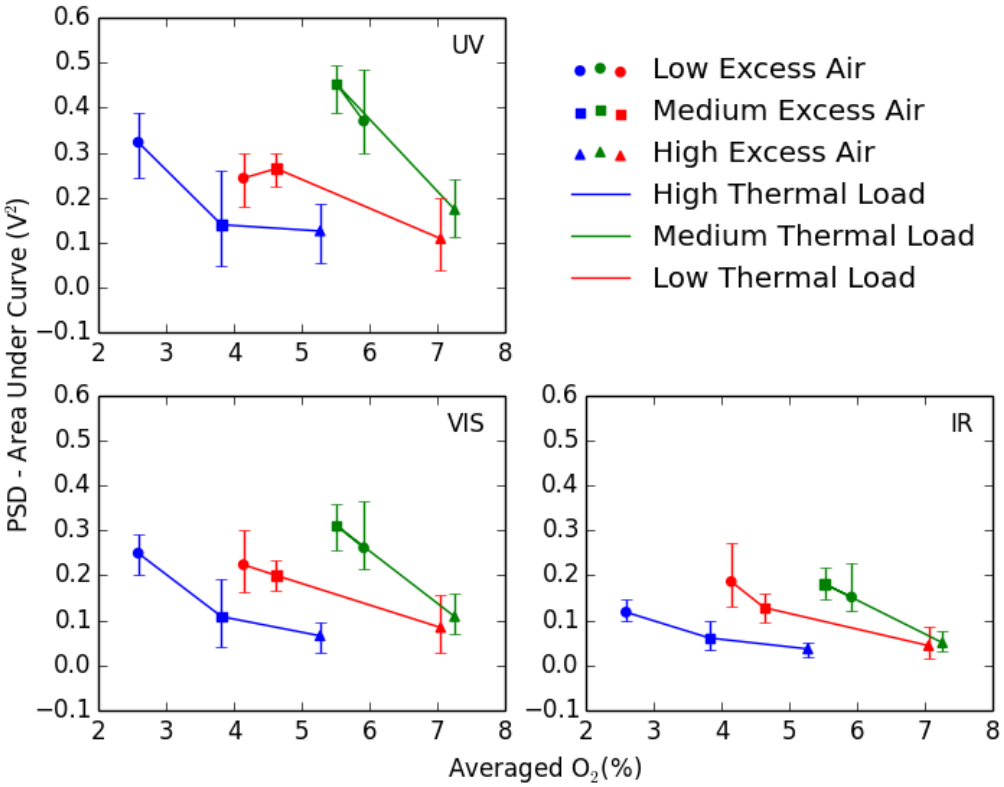

Figure B.44: PSD of UV, VIS & IR photodiode signals Vs averaged O_2 for Tests 64 to 72 - 80 % Coal & 20 % Straw - 60° Swirl

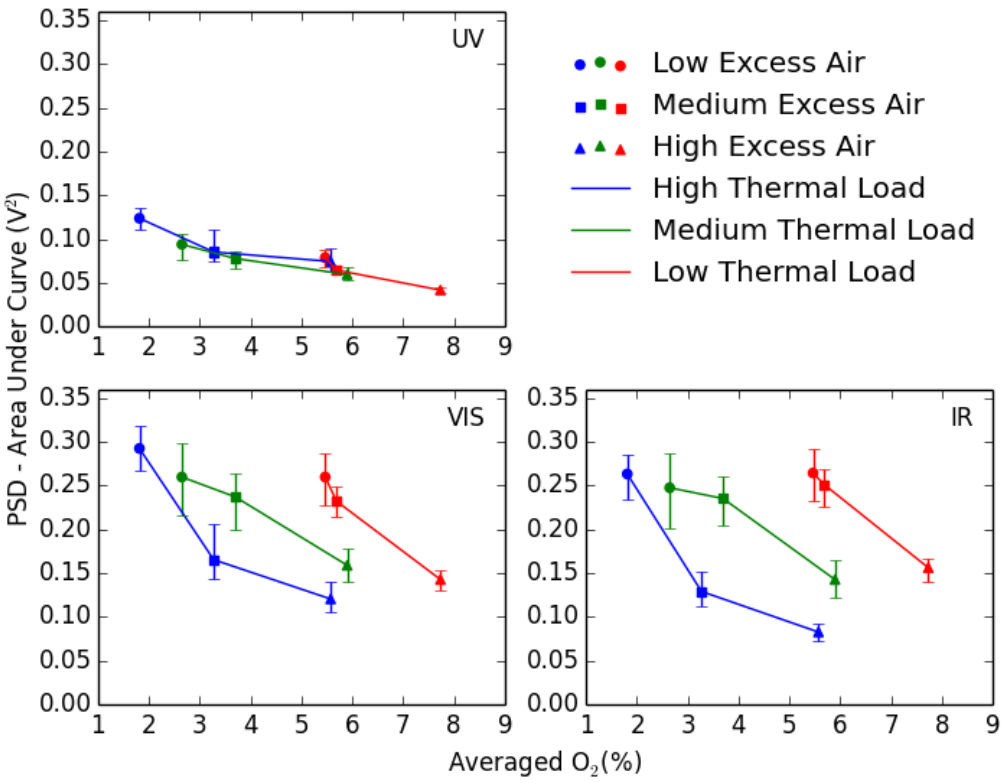

Figure B.45: PSD of UV, VIS & IR photodiode signals Vs averaged O_2 for Tests 28 to 36 - 100 % Coal - 40° Swirl

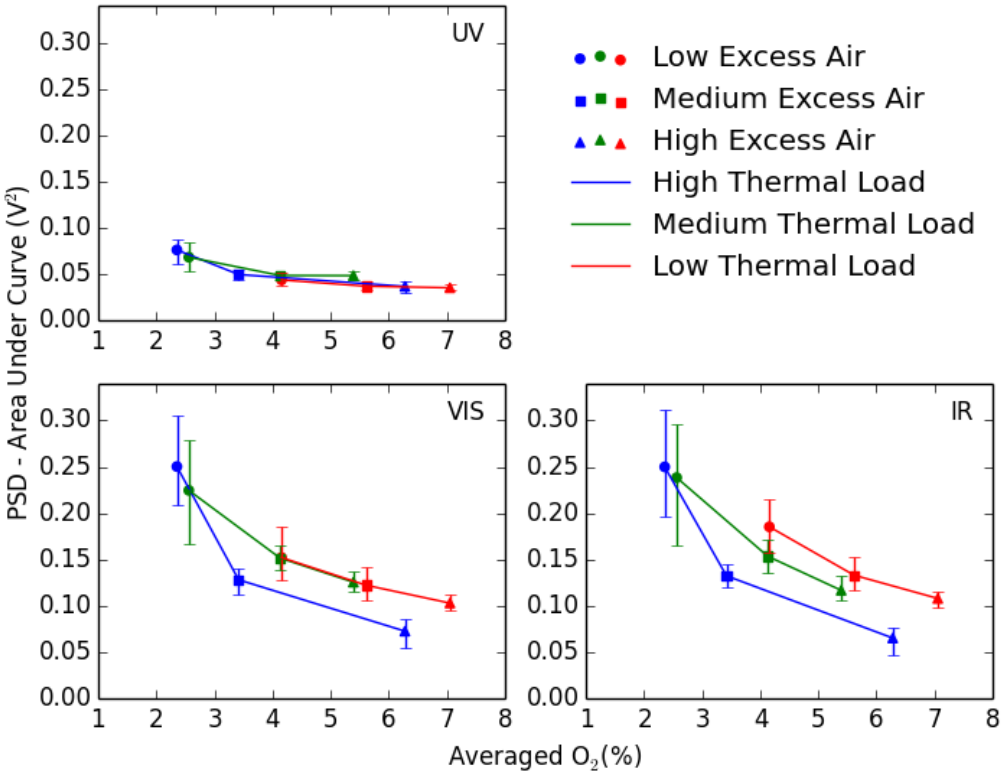

Figure B.46: PSD of UV, VIS & IR photodiode signals Vs averaged O_2 for Tests 19 to 27 - 90 % Coal & 10 % Straw - 40° Swirl

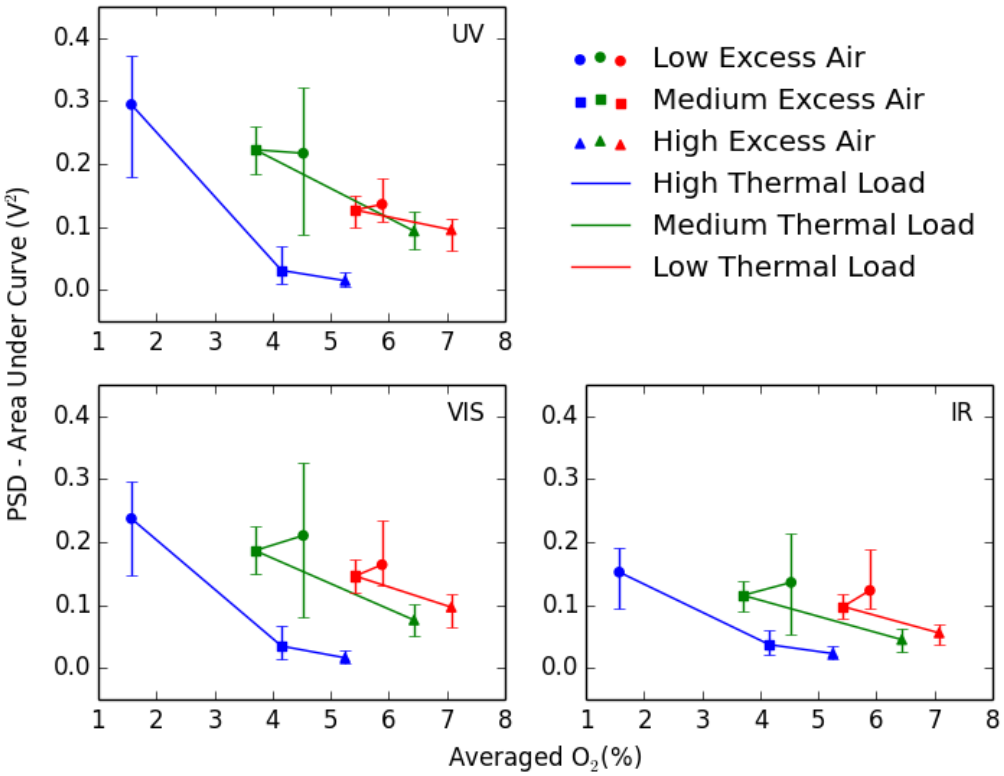

Figure B.47: PSD of UV, VIS & IR photodiode signals Vs averaged O_2 for Tests 73 to 81 - 80 % Coal & 20 % Straw - 40° Swirl

B.4 Wavelet results

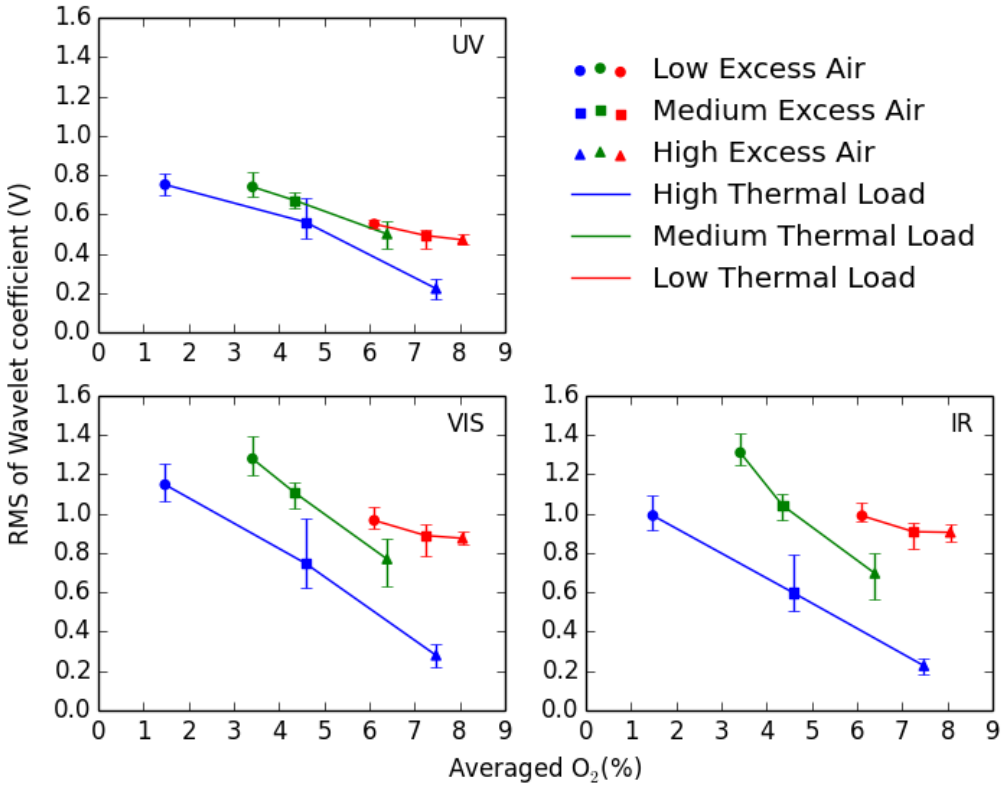

Figure B.48: RMS of largest wavelet coefficient of UV, VIS & IR photodiode signals Vs averaged O_2 for Tests 10 to 18 - 90 % Coal & 10 % Straw - 50° Swirl

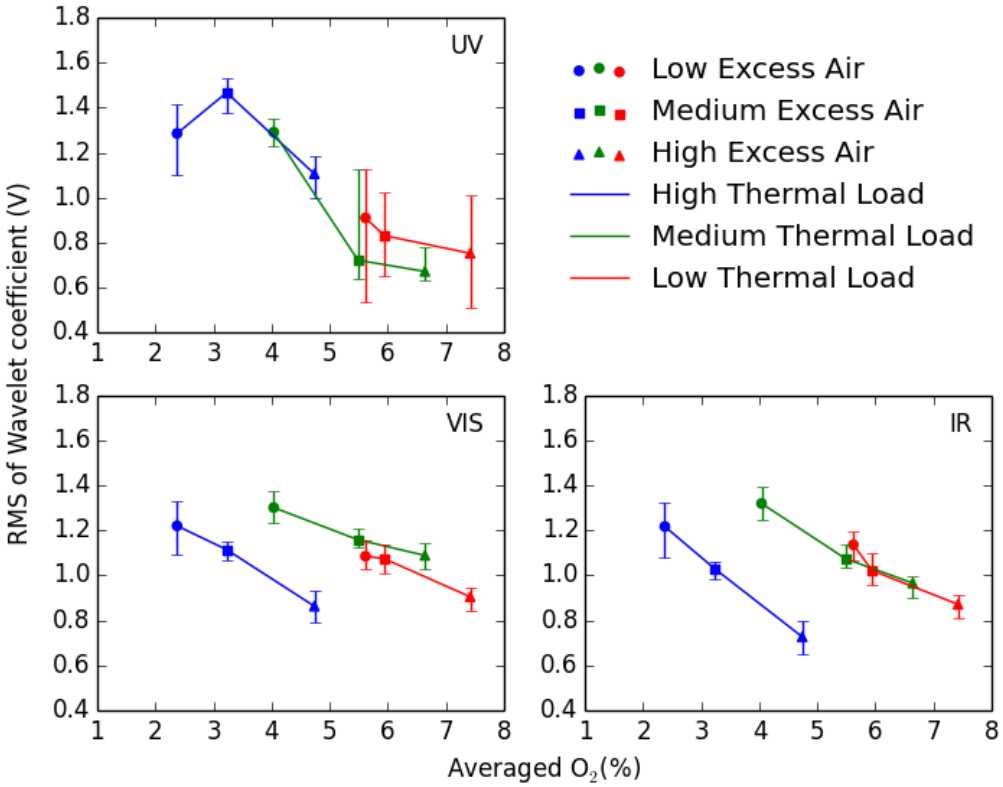

Figure B.49: RMS of largest wavelet coefficient of UV, VIS & IR photodiode signals Vs averaged O_2 for Tests 82 to 90 - 80 % Coal & 20 % Straw - 50° Swirl

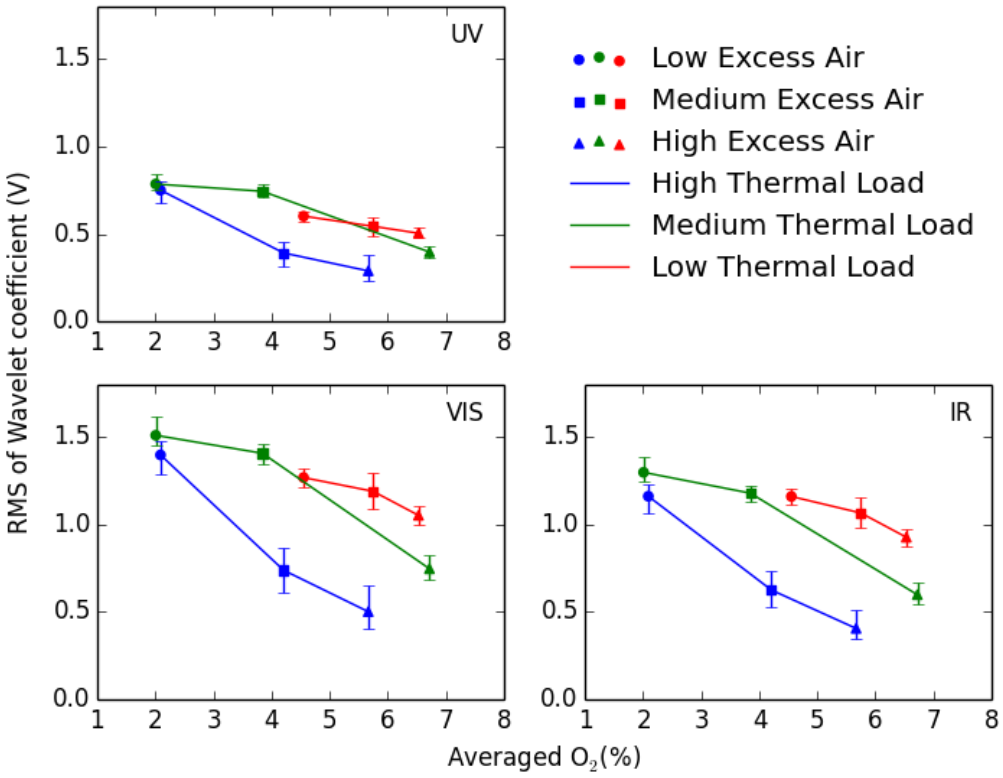

Figure B.50: RMS of largest wavelet coefficient of UV, VIS & IR photodiode signals Vs averaged O_2 for Tests 55 to 63 - 70 % Coal & 30 % Straw - 60° Swirl

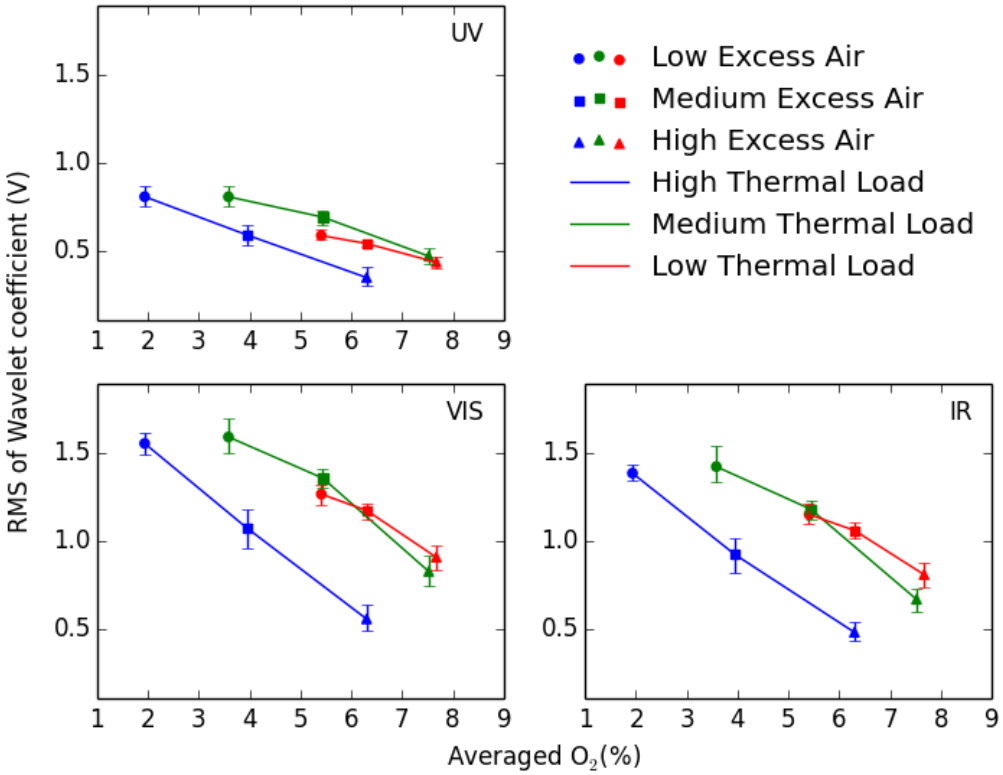

Figure B.51: RMS of largest wavelet coefficient of UV, VIS & IR photodiode signals Vs averaged O_2 for Tests 37 to 45 - 100 % Coal - 60° Swirl

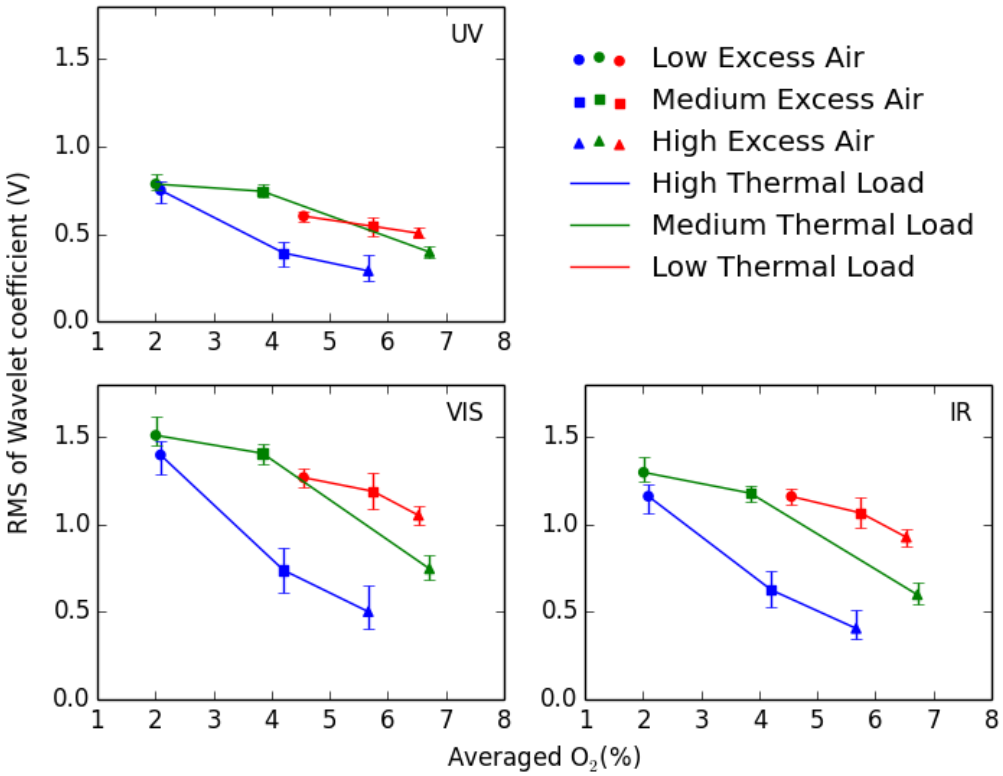

Figure B.52: RMS of largest wavelet coefficient of UV, VIS & IR photodiode signals Vs averaged O_2 for Tests 46 to 54 - 90 % Coal & 10 % Straw - 60° Swirl

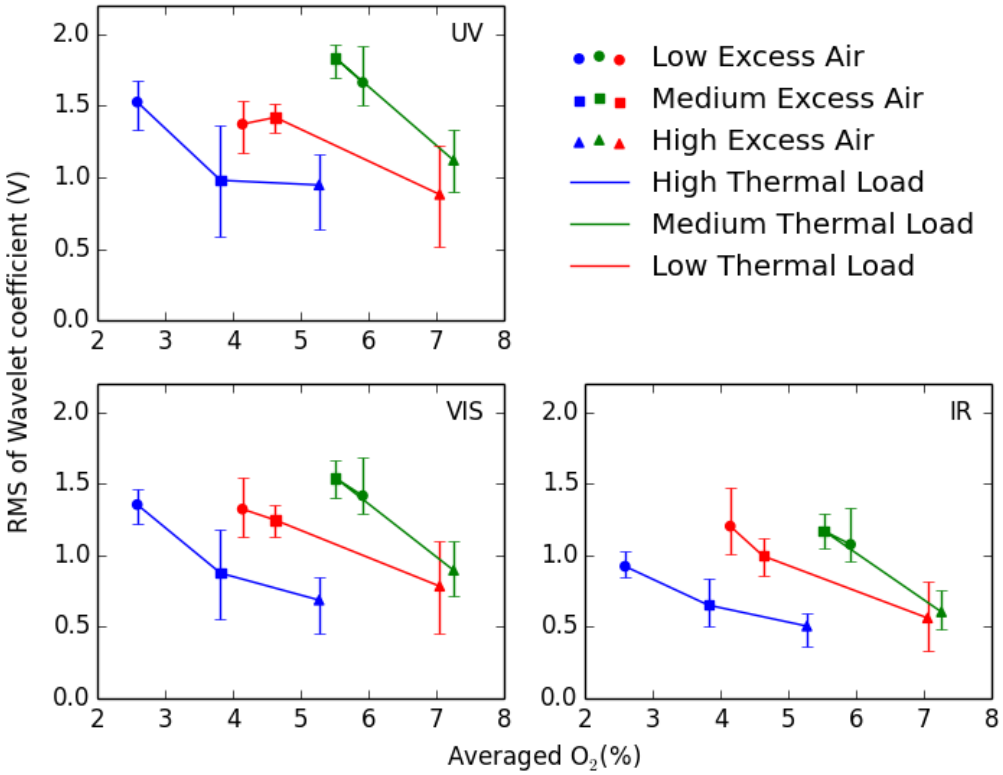

Figure B.53: RMS of largest wavelet coefficient of UV, VIS & IR photodiode signals Vs averaged O_2 for Tests 64 to 72 - 80 % Coal & 20 % Straw - 60° Swirl

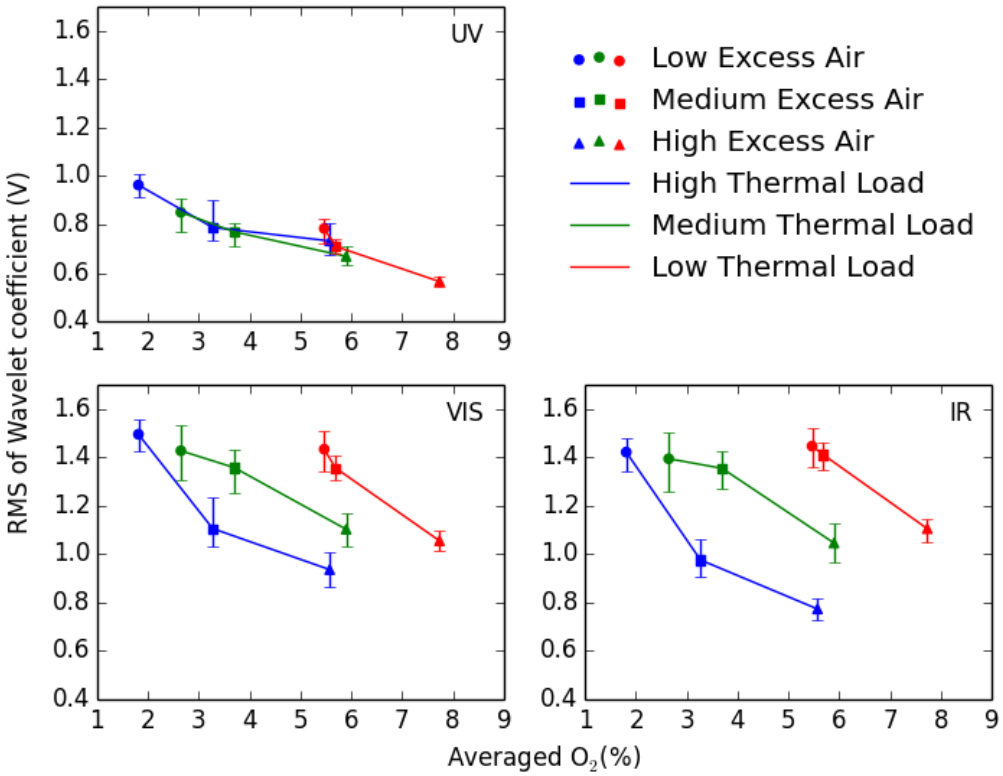

Figure B.54: RMS of largest wavelet coefficient of UV, VIS & IR photodiode signals Vs averaged O_2 for Tests 28 to 36 - 100 % Coal - 40° Swirl

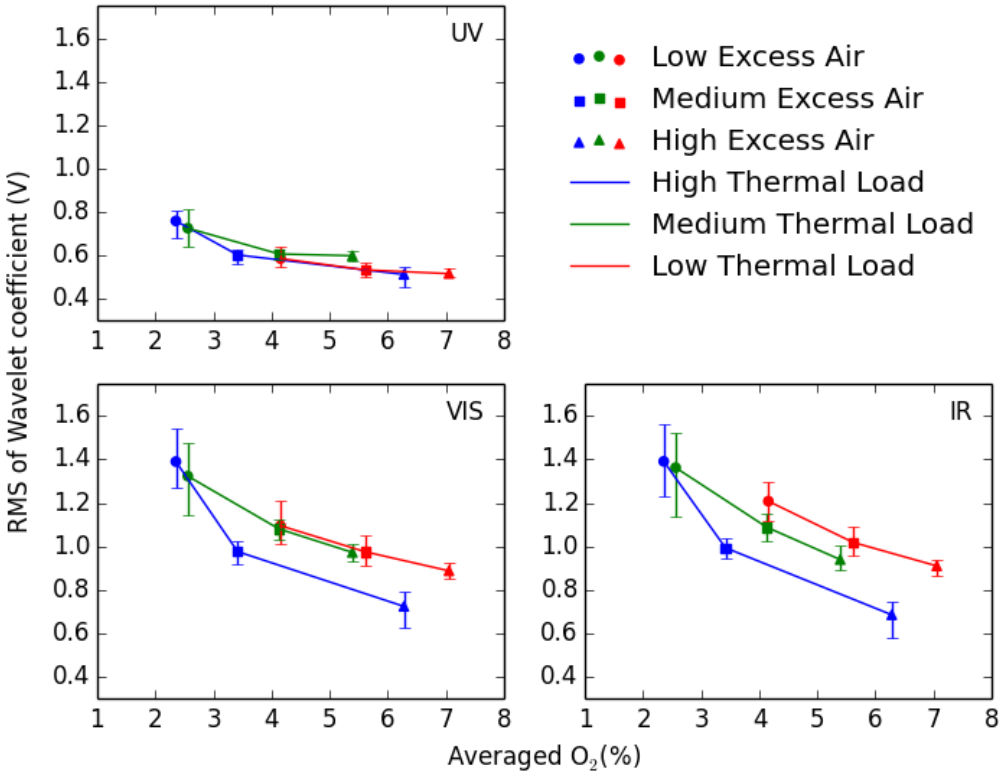

Figure B.55: RMS of largest wavelet coefficient of UV, VIS & IR photodiode signals Vs averaged O_2 for Tests 19 to 27 - 90 % Coal & 10 % Straw - 40° Swirl

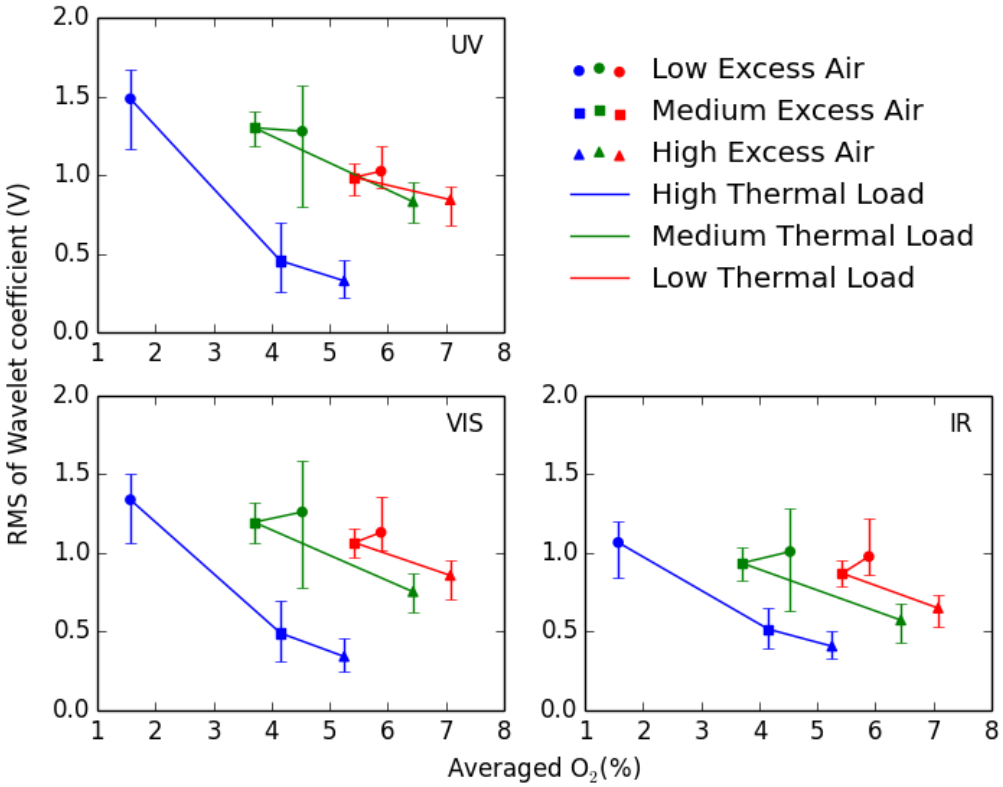

Figure B.56: RMS of largest wavelet coefficient of UV, VIS & IR photodiode signals Vs averaged O_2 for Tests 73 to 81 - 80 % Coal & 20 % Straw - 40° Swirl

B.5 WVD results

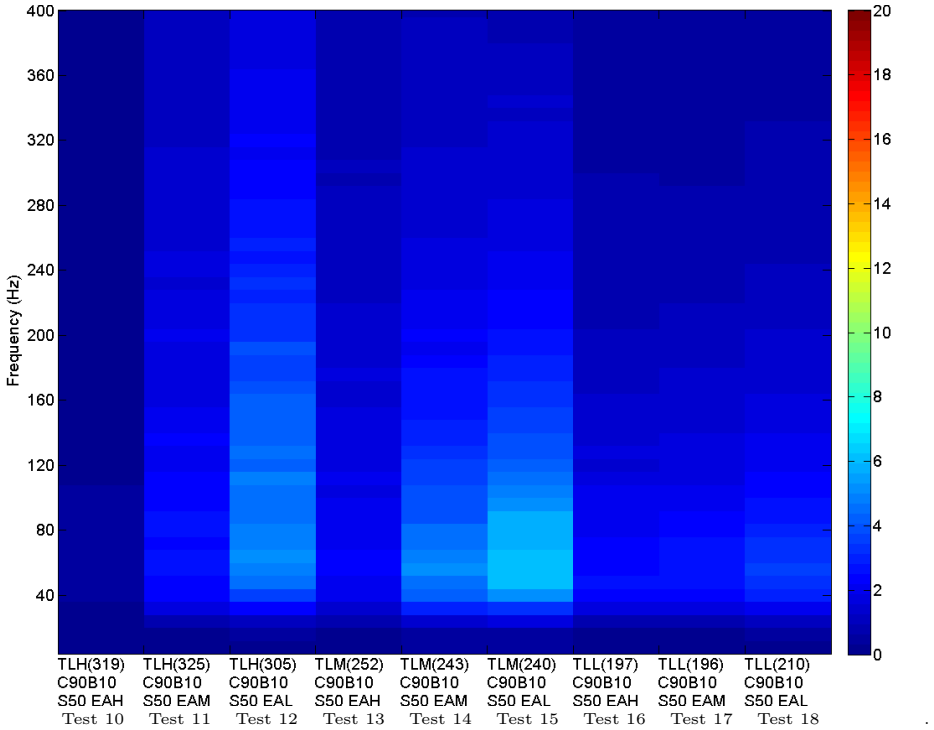

Figure B.57: WVD (averaged) of UV photodiode signal for Tests 10 to 18 - 90 % Coal & 10 % Biomass - 50° Swirl

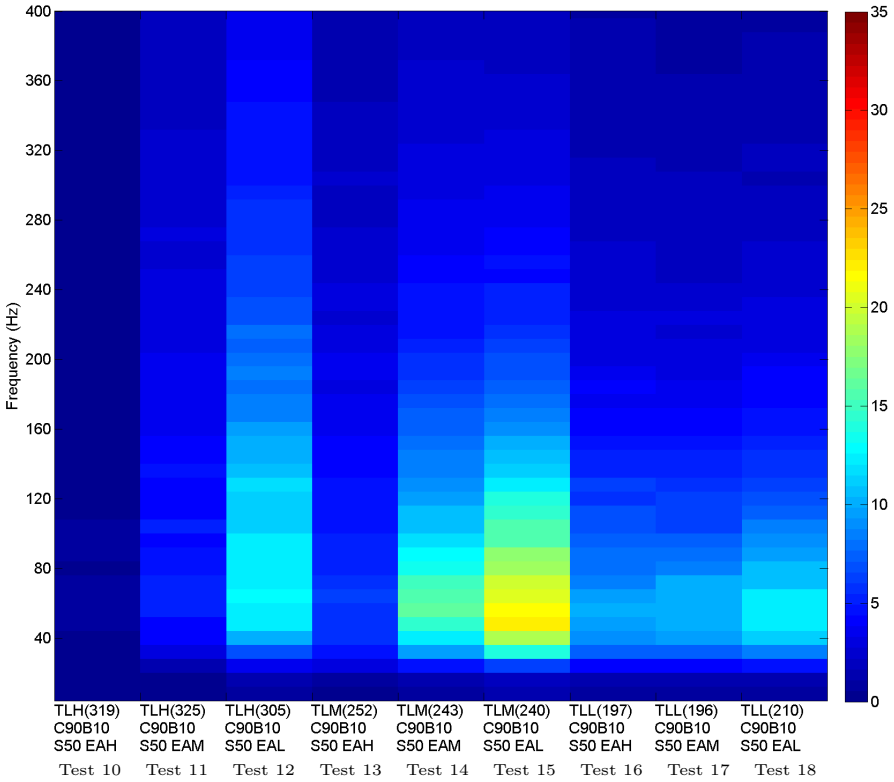

Figure B.58: WVD (averaged) of VIS photodiode signal for Tests 10 to 18 - 90 % Coal & 10 % Biomass - 50° Swirl

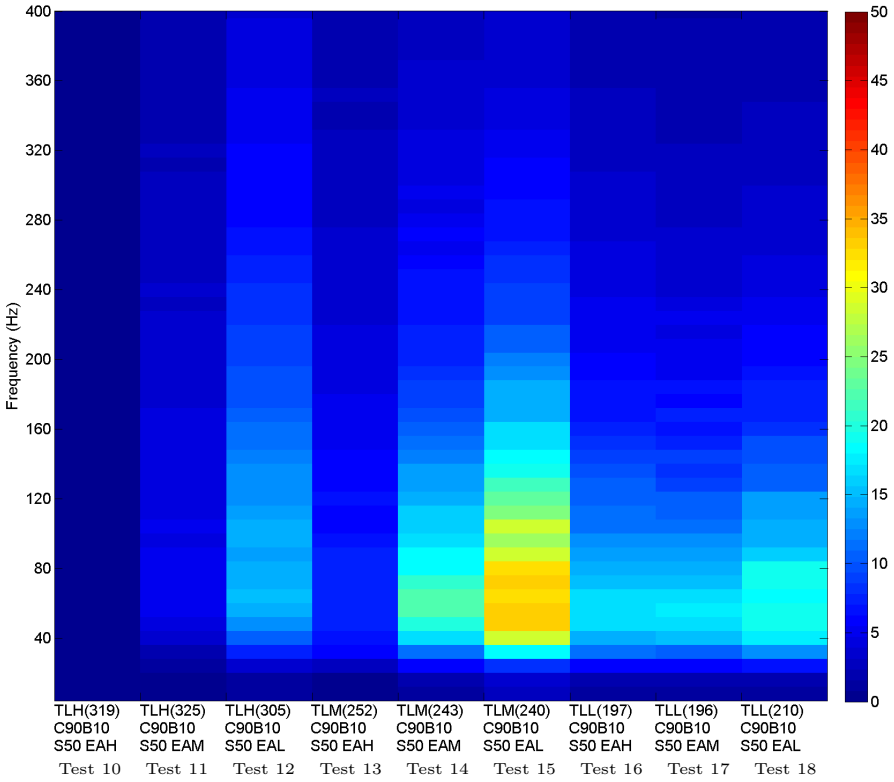

Figure B.59: WVD (averaged) of IR photodiode signal for Tests 10 to 18 - 90 % Coal & 10 % Biomass - 50° Swirl

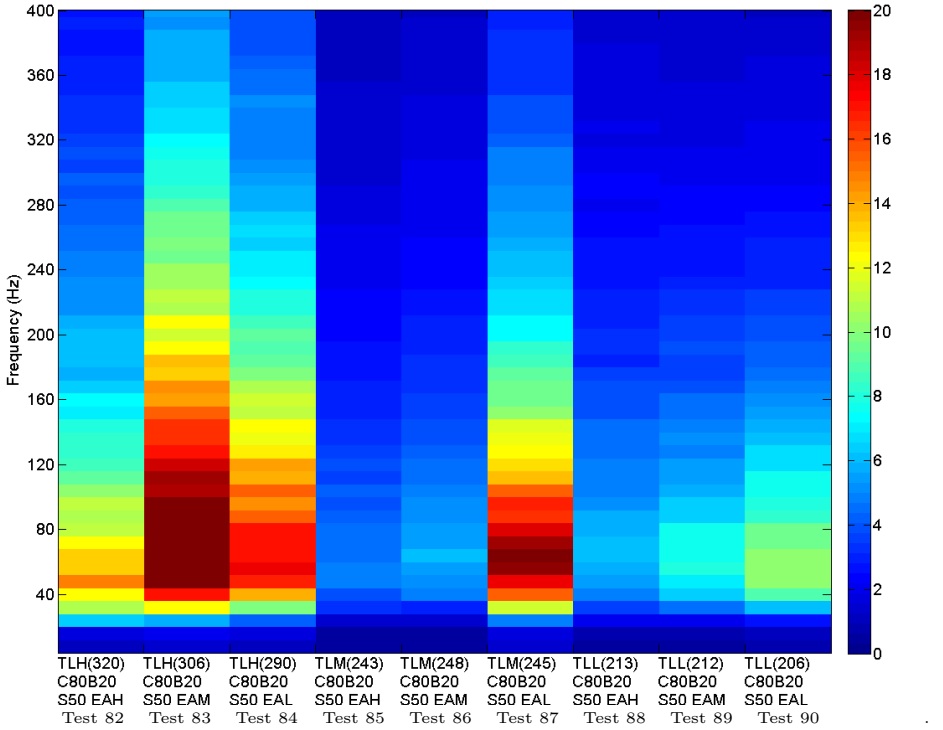

Figure B.60: WVD (averaged) of UV photodiode signal for Tests 82 to 90 - 80 % Coal & 20 % Biomass - 50° Swirl

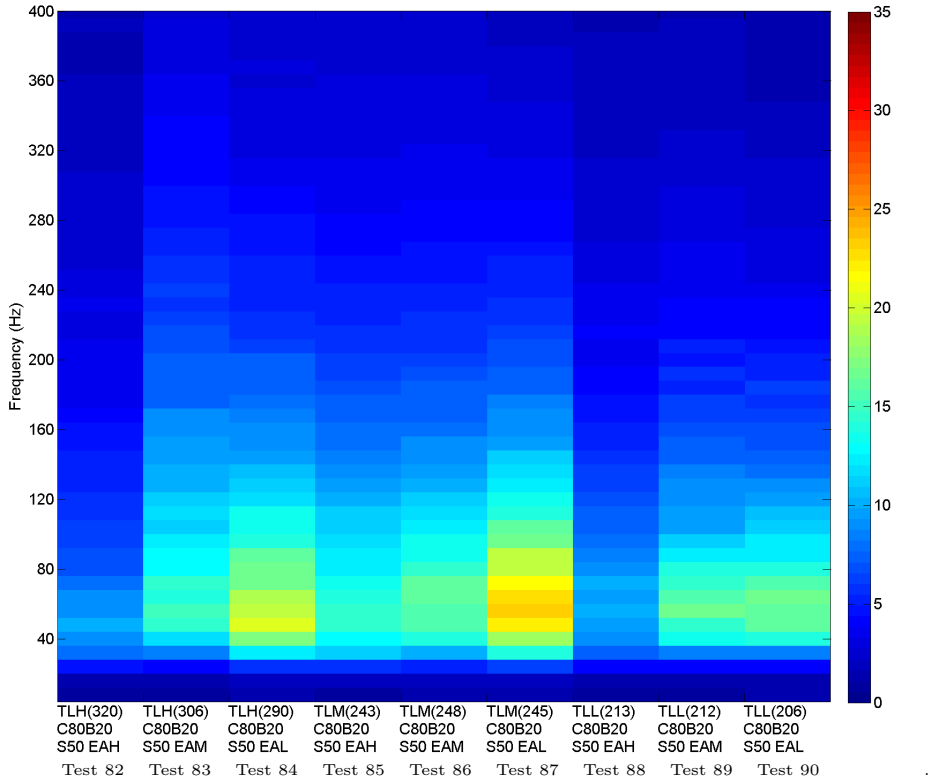

Figure B.61: WVD (averaged) of VIS photodiode signal for Tests 82 to 90 - 80 % Coal & 20 % Biomass - 50° Swirl

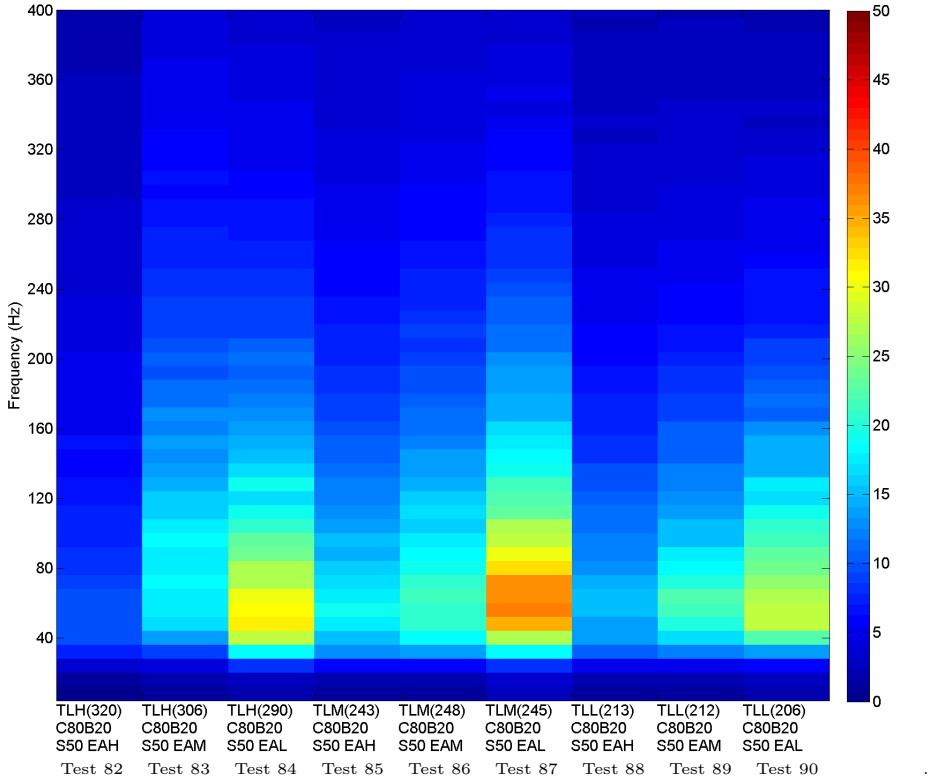

Figure B.62: WVD (averaged) of IR photodiode signal for Tests 82 to 90 - 80 % Coal & 20 % Biomass - 50° Swirl

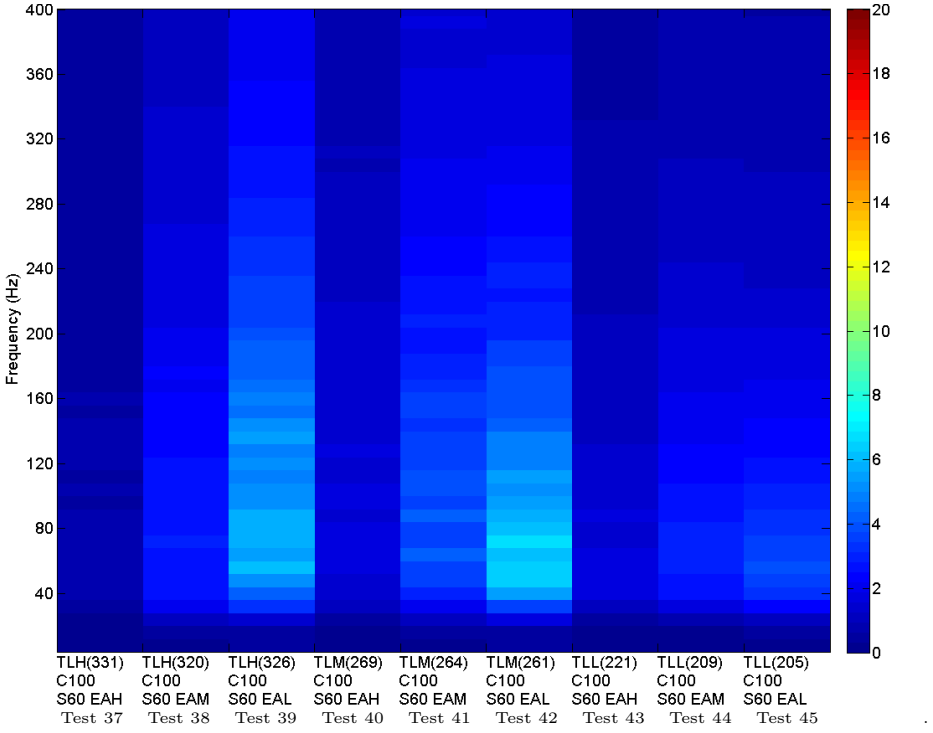

Figure B.63: WVD (averaged) of UV photodiode signal for Tests 37 to 45 - 100 % Coal - 60° Swirl

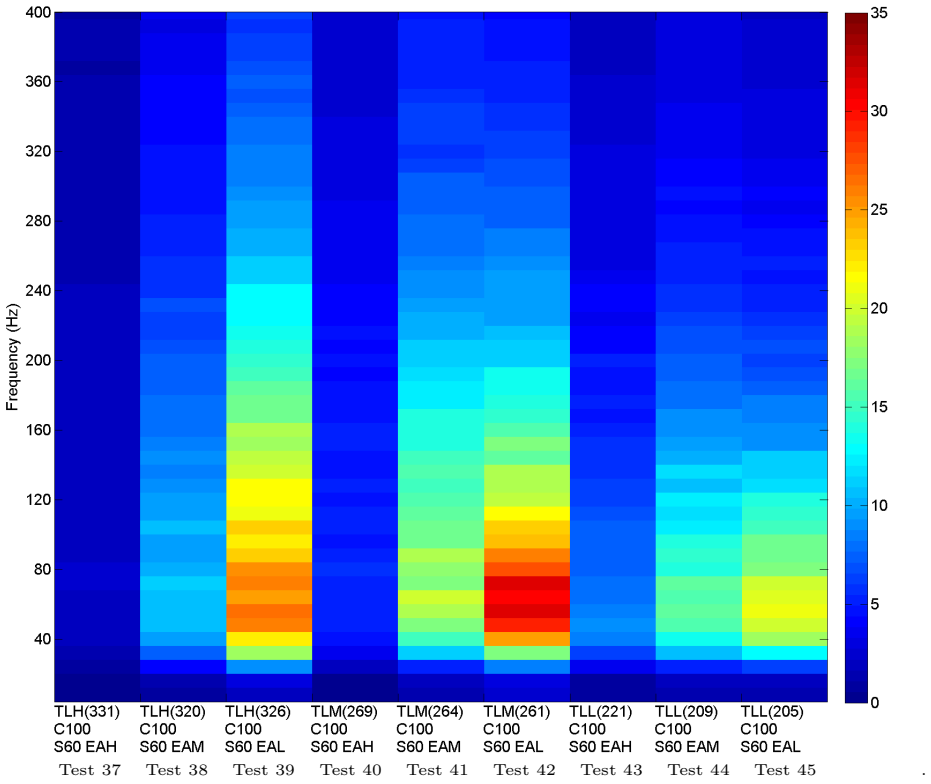

Figure B.64: WVD (averaged) of VIS photodiode signal for Tests 37 to 45 - 100 % Coal - 60° Swirl

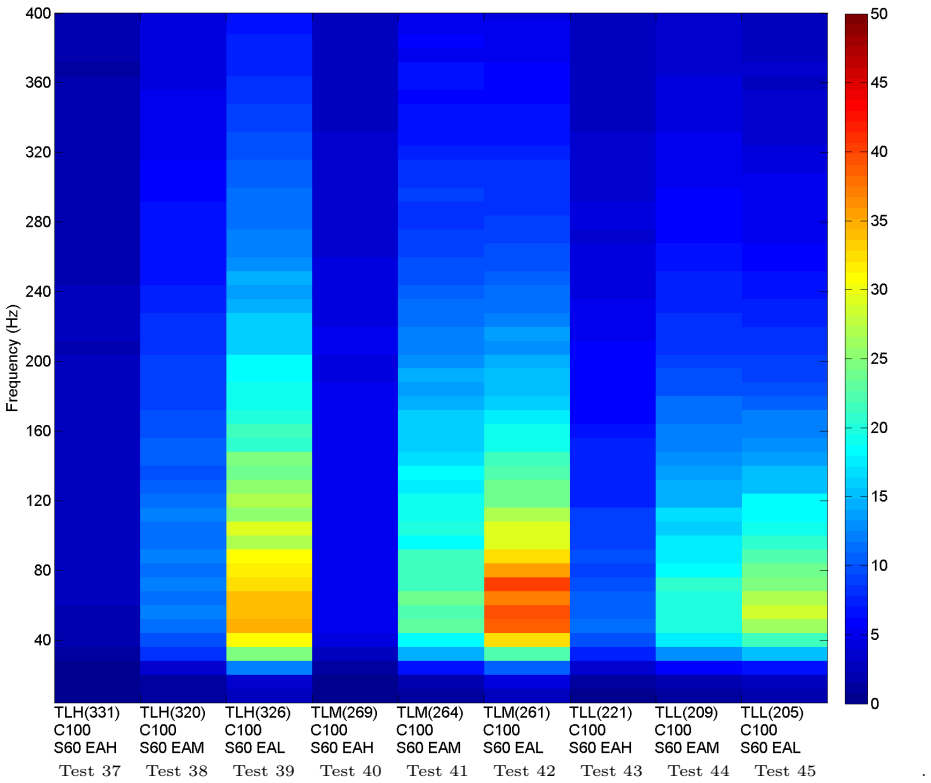

Figure B.65: WVD (averaged) of IR photodiode signal for Tests 37 to 45 - 100 % Coal - 60° Swirl

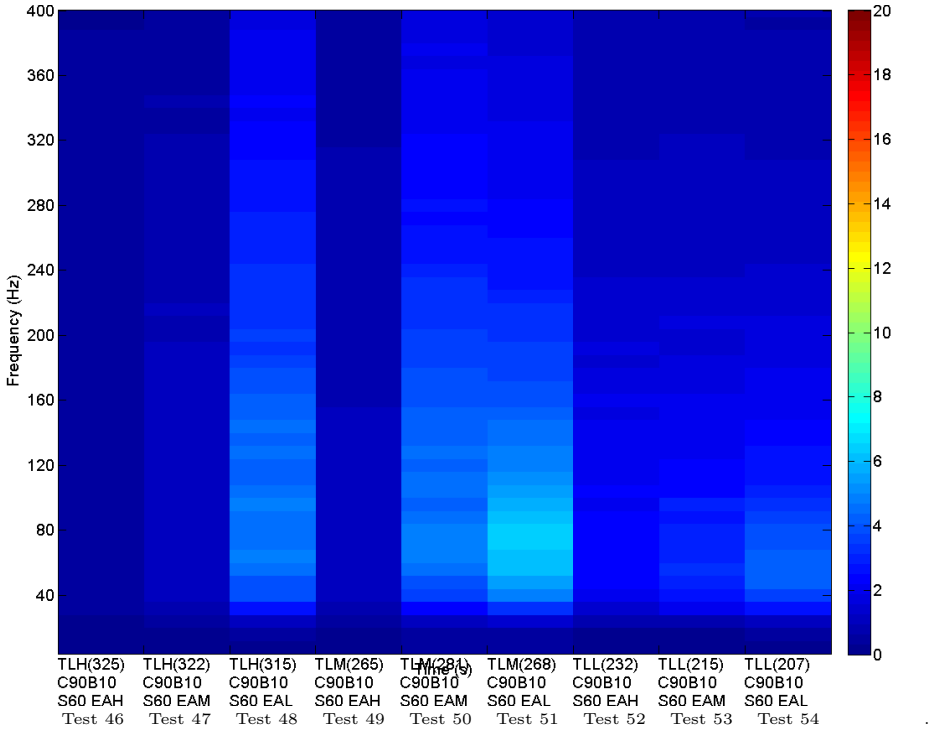

Figure B.66: WVD (averaged) of UV photodiode signal for Tests 46 to 54 - 90 % Coal & 10 % Biomass - 60° Swirl

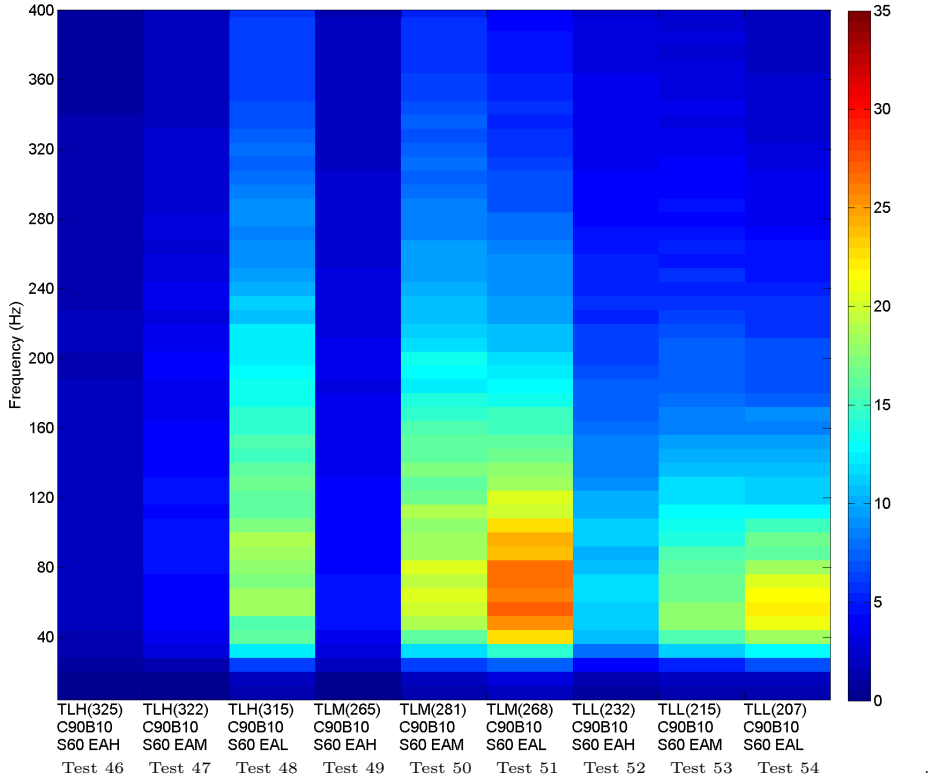

Figure B.67: WVD (averaged) of VIS photodiode signal for Tests 46 to 54 - 90 % Coal & 10 % Biomass - 60° Swirl

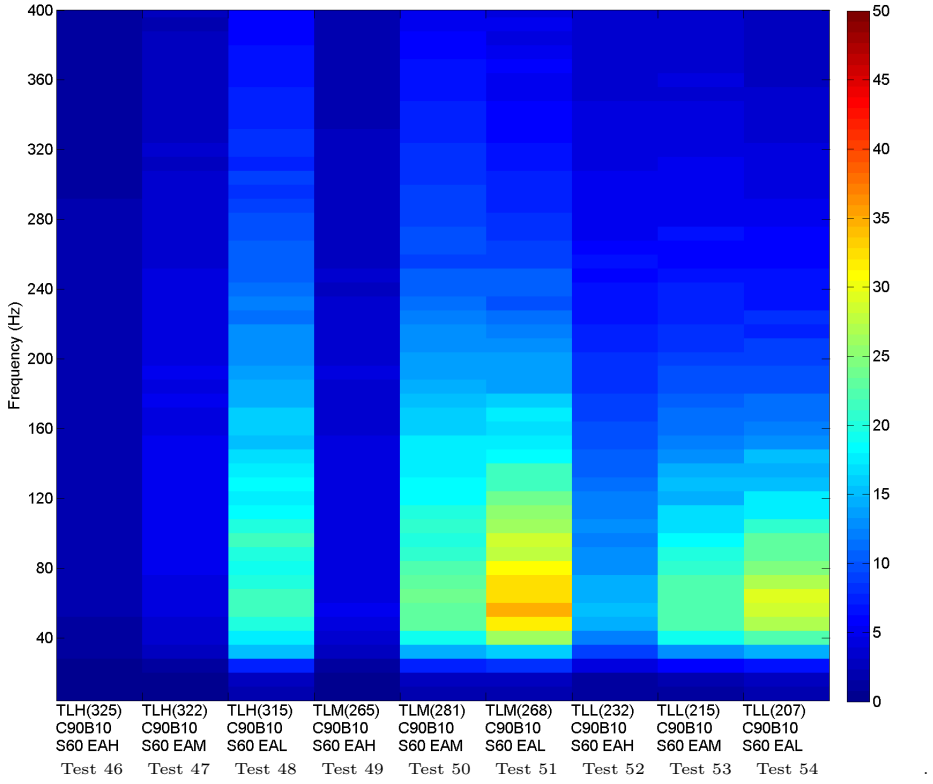

Figure B.68: WVD (averaged) of IR photodiode signal for Tests 46 to 54 - 90 % Coal & 10 % Biomass - 60° Swirl

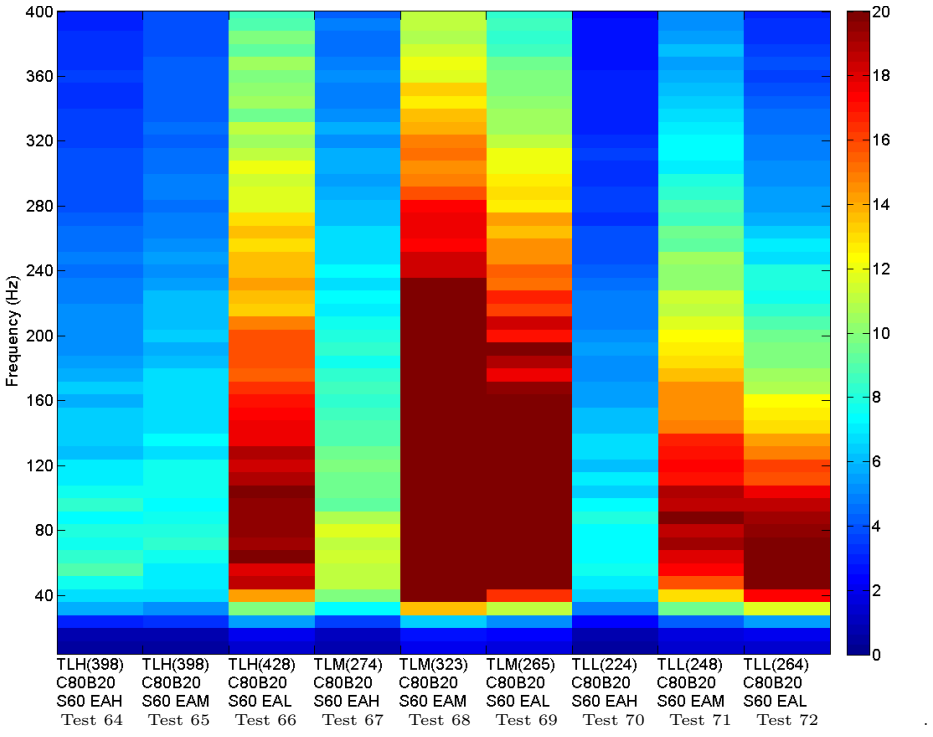

Figure B.69: WVD (averaged) of UV photodiode signal for Tests 64 to 72 - 80 % Coal & 20 % Biomass - 60° Swirl

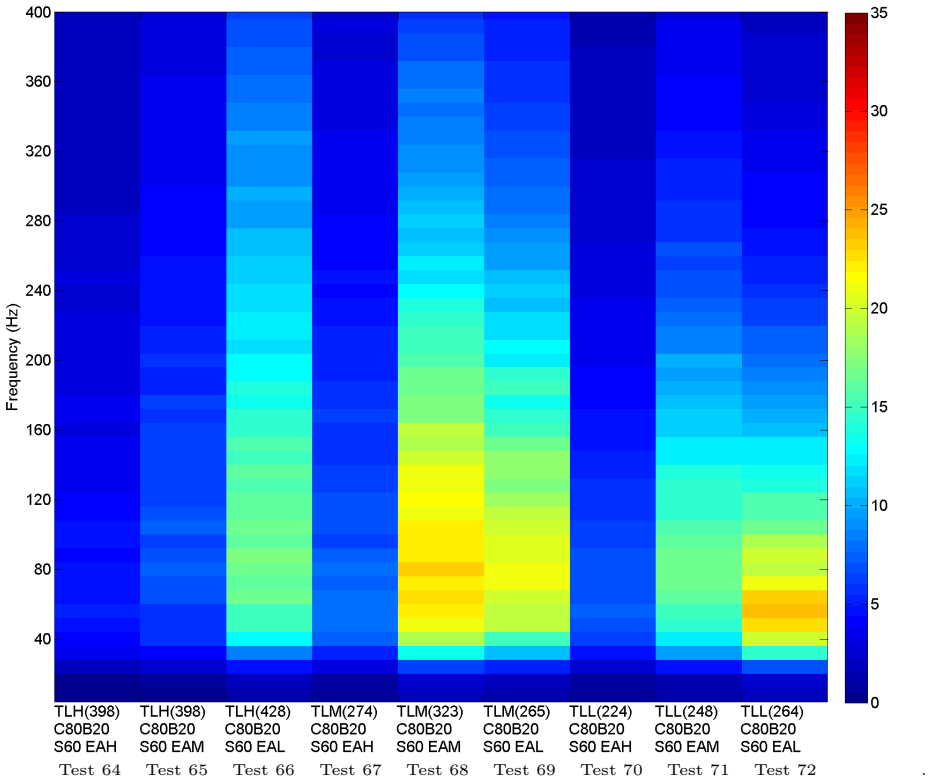

Figure B.70: WVD (averaged) of VIS photodiode signal for Tests 64 to 72 - 80 % Coal & 20 % Biomass - 60° Swirl

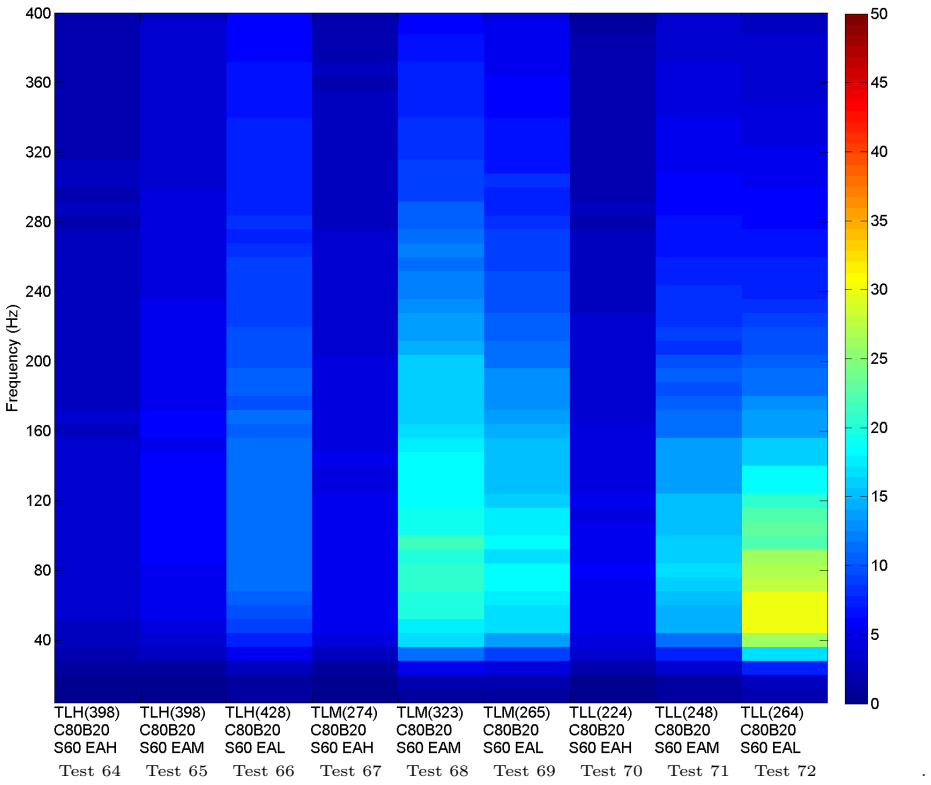

Figure B.71: WVD (averaged) of IR photodiode signal for Tests 64 to 72 - 80 % Coal & 20 % Biomass - 60° Swirl

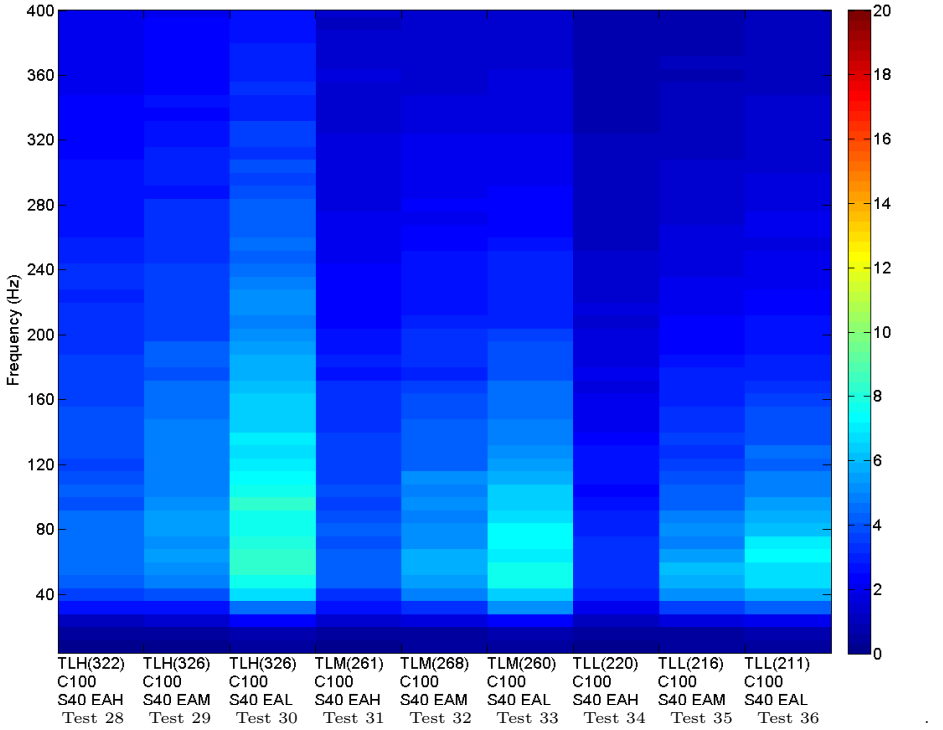

Figure B.72: WVD (averaged) of UV photodiode signal for Tests 28 to 36 - 100 % Coal - 40° Swirl

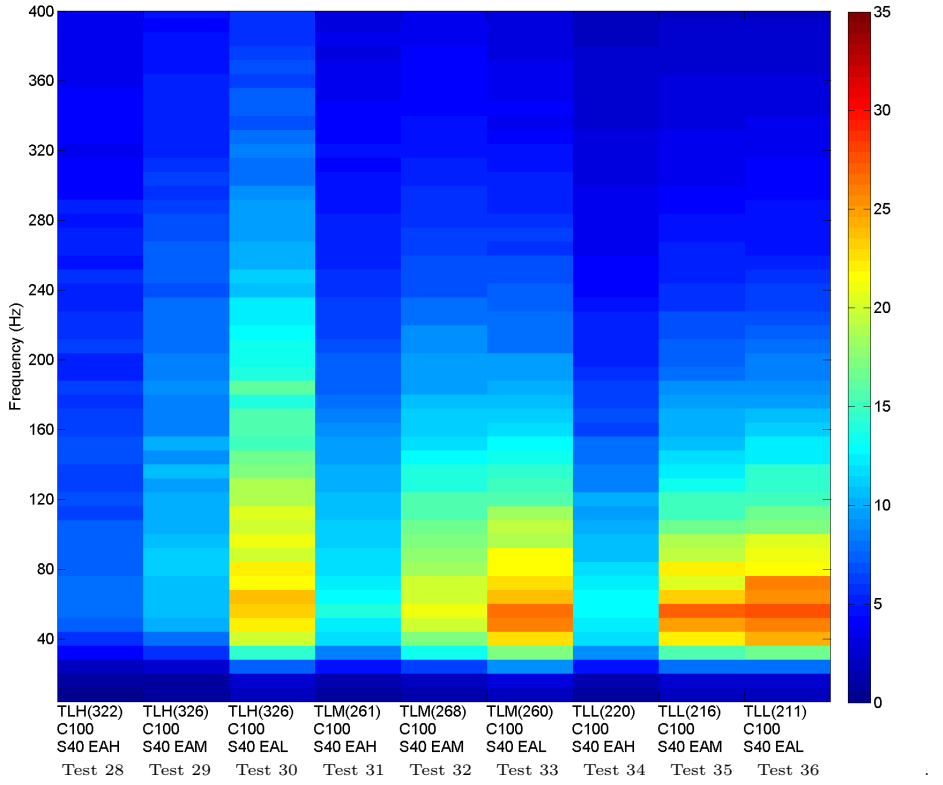

Figure B.73: WVD (averaged) of VIS photodiode signal for Tests 28 to 36 - 100 % Coal - 40° Swirl

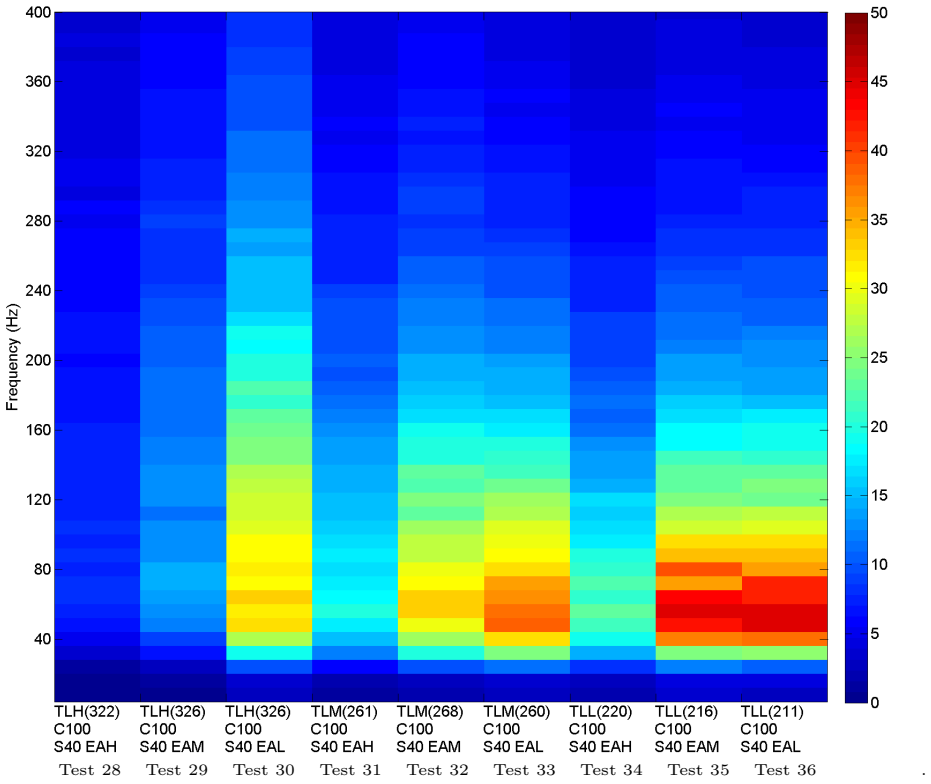

Figure B.74: WVD (averaged) of IR photodiode signal for Tests 28 to 36 - 100 % Coal - 40° Swirl

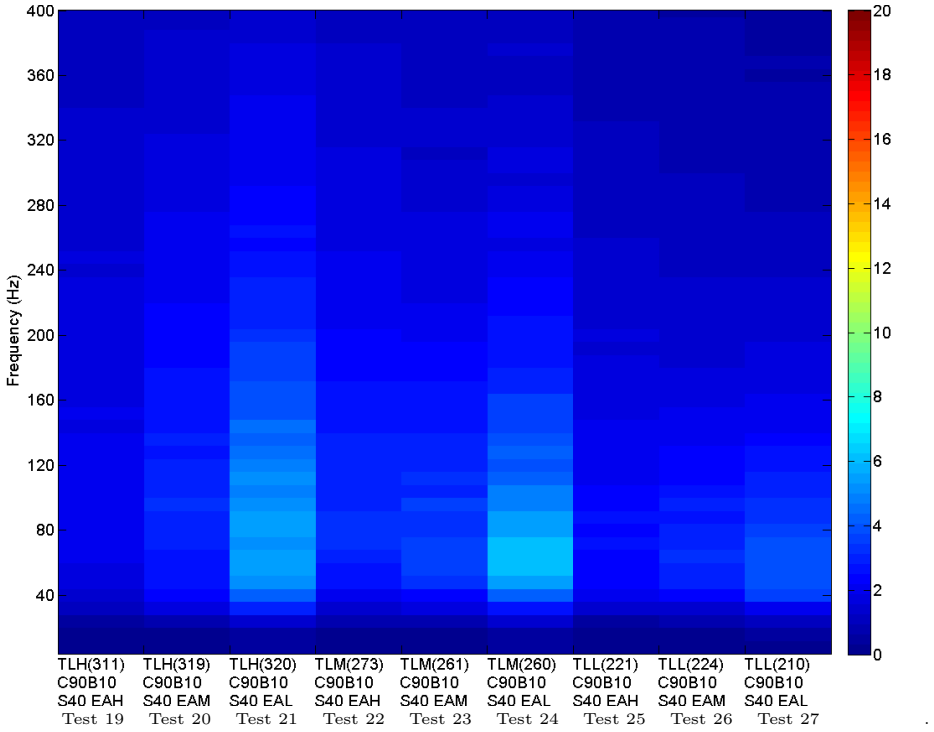

Figure B.75: WVD (averaged) of UV photodiode signal for Tests 19 to 27 - 90 % Coal & 10 % Biomass - 40° Swirl

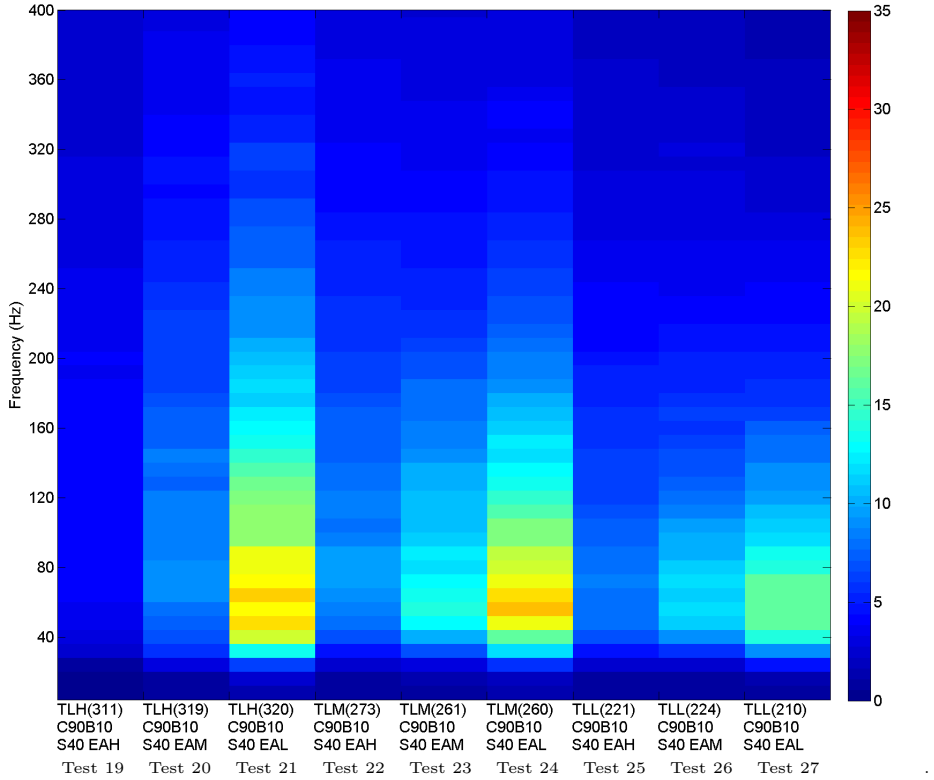

Figure B.76: WVD (averaged) of VIS photodiode signal for Tests 19 to 27 - 90 % Coal & 10 % Biomass - 40° Swirl

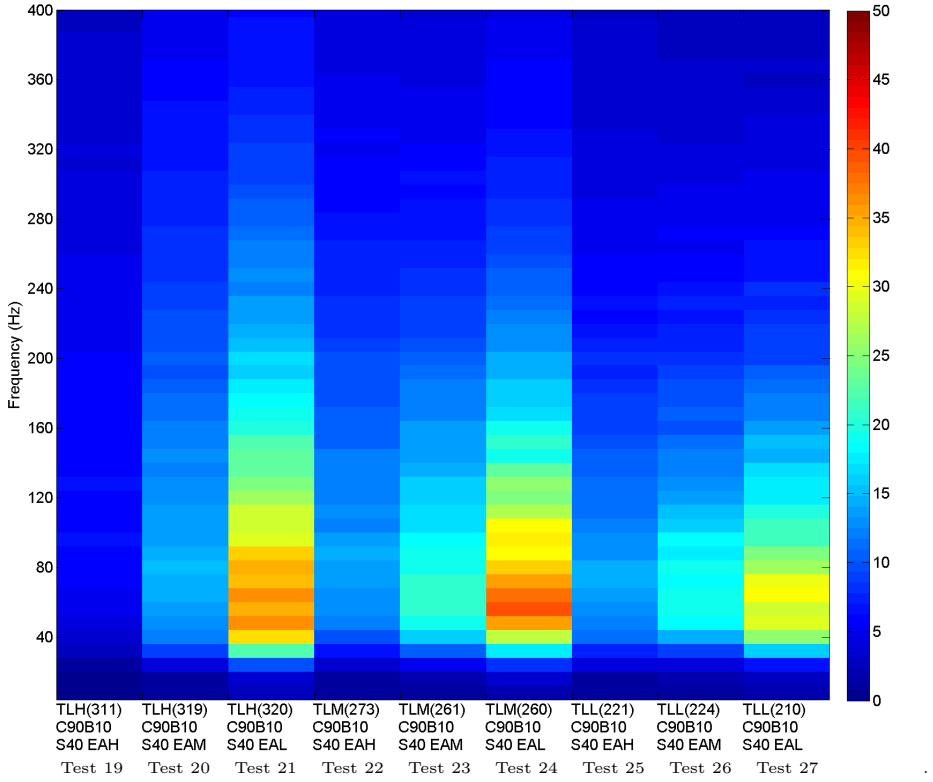

Figure B.77: WVD (averaged) of IR photodiode signal for Tests 19 to 27 - 90 % Coal & 10 % Biomass - 40° Swirl

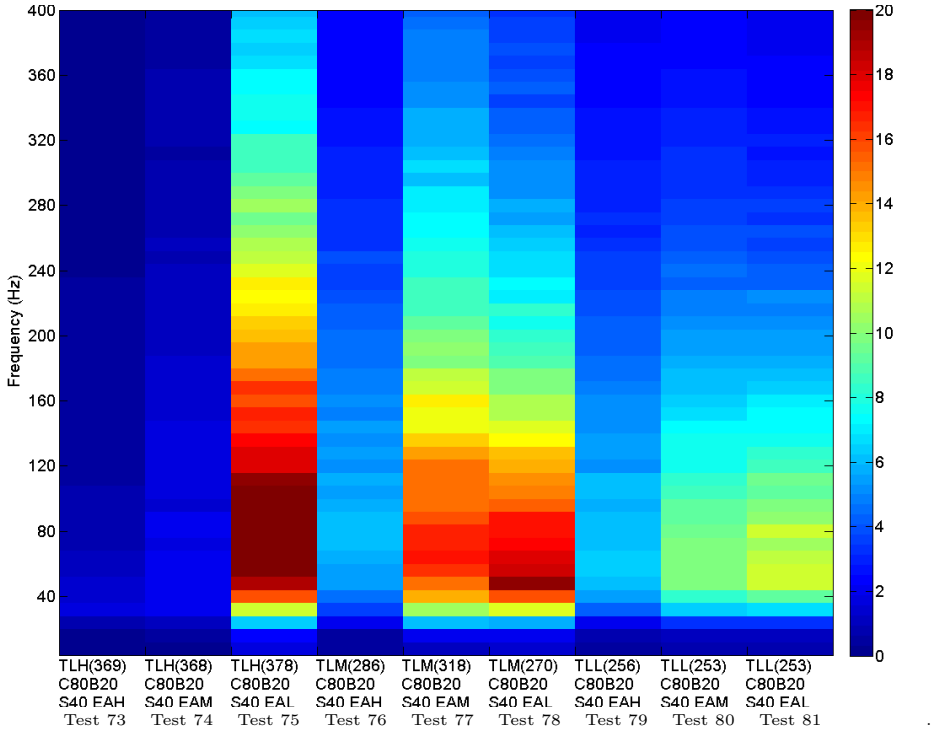

Figure B.78: WVD (averaged) of UV photodiode signal for Tests 73 to 81 - 80 % Coal & 20 % Biomass - 40° Swirl

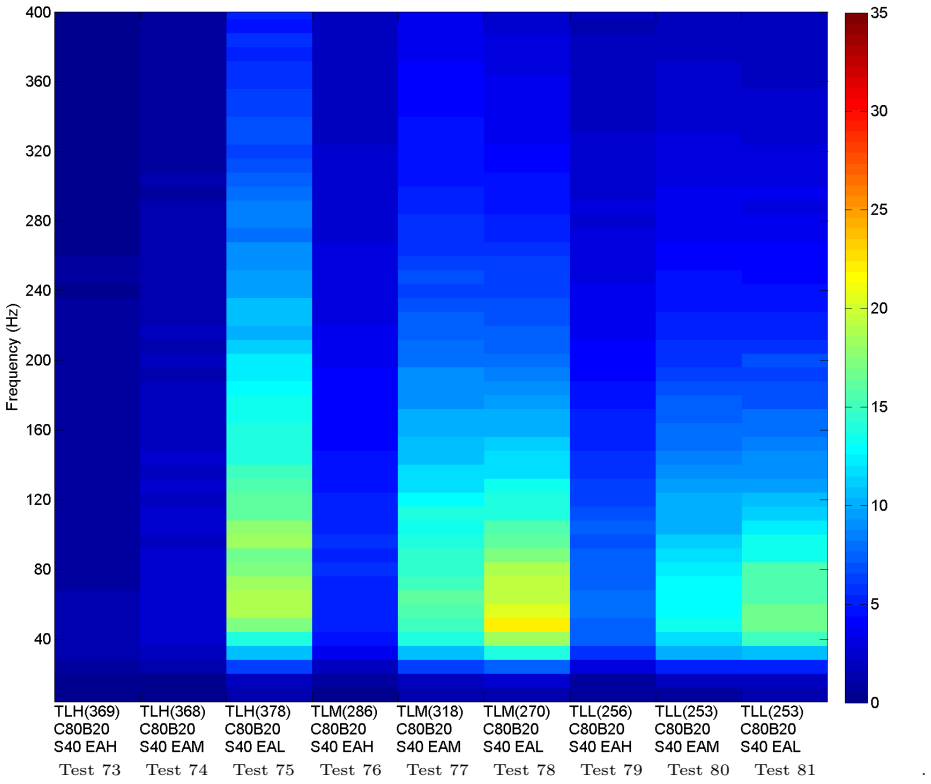

Figure B.79: WVD (averaged) of VIS photodiode signal for Tests 73 to 81 - 80 % Coal & 20 % Biomass - 40° Swirl

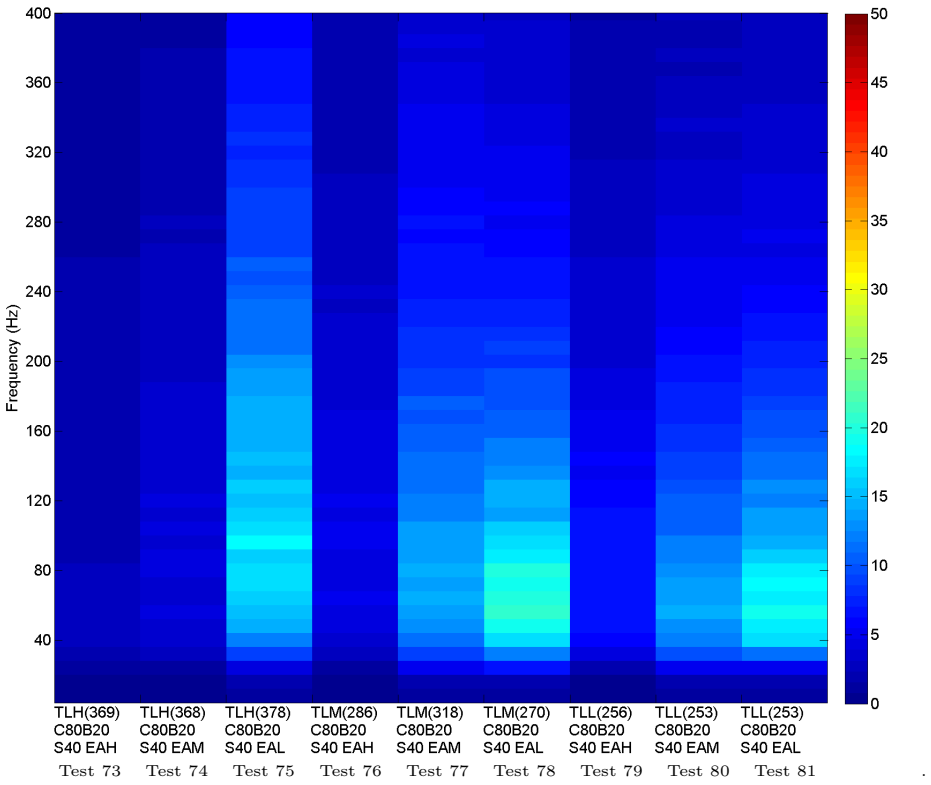

Figure B.80: WVD (averaged) of IR photodiode signal for Tests 73 to 81 - 80 % Coal & 20 % Biomass - 40° Swirl

Appendix C

WVD Results

C.1 Results for experiments with varying secondary airflow

C.1.1 UV Sensor

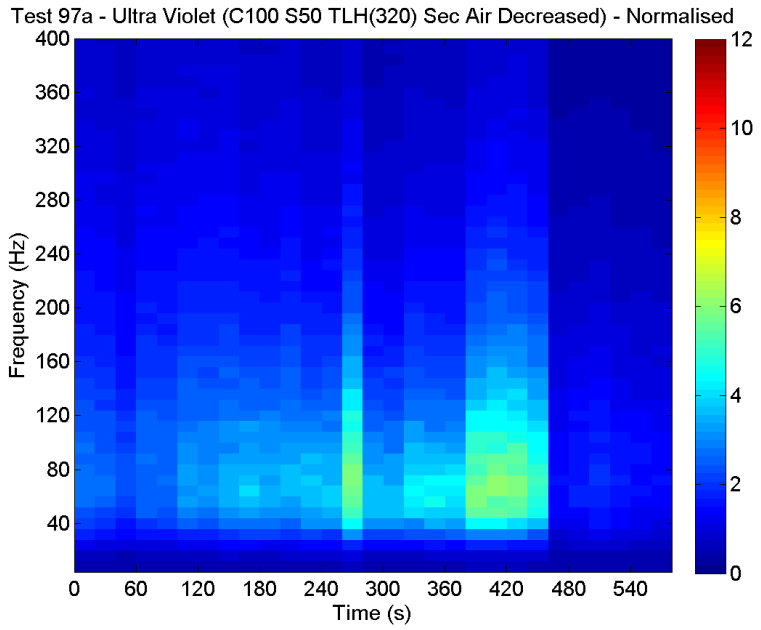

Figure C.1: WVD of the UV sensor signal for the test (Test 97a) with decreasing secondary air with 100% coal

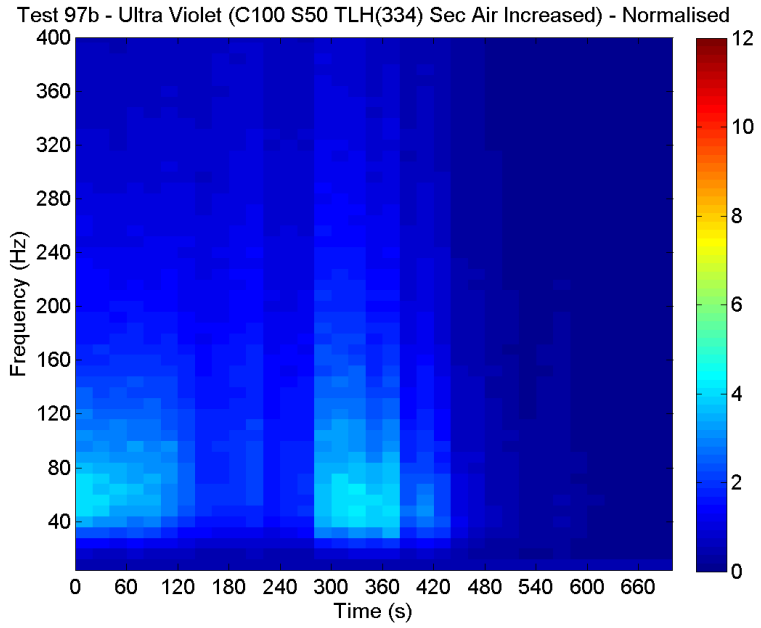

Figure C.2: WVD of the UV sensor signal for the test (Test 97b) with increasing secondary air with 100% coal

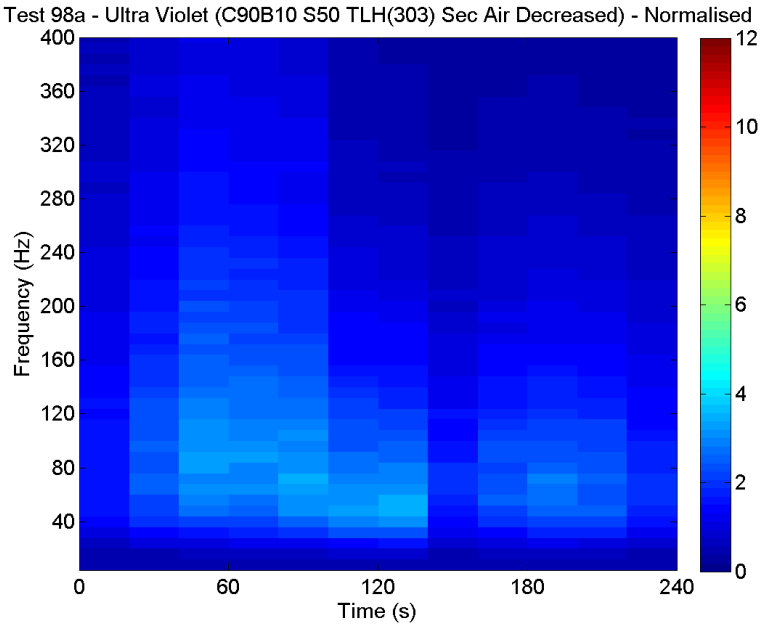

Figure C.3: WVD of the UV sensor signal for the test (Test 98a) with decreasing secondary air with 100% coal

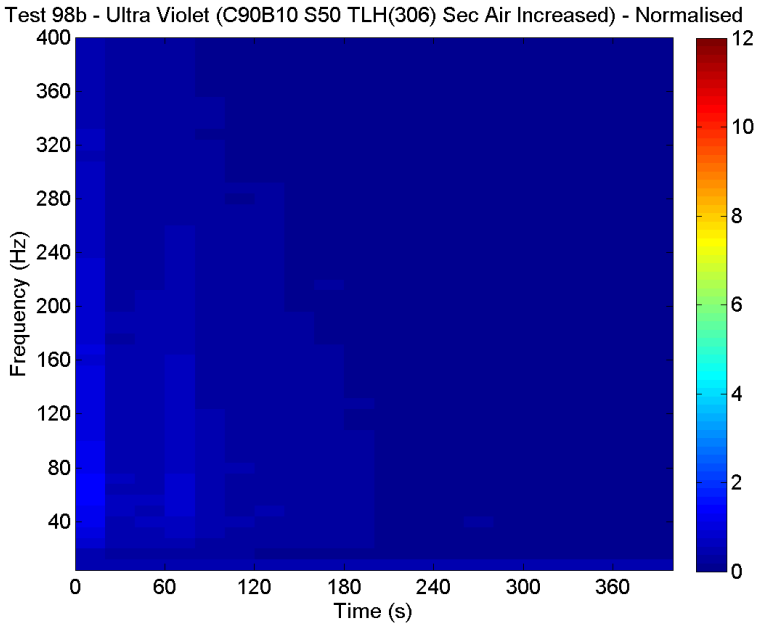

Figure C.4: WVD of the UV sensor signal for the test (Test 98b) with increasing secondary air with 100% coal

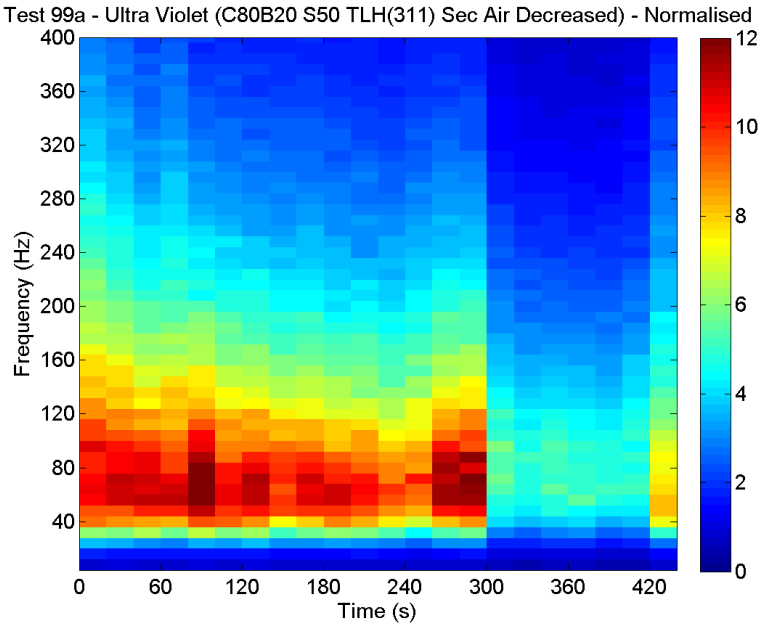

Figure C.5: WVD of the UV sensor signal for the test (Test 99a) with decreasing secondary air with 100% coal

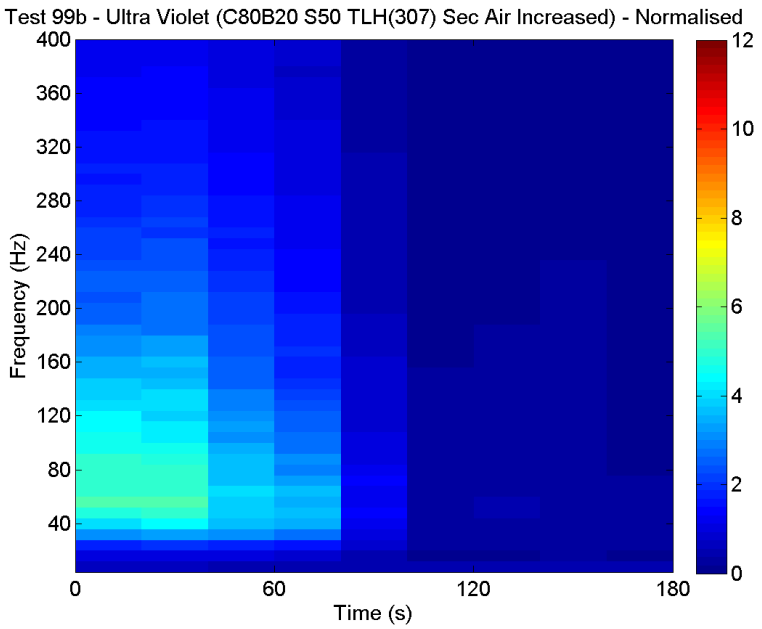

Figure C.6: WVD of the UV sensor signal for the test (Test 99b) with increasing secondary air with 100% coal

C.1.2 VIS Sensor

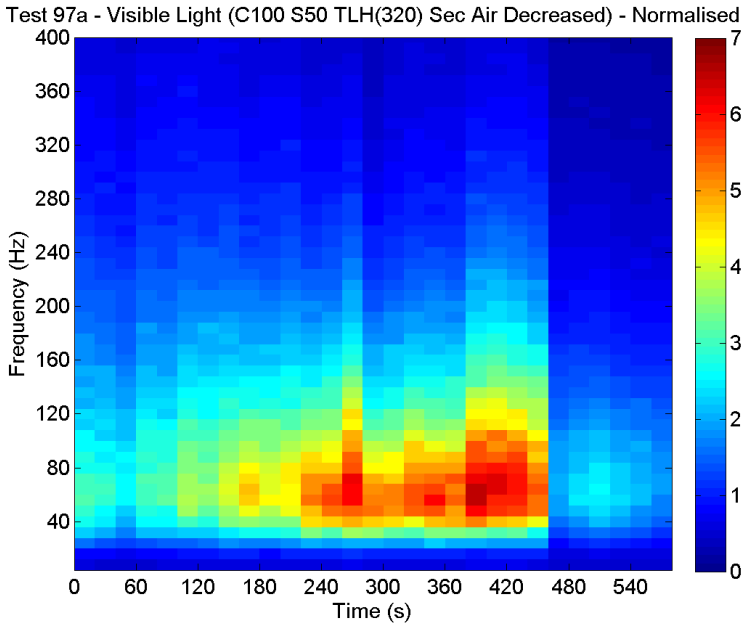

Figure C.7: WVD of the VIS sensor signal for the test (Test 97a) with decreasing secondary air with 100% coal

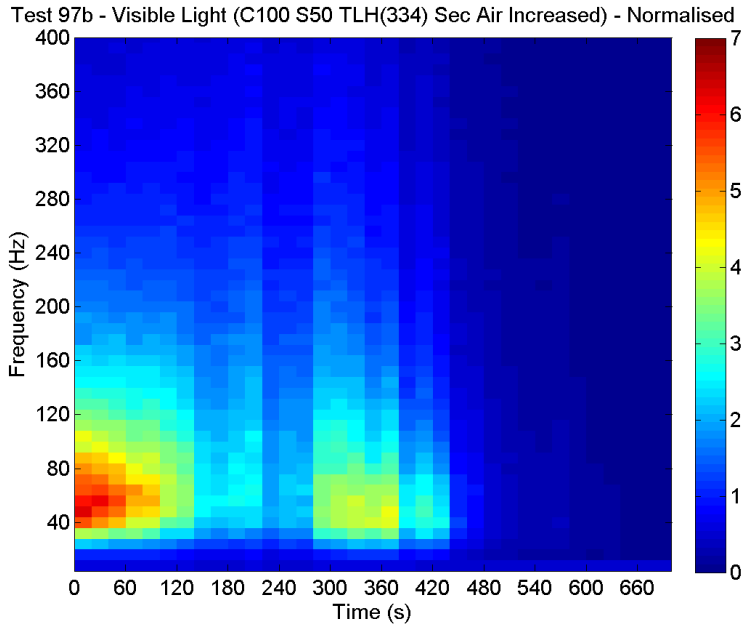

Figure C.8: WVD of the VIS sensor signal for the test (Test 97b) with increasing secondary air with 100% coal

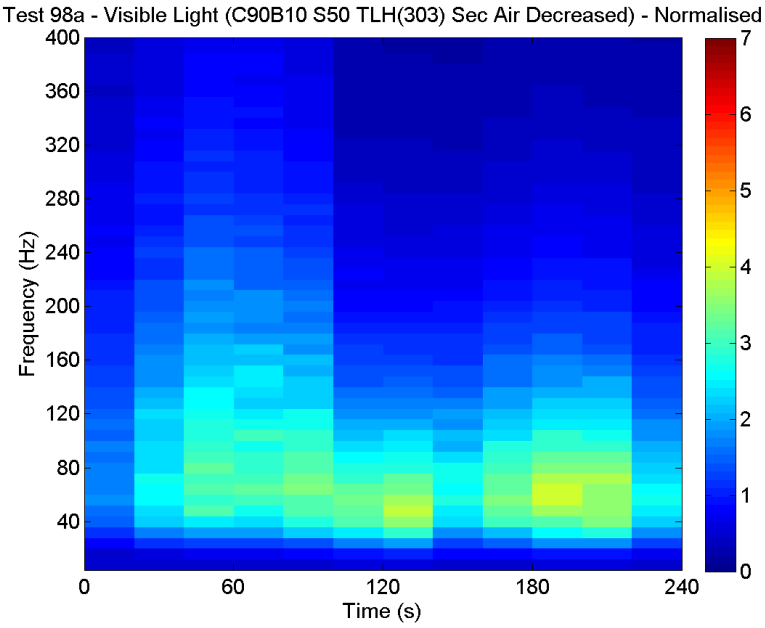

Figure C.9: WVD of the VIS sensor signal for the test (Test 98a) with decreasing secondary air with 100% coal

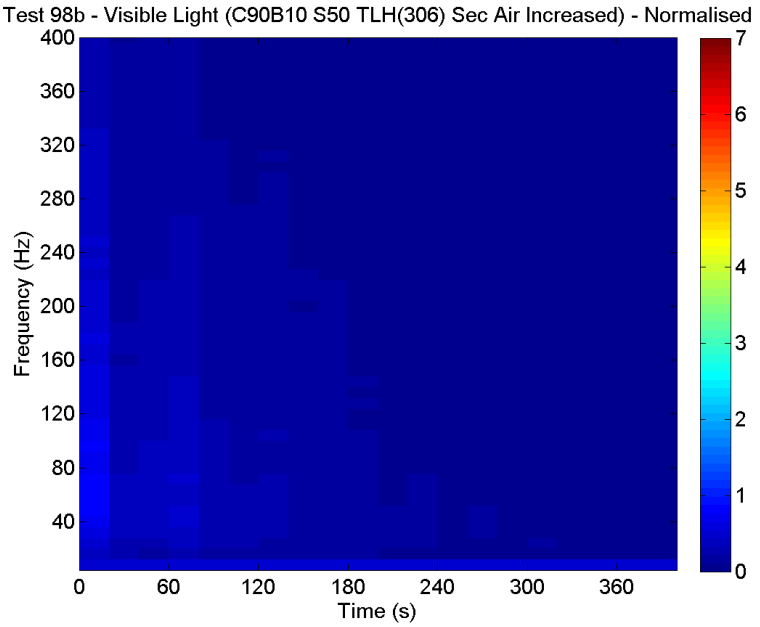

Figure C.10: WVD of the VIS sensor signal for the test (Test 98b) with increasing secondary air with 100% coal

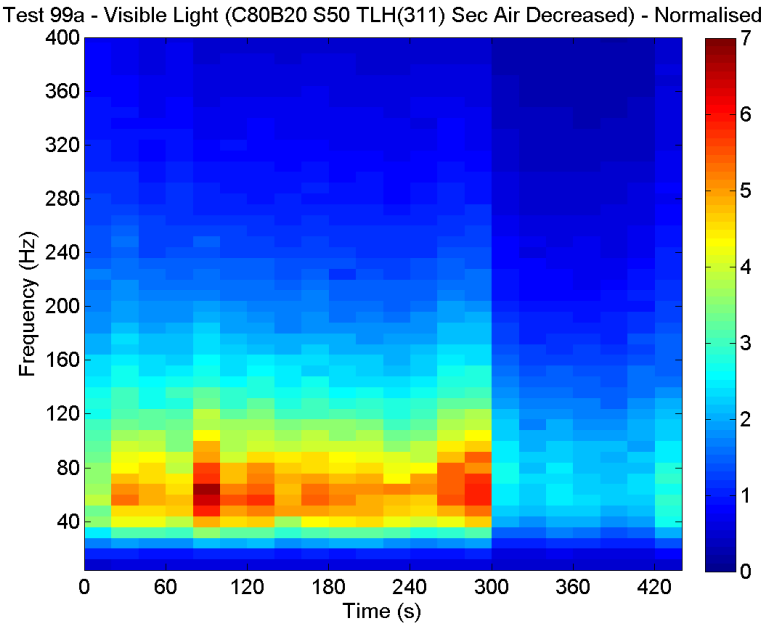

Figure C.11: WVD of the VIS sensor signal for the test (Test 99a) with decreasing secondary air with 100% coal

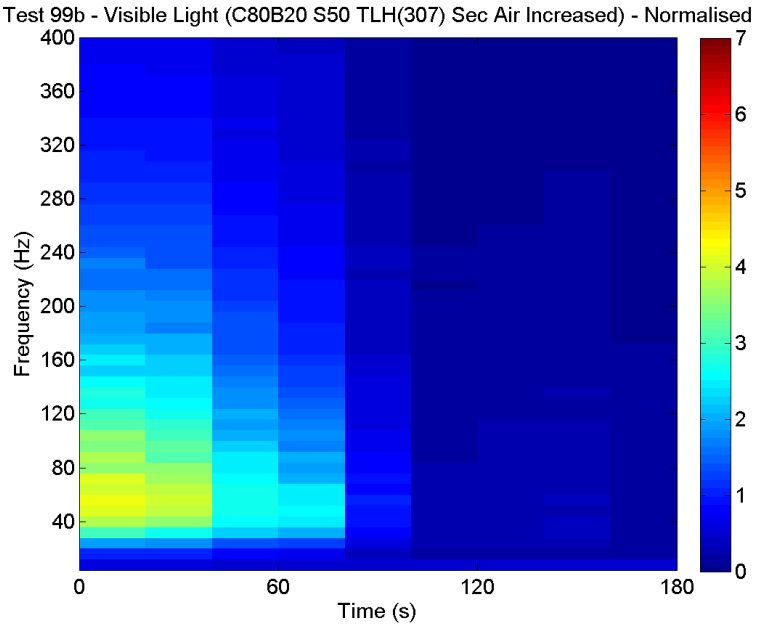

Figure C.12: WVD of the VIS sensor signal for the test (Test 99b) with increasing secondary air with 100% coal

PUBLICATIONS

1. Valliappan, P.; Thai, S. M.; Wilcox, S. J.; Ward, J.; Tan, C. K. & Jagiełło, K. "Detecting burner instabilities using joint-time frequency methods whilst co-firing coal and biomass". In: *ASME/JSME 2011 8th Thermal Engineering Joint Conference* (Mar 2011), pp. T20021-T20021-9. *doi:10.1115/AJTEC2011-44205*

2. Valliappan, P.; Jagiełło, K. & Wilcox, S. J. "The Monitoring and Control of Burners Co-Firing Coal and Biomass". In: *ASME 2012 International Design Engineering Technical Conferences and Computers and Information in Engineering Conference* (Aug 2012), pp. 139-149. *doi:10.1115/DETC2012-70237*

3. Valliappan, P.; Wilcox, S. J. & Jagiełło, K. "The Monitoring and Control of Burners Co-firing Coal and Biomass using Joint Time-Frequency Methods". In: *Combustion Diagnostics, Control, Computational Methods & Process Optimisation Conference, University of Kent* (2013).

4. Valliappan, P.; Wilcox, S. J.; Jagiełło, K. & Shao, Y. "Optimisation of Co-firing Burners". In: *Journal of Thermal Science and Engineering Applications* (May 2016). *doi:10.1115/1.4033582*